#### The Thesis entitled

# Spatio-Temporal Evolution of Spatially Confined Laser Ablative Plasma and Shockwaves: A 2D Numerical Simulative Approach

Submitted to University of Hyderabad

Towards partial fulfilment for the degree of

**Doctor of Philosophy** 

In

**Physics** 

by

D. P. S. L. Kameswari (15ACPA10)





Under the supervision of

Dr. P. Prem Kiran

Advanced Centre for Research in High Energy Materials **(ACRHEM)**School of Physics, University of Hyderabad
Hyderabad 500046, Telangana, India

Dedicated to

My Family





#### **Declaration**

I, D. P. S. L. Kameswari hereby declare that, the work reported in this thesis entitled, "Spatio-temporal evolution of spatially confined laser ablative plasma and shockwaves: a 2D numerical simulative approach", is original and has been carried out by me under the supervision of Dr. P. Prem Kiran, ACRHEM, School of Physics, University of Hyderabad, Telangana, India, as per the Ph. D ordinances of the University. I also declare that, this work is free from plagiarism and it has not been submitted for the award of a research degree at any other University. I hereby agree that my thesis can be deposited in Shodhganga or INFLIBNET.

A report on plagiarism statistics from the university library is enclosed.

(D. P. S. L. Kameswari)

Reg. No. 15ACPA10

Thesis Supervisor,

ACRHEM, School of Physics,

University of Hyderabad.

Dr. P. Prem Kiran Associate Professor School of Physics University of Hyderabad Hyderabad-500 046. (TS) INDIA





### Certificate

This is to certify that the thesis entitled "Spatio-temporal evolution of spatially confined laser ablative plasma and shockwaves: a 2D numerical simulative approach", submitted to the University of Hyderabad by Mrs. D. P. S. L. Kameswari bearing Reg. No. 15ACPA10 in partial fulfilment of the requirements for the award of Doctor of Philosophy in Physics is a bonafide work carried out by her under my supervision and guidance, which is a plagiarism free thesis. The thesis has not been submitted previously in part or in full, to this or any other University or Institution for the award of any degree or diploma.

> Dr. P. Prem Kiran Associate Professor School of Physics University of Hyderabad Hyderabad-500 046. (TS) INDIA

Thesis Supervisor,

ACRHEM, School of Physics,

University of Hyderabad.

Director,

ACRHEM,

University of Hyderabad. Director

V. Kes Line

ACRHEM

School of Physics,

M. Thanashyoun

University of Hyderabad.

DEAN School of Physics University of Hyderabad Hyderabad-500 046, INDIA



### **Certificate of Course Work**

This is to certify that the thesis entitled "Spatio-temporal evolution of spatially confined laser ablative plasma and shockwaves: a 2D numerical simulative approach", submitted to the University of Hyderabad by Mrs. D. P. S. L. Kameswari bearing Reg. No. 15ACPA10, in partial fulfilment of the requirements for the award of Doctor of Philosophy in Physics at ACRHEM, School of Physics, University of Hyderabad, is a bonafide work carried out by her under my supervision and guidance. This thesis is free from the plagiarism and has not been submitted previously in part or in full to this or any other University or Institution for the award of any degree or diploma. Further, the student has the following publications before submission of the thesis for adjudication:

- 1. **D. P. S. L. Kameswari**, Nagaraju Guthikonda, S. Sai Shiva, E. Manikanta, S. Sree Harsha, V. R.Ikkurthi and P. Prem Kiran, "Investigation of Stagnation Layer Dynamics of Counter Propagating Laser Induced Air Plasmas: Numerical simulations vis-à-vis experimental observations", Phys. Plasmas **28**, 043104 (2021) (**Chapter 4**)
- 2. Nagaraju Guthikonda, S. Sai Shiva, E. Manikanta, **D. P. S. L. Kameswari**, Ikkurthi, V. R, C. D. Sijoy, Prem Kiran Paturi, "Effect of Focusing Plane on Laser Blow-off Shock Waves from Confined Aluminum and Copper Foils", J. Phys. D: Appl. Phys. **55** 115202 (2021) (**Chapter-6**)
- 3. **D. P. S. L. Kameswari**, P. Prem Kiran, "Temperature evolution in silver nanoparticle doped PETN composite", AIP Conference Proceedings 1942(1):140051(2018) (Chapter 7)

Also, made presentations in the following conferences

- D. P. S. L. Kameswari, G. Nagaraju, S. Sai Shiva, P. Prem Kiran, "A Comparative Study of Laser Induced Ablative and Blow-off Pressures for Varied Foil Thickness", HEMCE 2019, 16th – 18th December, 2019, IITM, Chennai (Poster) (Received Best Outstanding Paper Award)
- D. P. S. L. Kameswari, Nagaraju guthikonda, S. Sai Shiva, E. Manikanta, S. Sree Harsha, V. R. Ikkurthi, P. Prem Kiran, "Dynamics Of Collinear Counterpropagating Laser Plasmas Under Ambient Atmospheric Conditions", IEEE International Conference on Plasma Science (ICOPS-2020), 6th – 10th December 2020, Online Conference (Oral) (Abstract to be published in IEEE Transactions on Plasma Sciences)

Further, the student has passed the following courses towards fulfilment of coursework requirement for Ph.D.

Course No.	Course Offered at	Title of the Course	Credits	Pass/Fail
PY804	School of Physics	Advanced Electro Magnetic Theory	4	Pass
PY805	School of Physics	Advanced Statistical Mechanics	4	Pass
PY804	School of Physics	Advanced Mathematical Methods	4	Pass
PY801	ACRHEM	Research Methodology	4	Pass

Dr. P. Prem Kiran
Associate Professor
School of Physics
University of Hyderabad
Hyderabad-500 046. (TS) INDIA

). () rem (1 vow) Dr. Prem Kiran) 29/12/21

Thesis Supervisor,

ACRHEM, School of Physics,

University of Hyderabad.

Director,

ACRHEM,

University of Hyderabad.

Director

M. Manashyam

School of Physics,

University of Hyderabad.

DEAN

School of Physics

University of Hyderabad

Hyderabad-500 046, INDIA

### **Acknowledgements**

I take this opportunity to thank the following people who has laid a basis to my education and who has been continuously lending their support and motivating me towards my goal.

Firstly, my sincere thanks to my supervisor *Dr. P. Prem Kiran*, who has been supporting and mentoring me throughout my Ph. D. I am immensely thankful to him for giving me a platform to resume my carrier in research field. He has been encouraging in viewing problems from new perspective and finding the solutions, in understanding the underlying physics and establishing the simulations for real time experiments. His wonderful support and encouragement helped a lot for the progress of my work.

My extended and sincere thanks to my doctoral committee members *Dr. G. Manoj Kumar* and *Dr. Nirmal K Viswanathan* for their constructive comments and suggestions. I am thankful to *Prof. Soma Venugopal, Prof. A. K. Chaudhary, Dr. G. S. Vaitheeswaran* for teaching Research methodology.

It is my pleasure to thank the past director *Dr. Venkateswara Rao*, and the present director *Dr. V. Kameswara Rao*, ACRHEM; *Prof. Ashok Chatterjee*, Dean School of Physics (SoP); former deans of SoP, University of Hyderabad, for their support towards completion of this work. I would like to thank DRDO, Govt of India through ACRHEM for their financial support and office staff (ACRHEM and School of Physics) for their administrative support.

My sincere thanks to *Dr. Sree Harsha* for his thought provoking discussions, *Dr. Sai Shiva* for his extended support throughout my Ph. D, *Dr. Manikanta* for his suggestions and fruitful discussions, *Dr. G. Nagaraju* for his experimental support and fruitful discussions. I am thankful to all my other seniors *Dr. Ch. Leela*, *Dr. Rakesh*, *Dr. Venkateswarlu* and group members *Mr. Samuel Anurag* and *Mr. Yelliah* for their help in academics. My special thanks to *Dr. Bharathi* for being with me in all my ups and downs, other friends and batch mates *Dr. Rajender*, *Dr. Chandu*, *Mr. Prathap*, *Mr. Subrotho*, *Mr. John*. I would like to thank all my ACRHEM and School of Physics friends for helping and supporting me unconditionally on this long and sometimes difficult journey.

I am grateful to *Dr. K. P. N. Murthy* my M. Tech supervisor who has led me in a right path during and after M. Tech with his suggestions and help. I am thankful to *Mr. Williams*, Physics lecturer in graduation, *Mr. Veerabhadra Rao*, school teacher for their trust on me. My special, heartfelt thanks to my dear husband *Mr. Girish Kumar*. Just a thanks is not sufficient for his

understanding my efforts and leading me to complete this Ph.D. My kids *Ms. Samyuktha* and *Master Jhaswanth* for teaching me patience and their endless affection, my In-Laws *Mr. Gandhi Naidu* and *Mrs. Bharathi* for understanding me and supporting me in all times. I am grateful to my parents *Mr. Subbarao*, *Mrs. Sitamaha Lakshmi* for their endless affection and always aimed at leading me towards a higher position, my sister *Mrs. Sampath Kumari* for her useful subjective doubts and all my cousin brothers for their support whenever required.

D. P. S. L. Kameswari

# **Contents**

Chapter-1	1
Introduction	1
1.1 Laser generated plasma from a so	lid target3
1.2 Laser Induced breakdown in air	3
1.3 Confinement of laser generated p	lasma4
1.4 Geometric confinement of laser g	renerated plasma5
1.5 Magnetic confinement of laser ge	nerated plasma9
1.6 Electrical confinement of laser gener	ated plasma10
1.7 Organization of the thesis	11
1.8 References	14
Chapter-2	20
Simulation Methodology	20
2.1 Introduction	21
2.1.1 Hydrodynamic formulation	23
2.1.3 Shock Tube Problem	26
2.2 Hydrodynamics of Laser Ablation	30
2.2.1 Evolution of Physical Parameters	34
2.3 Summary	
2.4 References:	38
Chapter-3	40
An Insight Into Laser Induced Air Plasma	40
3.1 Introduction	41
3.1.1 Simulation details	42
3.2 Inverse Bremsstrahlung absorption	43
3.3 Axi-symmetric evolution of plasma a	nd shock waves44
3.4 Effect of input laser intensity	51
3.4.1 Effect of energy	51
3.4.2 Effect of pulse duration & beam	waist56
3.5 Conclusion	58
3.6 References	58
Chapter-4	62
Interaction of Two Counter Propagating L	aser Induced Air Plasmas62

4.1 Introduction	63
4.1.1 Simulation details	65
4.2 Interaction of unequal energy sources	66
4.2.1 Stagnation layer dynamics in the unequal source interaction	68
4.2.2 Temporal evolution of electron temperature at stagnation layer	71
4.2.3 Shock wave dynamics for unequal source interaction $(S_1:S_2=1:2)$	73
4.3 Interaction dynamics of two equal sources separated by 4 mm	75
4.3.1 Stagnation layer dynamics in case of equal source interaction $(S_1:S_2=1:1)$	76
4.3.2 Temporal evolution of electron temperature at interaction zone	77
4.4 Temporal evolution of plasma parameters in counter propagating equal ( $S_1$ : $S_2$ = unequal sources ( $S_1$ : $S_2$ = 1:2)	-
4.5 Effect of separation distance on plasma parameters	82
4.5.1 Comparison of temporal evolution of plasma parameters for varied separation between seed plasmas	
4.5.2 Mass density with respect to separation distance	87
4.6 Conclusions	93
4.7 References	94
Chapter -5	97
Dynamics of Radially Confined Plasma and Shock Waves	97
5.1 Introduction	98
5.1.1 Simulation details	99
5.2 Plasma and SW dynamics in confined geometry	100
5.2.1 Internal dynamics during SW reflection	102
5.2.2 Electron Temperature and Electron Number Density	103
5.3 Effect of laser energy on SW and plasma dynamics	105
5.3.1 Electron temperature and number density	109
5.4 Effect of separation distance and material of confining geometry on SW and plas dynamics	
5.5 Plasma interaction with cavity material (d = 2 mm)	120
5.6 Conclusion	121
5.7 References	122
Chapter-6	125
Laser Irradiated Aluminum foil: ablation and blow-off shock waves	125
6.1 Introduction	126
6.2 Laser ablation from a thin foil	128

6.2.1 Spatio - temporal evolution of plasma and shock wave parameters	28
6.2.2 Effect of background gas pressure on SW and plasma parameters13	5
6.2.3 Effect of background gas: Air Vs Helium	8
6.3 Axial confinement using glass substrate	-1
6.4 Radial confinement of blow-off shock wave	4
6.5 Conclusions	-8
6.6 References	.9
Chapter -7	2
Laser Interaction of nanoparticle doped HEMs15	2
7.1 Introduction	3
7.2 Hot Spot Model	4
7.3 Optical Absorption and Scattering	5
7.3.1 Effect of metal nanoparticles on optical absorption	5
7.3.2 Effect of Hem on optical absorption	1
7.4 Thermal Conduction16	4
7.5 Conclusions	7
7.6 References	8
Chapter-8	0'
Conclusions and Future Scope	'O

# **List of Figures**

Fig. 1. 1 A schematic showing the interaction of a shock wave interacting and reflecting from a	
solid wall	
Fig. 1. 2 A schematic showing the illustration of laser driven blow-off	7
Fig. 1. 3 Schematic showing the confinement of laser generated from aluminium target using	
transverse magnetic field	9
Fig. 2. 1 Flow chart showing the procedure followed while solving a physical problem	23
Fig. 2. 2 A schematic showing the method followed in the design of a macro shock tube	
Fig. 2. 3 Infinitesimal volume showing from which a fluid is flowing	
Fig. 2. 4 A schematic of shock tube	
Fig. 2. 5 Spatial variation of (a) energy (b) pressure (c) density (d) velocity inside a shock tube	
driven from driver section	28
Fig. 2. 6 Spatial variation of the cell centred flux variables (a) mass density, (b) momentum	
density and (c) energy density inside the shock tube	29
Fig. 2. 7 Simulation domain	
Fig. 2. 8 A schematic of adaptive mesh refinement (AMR) showing more refinement near high	
density gradients (shown in zoomed view) and less refinement at low density gradients	
Fig. 2. 9 Evolution of electron temperature shown at (a) 10 ns and (b) 20 ns for the input laser	
energy of 50 mJ	
Fig. 2. 10 Spatio -temporal evolution of (a) pressure, (b) mass density and (c) electron	٠,
temperature for the input laser energy of 50 mJ. The solid line at $Z=0$ represents the position of	of
the target	
Fig. 3. 1 Simulation domain describing the direction (Z) of the laser beam, red color region	
describing the focal region where the laser beam is focused	
Fig. 3. 2 Spatial evolution of electron temperature at (a) 25 ns, (b) 50 ns, (c) 100 ns, (d) 500 ns	
and (e) a line profile of electron temperature at 25, 50, 100 and 500 ns along the laser	
propagation axis generated using 50 mJ laser source.	
Fig. 3. 3 (a) Spatial variation of mass density at (a) 0.5, (b) 1, (c) 2 and (d) 5 µs respectively and	
(e) line profile of mass density along the laser propagation axis for the input laser energy of 50	
mJ	
Fig. 3. 4 (a) Spatio-temporal evolution of mass density and (b) two dimensional view of electrons	
temperature at 20 us for the input laser energy of 50 mJ	••••
Fig. 3. 5 A comparison of the simulated shock velocities with the experimental velocities [51]	
along (a) -Z and (b) +Z directions for the input laser energy of 50 mJ	49
Fig. 3. 6 Temporal evolution of electron temperature and electron number density over a	
duration of 20 µs for the input laser energy of 50 mJ	
Fig. 3. 7 Spatial evolution of mass density at 0.5, 1 and 5 $\mu s$ for the input laser energy of (a) – (	
50 mJ, (d) – (f) 100 mJ, (g) - (i) 200 mJ and (j) - (l) 500 mJ respectively	51
Fig. 3. 8 Comparison of shock velocities along -Z and +Z directions respectively for the input	-
laser energy of (a-b) 50, (c-d) 100, (e-f) 200 and (g-h) 500 mJ respectively	53

Fig. 3. 9 Comparison of (a) electron temperature and (b) electron number density of the plasma along the laser propagation axis with respect to the input laser energy 50, 100, 200 and 500 mJ.55 Fig. 3. 10 Comparison of the spatial evolution of electron temperature with respect to the incident pulse duration (a –c) with $\tau$ = 7ns and (d -f) with $\tau$ = 10 ns at 0.5, 1 and 5 $\mu$ s respectively for the input laser energy of 50 mJ
Fig. 4. 1 Simulation domain showing the focal regions at which the laser beams were focused and the separation distance between the two sources 66
Fig. 4. 2 A comparison of evolution of (a) $-$ (f) simulated mass density and (g) $-$ (l) shadowgram images [24] at 1, 2, 5, 10, 20 and 30 $\mu$ s, for the case S1:S2 =1:2
Fig. 4. 4 Temporal evolution of electron temperature at stagnation layer Z=0, -0.5 mm (towards S1) and 0.5 mm (towards S2) formed due to interaction of 1:2 sources separated by d=4 mm71 Fig. 4. 5 Comparison of axial variation of shock radius source S1 along (a) -Z, (b) +Z and from source S2 along (c) –Z and (d) +Z directions respectively
when two unequal sources were interacting
Fig. 4. 8 Axial variation of (a) mass density, (b) pressure, (c) electron number and (d) electron temperature around the interaction zone at 1.05, 1.3, 2 and 5 $\mu$ s respectively in the case of equal energy source interaction S1 = S2
Fig. 4. 9 Temporal evolution of electron temperature at the stagnation layer formed due to interaction of two equal energy sources (S1:S2 = 1:1)
Fig. 4. 10 Comparison of temporal evolution of (a) electron temperature and (b) number density at the PC of single plasma source (50 mJ) alone, in the presence of equal (1:1) and unequal (1:2) sources
Fig. 4. 11 Temporal evolution of maximum temperature at the stagnation layer for d= 1, 2 and 4 mm in the case of (a) unequal source and (b) equal source interaction
interaction in PC <sub>1</sub>
mm and in case of equal source interaction for the separation distance of (e) d= 4 mm89

Fig. 4. 15 A comparison of mass density evolution at 20 μs in the case of unequal source interaction for the separation distance of (a) d= 4 mm, (b) d= 2 mm, (c) d= 1 mm and (d) d= 0 mm and in case of equal source interaction for the separation distance of (e) d=4mm
Fig. 5. 1 Simulation domain showing the dimensions of the confining geometry considered for simulations and focal point where laser energy deposition is taking place
106 Fig. 5. 7 Temporal variation of shock radius in the radial direction for (a) 50, (b) 200 and (c) 400 mJ respectively within a confining cavity of length 12 mm and diameter 8 mm (Vertical line ndicates the time of SW interacting with the glass boundary)
Fig. 5. 13 Variation of electron number density along the radial direction for the separation distances (a) d= 2mm (b) 4 mm, (c) 8 mm and the electron number densities for (d) d=2mm, (e) 4 mm and (f) 8 mm with materials of cavity glass, aluminum and copper for the input laser energy of 200 mJ

Fig. 5. 14 Average electron number density at region just before the contact point of the plasma
with the cavity wall (glass, aluminium and copper) along the radial direction for the input laser
energy of 200 mJ
Fig. 6. 1 Schematic showing the simulation domain where the laser beam is focussed onto the
front surface of aluminium foil
Fig. 6. 2 Spatial evolution of (a) – (b) electron temperature showing the plasma core (PC), shock
front (SF) and contact front (CF) and (c) - (d) pressure at 10 and 20 ns respectively for the input
laser energy of 50 mJ
Fig. 6. 3 Spatio-temporal evolution of the shock front in the ablative and blow-off regimes
generated using 50 mJ laser source in presence of ambient pressure of 1 atm
Fig. 6. 4 Two dimensional spatial evolution of (a)-(c) electron temperature and (d)-(e) pressure at
100, 200 and 500 ns respectively for the input laser energy of 50 mJ under the ambient pressure
of 1 atm132
Fig. 6. 5 Comparison of (a) Shock velocity (b) shock pressure (c) peak electron temperature and
number density along laser propagation axis in the ablation and blow-off regimes for the input
energy of 50 mJ
Fig. 6. 6 A comparison showing the pseudo plot of pressure at 50 ns when the background
pressure is (a) 0.1 (b) 0.2 (c) 0.5 and (d) 1 atm for the input laser energy of 50 mJ
Fig. 6. 7 Temporal evolution of the shock front (SF) and contact front (CF) of SW and plasma
generated at the background pressure of (a) 0.1 atm, (b) 0.2 atm, (c) 0.5 atm and (d) 1 atm
respectively for the input laser energy of 50 mJ
Fig. 6. 8 A comparison of (a) peak shock pressure in the ablation and blow-off regimes and (b)
peak electron temperature and electron number density existing at the plasma with respect to the
ambient pressure in the range 0.1 - 1 atm
Fig. 6. 9 Spatial evolution of the pressure in presence of (a)-(c) air and (d)-(f) He background at 1
atm background pressure at 100, 200 and 500 ns respectively
Fig. 6. 10 Variation of the (a) peak pressure at the shock front in the ablation and blow-off
regimes (b) peak electron temperature and (c) electron number density of plasma in presence of
air and helium with the background pressure varied between 0.1 - 1 atm
Fig. 6. 11 Simulation domain showing the axial confinement of the ablative regime using a glass
substrate
Fig. 6. 12 Spatial variation of electron temperature at (a) 10, (b) 20 and (c) 50 ns respectively for
the input laser energy of 50 mJ
of Al foil and its evolution and temporal evolution of the blow-off shock radius
Fig. 6. 14 (a) Shadowgram image of the blow-off SW and (b) mass density obtained from
simulations at 1.45 µs generated using 50 mJ energy laser source
Fig. 6. 15 Simulation domain showing the spatial confinement of the blow-off SW using a glass
cavity
Fig. 6. 16 Spatial evolution of mass density in the blow-off regime confined radially by a cavity at
(a) 0.5, (b) 1.0, (c) 1.5 and (d) 2.0 µs respectively generated using a 50 mJ laser source
Fig. 6. 17 Spatial variation of mass density in the blow-off regime confined radially by a cavity at
(a) 2.5. (b) 3.0. (c) 3.5 and (d) 4.0 us respectively generated using a 50 ml laser source

Fig. 6. 18 Temporal evolution of the blow-off shock pressure over a duration of 4 µs compared
in presence and in absence of the cavity in the blow-off regime
Fig. 7. 1 Flow chart showing the process taking place during the irradiation of laser beam on the
nanomaterial-HEM composite
Fig. 7. 2 Variation of optical absorption and scattering when (a-b) Al, (c-d) Ag and (e-f) Au
nanoparticles were doped to HMX respectively
Fig. 7. 3 Variation of optical absorption and scattering when (a-b) Al, (c-d) Ag and (e-f) Au
nanoparticles were doped to PETN respectively
Fig. 7. 4 Identifying the suitable metal nanoparticle Al, Ag and Au size to be added to PETN
when initiated with laser beam of different wavelengths
Fig. 7. 5 Variation of optical absorption when Ag nanoparticles of different sizes were doped to
different HEMs (PETN, HMX, Lead azide and Silver azide) excited at 420 nm
Fig. 7. 6 (a) Maximum optical absorption and (b) scattering observed in Ag nanoparticle doped
PETN at different excitation wavelengths
Fig. 7. 7 Temperature variation at the Ag nanoparticle and PETN interface with respect to size
of the nanoparticle
Fig. 7. 8 Temperature profile 35 nm radius Ag nanoparticle doped PETN at an excitation
wavelength of 532 nm
Fig. 7. 9 The temporal profile of the surface temperature of the nanoparticle of radius 35 nm
over a duration of 20 ns. T=0 represents the centre of the laser pulse

## **Chapter-1**

#### Introduction

interaction has gained a tremendous interest in understanding the phenomenon of laser interaction, plasma formation in the solids, liquids and gases. Laser beam focused into medium can deliver a very high energy that is capable of raising the temperature of the medium to the order of 105 K, followed by the evaporation of the material in the focused region. The expanding evaporated material cloud is called as the laser produced plasma (LPP). The fundamental mechanisms involved, the properties and dynamics of the subsequent laserproduced plasmas depend strongly on the laser beam parameters (pulse duration, fluence /intensity, wavelength and beam profile), and on the properties of the irradiated material. In general, for laser material processing, two different laser pulse duration regimes are used: they are (i) the long pulse regime (ns pulse duration) and (ii) short and ultra-short pulse regime (picosecond and femtosecond pulse durations). During the interaction of the ns-laser pulse with the material the material undergoes heating, melting and evaporation subsequently forming the plasma. This method is used in material ablation. However, in the case of short and ultra-short pulse interaction, the material is directly evaporated due to lower time span. This method is suitable for micro and nano-machining [1, 2]. The present work focuses on the ns – laser interaction under different background gases (air, He) and Al target of different thickness. In the long pulse, inverse bremsstrahlung is dominant absorption mechanism that takes place during the interaction of the laser beam with the medium [3-6]. In the short pulse regime, the dominant absorption mechanism that are expected to occur are multi-photon ionization (MPI) and tunnelling ionization [7].

Interaction of an intense laser beam with a medium (solid/gaseous) and its underlying physics

is a complex phenomenon. Since, the invention of high power lasers in 1960, the laser - matter

During the interaction of the laser beam with the material in the focal region the electrons absorb the photons from the leading pulse, the electrons after attaining the energy collide with the surrounding atoms and generate more number of free electrons and ions leading to an avalanche breakdown of the medium [3, 8]. During the breakdown of the material a rapid ionization takes place thus, a sudden increase in electron temperature and electron number density is observed leading to formation of plasma. The plasma formed after the breakdown

process absorbs the incoming laser energy (trailing part of the laser pulse) due to the availability of a large number of free electrons leading to further absorption of incoming laser beam (trailing edge) resulting to expansion of plasma plume towards the focusing lens.

The atomic processes taking place in plasma can be classified into three types based on the initial and final states of the electrons namely: bound-bound, bound-free and free-free transitions. The mechanism by which the energy transfer take place can be further classified into collisional and radiative mechanism.

The dominant atomic processes taking place in plasma are: (i) collisional excitation: collision of electrons with the neutral atoms in the plasma is leading to an increase in the kinetic energy and thus gains the sufficient excitation energy (Bound-Bound transition), (ii) collisional ionization: when the gained kinetic energy is sufficient to remove an electron the phenomenon is called collisional ionization (Bound-Free transition), (iii) photo excitation: electrons absorb the photons from the incident radiation gains kinetic energy sufficient for excitation (Bound-Bound transition) (iv) photo ionization: if the gained energy is sufficient to remove the electron from the neutral atom then the process is called as photo ionization (Bound-Free transition) and (v) bremsstrahlung: a collision of the electron with an ion of charge Ze in the excited state resulting in the de-excitation to the lower continuum state leading to emission of a photon. This process is called as bremsstrahlung (Free-Free transition) [3, 9].

However, in an inverse bremsstrahlung mechanism the electrons gains the energy from the incident photons, and the absorbed energy is converted into the kinetic energy (Free-Free transition). The bremsstrahlung and inverse bremsstrahlung are the key mechanism playing role in the laser induced plasma.

The plasma thus generated consists of three main regions: (i) plasma core region containing high temperatures (of the order of 10<sup>4</sup> - 10<sup>5</sup> K) where large number of collisions occur, (ii) Absorption front and (iii) shock front containing higher density, pressure[10]. The material/medium ablated from the focal volume is accumulated at the plasma front forming a thin dense layer called as the shock front. The accumulation of mass continues until the SW is completely built. The SW at later times detaches from the plasma and expands adiabatically into the background gas. The range of the temperature, number density generated at the plasma and the pressures, densities generated at the shock front depends on the medium in which the plasma/shock wave is generated. Though the interaction of the laser beam with the medium is similar in case of a solid substrate and a gaseous medium, the evolution dynamics of the plasma and the shock wave show a variation because of the variation in the density of

the interacting medium. The following section discusses the expansion/interaction dynamics of laser generated plasma with different media.

### 1.1 Laser generated plasma from a solid target

When the laser beam is incident on target material, a part of laser beam is reflected from the material surface (following Fresnel laws) and a part of the beam penetrates through the surface. The distance over which a laser beam penetrates through the target material is known as skin depth ( $\delta$ ) [11, 12] of the material given by:

$$\delta = \left(\frac{2}{\omega\mu\sigma}\right)^{\frac{1}{2}} \tag{1.1}$$

Where  $\omega$  is the frequency of the incident laser beam,  $\mu$  is the permeability of free space, and  $\sigma$  is the conductivity of the solid target. During the interaction of the laser beam with the solid target, the target material is heated, melted and vaporized leading to formation of the plasma. The ablative SW expanding into ambient air launches a compression wave on to the material due to momentum conservation. The launched SW travels through the material medium. Depending on the thickness of the target material, target properties and intensity of the incident beam, the SW reaches the rear end of the target and in few cases may lead to a blow-off of material from the rear end of the target [13]. The interaction of sufficiently intense ns laser pulse with thin foil target induces the material blow-off (plasma) or ejection of flyer from the rear side of target [14-16].

Laser ablation (LA) plumes or laser-produced plasmas (LPP) have applications such as pulsed laser deposition (PLD) [17], nanoparticle generation, nanostructure and cluster formation [18, 19] laser induced breakdown spectroscopy (LIBS) [19], and LA inductively coupled plasma mass spectrometry (LA-ICP-MS) [20] to name a few. On the other hand, laser induced material blow-off (plasma) or ejection of flyer from the rear side is a sophisticated tool and find its applications for the study of material behaviour that undergo shock compressions [21], generation of EOS [22], thrust generation for propulsion as to mention some.

#### 1.2 Laser Induced breakdown in air

The laser beam focussed into air (gaseous medium) leads o generation of plasma during the interaction of the leading pulse of the laser beam, while the trailing pulse of the incident laser beam interacts with the generated plasma leading to an asymmetric expansion of the plasma towards the incident laser beam [23-27]. Later due to the shifting of the absorption front, plasma expands along the laser propagation direction. This phenomenon is leading to the generation of multiple hot

spots in the generated air plasma. The plasma expansion is more dominant along the laser propagation axis compared to that along the radial direction. At longer timescales, the asymmetry in the plasma sustains but the SW after its detachment from the plasma expands freely into the surrounding medium, attains a spherical nature i.e., self-similar expansion in all the directions.

It is to be noted that the density of the medium from which the SW is generated effects the expansion dynamics of the SW. In the case of the solid target, the expansion is more dominant in the ablation regime (direction opposite to laser beam) less through the target (along the laser propagation axis). Whereas, the SW is expanding freely in all the directions when generated in gases (air). Factors such as intensity of the incident radiation [25, 27-29], background pressure [30-32], background gas species [31, 33] strongly influences the expansion dynamics and magnitudes of the temperature, number densities generated at the plasma and pressures generated at the SW.

The optical breakdown in gases, and subsequent formation of plasma and the generation of a shock wave (SW) initiated by intense laser pulses, have many practical applications, such as laser-spark ignition of fuel-air mixtures [29, 34, 35], laser propulsion systems such as laser thrusters [36] for wave drag reduction in a vehicle, localized flow control of blunt bodies [24, 37], laser triggering of switches [38] and laser induced breakdown spectroscopy (LIBS) [39, 40].

### 1.3 Confinement of laser generated plasma

When the laser-induced plasmas are spatial confined of by some medium, induces a complex phenomenon involving shock reflection/transmission from the confining media which further leading to shock-shock, shock-plasma, plasma - plasma interactions depending on the method of confinement chosen. When two shock waves were interacting with each other, the shock parameters such as pressure, density at the interaction zone will be enhanced leading to a local increment in the strength of the SW [41]. Whereas, when a SW is interacting with the plasma may lead to, an effective change in the plasma parameters i.e., increment in electron temperature and number density may occur depending on the intensity of the input laser beam and the direction of interaction (axial/radial), which further may also lead to an increment in the plasma lifetime. When two plasmas were interacting with each other, an effective change in the plasma dynamics, and plasma parameters occur that may lead to plasma jet-let formation depending on the plasma source energy.

A wide range of studies have been performed on the confinement of laser generated plasma using different methods viz., (i) spatial (geometric) confinement i.e., using rectangular [42-46], cylindrical [47, 48] cavities of different materials with no external input to the confining cavity, a micro hole[49], using another laser generated plasma interaction with different geometries (parallel [50-52], orthogonal [53-55], counter propagating [55-60], angular [56] interactions), in case of a solid target, the ablated plasma and SW were confined using a glass substrate [16, 61-65] (ii) magnetic confinement [66, 67] and (iii) electrical confinement [42]. To understand the plasma dynamics, an overview of the above mentioned processes is discussed in the following sections.

### 1.4 Geometric confinement of laser generated plasma

The laser generated plasma is confined using a cavity of different dimensions, different material, different geometries, using another laser induced plasma in different interacting geometries.

### 1.4.1 Confinement using a cavity

In this case the target is placed inside a cavity at a certain distance d from the walls of the cavity, focus the laser beam into the cavity and generate the plasma and SW. The generated plasma and SW due to the presence of the walls of the confining cavity interact with the walls and reflect back. The reflected plasma/SW interact with the plasma core leading to an enhancement in the plasma parameters. The separation distance between the cavity walls plays a crucial role in the spatial confinement of laser plasma which influences the shockwave expansion process. A wide range of research has been performed based on the laser induced breakdown spectroscopy (LIBS) applications. LIBS is a powerful popular elemental analysis technique used since decades. It has many advantages such as simultaneous detection of multiple elements, real time analysis, and nearly non-destructive method [68]. However, LIBS has a major drawback of low detection sensitivity of trace elements. If the LIBS signal from the trace element can be enhanced by some means it makes LIBS more sensible for the trace element detection. Few researchers have tried different methods to enhance the signal; Scaffidi et al. [69] had used multiple pulse excitation, while Guo et al. [70] had given a comparative study of confinement using multiple pulse and confinement of the plasma produced from the multiple pulse. Asimellis et al. [71] had used the inert gas background to enhance the LIBS signal. However, the above methods have a drawback of increased complexity in the setup of the experiments. To avoid such complexities a simple, flexible and cost-effective method of confinement is the spatial confinement of the laser induced plasma using a cavity of different geometries, different dimensions depending on the intensity of the incident laser beam and cavity made of different materials.

Laser induced shock wave interaction with the cavity material is a potential source of removing of the nano scale contaminating particles from silicon wafers called as laser shock cleaning (LSC) useful in semiconductor industry [72-74]. Fig. 1.1 shows a schematic of the generation of the laser induced air plasma a distance solid wall, the expanding SW after interaction with the wall reflects back traversing towards the plasma.

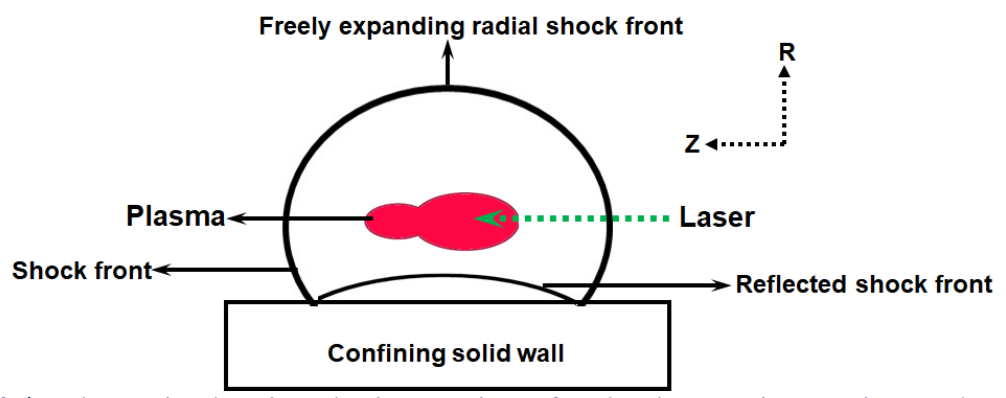


Fig. 1. 1 A schematic showing the interaction of a shock wave interacting and reflecting from a solid wall

A detailed study of the interaction of the SW with the cavity material, reflection from the cavity and interaction with the plasma gives a holistic understanding of the shock propagation in supersonic combustion [75], shock mitigation in foams [76-79], shock wave lithotripsy [80], study of inertial confinement fusions [81].

### 1.4.2 Confinement using a substrate overlay

This is a method of confined ablation where the expansion of the ablated plasma from the front surface of the target is stopped using a transparent material attached to it [16]. A laser pulse of sufficient intensity ablates a target surface. The ablated plasma is mechanically confined by the substrate that leads to the generation of stress waves. Which propagates into the target surface, leading to the blow-off or flyer that launches a flyer from the rear side of the target. This is the working principle of laser induced blow-off (LIBO) [82]. The flyer is a material ejected from the rear side of the target that is accelerated during blow-off [83]. In contrast to the conventional dynamic loading tools such as gas gun, z-pinch, explosives etc. the laser-based technique generate the pressures of higher magnitude within short durations

of time. This technique was proved to be most convenient and sophisticated tool for the study of material behaviour under shock compression [21, 84-86], generation of EOS [22, 87] thrust generation for propulsion [9, 10]. A significant enhancement in the blow-off shock and plasma parameters (pressure, velocity etc.) on the rear side of the foil are observed due to the mechanical confinement of the front end of the target material. Fig. 1.2 shows a schematic illustration of the launching of a blow-off SW from the rear side of the metal target. The metal target material is confined using a glass overlay for the confinement of the ablative plasma.

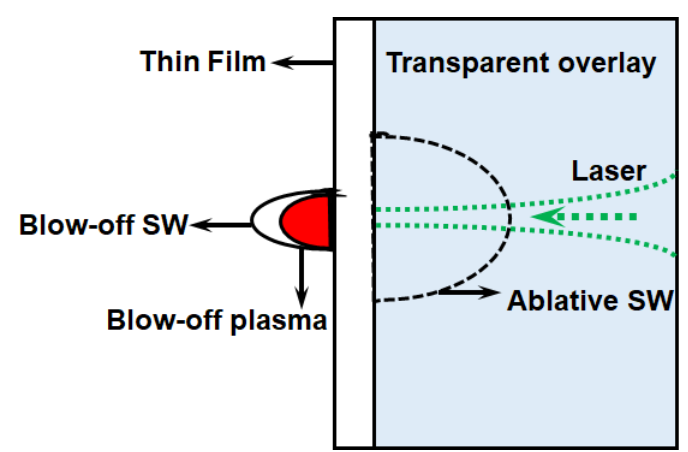


Fig. 1. 2 A schematic showing the illustration of laser driven blow-off

The ablated and blow-off plasma formed at the front and rear sides of the target depends on various parameters such as, input laser intensity (energy), wavelength, pulse duration, beam size on the target, thickness of the target material and its properties, surrounding ambient gas pressure conditions and the effective impedance of the foil and confined materials used [16]. A range of studies have been performed on the acceleration of aluminium and copper foils using high power laser pulses. Ripin et al. [88] has accelerated a thin metal foil to more than 100 km/sec using high intensity laser beam ( $I_p = 10^{12}\text{-}10^{13} \text{ W/cm}^2$ ). Paisley et al [82] has accelerated the aluminium and copper thin film of thickness 2-10  $\mu$ m to 5 km/sec. Later He et al [89] has accelerated aluminium foil of thickness  $10 \mu$ m to 13 km/sec using laser radiation of intensity ranging from  $20 - 400 \text{ GW/cm}^2$ .

Despite the successful acceleration of metal flyers in the experiments, the dynamic processes in laser-driven flyers are still unclear. The major challenges in the flyer acceleration is retaining the material properties when accelerated to very high velocities and altering the flyer velocity using laser parameters, film thickness and material of the film. Hence, a detailed study is needed to describe the absorption of laser energy as well as the metal foil rupture and acceleration process of the flyers.

### 1.4.3 Confinement using another plasma source

In this case the expansion of a laser generated plasma and SW were obstructed using another laser induced plasma. Initially the region at the interaction zone experiences a compression due to the expanding SW from the two sources resulting in an increase in the density and temperature at the interaction zone. Interaction of two such laser induced air plasmas can lead to two different phenomena: collision dominated and collision-less interaction. Collision dominated plasma interaction leads to either a formation of a stagnation layer or to an interpenetration of the two plasma sources, whereas in the case of collision-less interaction the two plasma sources tend to decelerate at the interaction zone [90]. Rambo and Procassini [55] have proposed that the interaction between the approaching plasmas depends on the ion—ion mean free path of the colliding fronts. The ion-ion mean free path in turn majorly depends on the relative velocity of the plasma plumes, the number densities at the plasma fronts before interaction and the average ionization state of the plasma. The SW from the two sources reflect or interpenetrate each other depending on the density at the SF. The velocity of the SW from the first source decreases as it is traversing through the shocked medium (i.e., a low pressure zone) generated by the second source [41]. The SW from the first source while interacting with the plasma core of the second source and vice-versa will be observed. If the interacting sources were of unequal energy then the SW from higher energy source while interacting with the lower energy source leads to a raise in kinetic energy. A part of the increased kinetic energy of the plasma is converted into thermal energy and a part of the energy is used in the formation of a plasma jet-let in the direction of the expanding SW from the other source. Harilal et al.[91] experimentally investigated the jet formation in laterally colliding plasma plumes and concluded that the plasma lifetime and the spatial expansion of plasma are enhanced in the colliding plasma more than with a single plasma.

A wide range of studies have been performed to understand the interaction dynamics of two plasmas under different geometries such as angular [56] lateral [50, 51, 92, 93] orthogonal [53, 54] counter streaming [55-58, 94] under vacuum conditions and a few studies in the presence of ambient air [51, 59, 60]. The interacting plasmas find application in the design of inertial confinement fusion (Hohlraums), x-ray laser research [81], high ionic temperature and charged particle acceleration using Thomson scattering in conjunction with proton radiography [95], understanding Supernovae (SNe), and Supernovae remnants (SNR) [96, 97] to model and understand various astrophysical processes via noble gases [98].

### Magnetic confinement of laser generated plasma

The effect of the transverse magnetic field on the freely expanding laser induced plasma is studied in this method of confinement. Transverse magnetic fields were applied to the plasmas using two permanent magnets [66], while confining the laser generated plasma using a torus shaped strong magnets is called as a Tokamak. Application of magnetic field on the freely expanding laser induced plasma leads to two extreme conditions depending on the particle and applied magnetic pressure (energy density associated with magnetic field). The ratio of particle pressure to magnetic pressure is defined by the parameter  $\beta$  of the plasma. In the case of low  $\beta$  plasma, i.e., in the non-diamagnetic limit the magnetic field just diffuses through the plasma. However, in the case of high  $\beta$ , i.e., in the diamagnetic limit, the plasma pressure is very much higher than the magnetic pressure and hence, thermal pressure pushes and expands the plasma along the direction of the field. As the plasma expands farther from the plasma source, thermal pressure drops and magnetic pressure dominates the motion of the plasma. As the plasma temperature drops, the magnetic fields originally begin to diffuse into the plasma structure [67, 99].

It was initially observed by Pisarczyk et al.[100] that the plasma is being elongated and a plasma column is formed along the axis of the applied magnetic field (20 T). Later it was quantified by Peyser et.al. [101] that high energy plasma expanding through magnetic field above 3 kG gives rise to long narrow plasma jets because of E×B drift which is not seen for magnetic fields < 3 kG. The presence of a magnetic field during the expansion of a laser-produced plasma may leads to interesting physical phenomena such as conversion of the plasma thermal energy into kinetic energy, plasma confinement, ion acceleration, enhancement in optical emissions, plasma instabilities [102].

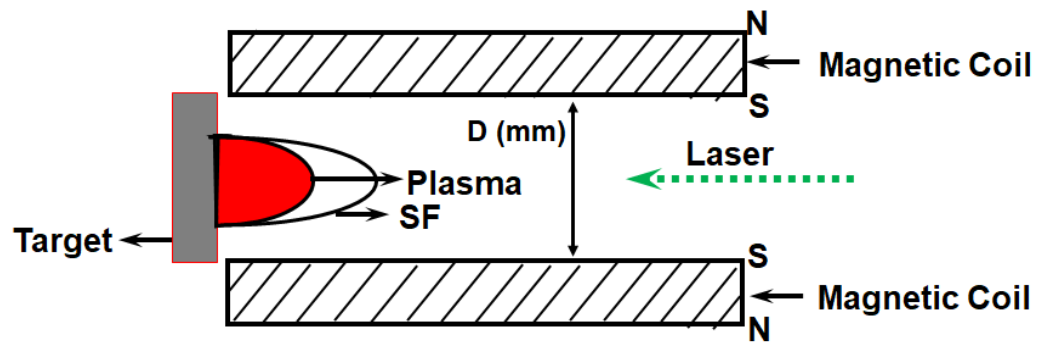


Fig. 1. 3 Schematic showing the confinement of laser generated from aluminium target using transverse magnetic field

Neogi and Thareja [99, 103] had studied the expansion of the carbon plasma in presence of the non-uniform magnetic field in presence of vacuum using emission spectroscopy and fast photography. Instabilities in the temporal profile of the ions at the edge of the plume were observed by Neogi and Thareja [99]. These oscillations were observed because of the edge instability in the magnetic field.

Laser produced plasma in presence of an externally applied magnetic field is found to be a good source of x-ray emission [100]. Understanding the evolution dyanmics of plasmas in strong magnetic fields helps in understanding many areas of plasma physics, ranging from basic and applied plasma physics to astrophysics, controlled fusion reactions, and Z-pinch experiments etc[104-106].

### 1.6 Electrical confinement of laser generated plasma

It is a well-known fact that the plasma generated from a metal target mainly consists of neutrals, ions and electrons. Generation of nanoparticles and thin film deposition using pulsed laser deposition (PLD) are one of the most important applications of the laser ablation (LA). In PLD, the plume propagates towards the substrate which is placed to the target. The quality of the film deposited depends on the plume characteristics such as the kinetic energy (KE) of the constituents of the plume. While the kinetic energy of the constituents of the plasma plume depends on the experimental parameters such as intensity, wavelength of the incident laser beam and background pressure. However, Izumi et al. [107] has shown that application of the electric filed between the target and the substrate is a most convenient way of manipulating the KE of the ions present in the plume.

A range of studies have been reported on the pulsed laser deposition from different metal targets to understand the temporal evolution of plasma generated using ns laser pulse with energies  $\leq 1$  J and pulse duration ( $\tau$ ) in the range of 1-30 ns in the presence of applied electric field.

Singh et al. [108] has studied the effect of the application of the electric field parallel to the expanding plasma in the formation of YBa<sub>2</sub> Cu<sub>3</sub> O<sub>7</sub> superconducting thin film using pulsed evaporation technique. A dc bias voltage of + 300 V was applied during the deposition process, resulting in the formation of superconducting thin film at a low temperature of 500 °C. Parl et al [109] has confirmed that the concentration of the electronically excited ions in the laser produced plasma and their kinetic energies depends on the biasing voltage applied externally. Many studies have been performed with the electric field applied parallel [108, 110] or

perpendicular [107-109, 111] to the target surface using solid electrodes, rings or grids with the low biasing voltage ( $\pm$  500 V) and low laser intensity ( $I_p < 10^9 \, \text{W//cm}^2$ ). A few studies have performed at higher intensities ( $I_p > 10^{10}$  -  $10^{16} \, \text{W//cm}^2$ ) and biasing voltage upto +50 kV for enhanced ion yield and directivity of the generated laser plasma plume for laser ion source (LIS) operation. [112-114].

Among all the above methods of confinement of laser plasma it is understood that the spatial confinement with no external forces applied on the expanding plasma is a cost-effective and hassle free method to obtain an effective method to attain a pronounced enhancement in the plasma properties. The work presented in this thesis includes the hydrodynamic simulation of spatial confinement of plasma and shock waves by different methods (as given below) generated [115] using second harmonic Nd:YAG laser pulses of 10 ns width for the intensities ranging between  $0.25 - 2.5 \times 10^{10}$  W/cm<sup>2</sup> (50 - 500 mJ).

A quantitative study of the spatial confinement of the laser plasma generated in air medium and the plasma generated from aluminum foil were discussed in detail. Laser generated plasma in air and from material is confined spatially via the following methods:

- i. Longitudinal confinement of air plasma in counter propagation geometry
- ii. Lateral (radial) geometric confinement of air plasma
- iii. Longitudinal Confinement of laser ablative plasma by a glass slab
- iv. Lateral geometric confinement of blow-off SW from a metal foil

Lateral confinement of blow-off shock wave generated at the rear end of the thin metal foil using a cavity of dimensions length L=12 mm and separation distance D= 8 mm.

### 1.7 Organization of the thesis

The organization of the thesis is as follows:

**Chapter-2** This chapter discusses about the simulation methodology used in formulating the hydrodynamics of laser - matter interaction. The factors playing role in the evolution dynamics of the generated plasma and shock waves were discussed in detail. A validation of the laser ablative shock wave dynamics generated from a bulk aluminium target is presented. The typical statistical error that occur in the plasma parameters such as electron temperature and electron number density using HLLC [116] scheme of order 1 and order 3 were discussed.

**Chapter-3** The laser induced breakdown of air, generation and evolution dynamics of plasma and shock wave were discussed in detail in the present chapter. The results were verified with

the experimentally obtained shock velocities [59, 115] and the evolution dynamics. The effect of the energy, pulse duration, intensity on the plasma and shock parameters were studied. The evolution dynamics of the plasma parameters such as electron number density and temperature were verified with the values existing in the literature [117, 118].

Chapter-4 The spatial confinement of the laser induced air plasma using another laser induced air plasma along the laser propagation axis is studied in the present chapter. The air plasma generated using a laser beam energy of 50 mJ (S<sub>1</sub>), pulse duration 10 ns with the excitation wavelength of 532 nm is confined using another source (S<sub>2</sub>) generated using input energy of 50 mJ/100 mJ. The effect of the separation distance (d) between the two sources and the acoustic impedance (gu) of the confining source (S<sub>2</sub>) on the evolution dynamics of the freely expanding source S<sub>1</sub> is studied in detail. The separation distance between the two sources is varied as d=0, 1, 2 and 4 mm. During the interaction of the two sources, the pressure and mass density were observed to be raised because of the interaction of the SFs. The interpenetration of the two SFs at the interaction zone is clearly visualized and confirmed from the line profiles of mass density and pressure along the laser propagation axis. However, the extent of interaction or interpenetration of the PC of the two sources is visualized and confirmed using the collisionality parameter (ζ) [50, 59, 60, 90, 119]. The collisionality parameter is calculated for all the combinations both the energy ratios for all the considered separation distances. The effect of the interaction of the SW with the PC is studied over a duration of 30 μs.

Chapter-5 The lateral confinement of the laser induced air plasma using a rectangular cavity of different materials (glass, aluminium and copper) and different dimensions is presented in this chapter. The length of the cavity is varied as L=8,10 and 12 mm while the separation distance between the cavity walls is varied as D=2, 4 and 8 mm respectively. The equation of state for the cavity material is generated by Sai Shiva et al. [120-123] by making the necessary modifications to the code given by Mac Farlane et al. [124]. A complete picture of the evolution of the freely expanding SW, its interaction and reflection from the cavity walls, interaction of the reflected SW with the plasma is clearly visualized and the corresponding effect on plasma parameters is studied over a duration of 30  $\mu$ s. The effect of the interaction of the reflected SW on plasma and SW parameters is studied in detail with respect to the separation distance between the cavity walls the material of the confining cavity is studied in detail.

**Chapter-6** This chapter is divided into three stages:

**Stage - 1** Ablation of aluminium thin foil under different ambient conditions such as varying background pressure (0.1 - 1 atm) and varying background gas (air, Helium). Initially the SW dynamics for the input laser energy of 50 mJ is verified with the experimental results. Later the SW and plasma parameters were simulated by varying the background conditions.

Stage - 2 The laser ablative plasma from the thin foil generated under background pressure of 1 atm in presence of air medium is confined using a glass slab of 1.8 mm thickness i.e., the aluminium metal foil is attached to a glass slab. The laser beam allowed to focus directly at the aluminium-glass slab interface. Aluminium - glass slab interface. The study is performed for the input laser energy of 50 mJ. During the interaction of the leading edge of the laser pulse plasma with much higher temperatures (of order of 10<sup>5</sup> K) is generated at the metal foil-glass interface. While ablation at the front surface of glass substrate (from glass substrate) is observed during the interaction of the trailing edge of the laser pulse. Launching of the material blow-off SW from the rear side of the metal foil and its expansion dynamics were studied over a duration of 3 μs. The obtained shock velocities were compared with the experimentally obtained shock velocities [13].

**Stage-3** The blow-off SW/plasma generated by the confining glass slab that is generated in stage-2 is confined using a glass cavity of length L=8 mm and separation distance between the cavity walls D = 2 mm. It is observed that the considered dimensions of the cavity are too large to observe an effective reflection of the SW from the glass walls and to interact with the plasma. While in the case of foil confined with a glass slab enhanced coupling of the stronger blow-off SW is observed as the confining tube geometry resulted in a strong reflected SW. The reflected SW further interacts with the plasma leading to an enhanced and multiple reflections leading to a micro blast.

Chapter-7 A detailed study of variation of the optical absorption in a metal nanoparticle doped high energy material (HEM) is presented in this chapter. The variation of the optical absorption when metal nanoparticles (aluminium, silver, gold) of different sizes (20-400 nm) were doped to HEMs (Penta Erythrtol Tetra Nitrate known as PETN, Octahydro-1,3,5,7-tetranitro-1,3,5,7-tetrazocine known as HMX) were studied in detail over the excitation wavelength of 400 – 1200 nm. Optical absorption of the composite material is determined using the concept of Mie theory. To understand the effect of the increment in the optical absorption on the temperature evolution in the composite material, thee heat conduction equation is solved using finite central difference method of fourth order accuracy [125]. The

critical energy density of the composite material i.e., energy required to initiate the ignition of the composite material is to be determined.

#### Chapter-8

A summary of the work done in the above chapters is discussed in this chapter. A road map to the designing of a micro shock tube of dimensions in the range of mm is discussed. Relating the work done in the thesis with the future scope were discussed in detail.

Confinement of laser plasma in air is used to understand the mechanisms involved, optimizing the parameters required for the geometric confinement of blow-off SW from metal foil. A detailed description of all the physical processes taking place from the point of interaction of laser beam with the material, effect of geometric/spatial confinement on SW, interaction of the modified SW (due to reflection from the confining geometry) with the plasma, enhancement in the plasma parameters, compression of the plasma by the SW were studied using FLASH 2D radiation hydrodynamic code [126] with relevant modifications.

Experiments have a limitation in diagnosing the complex physical processes occurring concurrently during the laser-matter interactions for example, the minimum time span of the evolution of plasma and SW, study of the dynamics inside an opaque object, evolution of plasma parameters such as number density, temperature, determination of the shock strength based on mass density and pressure etc., are difficult to diagnose and require setting up of large number of diagnosing methods. However, with numerical simulations all these processes can be understood simultaneously. Thus, they help to study the plasma and SW dynamics from the time of generation to a longer time scale with increased resolution. Hence, the present work is aimed at numerical investigation of the ns laser generated plasma and the consequent shock wave evolution when confined spatially using different methods. The work includes the experimental validation [115], followed by in depth understanding of the physical mechanism involved during the confinement of plasma. The work is further extended to experimental are hardly performed resulting in minimal trials.

#### 1.8 References

- 1. Ali, M., et al., Review of laser nanomachining. Journal of Laser Applications, 2008. 20(3): p. 169-184.
- 2. Yu, X., et al., Femtosecond laser nanomachining initiated by ultraviolet multiphoton ionization. Optics Express, 2013. **21**(20): p. 24185-24190.
- 3. Raizer, Y.B.Z.d.a.Y.P., *Physics of Shock Waves and HighTemperature Hydrodynamic Phenomena*. 2012: (Dover Publications.
- 4. Singh, R.K. and J. Narayan, *Pulsed-laser evaporation technique for deposition of thin films: Physics and theoretical model.* Physical Review B, 1990. **41**(13): p. 8843-8859.

- 5. Marla, D., U.V. Bhandarkar, and S.S. Joshi, *Critical assessment of the issues in the modeling of ablation and plasma expansion processes in the pulsed laser deposition of metals.* Journal of Applied Physics, 2011. **109**(2): p. 021101.
- 6. Shiva, S.S., et al., The effects of electron thermal radiation on laser ablative shock waves from aluminum plasma into ambient air. Physics of Plasmas, 2016. **23**(5): p. 053107.
- 7. Zel'dovich, Y.B. and Y.P. Raizer, *Physics of Shock Waves and HighTemperature Hydrodynamic Phenomena*. 2012: (Dover Publications).
- 8. Radziemski, L.J. and D.A. Cremers, *Laser-induced plasmas and applications*. 1989, United States: Marcel Dekker Inc.
- 9. Bittencourt, J.A., Fundamentals of Plasma Physics. 2013: Springer New York.
- 10. Porneala, C. and D.A. Willis, *Time-resolved dynamics of nanosecond laser-induced phase explosion*. Journal of Physics D: Applied Physics, 2009. **42**(15): p. 155503.
- 11. Amoruso, S., et al., *Characterization of laser-ablation plasmas*. Journal of Physics B: Atomic, Molecular and Optical Physics, 1999. **32**(14): p. R131-R172.
- 12. Cremers, D. and L. Radziemski, *Handbook of Laser-Induced Breakdown Spectroscopy: Second Edition*. Handbook of Laser-Induced Breakdown Spectroscopy: Second Edition, 2013.
- 13. Guthikonda, N., et al., Effect of Focusing Plane on Laser Blow-off Shock Waves from Confined Aluminum and Copper Foils. Journal of Physics D: Applied Physics, 2021.
- 14. Bakos, J.S., et al., Laser blow-off plasma propagating in low-pressure gas. Applied Physics Letters, 1987. **51**(10): p. 734-736.
- 15. Skeen, C.H. and C.M. York, LASER-INDUCED `BLOW-OFF" PHENOMENA. Applied Physics Letters, 1968. 12(11): p. 369-371.
- 16. Fabbro, R., et al., *Physical study of laser-produced plasma in confined geometry*. Journal of Applied Physics, 1990. **68**(2): p. 775-784.
- 17. Chrisey, D.B. and G.K. Hubler, Pulsed Laser Deposition of Thin Films. 1994: Wiley.
- 18. Amoruso, S., et al., Experimental and theoretical investigations of femtosecond laser ablation of aluminum in vacuum. Journal of Applied Physics, 2005. **98**(4): p. 044907.
- 19. Hahn, D.W. and N. Omenetto, Laser-Induced Breakdown Spectroscopy (LIBS), Part I: Review of Basic Diagnostics and Plasma—Particle Interactions: Still-Challenging Issues within the Analytical Plasma Community. Applied Spectroscopy, 2010. **64**(12): p. 335A-336A.
- Hassane and P. Kulkarni, The effect of ultrafast laser wavelength on ablation properties and implications on sample introduction in inductively coupled plasma mass spectrometry. Journal of Applied Physics, 2013. 114(2): p. 023103.
- 21. Batani, D., Matter in extreme conditions produced by lasers. EPL (Europhysics Letters), 2016. 114(6): p. 65001.
- 22. Dezulian, R., et al., *Hugoniot data of plastic foams obtained from laser-driven shocks.* Physical Review E, 2006. **73**(4): p. 047401.
- 23. DeMichelis, C., Laser induced gas breakdown: A bibliographical review. IEEE Journal of Quantum Electronics, 1969. **5**(4): p. 188-202.
- 24. Ghosh, S. and K. Mahesh, Numerical simulation of the fluid dynamic effects of laser energy deposition in air. Journal of Fluid Mechanics, 2008. **605**: p. 329-354.
- 25. Sai Shiva, S., et al., Numerical investigation of nanosecond laser induced plasma and shock wave dynamics from air using 2D hydrodynamic code. Physics of Plasmas, 2017. **24**(8): p. 083110.
- 26. Leela, C., et al., *Dynamics of laser induced micro-shock waves and hot core plasma in quiescent air.* Laser and Particle Beams, 2013. **31**(2): p. 263-272.
- 27. Sai Shiva, S., et al., Role of laser absorption and equation-of-state models on ns laser induced ablative plasma and shockwave dynamics in ambient air: Numerical and experimental investigations. Physics of Plasmas, 2019. **26**(7): p. 072108.
- 28. Manikanta, E., et al., Effect of laser intensity on temporal and spectral features of laser generated acoustic shock waves: ns versus ps laser pulses. Applied Optics, 2017. **56**(24): p. 6902-6910.
- 29. Mullett, J.D., et al., *The influence of beam energy, mode and focal length on the control of laser ignition in an internal combustion engine.* Journal of Physics D: Applied Physics, 2007. **40**(15): p. 4730-4739.
- 30. Tambay, R., et al., Laser induced air breakdown using 0.355, 0.532, and 1.06 μm radiation. Pramana, 1991. **37**(2): p. 163-166.
- 31. Gatti, M., et al., Spherical shock waves in laser produced plasmas in gas. Optics Communications, 1988. **69**(2): p. 141-146.

- 32. Thiyagarajan, M. and J. Scharer, Experimental investigation of ultraviolet laser induced plasma density and temperature evolution in air. Journal of Applied Physics, 2008. **104**(1): p. 013303.
- 33. Harilal, S.S., et al., On- and off-axis spectral emission features from laser-produced gas breakdown plasmas. Physics of Plasmas, 2017. **24**(6): p. 063304.
- 34. Phuoc, T.X., Laser spark ignition: experimental determination of laser-induced breakdown thresholds of combustion gases. Optics Communications, 2000. 175(4): p. 419-423.
- 35. Srivastava, D.K., K. Dharamshi, and A.K. Agarwal, Flame kernel characterization of laser ignition of natural gas—air mixture in a constant volume combustion chamber. Optics and Lasers in Engineering, 2011. **49**(9): p. 1201-1209.
- 36. Phipps, C., et al., Review: Laser-Ablation Propulsion. Journal of Propulsion and Power, 2010. 26: p. 609-637.
- 37. Bletzinger, P., et al., *Plasmas in high speed aerodynamics*. Journal of Physics D: Applied Physics, 2005. **38**(4): p. R33-R57.
- 38. Soubacq, S., et al., *Investigation of a gas breakdown process in a laser-plasma experiment.* Journal of Physics D: Applied Physics, 2004. **37**(19): p. 2686-2702.
- 39. Radziemski, L.J., From LASER to LIBS, the path of technology development. Spectrochimica Acta Part B: Atomic Spectroscopy, 2002. **57**(7): p. 1109-1113.
- 40. Khalil, A.A.I., W.O. Younis, and M.A. Gandol, *A comparative study of highly-ionized Al plasma based on dual pulse laser-induced breakdown spectroscopy.* Indian Journal of Physics, 2017. **91**(3): p. 327-336.
- 41. Cooper, P.W., Explosives engineering. 1996: Wiley-VCH.
- 42. Yeates, P. and E.T. Kennedy, *Diagnostics of laser plasma plume dynamics within an electrically biased confining cavity.* Journal of Applied Physics, 2011. **110**(6): p. 063303.
- 43. Yeates, P. and E.T. Kennedy, *Spectroscopic, imaging, and probe diagnostics of laser plasma plumes expanding between confining surfaces.* Journal of Applied Physics, 2010. **108**(9): p. 093306.
- 44. Yeates, P. and E.T. Kennedy, *Plasma dynamics of a confined extreme ultraviolet light source*. Physics of Plasmas, 2010. **17**(9): p. 093104.
- 45. Yeates, P. and E.T. Kennedy, *Spectroscopic diagnostics of plume rebound and shockwave dynamics of confined aluminum laser plasma plumes.* Physics of Plasmas, 2011. **18**(6): p. 063106.
- 46. Popov, A., F. Colao, and R. Fantoni, *Enhancement of LIBS signal by spatially confining the laser-induced plasma*. Journal of Analytical Atomic Spectrometry J ANAL ATOM SPECTROM, 2009. **24**.
- 47. Shen, X.K., et al., *Spectroscopic study of laser-induced Al plasmas with cylindrical confinement.* Journal of Applied Physics, 2007. **102**(9): p. 093301.
- 48. Wang, Q., et al., The role of cavity shape on spatially confined laser-induced breakdown spectroscopy. Physics of Plasmas, 2018. **25**(7): p. 073301.
- 49. Tao, S. and B. Wu, Nanosecond laser pulse interactions with breakdown plasma in gas medium confined in a microhole. Applied Physics B, 2013. 113(2): p. 251-258.
- 50. Rumsby, P.T., J.W.M. Paul, and M.M. Masoud, *Interactions between two colliding laser produced plasmas*. Plasma Physics, 1974. **16**(10): p. 969-975.
- 51. Yang, Z., et al., Experimental study of the behavior of two laser produced plasmas in air. Physics of Plasmas, 2015. **22**(7): p. 073511.
- 52. Kumar, B., et al., *Investigation of shock-shock interaction and Mach reflection in laterally colliding laser-blow-off plasmas*. Physics of Plasmas, 2015. **22**(6): p. 063505.
- 53. Al-Shboul, K.F., et al., *Interpenetration and stagnation in colliding laser plasmas*. Physics of Plasmas, 2014. **21**(1): p. 013502.
- 54. Gupta, S.L., P.K. Pandey, and R.K. Thareja, *Dynamics of laser ablated colliding plumes*. Physics of Plasmas, 2013. **20**(1): p. 013511.
- 55. Rambo, P.W. and R.J. Procassini, A comparison of kinetic and multifluid simulations of laser-produced colliding plasmas. Physics of Plasmas, 1995. **2**(8): p. 3130-3145.
- 56. Luna, H., K.D. Kavanagh, and J.T. Costello, *Study of a colliding laser-produced plasma by analysis of time- and space-resolved image spectra*. Journal of Applied Physics, 2007. **101**(3): p. 033302.
- 57. Sánchez-Aké, C., et al., *Analysis of two colliding laser-produced plasmas by emission spectroscopy and fast photography*. Spectrochimica Acta Part B: Atomic Spectroscopy, 2010. **65**(5): p. 401-408.
- 58. Zastrau, U., et al., *Tracking the density evolution in counter-propagating shock waves using imaging X-ray scattering.* Applied Physics Letters, 2016. **109**(3): p. 031108.
- 59. Guthikonda, N., et al., *Interaction of two counterpropagating laser induced plasmas and shock waves in air.* Physics of Plasmas, 2020. **27**(2): p. 023107.

- 60. Kameswari, D.P.S.L., et al., *Investigation of stagnation layer dynamics of counterpropagating laser induced air plasmas: Numerical simulations vis-à-vis experimental observations.* Physics of Plasmas, 2021. **28**(4): p. 043104.
- 61. Devaux, D., et al., Generation of shock waves by laser-induced plasma in confined geometry. Journal of Applied Physics, 1993. 74(4): p. 2268-2273.
- 62. Zhang, P., et al., Numerical simulation of the temperature field in laser-driven flyer plates by high power nanosecond laser-material interactions. Journal of Physics D: Applied Physics, 2009. **42**(22): p. 225302.
- 63. Gu, Z., et al., One-dimensional numerical simulation of laser-driven flyer plates. Journal of Applied Physics, 2004. **96**(6): p. 3486-3490.
- 64. Kumar, B., R.K. Singh, and A. Kumar, *Dynamics of laser-blow-off induced Li plume in confined geometry*. Physics of Plasmas, 2013. **20**(8): p. 083511.
- 65. Watson, S. and J.E. Field, *Measurement of the ablated thickness of films in the launch of laser-driven flyer plates.* Journal of Physics D: Applied Physics, 1999. **33**(2): p. 170-174.
- 66. Gebre, T., Y.F. Lu, and Y.X. Han, Magnetic confinement of plasmas in laser-induced breakdown spectroscopy for improving sensitivity and accuracy. International Congress on Applications of Lasers & Electro-Optics, 2005. 2005(1): p. P517.
- 67. Leal, L.S., et al., Modeling magnetic confinement of laser-generated plasma in cylindrical geometry leading to disk-shaped structures. Physics of Plasmas, 2020. **27**(2): p. 022116.
- 68. Gao, X., et al., *The role of spatial confinement on nanosecond YAG laser-induced Cu plasma*. Journal of Physics D: Applied Physics, 2015. **48**(17): p. 175205.
- 69. Scaffidi, J., et al., *Dual-pulse laser-induced breakdown spectroscopy with combinations of femtosecond and nanosecond laser pulses.* Applied Optics, 2003. **42**(30): p. 6099-6106.
- 70. Guo, L.B., et al., Optimally enhanced optical emission in laser-induced breakdown spectroscopy by combining spatial confinement and dual-pulse irradiation. Optics Express, 2012. **20**(2): p. 1436-1443.
- 71. Asimellis, G., et al., Controlled inert gas environment for enhanced chlorine and fluorine detection in the visible and near-infrared by laser-induced breakdown spectroscopy. Spectrochimica Acta Part B: Atomic Spectroscopy, 2005. **60**: p. 1132-1139.
- 72. Lee, J.M. and K.G. Watkins, Removal of small particles on silicon wafer by laser-induced airborne plasma shock waves. Journal of Applied Physics, 2001. **89**(11): p. 6496-6500.
- 73. Lim, H., et al., Correlation between particle removal and shock-wave dynamics in the laser shock cleaning process. Journal of Applied Physics, 2005. **97**(5): p. 054903.
- 74. Jang, D., et al., Enhanced efficiency of laser shock cleaning process by geometrical confinement of laser-induced plasma. Journal of Applied Physics, 2009. **106**(1): p. 014913.
- 75. Yang, J., T. Kubota, and E. Zukoski, *A model for characterization of a vortex pair formed by shock passage over a light-gas inhomogeneity.* Journal of Fluid Mechanics, 1994. **258**: p. 217-244.
- 76. Delale, C.F., S. Nas, and G. Tryggvason, *Direct numerical simulations of shock propagation in bubbly liquids*. Physics of Fluids, 2005. **17**(12): p. 121705.
- 77. Skews, B.W., M.D. Atkins, and M.W. Seitz, *The impact of a shock wave on porous compressible foams.* Journal of Fluid Mechanics, 1993. **253**: p. 245.
- 78. Onodera, H. and K. Takayama, *Shock Wave Structure in Polyurethane Foam.* JSME International Journal Series B, 1994. **37**(2): p. 268-274.
- 79. Song, B., B. Sanborn, and W.-Y. Lu, Experimental Measurement and Analysis of Stress/Shock Wave Propagation Speed through Pre-strained Silicone Foam Pads under Lateral Confinement. Journal of Dynamic Behavior of Materials, 2019. 5(2): p. 170-179.
- 80. Jamaluddin, A., G. Ball, and T. Leighton, Free-Lagrange Simulations of Shock/Bubble Interaction in Shock Wave Lithotripsy. 2012.
- 81. Dittrich, T.R., et al., Review of indirect-drive ignition design options for the National Ignition Facility. Physics of Plasmas, 1999. **6**(5): p. 2164-2170.
- 82. Paisley, D.L., et al., Laser-launched flyer plate and confined laser ablation for shock wave loading: Validation and applications. Review of Scientific Instruments, 2008. **79**(2): p. 023902.
- 83. Curtis, A.D., et al., Laser-driven flyer plates for shock compression science: Launch and target impact probed by photon Doppler velocimetry. Review of Scientific Instruments, 2014. **85**(4): p. 043908.
- 84. Benuzzi-Mounaix, A., et al., Laser-driven shock waves for the study of extreme matter states. Plasma Physics and Controlled Fusion, 2006. **48**(12B): p. B347-B358.
- 85. Chaurasia, S., et al., Development of in situ time-resolved Raman spectroscopy facility for dynamic shock loading in materials. Journal of Instrumentation, 2017. **12**(11): p. P11008-P11008.

- 86. Rastogi, V., et al., Raman spectroscopy of laser shocked polystyrene. Journal of Raman Spectroscopy, 2017. **48**(3): p. 458-464.
- 87. Batani, D., et al., Equation of State Data for Iron at Pressures beyond 10 Mbar. Physical Review Letters, 2002. 88(23): p. 235502.
- 88. Ripin, B.H., et al., Laser-plasma interaction and ablative acceleration of thin foils at 1012–1015 W/cm2. The Physics of Fluids, 1980. 23(5): p. 1012-1030.
- 89. He, H., T. Kobayashi, and T. Sekine, *Time-Resolved Measurement of the Launch of Laser-Driven Foil Plate.* AIP Conference Proceedings, 2002. **620**(1): p. 1339-1342.
- 90. Dardis, J. and J.T. Costello, Stagnation layers at the collision front between two laser-induced plasmas: A study using time-resolved imaging and spectroscopy. Spectrochimica Acta Part B: Atomic Spectroscopy, 2010. **65**(8): p. 627-635.
- 91. Harilal, S.S., M.P. Polek, and A. Hassanein, *Jetlike Emission From Colliding Laser-Produced Plasmas*. IEEE Transactions on Plasma Science, 2011. **39**(11): p. 2780-2781.
- 92. Mondal, A., et al., Spectroscopic investigation of stagnation region in laterally colliding plasmas: Dependence of ablating target material and plasma plume separation. Physics of Plasmas, 2019. **26**(2): p. 022102.
- 93. Kumar, B., et al., *Propagation dynamics of laterally colliding plasma plumes in laser-blow-off of thin film.* Physics of Plasmas, 2014. **21**(8): p. 083510.
- 94. Ross, J.S., et al., Characterizing counter-streaming interpenetrating plasmas relevant to astrophysical collisionless shocks. Physics of Plasmas, 2012. **19**(5): p. 056501.
- 95. Malka, V., et al., Laser-driven accelerators by colliding pulses injection: A review of simulation and experimental results. Physics of Plasmas, 2009. **16**(5): p. 056703.
- Spicer, D.S., R.W. Clark, and S.P. Maran, A Model of the Pre-Sedov Expansion Phase of Supernova Remnant--Ambient Plasma Coupling and X-Ray Emission from SN 1987A. The Astrophysical Journal, 1990. 356: p. 549.
- 97. Smith, R.A., et al., Colliding Blast Waves Driven by the Interaction of a Short-Pulse Laser with a Gas of Atomic Clusters. Astrophysics and Space Science, 2007. **307**(1): p. 131-137.
- 98. Raga, A.C., et al., *The connection between laboratory and astrophysical jets.* AIP Conference Proceedings, 2005. **784**(1): p. 195-204.
- 99. Neogi, A. and R.K. Thareja, *Dynamics of laser produced carbon plasma expanding in a nonuniform magnetic field.* Journal of Applied Physics, 1999. **85**(2): p. 1131-1136.
- 100. Pisarczyk, T., et al., Formation of an elongated plasma column by a magnetic confinement of a laser-produced plasma. Laser and Particle Beams, 1992. **10**: p. 767-776.
- 101. Peyser, T.A., et al., *Electron–ion hybrid instability in laser-produced plasma expansions across magnetic fields.* Physics of Fluids B: Plasma Physics, 1992. **4**(8): p. 2448-2458.
- 102. Harilal, S.S., et al., Confinement and dynamics of laser-produced plasma expanding across a transverse magnetic field. Physical Review E, 2004. **69**(2): p. 026413.
- 103. Neogi, A. and R.K. Thareja, Laser-produced carbon plasma expanding in vacuum, low pressure ambient gas and nonuniform magnetic field. Physics of Plasmas, 1999. **6**(1): p. 365-371.
- 104. Gotchev, O.V., et al., Laser-Driven Magnetic-Flux Compression in High-Energy-Density Plasmas. Physical Review Letters, 2009. 103(21): p. 215004.
- 105. Sinars, D.B., et al., Measurements of Magneto-Rayleigh-Taylor Instability Growth during the Implosion of Initially Solid Al Tubes Driven by the 20-MA, 100-ns Z Facility. Physical Review Letters, 2010. **105**(18): p. 185001.
- 106. Arefiev, A., T. Toncian, and G. Fiksel, *Enhanced proton acceleration in an applied longitudinal magnetic field.* New Journal of Physics, 2016. **18**(10): p. 105011.
- 107. Izumi, H., et al., Superconductivity and crystallinity of Ba2Y1Cu3O7-δ thin films prepared by pulsed laser deposition with substrate bias voltage. Journal of Applied Physics, 1990. **68**(12): p. 6331-6335.
- 108. Singh, R.K., et al., Effect of processing geometry in oxygen incorporation and in situ formation of YBa2Cu3O7 superconducting thin films by pulsed laser evaporation technique. Applied Physics Letters, 1989. **55**(22): p. 2351-2353.
- 109. Park, H., S. Nam, and S. Park, Laser Ablation of a Zn Target in Electric Field. Journal of Physics: Conference Series, 2007. **59**: p. 384-387.
- 110. Muramoto, J., et al., *Influence of electric field on the behavior of Si nanoparticles generated by laser ablation.* Applied Physics Letters, 1999. **75**(6): p. 751-753.
- 111. Fried, D., et al., The effects of the electric field associated with a laser-induced pulsed discharge on the ablation-generated plumes of YBa2Cu3O7-X. Journal of Applied Physics, 1992. 72(3): p. 1113-1125.

- 112. Yeates, P., J.T. Costello, and E.T. Kennedy, *The DCU laser ion source*. Review of Scientific Instruments, 2010. **81**(4): p. 043305.
- 113. Ogawa, M., et al., *High-current laser ion source based on a low-power laser.* Laser and Particle Beams, 2004. **21**(4): p. 633-638.
- 114. Yoshida, M., et al., *A simple time-resolved emittance measurement of a laser ion source with a digital camera.* Nuclear Instruments and Methods in Physics Research A, 2001. **464**: p. 582.
- 115. Guthikonda, N., *Dynamics of Confined Laser Induced/Ablative Plasmas and Shock Waves*, in *Physics*. 2020, University of Hyderabad: Hyderabad. p. 211.
- 116. Toro, E., Riemann Solvers and Numerical Methods for Fluid Dynamics: A Practical Introduction. 2009.
- 117. Sobral, H., et al., *Temporal evolution of the shock wave and hot core air in laser induced plasma*. Applied Physics Letters, 2000. **77**(20): p. 3158-3160.
- 118. Villagran-Muniz, M., H. Sobral, and E. Camps, *Shadowgraphy and interferometry using a CW laser and a CCD of a laser-induced plasma in atmospheric air.* IEEE Transactions on Plasma Science, 2001. **29**(4): p. 613-616.
- 119. Chenais-Popovics, C., et al., *Kinetic to thermal energy transfer and interpenetration in the collision of laser-produced plasmas.* Physics of Plasmas, 1997. **4**(1): p. 190-208.
- 120. D P S L Kameswari, N.G., S Sai Shiva, P. Prem Kiran\*, Energy Depenent Study of Confined Laser Generated Air Plasma, in 29th DAE-BRNS National Laser Symposium (NLS-29). 2021: Shri Vaishnav Vidyapeeth Viswavidyalaya, Indore.
- 121. Sai Shiva Sakaraboina, P.K.P., Venkata Ramana Ikkurthi, Three-dimensional radiation hydrodynamic simulations of laser-produced air plasma aluminum slab interaction\*, in APS March Meeting 2021. 2021.
- 122. D. P. S. L. Kameswari, N.G., E. Manikanta, S. Sai Shiva, S. Sree Harsha, V. R.Ikkurthi and P. Prem Kiran, *Material Dependence Of Lateral Confinement Of Laser Induced Air Plasma*, in *IEEE International Conference on Plasma Science (ICOPS-2020)*. 2021, IEEE Transactions on Plasma Science: Singapore.
- 123. S. SaiShiva, N.G., D. P. S. L. Kameswari, V. R.Ikkurthi and P. Prem Kiran. A Three Dimensional Three Temperature Radiation Hydrodynamic Simulations Of Laser Produced Air Plasma Dynamics In Ambient Atmospheric Air. in IEEE International Conference on Plasma Science (ICOPS-2020). 2020. Singapore: IEEE Transactions on Plasma Science.
- 124. Macfarlane, J.J., IONMIX a code for computing the equation of state and radiative properties of LTE and non-LTE plasmas. Computer Physics Communications, 1989. **56**(2): p. 259-278.
- 125. Kameswari, D.P.S.L. and P.P. Kiran, *Temperature evolution in silver nanoparticle doped PETN composite*. AIP Conference Proceedings, 2018. **1942**(1): p. 140051.
- 126. Fryxell, B., et al., FLASH: An Adaptive Mesh Hydrodynamics Code for Modeling Astrophysical Thermonuclear Flashes. The Astrophysical Journal Supplement Series, 2000. **131**(1): p. 273-334.

## **Chapter-2**

# **Simulation Methodology**

A hydrodynamic formalism of the shock wave and plasma dynamics were briefly described in this chapter. The conservative Euler equations describing a fluid flow, the numerical scheme used to solve these equations when a purely hydrodynamic evolution of shock wave is considered in fundamental problem such as a shock tube is discussed in detail. However, to describe and to visualize the mechanism undergoing and to understand the physical processes undergoing in the real time experiments such as laser matter interactions a 2D/3D hydrodynamic code is required. Hence FLASH 2D radiation hydrodynamic code is used to solve the conservative Euler equations when the energy deposition due to laser source is added. To verify the realistic phenomenon of laser ablation of 20 µm thick aluminium foil when a pulse of energy 50 mJ at a wavelength of 532 nm of the incident beam is studied. The dynamics of plasma and shock wave were studied and the spatio-temporal evolution of the physical parameters describing the shock strength i.e., mass density, pressure and plasma parameter electron temperature were described in detail. The orders of the physical parameters obtained were verified with the values observed in literature and found that the results were in line with the realistic phenomenon. The results of numerical simulations were validated with experimental results where ever possible before predicting the output of new experimental schemes.

# 2.1 Introduction

Laser - matter interaction is a complex phenomenon and remains a challenge in understanding the multi-physics nature of the absorption of light by the target material, thermodynamics (heating, phase transitions, cooling), gas dynamics, plasma physics (collisions, electric interactions) and laser-plume interaction (plasma heating by absorption of laser photons, inverse Bremsstrahlung, multi-photon ionization). Moreover, the fundamental mechanisms involved and the properties and dynamics of the subsequent laser-produced plasmas depend strongly on the laser beam parameters (pulse duration, fluence, wavelength, beam profile) and also on the properties of the irradiated material (conductivity, reflectivity, surface finishing etc.). A laser beam irradiated on to a material (air, solid target), heats the material, followed by rapid ionization resulting in release of free electrons and ion pairs [1]. These free electrons loses its energy by continuous collisions with the ions, excited and the neutral atoms and gains energy from the incoming laser beam resulting in an abrupt raise in the temperature at the focal volume. The so formed high temperature ionized gas is called as plasma [1, 2]. The process of the absorption of the photons from the laser beam continues until the laser pulse duration, the resultant plasma during this time expands supersonically towards the direction opposite to laser beam. This free electron cloud moving towards the laser beam forms a thin layer of matter in front of the focal volume shielding the direct absorption of laser beam with the material called as plasma shielding. The layer of matter formed due to accumulation of the material ejected is called as the shock wave (SW). The SW is a thin layer having very high density and pressure when compared to the surrounding medium. The SW when completely built detaches from the plasma and expands adiabatically into the back ground gas. Since, the laser pulse considered here has no time durations, the dominant absorption taking place is the inverse Bremsstrahlung absorption (IB) [2, 3]. The other absorption mechanism that are expected to occur are multi-photon ionization and tunnelling ionization which are dominant in the short and ultra-short laser pulses i.e., picosecond (ps) and femtosecond (fs) [2]. The main requirement for IB mechanism to take place is the existence of at least one free electron in the focal volume. In the IB, the incident photon is interacting with the electron, the mobilized electron in turn collides with the atoms and results in release of few more free electrons and ions via cascade ionization. Hence the inverse Bremsstrahlung is called as a three body mechanism [1]. During the interaction of laser with solid targets (metals, semiconductors and dielectrics) the formation of plasma at the front surface of the solid target is called as ablation [4-8] which has various applications in different background environments [9-12] under different background pressures [13]. So the laser ablation finds application in many areas of pulsed laser deposition (PLD), nanoparticle generation [4, 14, 15], micromachining and to name a few.

The density and pressure gradients at the shock front (SF) are very steep such that, a discontinuous flow across the SF is observed as a result. The SF characteristics are understood based on the Rankine – Hugoniot conditions are the jump conditions [16] which relates the shocked medium (medium behind the SW) and the un-shocked medium (medium ahead of SF).

In the case of solid targets, the ablative shock wave (SW) expanding into ambient air launches a compression wave through the material due to momentum conservation. The launched SW travels through the material medium depending on the thickness of the target material and intensity of the incident beam. In few cases the SW reaches the rear end of the target and a blow-off SW is launched in the rear end of the target [17-19].

Simulation using molecular dynamics have the capability of modelling the ultra-short pulse laser ablation. However, it is to be noted that it takes a longer time to study the plasma dynamics under high pressures. This is due to the number of molecules to be considered is very large in case of dense targets and high pressures [20, 21].

The evolution of shock wave and plasma were explained by solving the hydrodynamic equations [16, 22] in the present work. In order to understand the shock characteristics and its spatial-temporal evolution a shock tube problem is carried out. This is understood using insitu developed one-dimensional hydrodynamic code. The pressure gradient between two chambers separated by a thin diaphragm is explained in this chapter. The basic hydrodynamic equations are solved using Godonov method [16] However, since our problems (LMI, and ablation) dealt with high pressure, high temperature fluids which require different source terms such as laser deposition, energy transfer through heat, radiation and collisions. Moreover, the multi-dimensional nature of laser matter interaction can be well understood by either 2D or 3D numerical simulations. Hence, to understand the phenomenon of laser ablation and the occurrence of different physical processes and to visualize the evolution of SW in ambient atmospheric air we have employed FLASH 2D radiation hydrodynamic code [23] which is well developed and widely used code. This code supports different source terms such as, the laser energy deposition, heat and radiation transfer mechanisms. The SW evolution at the early time

scales is presented in this chapter. Our experimental data gives 2D expansion of shock wave. Hence, the 2D simulations are ideal for us to predict the evolution in complex experiments.

## 2.1.1 Hydrodynamic formulation

The basic idea of hydrodynamics is to give a complete description of motion of a fluid element at any instant of time, and describe how the motion changes with respect to the applied forces. Hydrodynamic simulations of laser-produced plasmas are a useful tool allowing one to investigate the processes that take place during laser-plasma interaction, the evolution of plasma from the initial time of generation, internal structures of plasma, formation and evolution of shock wave which are often impossible to observe directly during the experiments. They allow not only the interpretation of experimental results, but are also often used for designing the experimental setup or detailed analysis of particular processes during the experiment. The physical quantities of interest in the motion of a fluid element are its mass density, the velocity and the forces that change these quantities such as stress, viscosity, thermal conductivity etc. The simplest starting point is to assume the material to be compressible ideal fluid that is non-viscous and non-conducting. The methodology followed while studying a physical problem is described in the following fig. 2.1.

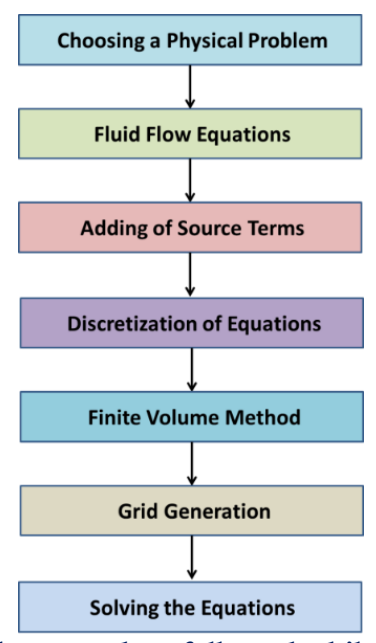


Fig. 2. 1 Flow chart showing the procedure followed while solving a physical problem

The propagation of the SW and its effects through a medium are governed by the three laws: conservation of mass or continuity, momentum and energy where the shocked material is considered as a fluid. The conservation equations are the partial differential equations (PDEs) that are generally solved by either Eulerian or Lagrangian or arbitrary Lagrangian-Eulerian [24]

formalisms. There exists a variety of numerical techniques that are implicit [22, 24], explicit [16] that are used to numerically discretize the PDEs where each technique has its own advantage and disadvantage over the other. Hence the numerical technique can be adopted depending on the complexity of problem. The main aim of the thesis is to design of a millimetre size macro shock tube which involves different steps and different levels of confinement and refinement. Fig. 2.2 shows a schematic of the method followed in achieving the design of a macro shock tube.

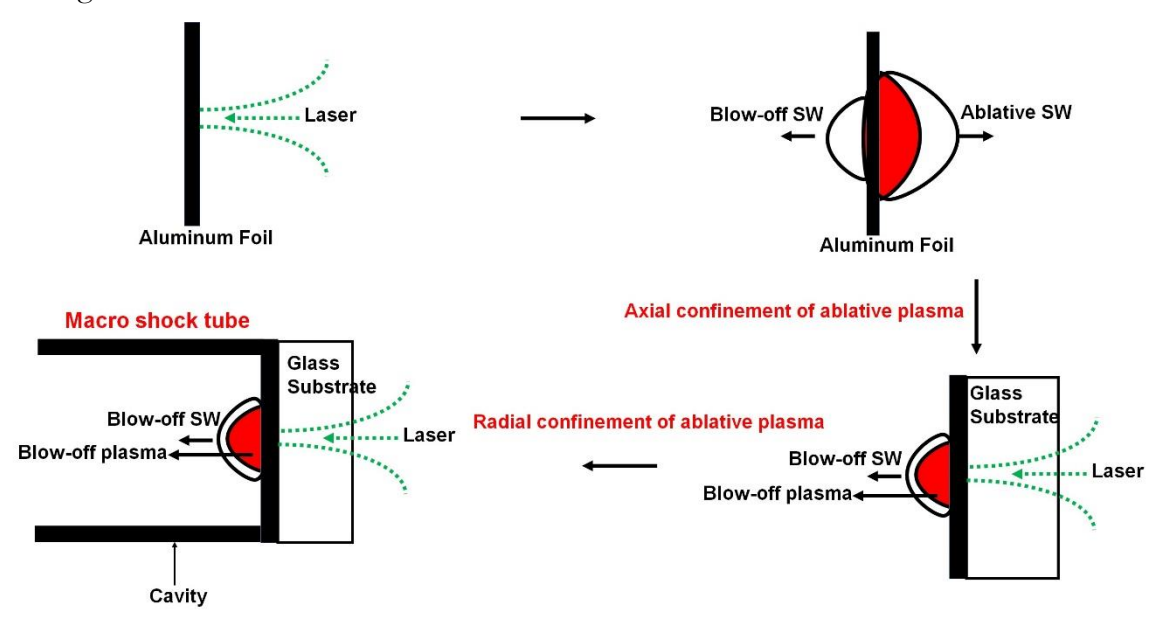


Fig. 2. 2 A schematic showing the method followed in the design of a macro shock tube

Each step of process shown in Fig 2.2 involves a refinement of different level depending on the regions of higher density gradients. In the first stage of the above process, a thin aluminium foil of thickness 20 µm is considered, laser beam of fixed energy is focussed onto the foil. The interaction of the laser beam with the metal foil results in generation of plasma and SW in the ablation and blow-off regimes as can be seen in stage two. The ablative plasma is confined using a glass substrate in the third stage. This has resulted in the increment of the plasma and SW strength. In the fourth stage, the blow-off plasma and SW were spatially confined using a glass cavity of fixed dimensions. To study the complex behaviour of plasma and SW generated, their expansion dynamics a better understanding of generation and propagation of a SW in a cell (assumed as fluid) is required. The effect of step size, initial conditions, discretization method on SW (assuming SW as a fluid) generation and propagation gives a better understanding in the design of complex laser generated plasma and SW applications. Hence initially the formulation of a shock tube with no source terms is studied, which is then extended to the laser generated plasma and SW.

# 2.1.2 Hydrodynamic equations

Let us assume that the fluid is entering into an arbitrary cell of volume V from -X direction through the face ABCD having an area A, with a velocity  $u_x$  as shown in Fig. 2.3. The fluid is leaving from the other face EFGH with a velocity  $u_x$ +  $du_x$ . There is a net change in the flux parameters (density, pressure, energy), because of the moving fluid.

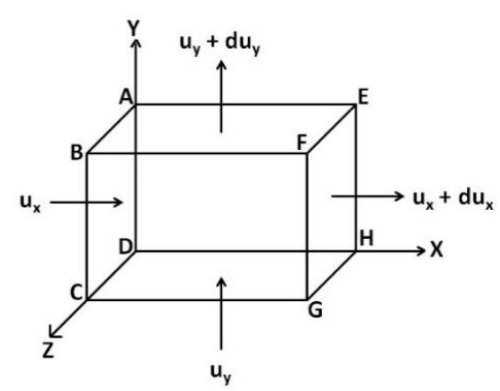


Fig. 2. 3 Infinitesimal volume showing from which a fluid is flowing

The first conservative equation is the mass conservation or continuity equation. According to this, the net mass flux entering the cell  $(\varrho u_x)$  is equal to the net mass flux leaving the cell  $(\varrho(u_x+du_x))$  i.e., the change in the density inside the volume V is due to the fluid flowing through the cell. The mass conservation equation in the generalized form is given in eq. 2.1

$$\frac{\partial \rho}{\partial t} = -\vec{\nabla}.\left(\rho u\right) \tag{2.1}$$

The second conservative equation is the conservation of momentum which states that the net rate of momentum  $(\rho \vec{u}_x)$  entering the volume V is equal to the net momentum leaving the volume. The momentum conservation equation is given by eq. 2.2

$$\frac{\partial(\rho\vec{u})}{\partial t} = -\vec{\nabla}.\left(\rho\vec{u}\vec{u}\right) - \vec{\nabla}P\tag{2.2}$$

The time rate of change of total energy in the control volume (eq. 2.3) is equal to the influx of energy per unit time plus all the forces acting on the volume

$$\frac{\partial(\rho E)}{\partial t} = -\vec{\nabla}. \left[ (\rho E + P)\vec{u} \right] \tag{2.3}$$

where  $\rho$  is the mass density of fluid,  $\vec{u}$  is the velocity of fluid, E is the energy, e is the internal energy =  $\frac{1}{2}u^2$  and P is the pressure. The total energy of the fluid in a volume is  $E = \rho$  (e +  $\frac{1}{2}u^2$ ). The set of equations (2.1) – (2.3) are in the Eulerian form [16] where the control volume is fixed and the fluid flows with reference to this fixed volume.

A study of spatial evolution of physical parameters of the fluid i.e., mass density, momentum density and energy density were studied in a shock tube problem by solving the above conservative equations using Godonov method is presented in the following section.

#### 2.1.3 Shock Tube Problem

A shock wave is a thin transitive layer propagating with supersonic speed (velocity much higher than velocity of sound) in a medium. It is a compressive wave which moves forward by compressing the medium ahead of it. A SW is always followed by a sharp density and pressure gradient because of which it moves supersonically into the surrounding medium. Shock waves arise during explosions, detonation, supersonic movements of bodies, powerful electric discharges etc. A detonation wave is a SW in a reactive medium that is sustained by energy released in the form of chemical reactions.

A shock tube is a device comprising two chambers of different density and pressure separated by a thin diaphragm. The density and pressure of the gas present on one side of the chamber (diaphragm) are higher in one chamber (known as driver section) than that on the other side of diaphragm were the ambient air conditions. Due to the existence of pressure or density gradients at the interface of diaphragm, the diaphragm bursts and a SW is launched into the chamber having low pressure and density. The SW thus launched moves forward in the chamber compressing the material ahead resulting in an increase in the density and pressure at the SF. Fig. 2.4 shows the schematic of a shock tube. The material inside the shock tube in both the chambers is assumed to be at rest initially i.e., fluid velocity on both sides is zero. Assuming the material to be air the density on the either sides of the diaphragm is assumed to be 1.3 kg/m<sup>3</sup>. However, the pressure in the left chamber is assumed to be 10 times more than that in the right chamber, which resulted in a pressure gradient between the two chambers. Due to the pressure gradient between the two chambers the diaphragm separating the two chambers bursts and launches a SW into the right chamber. To describe the spatial evolution of the physical parameters describing the system (density, pressure and velocity) Godonov scheme [16] is used.

Godunov's method [25] uses a finite-volume spatial discretization of the Euler equations together with an explicit forward time difference. Time-advanced fluxes at cell boundaries are computed using the numerical solution to Riemann's problem. A Riemann problem, consists of an initial value problem described by conservation equation together with piecewise constant data having a single discontinuity.

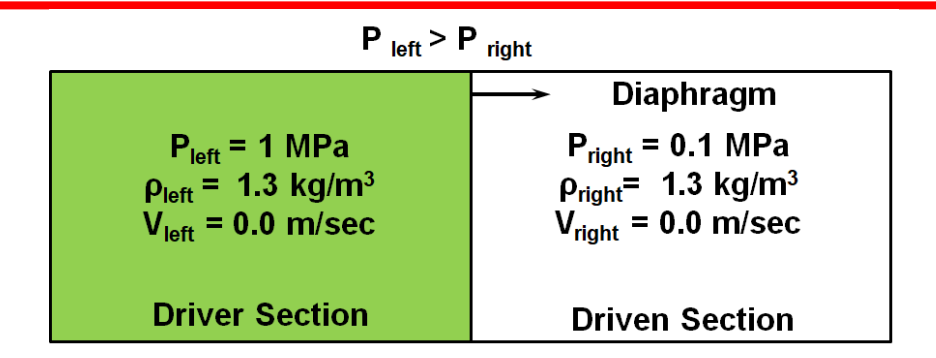


Fig. 2. 4 A schematic of shock tube

According to the scheme, if the conservative equations from (2.1 - 2.3) can be represented as shown in eq. 2.4

$$U_t = -F(U)_x \tag{2.4}$$

Where  $U_t$  being the vector of conservative variables (node centered variables) density, momentum and energy,  $F(U)_x$  being the vector of the flux (cell centered variables) entering and leaving cell as shown in eq. 2.5

$$U_{x} = \begin{bmatrix} \rho \\ \rho v \\ E \end{bmatrix} \text{ and } F(U)_{x} = \begin{bmatrix} \rho v \\ \rho v^{2} + P \\ v(E+P) \end{bmatrix}$$
 (2.5)

To solve a set of equations, divide the whole system into number of equal grids in terms of position and time. Since there are four variables ( $\varrho$ , v, P and E), and three equations, a relation is required among the four variables to close the equations. The relation that is used to close the equations is called as the equation of state (EOS). The three equations are closed by the ideal gas EOS shown in eq. 2.6

$$P = (\gamma - 1)\rho E \tag{2.6}$$

According to Godonov scheme, the conserved variables at the next time step t<sup>n</sup> is given by the eq. 2.7

$$U_i^{n+1} = U_i^n + \frac{\Delta t}{\Delta x} (F_{i-1/2} + F_{i+1/2})$$
(2.7)

Where  $F_{i-1/2}$  is the cell centered flux which is the average of the fluxes between i-1,i and i+1. Here, in order to solve the above condition the cell centered flux is to be evaluated. There are many numerical methods to calculate the cell centered flux. Here we are using the Lax-Frederick method [16]. According to Lax –Frederick method the cell centered flux is evaluated using the eq. 2.8

$$F_{i+\frac{1}{2}} = \frac{1}{2} \left( F_i^n + F_i^{n+1} \right) + \frac{1}{2} \frac{\Delta x}{\Delta t} \left( U_i^n - U_{i-1}^n \right)$$
 (2.8)

Each step is controlled by the Courant-Friederichs - Lewy relation (CFL) [16, 22, 24].

$$c = \frac{v \,\Delta t}{\Delta x} \tag{2.9}$$

with a condition that 0 < c < 1. The grid size considered here is in  $1.0 \times 10^{-9}$  m ( $\Delta x$ ). This is the condition which controls the velocity of the fluid. The spatial variation of conservative variables is presented in fig. 2.5.

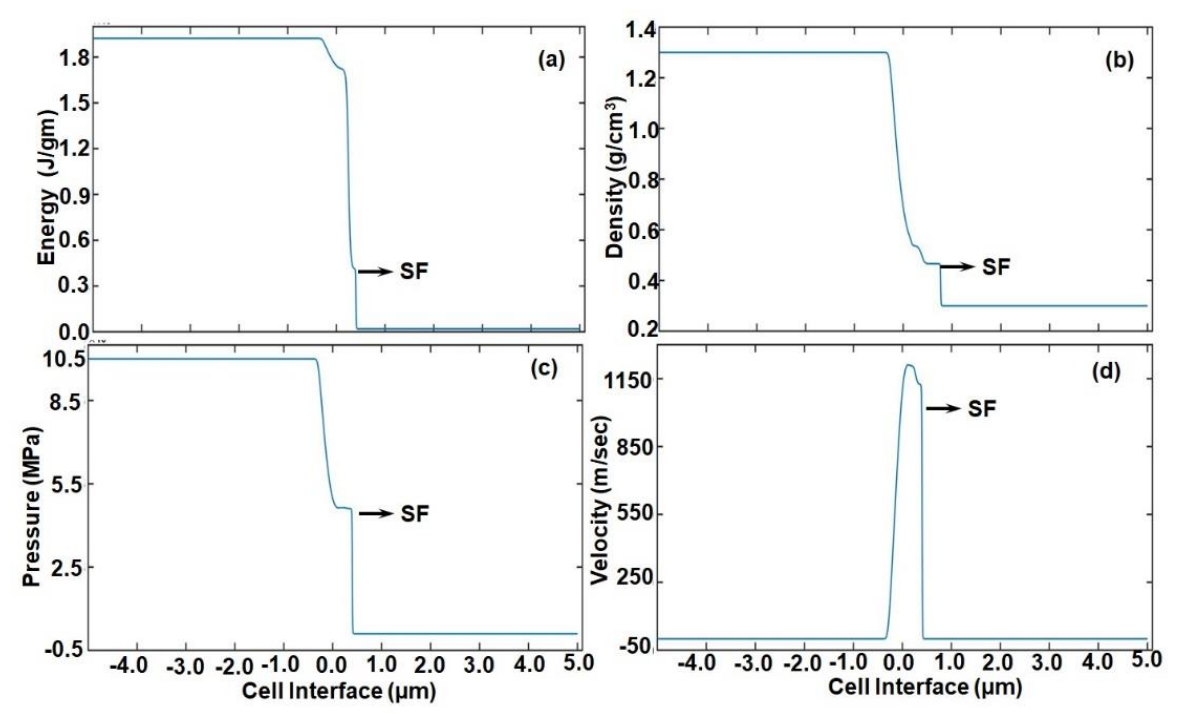


Fig. 2. 5 Spatial variation of (a) energy (b) pressure (c) density (d) velocity inside a shock tube driven from driver section

Fig 2.5 (a) - (d) shows the spatial variation of the conservative variables energy, density and the

physical parameters velocity and pressure inside the shock tube showing the evolution of SW. Fig 2.5 (a) shows the variation of energy. It is clearly visible that the energy of the chamber in the right side has increased. This is observed because; initially the particles on either sides of the diaphragm are at rest. However, due to the existence of pressure gradient, when the diaphragm is released the work is done (momentum equation) on the right side of the chamber. Hence, the particles that are in contact and near to the diaphragm start moving with the shock velocity i.e., with the diaphragm. As a result, the particle collisions with each other and with the walls of the chamber were initiated leading to a raise in their kinetic energy leading to increment in the internal energy. As a result, the temperature of the chamber also increases. Hence, a steep increase in energy, velocity was observed as shown in fig. 2.5 (a) & (d). (Internal energy  $e = (1/2) v^2$ ). Now, by the movement of the diaphragm the particles in the right

chamber were compressed leading to formation of a strong shock front as the peak can be observed in density and pressure (shown in fig. 2.5 (b) &(c)). The density has increased because of the accumulation of all the particles with the moving diaphragm. Similarly, the pressure has increased because of the force that is being exerted on the particles. The wave followed by SW is a rarefaction wave. Where a SF is a compressing wave, rarefaction wave is an expansion wave trying to recover the system back to its original state. But, the system cannot reach its original position after the shock traverses the medium.

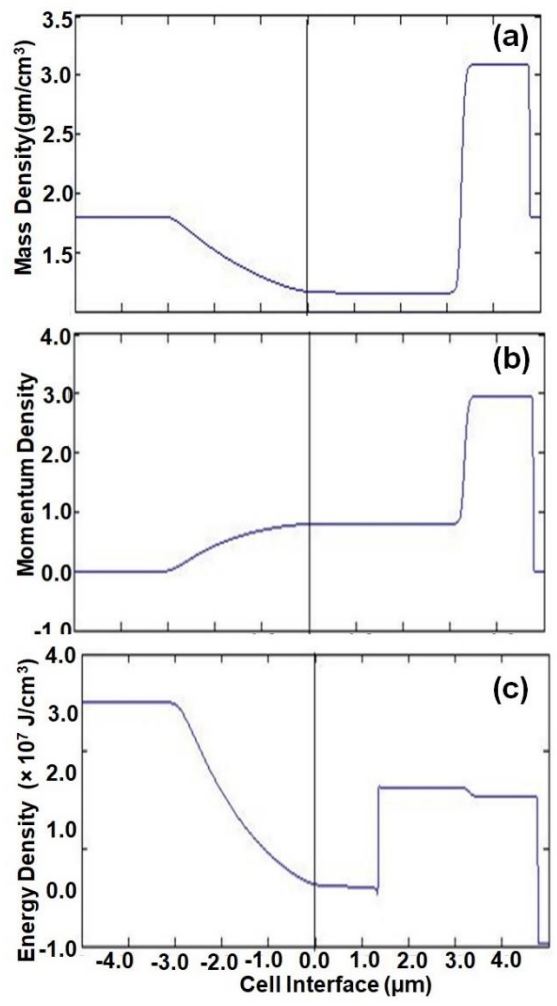


Fig. 2. 6 Spatial variation of the cell centred flux variables (a) mass density, (b) momentum density and (c) energy density inside the shock tube

Fig. 2.6 shows the variation of the flux variables i.e., variation of the physical parameter per unit volume (since the equations were solved in 1D, per unit length is considered). Fig. 2.6 (a) shows the variation of mass density, (b) momentum density and (c) energy density. A steep raise in the physical variables is observed in fig (2.5) & (2.6) after the diaphragm which shows the shock front position. However, the problem considered till now is just a hydrodynamic evolution where no source terms were involved. However, to visualize and analyse the realistic

phenomenon taking place during and after the laser is irradiated on to a material, a two dimensional/ three dimensional code with source terms added is required. Hence we have adopted FLASH 2D radiation hydrodynamic code is brought into picture in this thesis.

# 2.2 Hydrodynamics of Laser Ablation

To study the complex laser-matter interaction, behaviour of plasma and shock waves, effect of energy deposition onto a metal target, is studied in this section. When the laser beam is focused on to a metal target, the optical energy may be converted into thermal, radiation and mechanical energy depending on the intensity (I) of the laser beam and breakdown threshold intensity (I<sub>br</sub>) of the target material. If the peak intensity of the incident laser beam is less than I<sub>br</sub> then the material is just heated and may be partially or fractionally ionized. However with the increasing laser intensity the thermal effects become dominant and also other effects such as the radiation energy (from plasma) and mechanical energy in the form of SW becomes more significant [26]. The strength of SW generated from ablated plasma increases with the increasing intensity which also depends on the other variables such as laser pulse duration, wavelength, target properties and surrounding gas conditions. Laser ablation process can be divided in to two stages: i) evaporation of the solid target and formation of laser plasma, ii) expansion of ablated vapour cloud into background gas. The dominant photo absorption process in ns- laser produced plasma is inverse Bremsstrahlung absorption (IB).

During the process of plasma formation a number of free electrons are created, because of the incident photons (multi photon ionization) leading to a linear increment in electron number density (N<sub>e</sub>) with time. The electrons thus released re-absorb incident photon energy, leading to the excitation of the electron. The excited electron, collides with the surrounding particles (electrons, neutrals and ions) until the electron ionize a neutral atom. This process involving three – body (photon, electron and neutral atom) leading to ionization of the target material and plasma formation is called as inverse Bremsstrahlung process.

The free electrons generated in the plasma by different processes, receive energy from the incoming photons, resulting in the increase of kinetic energy (electron temperatures). The process of gaining and losing the electron energy continues because, the nanosecond pulse duration is longer than the excitation and de-excitation times of the electrons leading to the increase in the thermal energy and ionization. The temperatures, ionization, electron number density, pressures, total specific energy of the plasma increases that causes the expansion of the plasma. During the expansion process, a rapid thermal energy transfer between the

particles of the hot plasma and surrounding gas takes place within a thin layer of few orders of mean free path [2, 12] resulting in accumulation of the energy and increasing in entropy. According to kinetic theory of gases, the temperature of the electrons is much higher than that of the ions. The electrons are in continuous collisions with the surrounding electrons and ions, hence the temperature of the electrons is very high. However, as the ions have the heavy mass compared to electrons, the collision frequency is less and as a result, have less temperature when compared to that of electrons. However, after few micro seconds electron and ion temperatures come to equilibrium state. The mechanisms that cause plasma to emit or absorb radiation can be classified into two types as: radiation from emitting atoms or molecules, and radiation from accelerated charges. During the process of plasma ionization due to incident laser beam and due to continuous collisions, [26] that is recombination of the ions and electrons to form neutral particles, also occurs. A radiation is emitted when the excited particle decay down to the ground state. This radiation constitutes the line spectra of plasmas. The transition is called as the bound-bound transition. On the other hand, radiation emitted whenever a charged particle is decelerated by making some kind of collisional interaction is called bremsstrahlung. If the charged particle remains unbound, both before and after the collision is called free-free transition. If the originally unbound charged particle is captured by another bound particle by emitting a radiation, the process is called free-bound transitions.

To understand and visualize the process of formation and expansion of laser induced plasma and SW, the laser ablation of an aluminium target of thickness 20  $\mu$ m is irradiated with a laser beam of energy 50 mJ at incident wavelength 532 nm and spot size of 500  $\mu$ m at 0.1 MPa baground gas pressure is presented below. Fig. 2.7 shows the simulation domain. The size of the two dimension domain considered is  $600 \times 1000 \,\mu$ m.

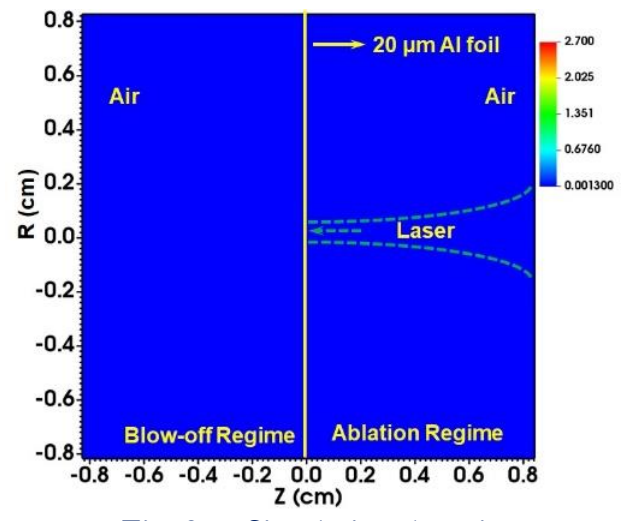


Fig. 2. 7 Simulation domain

#### Simulation Methodology

To describe the system considered and study the evolution of physical parameters, such as mass density, pressure, temperature the system of the three conservative equations similar to that shown in eq. (2.1 - 2.3) is to be considered. However, the extra source terms such as thermal conduction, energy deposition are to be added to the energy equation [2, 23] as shown below.

$$\frac{\partial \rho}{\partial t} + \vec{\nabla} \cdot (\rho \vec{v}) = 0 , \qquad (2.10)$$

$$\frac{\partial(\rho\vec{v})}{\partial t} + \vec{\nabla}.(\rho\vec{v}\vec{v}) + \nabla P_{tot} = 0, \qquad (2.11)$$

$$\frac{\partial E_{tot}}{\partial t} + \vec{\nabla} \cdot [(\rho E_{tot} + P_{tot}) \vec{v}] = Q_{las} - \nabla q, \qquad (2.12)$$

Here,  $\varrho$  is the total mass density, v is the average particle velocity,  $P_{tot}$  and  $E_{tot}$  are the total pressure and total specific energy which are the sum of electron, ion and radiation pressures,  $P_{tot} = P_{ele} + P_{ion}$ .

 $Q_{las}$  is the energy due to laser heating. The Harten-Lax-van Leer-Contact (HLLC) scheme [16] is used to determine the inter cell fluxes. q is the total heat flux due to radiation and electron conductivity. The thermal conductivity is calculated using the SpitzerHighZ model of electron thermal conduction given by the relation as shown in eq. 2.13 [23].

$$q_{ele} = \left(\frac{8}{\pi}\right)^{3/2} \frac{k_B^{7/2}}{e^4 \sqrt{m_e}} \left(\frac{1}{1+3.3/\bar{z}}\right) \frac{T_e^{5/2}}{\bar{z} l n \Lambda_{ei}}$$
(2.13)

 $q_{ele}$  is the electron conductivity,  $k_B$  is the Boltzmann constant, e is the electron charge,  $m_e$  is the mass of an electron,  $\bar{z}$  is the average ionization as computed by the EOS,  $T_e$  is the electron temperature  $ln\Lambda_{ei}$  is the Coulomb logarithm associated with electron-ion collisions.

To close the above equations (2.10-2.12), the multi-temperature gamma equation of state (EOS) for air is taken [3]. This EOS implements the ideal gas conditions separately for ion as well as for electron. The radiative transfer equation is solved in the grey diffusion model by assuming the black body radiation. Ionmix EOS is used for aluminum target [23]. The laser power deposited in a cell is calculated based on the inverse Bremsstrahlung (IB) power in the cell and depends on the local electron number density and electron temperature gradient. The IB frequency factor is given by:[23]

$$\vartheta_{\rm IB} (s^{-1}) = \left(\frac{4}{3}\right) \left(\frac{2\pi}{m_{\rm e}}\right)^{1/2} \frac{Ze^4}{n_{\rm c}K_{\rm B}^{3/2}} \frac{n_{\rm e}[r(t)]^2 \ln(\Lambda[r(t)])}{T_{\rm e}[r(t)]^2}$$
(2.14)

where  $\ln \Lambda = \ln \left[ \frac{3}{2Ze^3} \left( \frac{k_B^3 T_e^3}{\pi n_e} \right)^{\frac{1}{2}} \right]$  is the Coulomb logarithm [2]. Z is the charge state of target material, e is the electro-static charge of electron,  $N_e$  the electron number density,  $k_B$  is Boltzmann constant,  $T_e$  electron temperature, and  $m_e$  is the mass of electron. Hence it can be understood that the rate of IB absorption depends on the electron number density and the electron temperature, both of which are functions of the position, and, since the position changes with time, it ultimately is also a function of time. To solve the above set of equations, FLASH code is used and to visualize the plasma and shock parameters. VisIT [27]

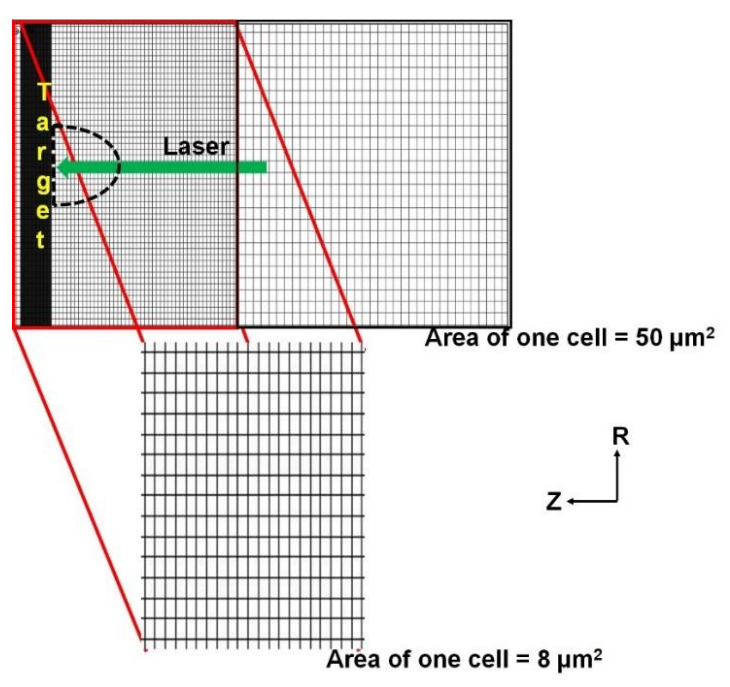


Fig. 2. 8 A schematic of adaptive mesh refinement (AMR) showing more refinement near high density gradients (shown in zoomed view) and less refinement at low density gradients

FLASH is a parallel, adaptive-mesh refinement (AMR) code with block structured AMR, designed for compressible reactive flows and can solve a broad range of (astro) physical problems. FLASH supports Cartesian - 1D, 2D, 3D, Cylindrical - 2D, (3D), Spherical - 1D, (2D), (3D), and Polar - (2D) geometries. Grid implementation makes use of paramesh supported grid geometry. Paramesh is an adaptive mesh refinement (AMR) method in which the level of refinement throughout the domain is not the same but varies from region to region. The refinement level is more at the interfaces with steep gradients (pressure, density, energy etc.,) in the domain or at the point where the energy is being deposited. The refinement level decrease as we move away from the interfaces Fig. 2.8 shows the variation between paramesh and uniform grid.

### 2.2.1 Evolution of Physical Parameters

Solving the conservative equations eq. (2.10 - 2.12) using FLASH code, the spatio – temporal evolution of physical parameters describing the system i.e., mass density, pressure, temperature were studied. To study the evolution of plasma, spatial variation of electron temperature is studied since most of the contribution to plasma temperature is due to the free charge carriers. Fig. 2.9 (a) & (b) shows the spatial evolution of electron temperature ( $T_e$ ) at 10 and 20 ns i.e., during the pulse duration.

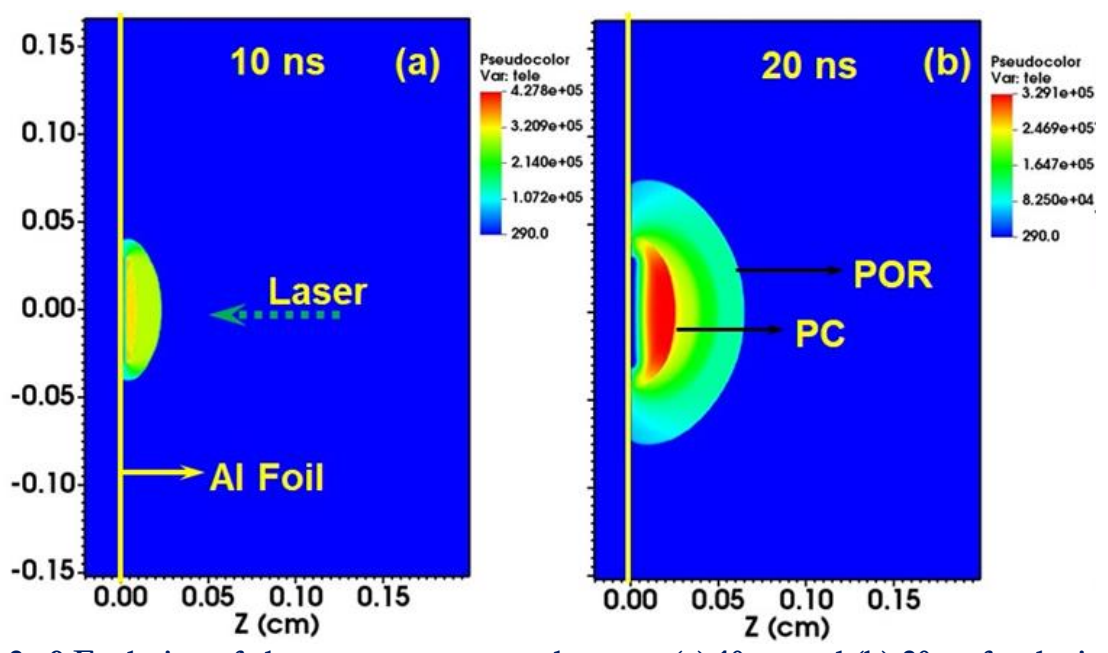


Fig. 2. 9 Evolution of electron temperature shown at (a) 10 ns and (b) 20 ns for the input laser energy of 50 mJ

Fig 2.9(a) shows the variation of  $T_e$  at 10 ns. the hottest and the densest part of the plasma called plasma core; in this region, the material is mostly found in the ionized state because of high temperatures which is at  $4.7 \times 10^5$  K represents the plasma core the most heated zone. In the plasma core regions, ions and neutrals exist due to the ongoing ionization and recombination processes. The outer edge of the plasma core is the SF and the outermost region of the plasma is relatively cold, where the population of neutrals dominates [28]. A clear view of shock front and plasma front (PF) were clearly visible in the fig. 2.9(b).

To understand the dynamics of shock wave, such as the strength of the SW, formation, detachment and expansion of SW into the ambient gas can be understood by studying the parameters such as pressure and density. The spatio- temporal evolution of pressure, mass density and electron temperature were presented in Fig. 2.10 (a) - (c) at different time scales

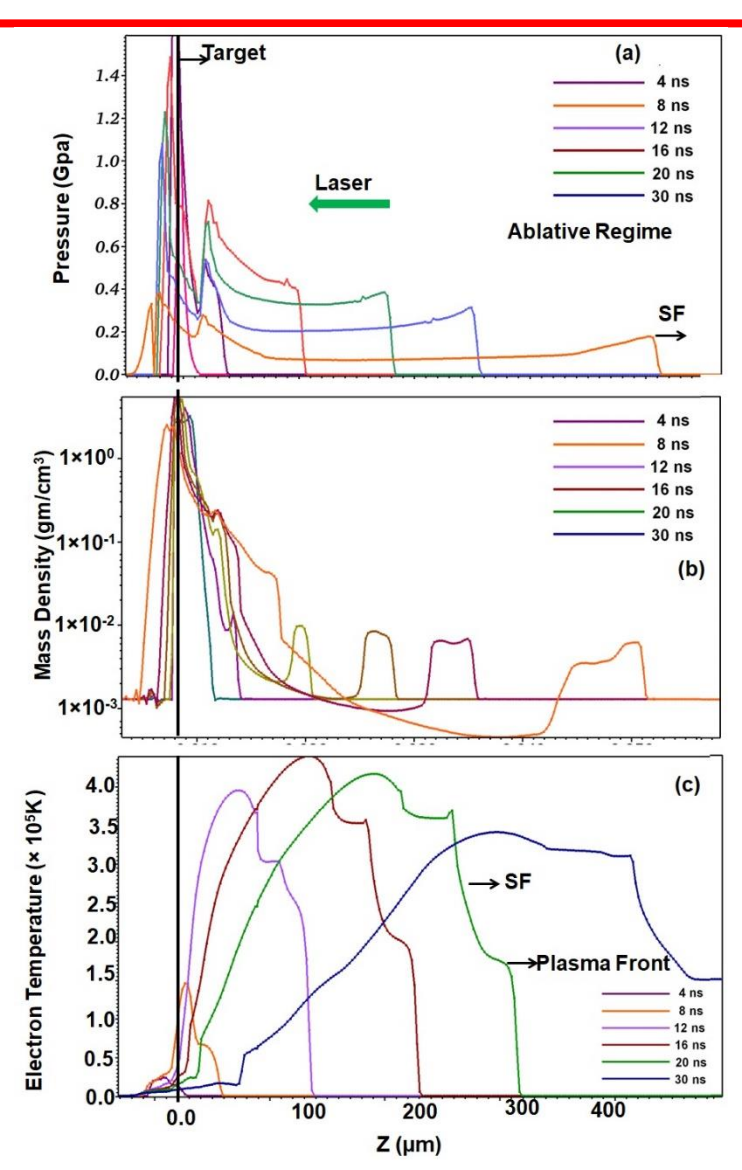


Fig. 2. 10 Spatio -temporal evolution of (a) pressure, (b) mass density and (c) electron temperature for the input laser energy of 50 mJ. The solid line at Z=0 represents the position of the target

Pressure as shown in fig 2.10 (a) at 4 ns shows that the SW has not formed yet but the pressure at the interface of air and target increased to 1.4 GPa which is 0.1 MPa before the interaction of the laser beam. This pressure is created because of the force exerted by the plasma plume created at the front surface. However, the SF is clearly visible at 8 ns with a shock pressure of 0.4 GPa. The strength of the SW increase as it travels with plasma because of accumulation of mass removed the focal region. Hence an increase in shock pressure observed from 8 ns to 12 ns upto 0.5 GPa.

When the SW detaches from the plasma the strength of the SW decreases as it expands adiabatically into the surrounding medium. The strength of the SW decreases during the

expansion due to the energy dissipation to the surrounding medium. The SW traverses in the forward direction because of its high pressure gradient at the shock front (SF) and the medium.

The pressure and density of the shocked region (medium after the traversal of the SW) increases since the SW compresses the medium as it moves ahead. The expansion of the SW in the ablative regime is shown upto 30 ns in the fig 2.10 (c) (1.8 GPa) showing a decrease in the shock strength as it moves in the forward. The peak region visible behind the SF is the plasma region. At 30 ns an ablative SW is launched into the blow-off regime. As the thickness of the target is very less the SW launched into the target at 8 ns has reached the rear side of the target. The strength of the SW has decreased from the time it is launched at the interface (1.8 GPa) [29] to that has reached the rear side of the target to 0.3 GPa. It is also noteworthy that the pressure created at the target interface is 1.8 GPa and the SW launched into the ablation regime is 0.6 GPa (i.e., in air) because of the atomic arrangement in solids and gases. In metal target (solid) the atoms are closely arranged and hence the force exerted on the target is more, however, the atoms are freely distributed in air and hence the compression of the gases leads to less pressure.

Fig. 2.10 (b) shows the variation of mass density clearly showing the movement of the SF. A clear increment in the strength of the SW (density at the front end) is visible from 8 ns to 12 ns. The region behind the SF in density plot is the plasma showing that all the mass is accumulating at the SF and hence the mass density behind the SF is very less and high at the SF.

Fig 2.10 (c) shows the variation of electron temperature upto 30 ns. It can be clearly seen that the temperature has increased from room temperature (290 K) before laser deposition to 1.6  $\times$  10<sup>5</sup> K [12] at 12 ns because of the laser absorption. After 12 ns the temperature has started to decrease till 20 ns and increased at the plasma front (PF) because of the shielding of the free electron cloud at the front surface after which the laser is not directly interacting with the target but absorption is taking place at the front surface. A clear view of plasma and shock fronts can be seen after 16 ns. It is also noteworthy that the temperature at the plasma core is more, but the pressure and density were high at the SF.

To determine the accuracy of the plasma parameters determined, the same simulations i.e., study of laser ablation and plasma generation using 50 mJ source is performed using different orders of Harten-Lax-van Leer-Contact (HLLC) scheme [16]. The statistical error in

determining the inter-cell fluxes using HLLC scheme is determined. Beyond order 3, no change in the cell fluxes is observed which is confirmed by the best convergence of the solutions. The statistical errors are obtained by comparing the electron temperature ( $T_e$ ) and number density ( $N_e$ ) obtained for Order 1 and Order 3. Table- 2.1 compares the peak electron temperature ( $T_e$ ) and number density ( $N_e$ ) obtained for Order 1 and Order 3, respectively at different times from 0.5 – 10  $\mu$ s. The statistical error in temperature and number density is estimated to be  $T_e = 0.26 \times 10^4$  K and  $N_e = 0.82 \times 10^{17}$  cm<sup>-3</sup> respectively. No much variation in the statistical error is observed with the further increase in the order of the HLLC scheme.

Table 2.1: Comparison of electron temperature and number density for Order 1 and Order 3 at different times.

Time (µs)	Order =1		Order = 3			
	$T_{e}(K)$	$N_e(1/cc)$	$T_{e}(K)$	$N_e(1/cm^3)$	$T_e(K)$	$N_e$ (1/cm <sup>3</sup> )
0.5	$2.35 \times 10^{4}$	$12.2 \times 10^{17}$	$2.55 \times 10^{4}$	$9.72 \times 10^{17}$	$0.2 \times 10^4$	$2.48 \times 10^{17}$
1	$1.841 \times 10^4$	$7.59 \times 10^{17}$	$2.00 \times 10^4$	$7.00 \times 10^{17}$	$0.16 \times 10^4$	$0.59 \times 10^{17}$
5	$1.00 \times 10^{4}$	$0.54 \times 10^{17}$	$1.29 \times 10^4$	$0.68 \times 10^{17}$	$0.29 \times 10^4$	$0.14 \times 10^{17}$
10	$0.37 \times 10^4$	$0.12 \times 10^{17}$	$0.77 \times 10^4$	$0.21 \times 10^{17}$	$0.40 \times 10^4$	$0.09 \times 10^{17}$
				Average	$0.26 \times 10^{4}$	$0.83 \times 10^{17}$

The obtained values of the temperature, number density and the pressures were verified with the values published the literature [30-33]. With the confirmation that the methodology followed is in accordance with the physical process taking place in the real time experiment, the simulations were extended to the next level of application to laser matter interaction.

# 2.3 Summary

A brief description of the conservation equations of density, momentum, energy when purely hydrodynamic evolution of SW is considered where no source terms were present. A shock tube problem is considered where two chambers are separated by a thin diaphragm. When the diaphragm burst due to the pressure gradient between the two chambers a SW is generated. Its spatial evolution is studied by solving the hydrodynamic conservative equations combining the Godonov scheme with Lax- Friederichs method which relates the conservative variables i.e., density, velocity and energy (face cantered variables) and flux variables i.e., mass density, momentum density and energy density (cell cantered variables). However, to study the real time applications such as laser ablation / laser deposition model, FLASH 2D radiation hydrodynamic code is used.

Initially laser ablation study of aluminium target of 20 µm thickness is irradiated with a laser beam of energy 50 mJ energy at incident wavelength of 532 nm during the time of laser deposition is studied using FLASH code. To study the hydrodynamics of plasma and shock evolution during energy deposition and the expansion dynamics of SW and plasma, the three conservative equations were solved, where the source terms due to laser energy deposition and thermal conductivity were added to the energy conservation equation. The spatio-temporal evolution of plasma is studied by studying the electron temperature evolution, the SW evolution is understood using the mass density and pressure variables.

The dynamics of plasma and SW, the orders of mass density, pressure and temperature were verified with literature. Standardization of the code with the experiments conducted in laboratory is described in the chapter 3 and then moved forward towards the confinement of laser plasma geometrically in different ways described in further chapters.

#### 2.4 References:

- 1. Radziemski, L.J. and D.A. Cremers, *Laser-induced plasmas and applications*. 1989, United States: Marcel Dekker Inc.
- 2. Raizer, Y.B.Z.d.a.Y.P., *Physics of Shock Waves and HighTemperature Hydrodynamic Phenomena*. 2012: (Dover Publications.
- 3. DeMichelis, C., Laser induced gas breakdown: A bibliographical review. IEEE Journal of Quantum Electronics, 1969. **5**(4): p. 188-202.
- 4. Singh, R.K. and J. Narayan, *Pulsed-laser evaporation technique for deposition of thin films: Physics and theoretical model.* Physical Review B, 1990. **41**(13): p. 8843-8859.
- 5. Mościcki, T., J. Hoffman, and Z. Szymanski, *Modelling of plasma formation during nanosecond laser ablation*. Archives of Mechanics, 2011. **63**: p. 99-116.
- 6. Porneala, C. and D.A. Willis, *Time-resolved dynamics of nanosecond laser-induced phase explosion*. Journal of Physics D: Applied Physics, 2009. **42**(15): p. 155503.
- 7. Wood, R.F., et al., *Dynamics of plume propagation, splitting, and nanoparticle formation during pulsed-laser ablation.* Applied Surface Science, 1998. **127-129**: p. 151-158.
- 8. Shiva, S.S., et al., Radiation effects of the laser ablative shockwaves on aluminium under atmospheric conditions. Journal of Physics: Conference Series, 2017. **823**: p. 012013.
- 9. Wynne, A.E. and B.C. Stuart, Rate dependence of short-pulse laser ablation of metals in air and vacuum. Applied Physics A, 2003. **76**(3): p. 373-378.
- 10. Gomes, A., et al., Experimental and theoretical study of the expansion of a metallic vapour plasma produced by laser. Journal of Physics D: Applied Physics, 2004. **37**(5): p. 689-696.
- 11. Bogaerts, A. and Z. Chen, Effect of laser parameters on laser ablation and laser-induced plasma formation: A numerical modeling investigation. Spectrochimica Acta Part B: Atomic Spectroscopy, 2005. **60**(9): p. 1280-1307.
- 12. Harilal, S.S., et al., Experimental and computational study of complex shockwave dynamics in laser ablation plumes in argon atmosphere. Physics of Plasmas, 2012. **19**(8): p. 083504.
- 13. Tao, Y., et al., Effect of shockwave-induced density jump on laser plasma interactions in low-pressure ambient air. Journal of Physics D: Applied Physics, 2006. **39**: p. 4027.
- 14. Radziemski, L.J., From LASER to LIBS, the path of technology development. Spectrochimica Acta Part B: Atomic Spectroscopy, 2002. 57(7): p. 1109-1113.

- 15. Miziolek, A.W., V. Palleschi, and I. Schechter, *Laser Induced Breakdown Spectroscopy*. 2006: Cambridge University Press.
- 16. Toro, E., Riemann Solvers and Numerical Methods for Fluid Dynamics: A Practical Introduction. 2009.
- 17. Bakos, J.S., et al., Laser blow-off plasma propagating in low-pressure gas. Applied Physics Letters, 1987. **51**(10): p. 734-736.
- 18. Skeen, C.H. and C.M. York, *LASER-INDUCED* `BLOW-OFF" PHENOMENA. Applied Physics Letters, 1968. **12**(11): p. 369-371.
- 19. Fabbro, R., et al., *Physical study of laser-produced plasma in confined geometry*. Journal of Applied Physics, 1990. **68**(2): p. 775-784.
- 20. Chen, Z. and A. Bogaerts, Laser ablation of Cu and plume expansion into 1atm ambient gas. Journal of Applied Physics, 2005. **97**(6): p. 063305.
- 21. Wen, S.-B., et al., Expansion of the laser ablation vapor plume into a background gas. I. Analysis. Journal of Applied Physics, 2007. **101**(2): p. 023114.
- 22. Anderson, J.D., Computational Fluid Dynamics. 1995: McGraw-Hill Education.
- 23. Fryxell, B., et al., FLASH: An Adaptive Mesh Hydrodynamics Code for Modeling Astrophysical Thermonuclear Flashes. The Astrophysical Journal Supplement Series, 2000. **131**(1): p. 273-334.
- 24. Anderson, R.W., R.B. Pember, and N.S. Elliott, A dynamically adaptive arbitrary Lagrangian-Eulerian method for hydrodynamics, in Computational Fluid and Solid Mechanics 2003, K.J. Bathe, Editor. 2003, Elsevier Science Ltd: Oxford. p. 1232-1236.
- 25. Godunov, S.K., A difference scheme for numerical solution of discontinuous solution of hydrodynamic equations. Math. Sbornik, 1959. 47: p. 271-306.
- 26. Bittencourt, J.A., Fundamentals of Plasma Physics. 2013: Springer New York.
- 27. Hank Childs et al., VisIt: An End-User Tool For Visualizing and nalyzing Very Large Data. 2012: p. 357-372.
- 28. Chaudhary, K., Z. Haider, and J. Ali, Laser-Induced Plasma and its Applications. 2016.
- 29. Sai Shiva, S., Numerical Investigations of ns Laser Induced Shock Waves from Aluminum and Air. 2016, University of Hyderabad: Hyderabad. p. 188 (Ph. D Thesis)
- 30. Sobral, H., et al., *Temporal evolution of the shock wave and hot core air in laser induced plasma*. Applied Physics Letters, 2000. **77**(20): p. 3158-3160.
- 31. Villagran-Muniz, M., H. Sobral, and E. Camps, *Shadowgraphy and interferometry using a CW laser and a CCD of a laser-induced plasma in atmospheric air.* IEEE Transactions on Plasma Science, 2001. **29**(4): p. 613-616.
- 32. Harilal, S., B. Brumfield, and M. Phillips, *Lifecycle of laser-produced air sparks*. Physics of Plasmas, 2015. **22**: p. 063301.
- 33. Harilal, S.S., et al., *Internal structure and expansion dynamics of laser ablation plumes into ambient gases.* Journal of Applied Physics, 2003. **93**(5): p. 2380-2388.

# Chapter-3

# An Insight Into Laser Induced Air Plasma

An introduction to simulation of laser-induced breakdown in air from the initial laser pulse interaction up to 20 µs was presented in this chapter. The process of laser energy deposition, plasma formation and expansion, launching shock wave into the background gas were discussed in detail in this chapter. The role of the governing hydrodynamic equations on the expansion dynamics of plasma and shock wave were understood. The laser-matter interaction model considered is: the inverse bremsstrahlung absorption coefficient for laser energy deposition as this is the dominant process that occur for nanosecond laser pulse - matter interactions. Ideal gas equation-of-state (EOS) is used to close the conservation equations. The role of input laser parameters such as pulse energy, pulse duration and spot-size, on the evolution of the plasma and shock wave (SW) were presented. The considered input laser intensities were in the range of  $0.25 - 2.5 \times 10^{10}$ W/cm<sup>2</sup>. The simulated shock velocities were validated and found to be in line with the experimentally obtained values. The effect of the input energy on the asymmetric shock wave expansion is discussed in terms of the shock velocities along laser propagation axis. The presence of multiple hotspots inside the plasma during the initial time scales and formation of vortex rings by the plasma due to plasma rolling at latter were discussed. The temporal evolution of plasma parameters such as number density, and temperature, with respect to aforementioned varied laser parameters were presented. The peak temperatures at the initial time scales were observed to be in the range of  $10^4 - 10^5$  K and the number density in the 10<sup>16</sup>- 10<sup>19</sup> /cm<sup>3</sup>. The results showed that the intensity of the laser beam is highly influencing the plasma parameters.

### 3.1 Introduction

An intense laser beam focused into a gaseous medium, interacts with the medium, resulting in the breakdown of the medium leading to an intense spark generation [1-6]. This phenomenon is known as laser—induced breakdown (LIB) of a gas, where the breakdown is observed because of the cascade or avalanche ionization [2, 7, 8]. This high-pressure region develops a shock wave into the ambient medium that has sufficient strength to ignite a gaseous mixture [9] or to extinguish a diffusion flame [10]. Since the first reports of the laser induced breakdown (LIB) in air by Maker et al [11], Meyerand and Haught et al [12], there has been an enormous growth of interest in the subject of LIB in gaseous medium. Laser-induced gaseous plasmas has a wide range of applications including detecting airborne biological agents [13], elemental analysis [14, 15], quantitative analysis of aerosols [16], ultrafast shutters [17], production of X-rays and soft X-rays [18, 19], ignition of gas mixtures [9, 20], localized flow control across the blunt bodies [21, 22] and many. Gas breakdown studies laid the initial step in research in inertial confinement fusion (ICF) and plasma heating by laser radiation [23].

To understand the process of laser-induced breakdown it requires an understanding of the initial stages of various processes involved during laser-matter interaction, that is plasma formation, and its subsequent expansion. The mechanism behind the laser induced breakdown (LIB) of air can be defined as four stage process: (1) generation of free electrons in the focal volume (for incident photon flux) followed by cascaded ionization of the gas leading to generation of secondary electrons, (2) formative growth, and plasma development followed by (3) shock wave generation and supersonic propagation in the surrounding gas and 4) fourth and final stage, is the expansion/decay of the plasma leading to formation of the blast wave and its propagation into the ambient medium, attaining sound speed[1, 24, 25]. The main absorption mechanism that leads to breakdown of the air medium and plasma formation during the nanosecond pulse laser –matter interaction is the inverse bremsstrahlung observed due to the electron-ion collisions [12, 26].

The plasma thus created attains a very high temperature (~10<sup>5</sup> K), pressure, energy, number density, whose magnitude depends on various parameters such as laser energy [4, 6, 27, 28], wavelength [29-31], pulse duration [32] of the incident laser beam, background pressure [29, 33-38] and background gas species [31, 37]. Due to the high temperature (>1 eV) the molecules in the air are dissociated to atoms and ions while excited molecular species are assumed to be formed during plasma cooling [8, 39, 40].

A detailed study of the expansion dynamics of such laser generated air plasma and shock wave for different energies (50-500 mJ) and pulse duration ( $\tau$  = 10 ns and 7ns) were performed using FLASH 2D radiation hydrodynamic code [41]. The equations describing the evolution dynamics were explained in chapter-2. Ideal gas equation of state is used to close these system of equations [2]. The ionization model used to determine the charge state by default given in FLASH describing the N-body. This ionization model used in FLASH is replaced with Atzeni model of ionization to estimate the charge state of an atom [4, 6, 42]. The simulation details and the evolution dynamics of plasma, shock wave and the plasma parameters were discussed in the following sections.

#### 3.1.1 Simulation details

A laser beam with a pulse duration (FWHM) of 10 ns, with the input laser energy varied between 50 - 500 mJ, and with excitation wavelength of 532 nm is focused into the ambient air at 1.0 atm of ambient pressure. The spot size is considered to be 250 µm. Fig. 3.1 shows the simulation domain illustrating the dimensions of the computational domain along (Z, R) direction, focal region where the laser beam is being focused, and the direction of the focused laser beam.

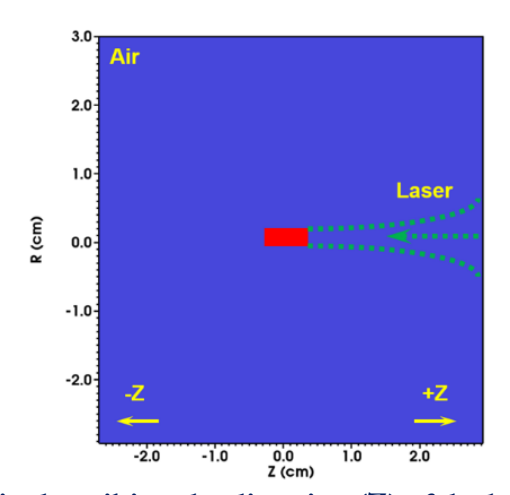


Fig. 3. 1 Simulation domain describing the direction (Z) of the laser beam, red color region describing the focal region where the laser beam is focused

The meshing of the simulation domain is built using PARAMESH, which uses an adaptive mesh refinement (AMR) method[41]. The AMR meshing which considers fine refinement at regions where the steep density gradients exist in the computational domain i.e., initially the mesh refinement is more near the target surface ( $30 \times 60 \,\mu\text{m}$ ) along the laser propagation axis, that extends to the regions where plasma and SW expansion is taking place. In the regions far away from target surface, the mesh has the dimensions of  $60 \times 120 \,\mu\text{m}$ .

### 3.2 Inverse Bremsstrahlung absorption

The inverse bremsstrahlung (IB) absorption mechanism can be described as a three body mechanism. The intense photon flux when incident in the focal region, interacts with the free electrons in the focal region. The free electron loses its kinetic energy when passes through the ion vicinity, which then immediately acquires the photon energy from the incident laser energy. With the continuous collision of the free electrons with the neutral atoms and ions leads to an avalanche of free electrons inducing the breakdown of the medium and formation of plasma [2, 43]. During these collisions a raise in temperature in the focal region is observed because of the conversion of the kinetic energy into thermal energy [6, 8, 44]. The plasma generated during the leading edge of the laser pulse expands in the direction opposite to laser propagation direction owing to momentum conservation [4, 6, 45]. The trailing part of the laser pulse then interacts with the generated plasma thus, resulting in asymmetric expansion of the plasma along the Z-axis. The asymmetry in the plasma expansion increases with increasing input laser energy. According to Raizer et al., [8, 46] the asymmetric deposition of the laser energy occurs due to one of the following mechanisms: shifting of the absorption front (AF), radiation driven shock wave (RDSW), and laser supported detonation wave [47, 48] (LSDW). Due to the lower laser intensities used for generating the plasma, the simulations performed in this thesis assumes the radiation effects to be negligible [4, 6, 49]. Hence, the asymmetric expansion observed is due to the shifting of the the absorption front location. In this mechanism, the movement of the AF starts at the onset of the breakdown at the focal point. The laser power deposited in a cell is calculated based on the inverse bremsstrahlung power in the cell that depends on the local electron number density gradient and local electron temperature gradient. The inverse bremsstrahlung frequency factor is given by the formula ( $\vartheta_{ib}(t)$ ) as shown in equation 3.1

$$\vartheta_{ib}(t) = \frac{4}{3} \left(\frac{2\pi}{m_e}\right)^{\frac{1}{2}} \frac{Ze^4}{n_c k_B^{3/2}} \frac{n_e[r(t)]^2 \ln(\Lambda[r(t)])}{T_e[r(t)]^{3/2}} \quad \text{sec}^{-1}$$
(3.1)

where 
$$\ln \Lambda = \ln \left[ \frac{3}{2Ze^3} \left( \frac{k_B^3 T_e^3}{\pi n_e} \right)^{\frac{1}{2}} \right]$$
 is the Coulomb logarithm [8, 50] (3.2)

Here, Z is the average ionization, e is the charge of electron,  $n_e$  is the electron number density,  $n_e$  is the critical density defined by the following relation (equation 3.3).

$$n_c = \frac{m_e \pi c^2}{\lambda^2 e^2} \tag{3.3}$$

 $T_e$  is the electron temperature,  $\lambda$  is the wavelength of the incident radiation,  $\varepsilon$  speed of light,  $m_e$  is the mass of electron,  $k_B$  is the Boltzmann constant. Hence, from the above expressions it can be understood that the percentage absorption of the incident radiation at the focal region depends on the wavelength of the incident radiation, average ionization of the medium, electron number density and electron temperature, respectively. All the parameters were taken in CGS unit system. The average ionization of the medium and electron number density were inter related to each other by the equation (3.4).

$$n_e = \frac{Z\rho}{Am_p} \tag{3.4}$$

 $\varrho$  is the mass density, A is the atomic mass number and  $m_p$  is the mass of proton (1.67 × 10<sup>-27</sup> g). Hence, it can be considered that electron number density and electron temperature were the two factors influencing the absorption percentage. Hence, in this chapter, the factors effecting the electron number density and electron temperature of the plasma and SW dynamics were discussed in detail. Before we present the details of this, we first understand the evolution dynamics of the plasma and SW generated by 50 mJ laser source and validate the results with the experimental results [51].

## 3.3 Axi-symmetric evolution of plasma and shock waves

The present section deals with a detailed explanation of expansion dynamics of laser induced air plasmas for the input laser energy of 50 mJ. The simulations presented were performed with axi-symmetry i.e., considering the laser propagation axis (Z) of symmetry in the cylindrical geometry. The deposition of the laser energy in the focal volume is performed by the ray tracing algorithm [41]. Initially the threshold energy i.e., 5 mJ, (the breakdown threshold of air taken from experiments [45]) required for the breakdown of the air is deposited in the focal volume by raising the temperature of the focal volume by 0.5 eV. This helps in creating the seed electrons inside the focal volume that results in the deposition of laser energy [4, 52]. The plasma and shock wave thus generated due to the absorption of the incident laser energy have a very high temperature and density gradients with respect to the ambient conditions. Hence, a fine meshing of the domain is required where the steep gradients exist. The fine meshing of the domain causes slowing down of the simulations which influences the total simulation output time of the problem. However, this is reduced by considering the half-plane of the computational domain where the laser propagation axis (Z) is taken as axis-symmetric plane. The simulations were performed for +R direction and replicated for the –R directions [41].

Hence, the plasma and shock dynamics along the –R and +R directions were the same. However, one cannot consider the R axis as the axis of symmetry in the present scenario as the assumption changes the physical nature of the plasma which is asymmetric in nature along the laser propagation axis. The spatial evolution of the electron temperature generated using 50 mJ laser source at different timescales is shown in fig. 3.2 (a) - (e). Fig. 3.2 (a) - (d) shows the pseudo image of electron temperature from 25 - 500 ns.

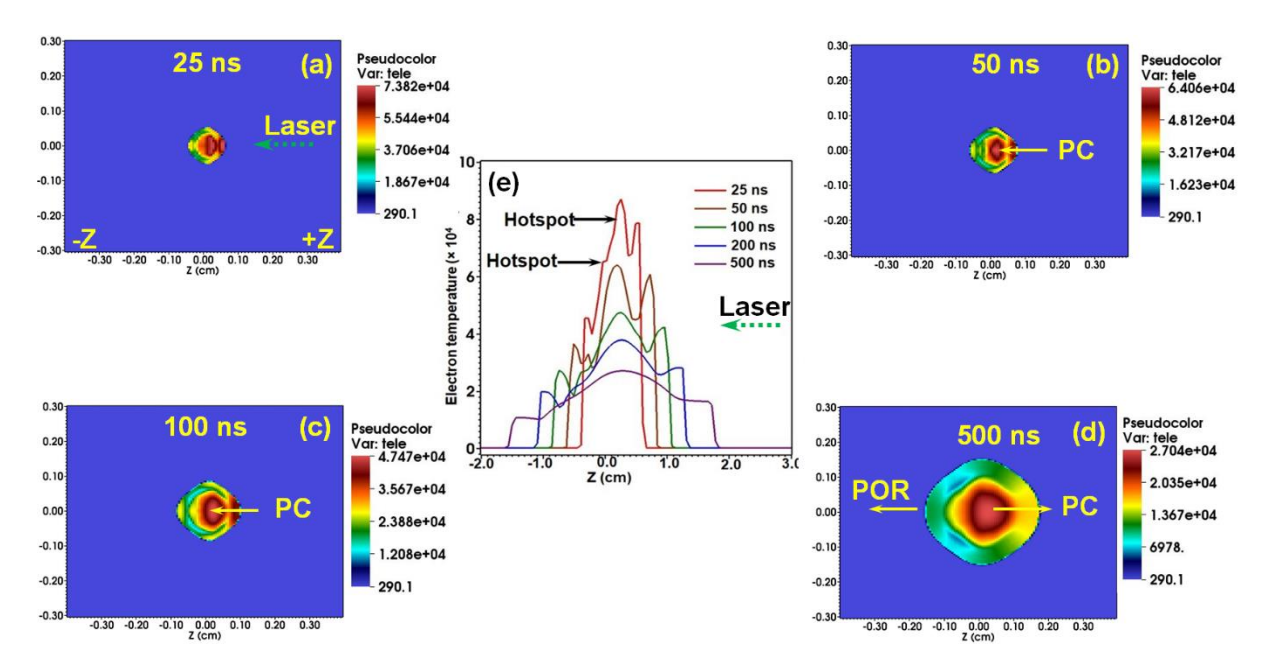


Fig. 3. 2 Spatial evolution of electron temperature at (a) 25 ns, (b) 50 ns, (c) 100 ns, (d) 500 ns and (e) a line profile of electron temperature at 25, 50, 100 and 500 ns along the laser propagation axis generated using 50 mJ laser source.

It is observed that the generated air plasma is expanding asymmetrically more along the direction opposite to laser propagation direction. The formation of plasma in ambient atmospheric air takes place enduring the interaction with the leading edge of the laser pulse. The plasma thus formed appears as a tear—drop shape with very high temperature and pressure with respect to the surrounding air. It can be observed that the high temperature plasma core (PC) is surrounded by the low temperature region called as the plasma outer region (POR). T spatial evolution of temperature can be understood by taking the line profile of the temperature along the laser propagation axis (Fig. 3.2(e)).

Fig. 3.2(e) shows the spatio-temporal evolution of the electron temperature at the initial timescales i.e., from 25 - 500 ns. During the initial timescales and after the termination of the laser pulse i.e., at 25 ns the plasma temperatures were found to be very high as can be seen in Fig. 3.2(a). As a result, continuous collision between the electrons and the ions takes place. It

is to be noted that the temperature is high at the plasma core region. Hence, the mass density in the PC region is very low. The temperature decreases as moved away from the PC towards the POR and hence the mass density increases and attains a maximum value at the interface between the POR and ambient gas (discussed in Fig. 3.3). This is observed because of the pressure gradient between the POR and the ambient gas [52].

The line profile of the electron temperature shows that the maximum temperature is attained at 25 ns which is observed to be  $\sim 8.8 \times 10^4 \, \mathrm{K}$  ( $\sim 8 \, \mathrm{eV}$ ). On either side of the peak temperature, it is also observed that the existence of two distinct peaks as observed whose temperature is found to be  $6 \sim 7 \, \mathrm{eV}$ . This clearly shows the existence of hotspots in the plasma region which are formed due to the asymmetric deposition of input laser energy at the focal plane. In Fig. 3.2 (a) - (c) & 3.2 (e), multiple hotspots were observed to be appearing till less than 500 ns and disappear at later time scales of >500 ns (3.2 (d)). The two peaks appearing on either sides of the plasma core (seen in Fig. 3.2 (e)) have less temperature compared to that of the core region. They represent the plasma outer region (POR) where the SF builds up.

The specific internal energy of the plasma is converted into the kinetic energy which is utilized in the expansion of the plasma. Hence a decrease in the temperature at the focal region is observed at the later time scales as shown in Fig. 3.2 (b) – (d). The peak temperature at the plasma core over the given time scales of 25 – 500 ns (Fig. 3.2(a)-(d)) is observed to be in the range 8.8-2.8 eV, while the maximum temperature at the plasma outer region (POR) is in the range 7-2 eV. The plasma thus formed has different energy spots in the internal regions. The mass that is removed from the focal region accumulates at the front end of the plasma forming a shock front (SF). Fig. 3.3 (a) - (d) shows the two-dimensional (R, Z) evolution of mass density at 0.5, 1, 2 and 5 μs respectively. While Fig. 3.3 (e) shows the line profile of mass density taken along the laser propagation axis at 0.5, 1, 1.5, 2, 2.5 and 3 μs respectively.

A shock wave (SW) is a thin region with high pressure and density advancing in the forward direction. The SF builds up and expands along with the plasma until few hundreds of nanoseconds, attains sufficient energy and detaches from the plasma and expands into the surrounding medium adiabatically with velocity much higher than the local sound speed. However, after few microseconds of the detachment it attains a spherical shape. The SW advances into the surrounding medium because of the pressure gradient existing between the SF and the surrounding medium

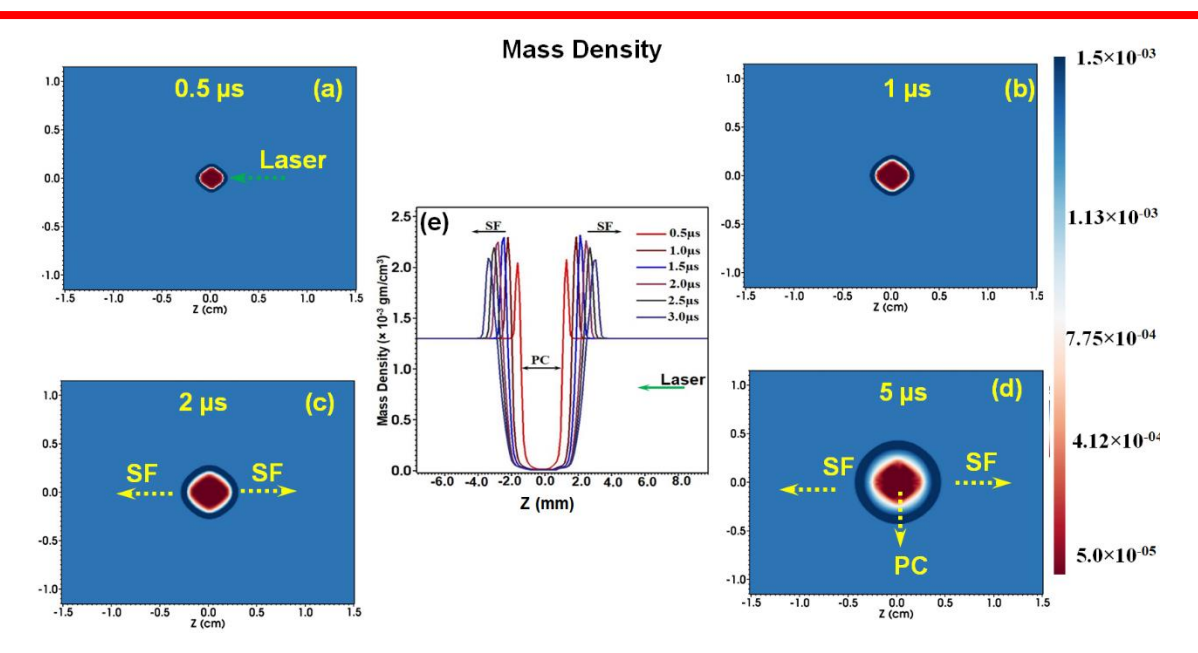


Fig. 3. 3 (a) Spatial variation of mass density at (a) 0.5, (b) 1, (c) 2 and (d) 5 µs respectively and (e) line profile of mass density along the laser propagation axis for the input laser energy of 50 mJ.

From momentum conservation equation (Eq. 2.11 explained in chapter-2) it can be understood that when the pressure gradient between the SF and surrounding medium is more, then the velocity gradient is more i.e., velocity of the SF is more [53, 54]. While the SW is advancing in the forward direction it loses its kinetic energy by exchanging energy to the surrounding medium. Thus, the pressure at the SF decreases resulting in a decrease of shock velocity. Hence, after few microseconds (> 5 µs) the SW is attaining a spherical nature and finally transforming to an acoustic SW (shock velocity approaching the local sound speed) [32] at longer times (few hundreds of microseconds) depending on the input laser energy.

Fig. 3.3 (a) shows the two dimensional evolution of mass density at  $0.5~\mu s$ . The red colored region appearing at the centre is the plasma core. While the thin boundary around the PC is the SF. It is to be observed that the SF has not detached but travelling with the plasma core. During the initial time scales (< 1  $\mu s$ ), the expansion is asymmetric in nature. The expansion of the plasma and the SW is more along +Z direction when compared to that along -Z directions. The expansion is dominant along the laser propagation axis when compared to that along the radial direction. The SF is observed to be travelling with the PC till 2  $\mu s$  as can be seen in Fig. 3.3 (b) & (c). However, the freely expanding SW after detaching from the PC can be seen in Fig. 3.3 (d). Fig. 3.3 (e) shows visualization of the variation of the mass density along the laser propagation axis.

The peaks appearing (Fig. 3.3 (e)) along the –Z and +Z directions are the SFs expanding into the ambient air that are generated due to the removal of mass at the focal region. The dip at Z=0 represents the plasma core from where the mass is removed, which is accumulated at the SFs. It is observed that during the initial timescales ( $< 1 \,\mu s$ ) the shock strength and its expansion along +Z direction is more when compared to that along the -Z direction. This is because of the shifting of the absorption front (AF) towards the laser beam during the trailing edge of the laser pulse. The AF comprises of both electron and ion clouds generated at the focal region during the leading edge of the laser pulse [6]. The maximum mass density attained at the SF is  $\sim 2.3 \times 10^{-3} \,\mathrm{g/cm^3}$  at 1.5 µs along –Z direction which is  $\sim 1.7$  times higher than the ambient air density ( $1.3 \times 10^{-3}$  g/cm<sup>3</sup>). However, after few hundreds of nanoseconds the density at both the SFs is almost the same. The asymmetric expansion of the plasma and shock wave is not much prominent because of the low intensity (2.5 GW/cm<sup>2</sup>) of the incident laser beam. The density at the SF is observed to be increasing till 2 µs and thereafter decreases. It is also to be noted that as long as the density at the SF is increasing, the mass density at the PC is decreasing. Also, the increase in mass density represents that both the SF and plasma are in contact with each other and travelling with the same velocity. So, when the SW has attained sufficient energy it has detached from the plasma. Hence, a decrease in mass density is observed at the SF after 2 μs. Fig. 3.4 (a) - (b) shows the two dimensional view of evolved mass density and electron temperature at 20 µs, respectively.

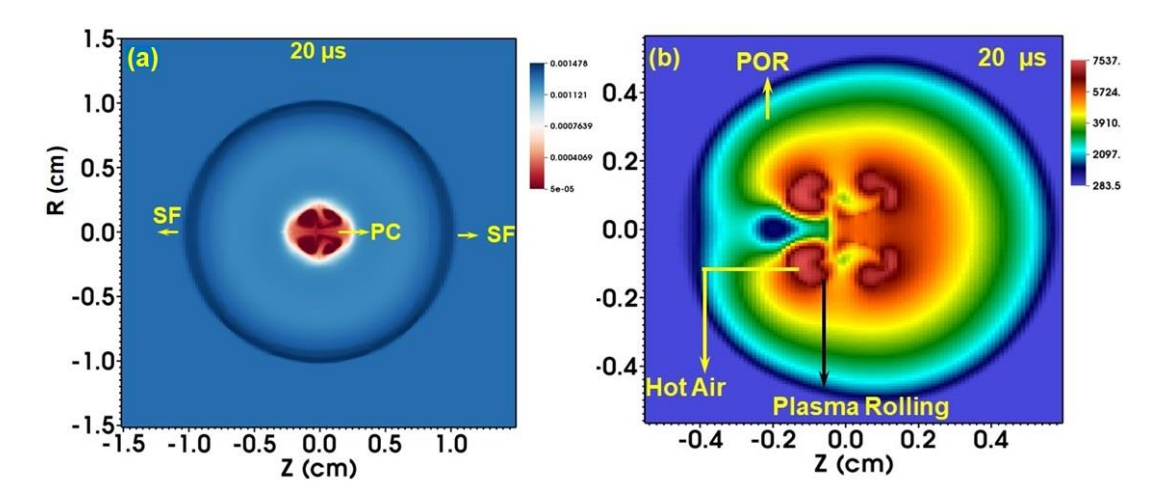


Fig. 3. 4 (a) Spatio-temporal evolution of mass density and (b) two dimensional view of electron temperature at 20 us for the input laser energy of 50 mJ

The mass density and electron temperature at 20 µs were clearly depicting the PC, and expanding SW in all the directions. The asymmetry in the plasma core is sustaining even at 20 µs. The SW is observed to attain a spherical structure travelling with almost same velocity in all

the directions. A rolling of the plasma core is observed due to the hydrodynamic instabilities called as Rayleigh-Taylor instabilities [4] occurring within the plasma region.

Fig. 3.4(b) shows a two dimensional view of electron temperature at 20 µs. The red color region appearing at the centre is the plasma core. As observed from the temperature line profiles, the magnitude of the temperature is decreasing as approaching towards the outer region of the plasma. It is also observed that there exists localized regions within the plasma with different temperatures confirming the existence of temperature gradients [55].

The plasma rolling is observed at initial time scales (1 µs) and a toroidal vortex ring is observed by 20 µs [56, 57]. It is observed from Fig. 3.4 (a) & (b) that the temperature is maximum and density is minimum at the regions where the plasma rolling occurs.

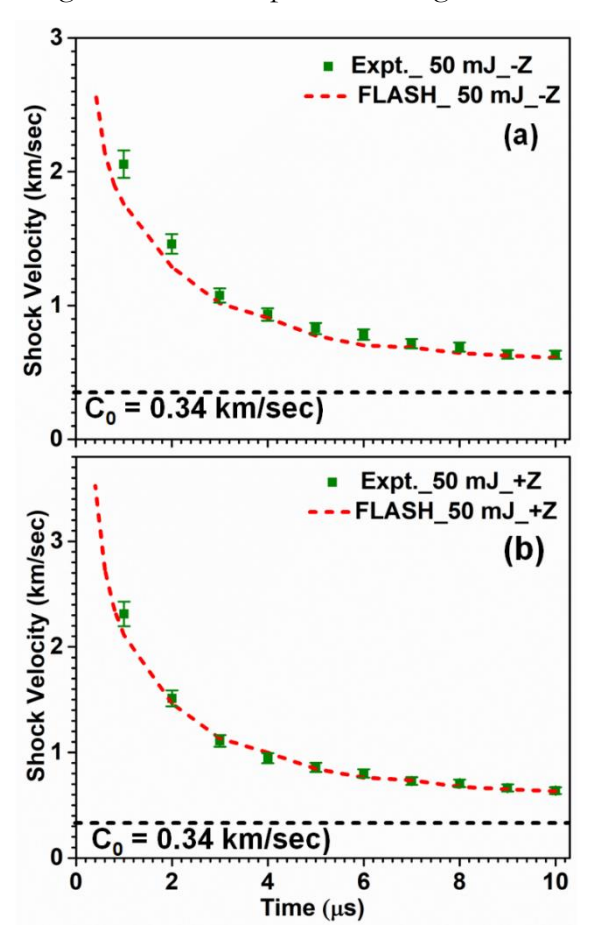


Fig. 3. 5 A comparison of the simulated shock velocities with the experimental velocities [51] along (a) -Z and (b) +Z directions for the input laser energy of 50 mJ

As discussed previously, temperature is maximum at the core and less at the outer region, where as the mass density is following the inverse relation. Hence, the gradient of temperature is acting in the outward direction, while the gradient of mass density is acting in the inward direction. As a result the plasma fluid experiences Rayleigh-Taylor (RT) instabilities at these points [4, 58, 59]. The instabilities occurring between the two layers with high and low densities (more density

gradient) are called as the RT instabilities [60]. As time progresses, the RT instability occurs at multiple points leading to rolling of plasma at multiple points. The temporal variation of the shock velocities along –Z and +Z directions were presented in Fig. 3.5 (a & b) to understand the temporal evolution of SW and plasma over a duration of 10 µs.

The shock velocities along –Z and +Z directions presented in Fig. 3.5 (a) clearly explains the asymmetry in shock expansion during the initial time scales. This is observed because the SF is travelling with the plasma during the initial time scales. At 0.2 μs the shock velocity along the +Z direction (direction opposite to laser propagation direction) is observed to be 3.5 km/sec while that along the –Z is 2.5 km/sec. A slight variation in the shock velocities along –Z & +Z directions is observed till 2 μs. After 2 μs, the variation in the shock velocities were almost equal in both the directions. This is observed because of the detachment of the SF from the plasma. After few 100's of μs the shock velocities along both the directions approaches the local sound velocity (340 m/sec). Hence, the SW can be called as the acoustic SW [27]. The simulated shock velocities were verified and found to be in line with the experimental shock velocities [51]. Fig. 3.6 shows the temporal evolution of the electron temperature and electron number density along the laser propagation axis over a duration of 20 μs.

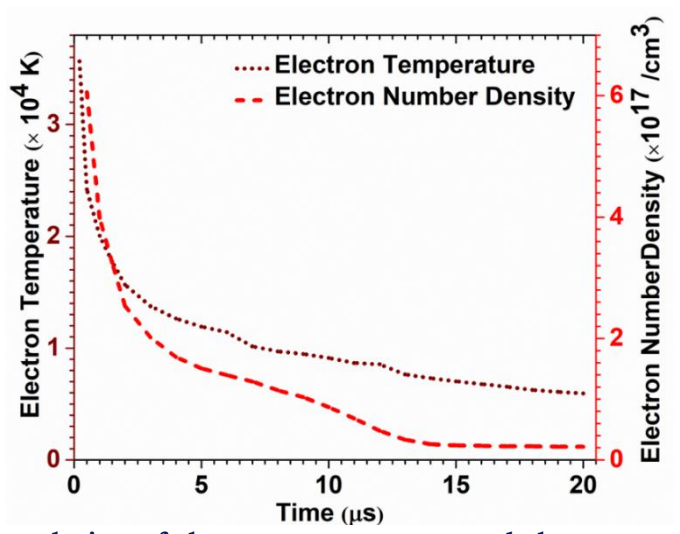


Fig. 3. 6 Temporal evolution of electron temperature and electron number density over a duration of  $20~\mu s$  for the input laser energy of 50~mJ

Fig. 3.6 shows the temporal evolution of the electron temperature and the electron number density of the plasma over a duration of 20 µs. The temperature and number density were very high at the plasma core during the initial time scales. The amount of energy generated at the plasma core is further utilized in the expansion of the plasma. Hence, a decrease in the plasma parameters is observed over a duration of time. The obtained values of the electron

temperature and number density were in line with the range that were reported in the literature [39, 61]. The rate of decay is observed to be more during the initial time scales due to the sudden expansion of the plasma and recombination of large number of electrons with ions while, the rate of decay decreases at the later time scales. The intensity of the input laser pulse plays a crucial role on the expansion dynamics and the plasma parameters and their decay rate. Intensity in turn depends on the energy of the input laser pulse, pulse duration and the spot size of the laser beam at the focal point. Hence, the effect of the energy and pulse duration on plasma parameters is discussed in the following sections.

## 3.4 Effect of input laser intensity

# 3.4.1 Effect of energy

At a fixed wavelength of 532 nm, pulse duration of 10 ns and spot size of  $500 \pm 100 \,\mu\text{m}$ , and input laser energy varied between  $50 - 500 \,\text{mJ}$  (Intensity in the range  $0.25 - 2.5 \times 10^{10} \,\text{GW/cm}^2$ ) the spatio - temporal evolution of the SW and plasma parameters were studied in the present section. The absorption percentage is observed to be increasing with the increase in energy [62].

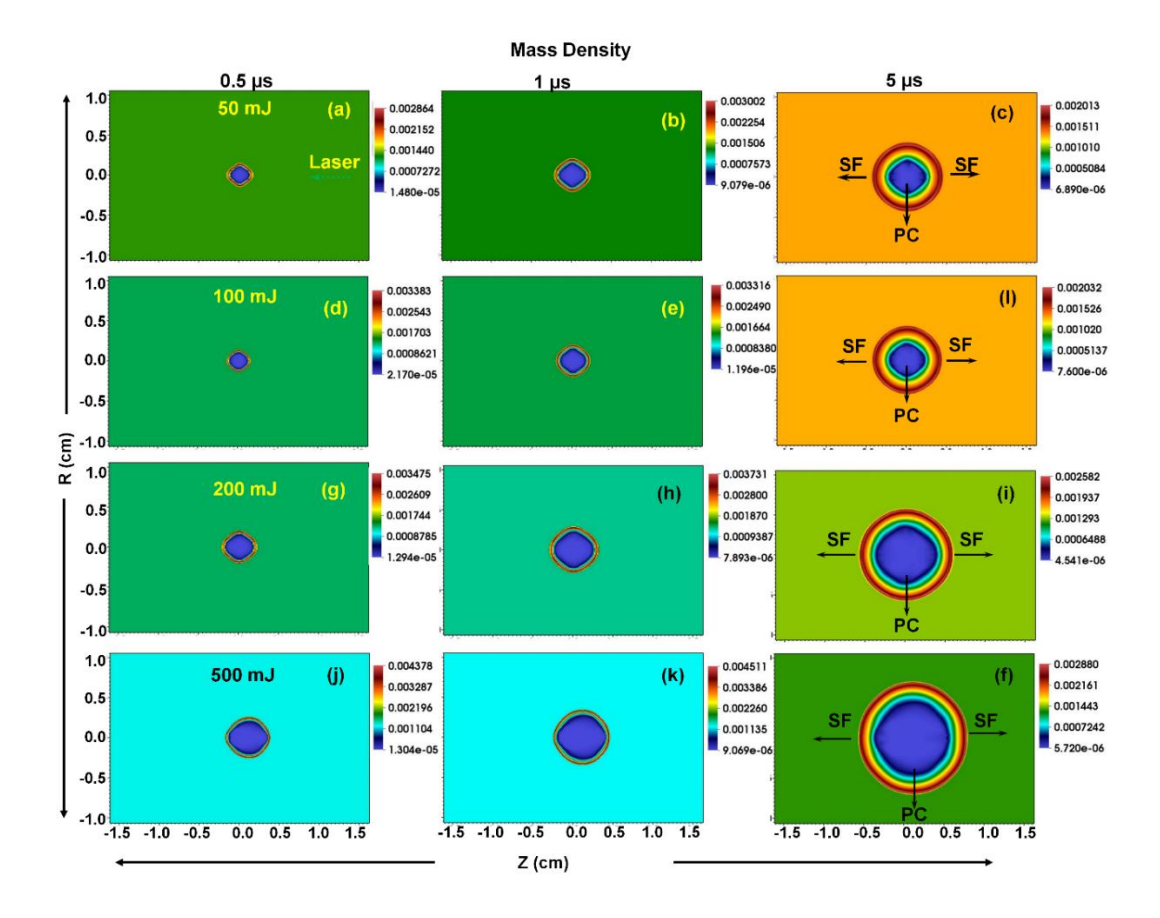


Fig. 3. 7 Spatial evolution of mass density at 0.5, 1 and 5  $\mu$ s for the input laser energy of (a) – (c) 50 mJ, (d) – (f) 100 mJ, (g) - (i) 200 mJ and (j) - (l) 500 mJ respectively

The percentage of absorbed laser energy for input laser energy of 50 mJ was observed to be in the range of 25-30 % while that for 500 mJ is in the range of the 40-45 %. The considered absorption percentages were in line with the values reported in literature [45, 51, 52, 63]. A clear variation in the expansion of the mass density with respect to the energy can be observed in Fig. 3.7 (a-l). Fig. 3.7 (a-c) were showing the mass density variation for the input laser energy of 50 mJ. Initially at 0.5 μs, the plasma and SW appear as a tear drop shape. As the time is progressing i.e., at 5μs the SW becomes spherical and expands freely in all the directions. The asymmetry in the plasma and SW expansion is observed to be increasing with the increasing energy. Asymmetric expansion is more dominantly observed for 500 mJ (Fig. 3.7 (j-l)) especially at 1 μs. The expansion of the SW over the considered duration is also observed to be increasing with the energy. The detachment of the SW from the PC and its free expansion can be observed more clearly at 5 μs. The variation of the shock velocity with respect to the laser energy (50,100, 200 and 500 mJ respectively) along –Z and +Z (opposite to laser propagation direction) directions and the obtained shock velocities with the experimental values were presented in Fig. 3.8 (a - h) over a duration of 0.2 – 10 μs.

Fig. 3.8 (a) & (b) shows the comparison of the evolution of shock velocities along +Z directions for the input laser energy of 50 mJ. The maximum shock velocity is observed at 0.2  $\mu$ s over the considered duration of time. The maximum shock velocity along -Z direction is 2.6 km/sec and that along the +Z direction is 3.6 km/sec i.e, the shock velocity is more along the direction opposite to the laser propagation direction. The shock velocity has reached  $\sim$ 1 km/sec at 2.5  $\mu$ s along both -Z and +Z directions. As the shock velocity is approximately the same along -Z and +Z directions it has attained the spherical nature by 2.5  $\mu$ s after which

Fig. 3.8 (c) & (d) shows the temporal variation of the shock velocity along -Z and +Z directions for the input laser energy of 100 mJ. The maximum shock velocity along the -Z and +Z directions were 3.1 and 4.5 km/sec respectively at 0.2  $\mu$ s. The shock velocities were reaching < 1 km/sec after 4.5  $\mu$ s. For the input energy of 200 mJ (Fig. 3. 8 (e) & (f)), the shock velocity is reaching below 1 km/sec after 4.5  $\mu$ s and that in case of 500 mJ (Fig. 3. 8 (g) & (h)) the shock velocities have reached below 1 km/sec after 6  $\mu$ s. Hence, it can be observed that after 6  $\mu$ s, the shock velocities with respect to all input energies were almost attaining the same velocity (0.6 km/sec).

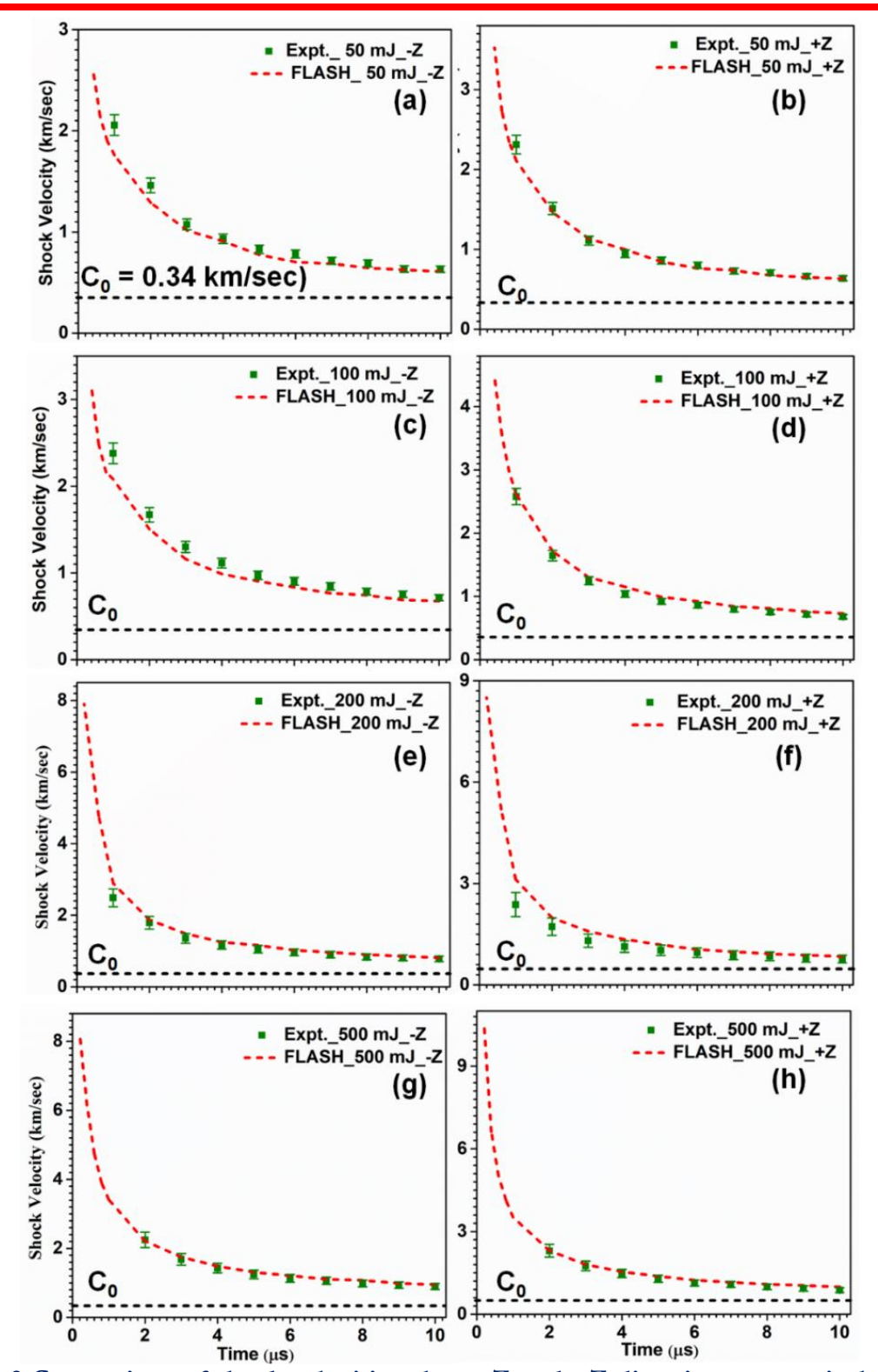


Fig. 3. 8 Comparison of shock velocities along -Z and +Z directions respectively for the input laser energy of (a-b) 50, (c-d) 100, (e-f) 200 and (g-h) 500 mJ respectively

Table 3.1 summarizes the maximum shock velocities along –Z and +Z directions respectively. From table 3.1 it can be understood that the shock velocity is increasing with the increase in the laser energy. For the considered energies, the shock velocity along +Z direction is more when compared to that along - Z direction confirming the asymmetry in SW expansion.

Table 3. 1 A summary of the maximum shock velocity in the -Z and +Z directions at .2 us with respect to the input laser energy

Energy(mJ)	Shock Velocity (km/sec)	Shock Velocity (km/sec)	
	(-Z Direction)	(+Z Direction)	
50	2.6	3.6	
100	3.1	4.5	
200	7.8	8.8	
500	8.2	10.3	

It is a known fact that the absorption at the focal region starts only when the breakdown threshold of the medium in the focal region is reached. For higher incident laser power, the absorption starts earlier, and the process lasts for a longer time. The fraction of absorbed energy increases leading to a significant growth in the electron density and temperatures at the focal region [63, 64]. As a result the fractional internal energy that is being converted into the kinetic energy also increases. This results in the increment of the shock/plasma velocities during the initial time scales. This can be confirmed from the energy conservation (Eqn. (2.12) shown in chapter-2). Where the total specific energy Etot is given by the sum of the total internal specific energy and the specific kinetic energy.

i.e., 
$$E_{\text{tot}} = E_{\text{ele}} + E_{\text{ion}} + \frac{1}{2} v. v$$
 (3.5)

Hence, an increase in the shock velocity with the increase in the energy is observed at the initial time scales. However, when the SF attains sufficient energy and detaches from the plasma and starts expanding supersonically into the background gas, the shock velocity decreases and almost all the energies attain the same velocity at time scales > 6 µs. Similar is the case with the shock velocities along –Z direction (along the laser propagation direction). The maximum shock velocity for the input energy of 500 mJ is observed to be 10.6 km/s along +Z direction and 8 km/s along -Z direction. Similarly, the maximum shock velocity for the input energy of 50 mJ which is observed to be 3.5 km/s along +Z direction and 2.4 km/s along -Z direction (shown in fig. 3.6(b) and table 3.1). Thus the difference in the shock velocities between 50 and 500 mJ along +Z direction is 6.7 km/s and 5.6 km/sec along –Z directions. Hence, it can be confirmed that with the increase in the input energy, the asymmetry in the plasma expansion is being reflected in the shock velocities along –Z & +Z directions as can be observed in Fig. 3.8 (a - h). The effect of the input laser energy on plasma parameters is shown in Fig. 3.9 (a) & (b).

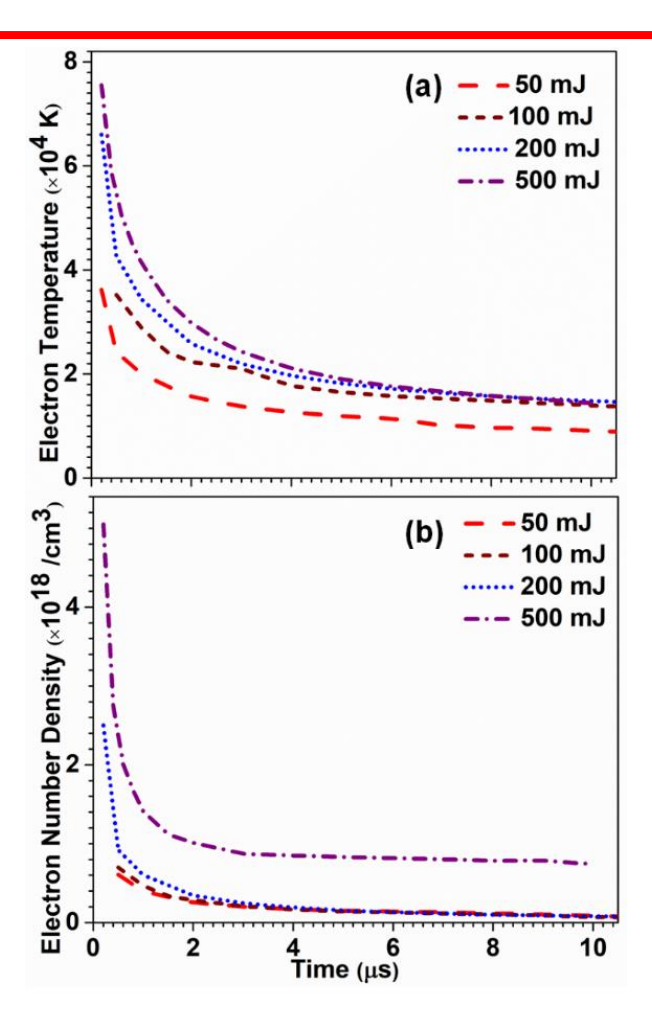


Fig. 3. 9 Comparison of (a) electron temperature and (b) electron number density of the plasma along the laser propagation axis with respect to the input laser energy 50, 100, 200 and 500 mJ.

Fig. 3.9 (a) shows the temporal evolution of the electron temperature over a duration of  $10 \, \mu s$  with respect to the input laser energy. As discussed above with the increase in the power/energy the energy that is being absorbed in the focal region is increasing. This has resulted in the increase of the thermal energy at the core region. However, after  $5 \, \mu s$ , the temperature profile of all the energies is approaching a similar trend. Similarly the number densities were high for  $500 \, \text{mJ}$  during the initial time scales but decaying to the range of the lower energies quickly after  $5 \, \mu s$  (Fig. 3.9 (b)). It is discussed in the previous section that the decay in the plasma parameters in the early timescales is due to the sudden expansion of the plasma and recombination of the large number of electrons and ions. Since, the expansion rate of the plasma with higher energy is more during the initial time scales the decay rate of the plasma parameters is high during the initial time scales. The decay rate slows down when the plasma expansion reaches the maximum plasma length.

### 3.4.2 Effect of pulse duration & beam waist

The effect of pulse duration ( $\tau$ ) and beam waist on laser generated plasma parameters were discussed in the present section. The two experimental conditions used to generate plasma were: i) laser beam with pulse duration 10 ns, beam diameter  $500 \pm 100 \,\mu m$  at the focal region, generated using input energies of 50 and 100 mJ (Intensity 0.25 & 0.5 ×  $10^{10} \, \text{W/cm}^2$ ), excitation wavelength of 532 nm, and ii) with pulse duration 7 ns, beam diameter of  $140 \pm 10 \,\mu m$  using energies of 50 and 100 mJ (Intensity 5 &  $10 \times 10^{10} \, \text{W/cm}^2$ ) with the excitation wavelength of 532 nm. A comparison of the two dimensional evolution of the electron temperature with respect to the intensity were shown in Fig. 3.10 (a – f).

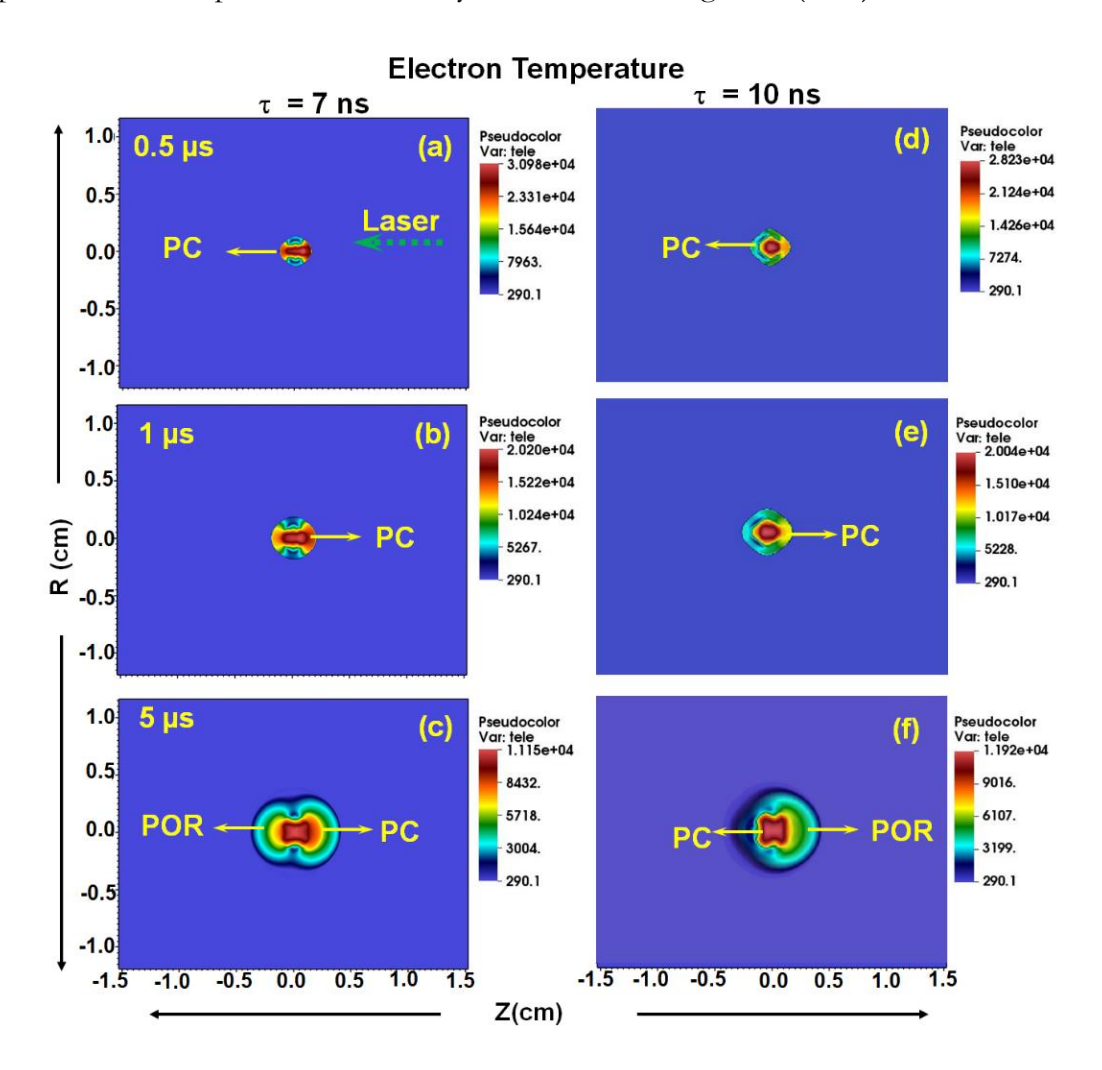


Fig. 3. 10 Comparison of the spatial evolution of electron temperature with respect to the incident pulse duration (a -c) with  $\tau$ = 7ns and (d -f) with  $\tau$ = 10 ns at 0.5, 1 and 5 µs respectively for the input laser energy of 50 mJ

Fig. 3.10 (a) & (d) shows the comparison of the electron temperature at 0.5 µs for the two input laser pulse durations of 7 and 10 ns respectively. The temperature distribution is more directional along laser propagation axis and asymmetry in the deposition is more dominant for

 $\tau = 7$  ns when compared to that of  $\tau = 10$  ns. The peak temperature at the PC is  $3.09 \times 10^4$  K for  $\tau = 7$  ns and  $2.82 \times 10^4$  K for  $\tau = 10$  ns. Hence, increase in the intensity ( $\tau = 7$  ns) is leading to an increase in the temperature at the PC.

Existence of the two hotspots in the PC is more dominant at 1  $\mu$ s for  $\tau$  = 7 ns than that for  $\tau$  = 10 ns (Fig. 3.10 (b) & (e)). The asymmetric distribution of the temperature along laser propagation axis and initiation of the rolling of the plasma is visible in both Fig. 3.10 (c) & (f). The temperature at the PC is more when compared to that at the plasma outer region (POR). The temporal evolution of the plasma parameters were shown in Fig. 3.11 (a - d) over a duration of 20  $\mu$ s.

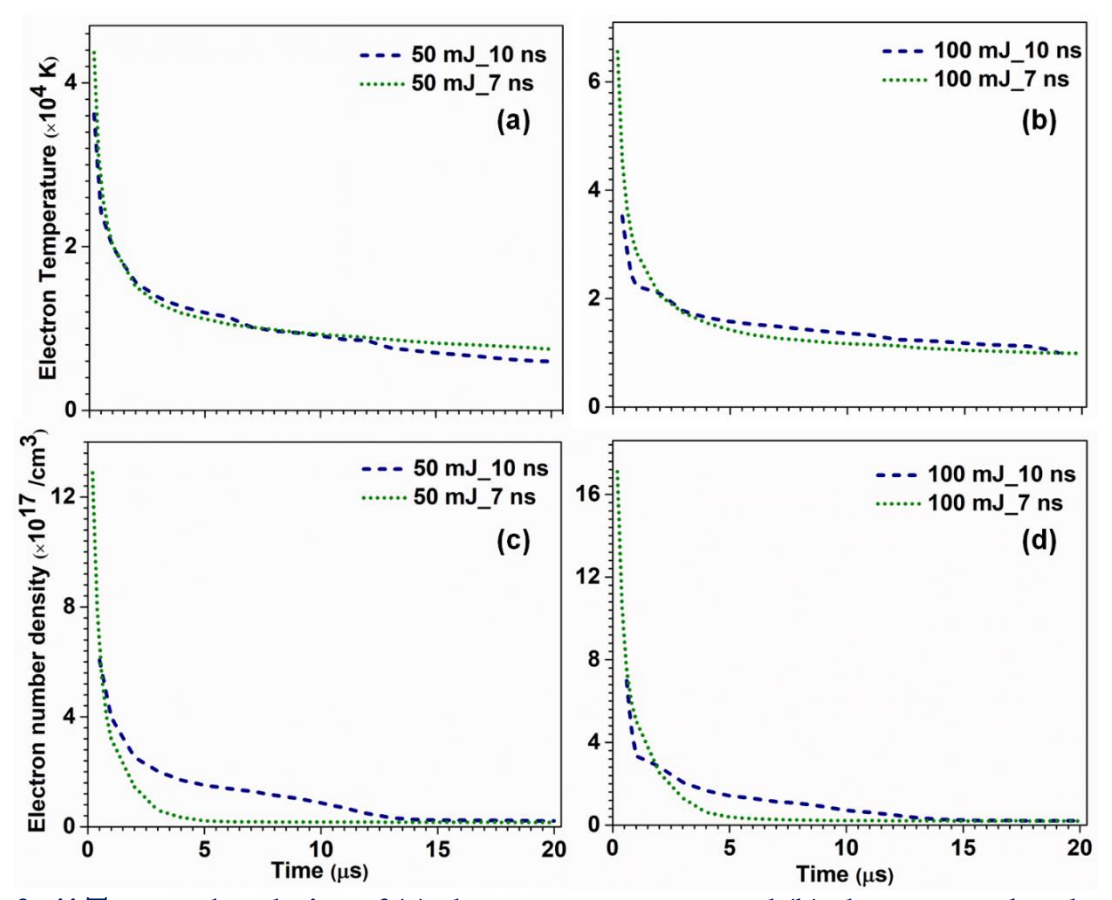


Fig. 3. 11 Temporal evolution of (a) electron temperature and (b) electron number density with respect to pulse duration  $\tau = 10$ , 7 ns and energy 50 and 100 mJ respectively of the laser beam along the laser propagation axis

Fig. 3.11(a) & (c) shows the comparison of the temporal variation of the electron temperature and number density for the input laser energy of 50 mJ. Initially at 0.2  $\mu$ s, the temperature of the PC generated using 7 ns laser pulse is  $4.4 \times 10^4$  K and that using 10 ns laser pulse is  $3.6 \times 10^4$  K. It can be observed from Fig. 3.11 (a) that the maximum variation in the temperature between the two sources is existing at the initial time scales (< 1  $\mu$ s). Later, the temperature is

almost the same in both the sources. However, the number density ( $N_e$ ) at the initial time scales ( $< 2 \,\mu s$ ) is high for 7 ns source while after 2  $\mu s$  the  $N_e$  for 10 ns plasma is high up to 12  $\mu s$ . This can be once again interpreted as the higher decay rate existing because of the fast expansion of the plasma generated using high intensity laser source.

The peak temperature obtained for 100 mJ energy generated using 7 ns laser beam is observed to be  $6.6 \times 10^4$  K at 0.2 µs. While the temperature attained with 10 ns is  $3.8 \times 10^4$  K. Similarly the number density attained is observed to be of the order of  $10^{18}$  /cm<sup>3</sup> even at 0.2 µs for both 7 and 10 ns pulses. However, after 2 µs the electron temperature and the number density of the higher intensity source is less than that obtained for lower intensity source. The decay in density with time is taking place due to increased recombination rate of the electrons with ions between electrons and ions because of reduced temperatures [31, 52].

#### 3.5 Conclusion

The generation and expansion dynamics of laser induced air plasma and shock waves under different input laser energies were discussed in detail. The simulations were performed at atmospheric air pressure (0.1 MPa). The asymmetry in the plasma expansion is observed to be less for lower intensities and is becoming more prominent for higher energies. The spatiotemporal evolution of the shock and plasma parameters such as the shock velocities along the laser propagation axis, electron temperature and number densities at the plasma were studied for varied intensities (energy and pulse duration). The number density and temperatures were found to be high during the initial time scales. The increase in the intensity is observed to be effecting the plasma and shock parameters during the initial time scales up to 5 µs. Beyond these times, all the parameters irrespective of the laser energy were observed to be following the same trend and attaining almost the same values. After 5 µs, the shock velocities for all the input laser energies were decreasing rapidly. Mass density and temperature were observed to be following the inverse relation with respect to each other at the plasma and the SF. The hydrodynamic instabilities in the plasma were observed to result in rolling of the plasma at multiple points.

#### 3.6 References

- 1. Morgan, C.G., Laser-induced breakdown of gases. Reports on Progress in Physics, 1975. **38**(5): p. 621-665.
- 2. DeMichelis, C., Laser induced gas breakdown: A bibliographical review. IEEE Journal of Quantum Electronics, 1969. **5**(4): p. 188-202.

- 3. Ghosh, S. and K. Mahesh, Numerical simulation of the fluid dynamic effects of laser energy deposition in air. Journal of Fluid Mechanics, 2008. **605**: p. 329-354.
- 4. Sai Shiva, S., et al., Numerical investigation of nanosecond laser induced plasma and shock wave dynamics from air using 2D hydrodynamic code. Physics of Plasmas, 2017. **24**(8): p. 083110.
- 5. Harilal, S.S., B.E. Brumfield, and M.C. Phillips, *Lifecycle of laser-produced air sparks*. Physics of Plasmas, 2015. **22**(6): p. 063301.
- 6. Sai Shiva, S., et al., Role of laser absorption and equation-of-state models on ns laser induced ablative plasma and shockwave dynamics in ambient air: Numerical and experimental investigations. Physics of Plasmas, 2019. **26**(7): p. 072108.
- 7. Browne, P.F., *Mechanism of gas breakdown by lasers*. Proceedings of the Physical Society, 1965. **86**(6): p. 1323-1332.
- 8. Raizer, Y.B.Z.d.a.Y.P., *Physics of Shock Waves and HighTemperature Hydrodynamic Phenomena*. 2012: (Dover Publications.
- 9. Phuoc, T.X. and F.P. White, *Laser-induced spark ignition of CH4/air mixtures*. Combustion and Flame, 1999. **119**(3): p. 203-216.
- 10. Schmieder, R.W., Laser spark ignition and extinction of a methane-air diffusion flame. Journal of Applied Physics, 1981. **52**(4): p. 3000-3003.
- 11. Maker, P.D., R.W. Terhune, and C.M. Savage. Optical Third Harmonic Generation. 1964.
- 12. Meyerand, R.G. and A.F. Haught, *Gas Breakdown at Optical Frequencies*. Physical Review Letters, 1963. **11**(9): p. 401-403.
- 13. Hybl, J.D., G.A. Lithgow, and S.G. Buckley, Laser-Induced Breakdown Spectroscopy Detection and Classification of Biological Aerosols. Applied Spectroscopy, 2003. 57(10): p. 1207-1215.
- 14. Nordstrom, R.J., Study of Laser-Induced Plasma Emission Spectra of N2, O2, and Ambient Air in the Region 350 nm to 950 nm. Applied Spectroscopy, 1995. **49**(10): p. 1490-1499.
- 15. L. Dudragne, P.A., J. Amouroux, *Time-Resolved Laser-Induced Breakdown Spectroscopy:Application for Qualitative and Quantitative Detection of Fluorine, Chlorine, sulfur, and Carbon in Air.* Applied Spectroscopy, 1998. **52**(10).
- 16. Hahn, D.W. and M.M. Lunden, *Detection and Analysis of Aerosol Particles by Laser-Induced Breakdown Spectroscopy*. Aerosol Science and Technology, 2000. **33**(1-2): p. 30-48.
- 17. Dhareshwar, L.J., P.A. Naik, and D.D. Bhawalkar, *A plasma shutter to generate a synchronized subnanosecond pulse for optical probing of laser-produced plasmas*. Review of Scientific Instruments, 1991. **62**(2): p. 369-375.
- 18. Fiedorowicz, H., et al., *Demonstration of a neonlike argon soft-x-ray laser with a picosecond-laser-irradiated gas puff target.* Optics Letters, 2001. **26**(18): p. 1403-1405.
- 19. Doron, R., et al., Spectroscopic signature of strong dielectronic recombination in highly ionized xenon produced by irradiating a gas puff with laser. Physical Review A, 1999. **59**(1): p. 188-194.
- 20. Phuoc, T.X., Laser spark ignition: experimental determination of laser-induced breakdown thresholds of combustion gases. Optics Communications, 2000. 175(4): p. 419-423.
- 21. Bletzinger, P., et al., *Plasmas in high speed aerodynamics*. Journal of Physics D: Applied Physics, 2005. **38**(4): p. R33-R57.
- 22. Phuoc, T.X., Laser-induced spark ignition fundamental and applications. Optics and Lasers in Engineering, 2006. 44: p. 351.
- 23. Dittrich, T.R., et al., Review of indirect-drive ignition design options for the National Ignition Facility. Physics of Plasmas, 1999. **6**(5): p. 2164-2170.
- 24. Yan, H., et al., Laser Energy Deposition in Quiescent Air. AIAA Journal, 2003. 41(10): p. 1988-1995.
- 25. Kandala, R. and G.V. Candler, *Numerical Studies of Laser-Induced Energy Deposition for Supersonic Flow Control.* AIAA Journal, 2004. **42**(11): p. 2266-2275.
- 26. Ireland, C.L.M. and C.G. Morgan, *Gas breakdown by a short laser pulse*. Journal of Physics D: Applied Physics, 1973. **6**(6): p. 720-729.

- 27. Manikanta, E., et al., Effect of laser intensity on temporal and spectral features of laser generated acoustic shock waves: ns versus ps laser pulses. Applied Optics, 2017. **56**(24): p. 6902-6910.
- 28. Mullett, J.D., et al., The influence of beam energy, mode and focal length on the control of laser ignition in an internal combustion engine. Journal of Physics D: Applied Physics, 2007. **40**(15): p. 4730-4739.
- 29. Tambay, R., et al., *Laser induced air breakdown using 0.355, 0.532, and 1.06 μm radiation.* Pramana, 1991. **37**(2): p. 163-166.
- 30. Simeonsson, J.B. and A.W. Miziolek, Spectroscopic studies of laser-produced plasmas formed in CO and CO2 using 193, 266, 355, 532 and 1064 nm laser radiation. Applied Physics B, 1994. **59**(1): p. 1-9
- 31. Harilal, S.S., et al., On- and off-axis spectral emission features from laser-produced gas breakdown plasmas. Physics of Plasmas, 2017. **24**(6): p. 063304.
- 32. Manikanta, E., et al., Effect of pulse duration on the acoustic frequency emissions during the laser-induced breakdown of atmospheric air. Applied Optics, 2016. **55**(3): p. 548-555.
- 33. Zhang, H., et al., *Spatiotemporal evolution of laser-induced plasmas in air: Influence of pressure.* Spectrochimica Acta Part B: Atomic Spectroscopy, 2021. **177**: p. 106103.
- 34. Glumac, N. and G. Elliott, *The effect of ambient pressure on laser-induced plasmas in air.* Optics and Lasers in Engineering, 2007. **45**(1): p. 27-35.
- 35. Wang, B., K. Komurasaki, and Y. Arakawa, *Influence of ambient air pressure on the energy conversion of laser-breakdown induced blast waves.* Journal of Physics D: Applied Physics, 2013. **46**(37): p. 375201.
- 36. Mori, K., K. Komurasaki, and Y. Arakawa, Energy transfer from a laser pulse to a blast wave in reduced-pressure air atmospheres. Journal of Applied Physics, 2004. **95**(11): p. 5979-5983.
- 37. Gatti, M., et al., *Spherical shock waves in laser produced plasmas in gas.* Optics Communications, 1988. **69**(2): p. 141-146.
- 38. Thiyagarajan, M. and J. Scharer, Experimental investigation of ultraviolet laser induced plasma density and temperature evolution in air. Journal of Applied Physics, 2008. **104**(1): p. 013303.
- 39. Villagran-Muniz, M., H. Sobral, and E. Camps, Shadowgraphy and interferometry using a CW laser and a CCD of a laser-induced plasma in atmospheric air. IEEE Transactions on Plasma Science, 2001. **29**(4): p. 613-616.
- 40. Camacho, J.J., et al., *Time-resolved optical emission spectroscopy of laser-produced air plasma*. Journal of Applied Physics, 2010. **107**(8): p. 083306.
- 41. Fryxell, B., et al., FLASH: An Adaptive Mesh Hydrodynamics Code for Modeling Astrophysical Thermonuclear Flashes. The Astrophysical Journal Supplement Series, 2000. **131**(1): p. 273-334.
- 42. Atzeni, S. and J. Meyer-ter-Vehn, *The Physics of Inertial Fusion: Beam Plasma Interaction, Hydrodynamics, Hot Dense Matter.* 2004: OUP Oxford.
- 43. Radziemski, L.J. and D.A. Cremers, *Laser-induced plasmas and applications*. 1989, United States: Marcel Dekker Inc.
- 44. Kameswari, D.P.S.L., et al., Investigation of stagnation layer dynamics of counterpropagating laser induced air plasmas: Numerical simulations vis-à-vis experimental observations. Physics of Plasmas, 2021. **28**(4): p. 043104.
- 45. Leela, C., et al., *Dynamics of laser induced micro-shock waves and hot core plasma in quiescent air.* Laser and Particle Beams, 2013. **31**(2): p. 263-272.
- 46. Y. P. Raizer, V.I.K., and J. E. Allen, *Gas Discharge Physics*. 1 ed. 2011: (Springer, Berlin, Heidelberg.
- 47. Wang, B., et al., *Energy conversion in a glass-laser-induced blast wave in air.* Journal of Applied Physics, 2010. **108**(12): p. 124911.
- 48. Daiber, J.W. and H.M. Thompson, *Laser-Driven Detonation Waves in Gases*. The Physics of Fluids, 1967. **10**(6): p. 1162-1169.
- 49. Raizer, I.P. Laser-induced discharge phenomena. 1977.
- 50. Mulser, P., G. Alber, and M. Murakami, Revision of the Coulomb logarithm in the ideal plasma. Physics of Plasmas, 2014. **21**(4): p. 042103.

#### An Insight Into Laser Induced Air Plasma

- 51. Guthikonda, N., et al., *Interaction of two counterpropagating laser induced plasmas and shock waves in air.* Physics of Plasmas, 2020. **27**(2): p. 023107.
- 52. Sai Shiva, S., Numerical Investigations of ns Laser Induced Shock Waves from Aluminum and Air. 2016, University of Hyderabad: Hyderabad. p. 188.(Ph. D Thesis)
- 53. Toro, E.F., Riemann Solvers and Numerical Methods for Fluid Dynamics: A Practical Introduction. 2009: Springer Berlin Heidelberg.
- 54. Anderson, J.D., Computational Fluid Dynamics. 1995: McGraw-Hill Education.
- 55. Malyutin, A.A., V.A. Podvyaznikov, and V.K. Chevokin, *Density jumps in the plasma of a nanosecond laser-induced spark and their dynamics*. Quantum Electronics, 2011. **41**: p. 38.
- 56. Meyerand, R.G. and A.F. Haught, *Optical-Energy Absorption and High-Density Plasma Production*. Physical Review Letters, 1964. **13**(1): p. 7-9.
- 57. Ghosh, S. and K. Mahesh, Direct Numerical Simulation of the Thermal Effects in Plasma/Turbulence Interaction, in 45th AIAA Aerospace Sciences Meeting and Exhibit. 2007, American Institute of Aeronautics and Astronautics.
- 58. Drake, R.P., L. Davison, and Y. Horie, *High-Energy-Density Physics: Fundamentals, Inertial Fusion, and Experimental Astrophysics, with 172 figures.* High Energy Density Physics, 2006.
- 59. Dors, I.G. and C.G. Parigger, *Computational fluid-dynamic model of laser-induced breakdown in air.* Applied Optics, 2003. **42**(30): p. 5978-5985.
- 60. Kull, H.J., Theory of the Rayleigh-Taylor instability. Physics Reports, 1991. 206(5): p. 197-325.
- 61. Sobral, H., et al., *Temporal evolution of the shock wave and hot core air in laser induced plasma*. Applied Physics Letters, 2000. **77**(20): p. 3158-3160.
- 62. Guthikonda, N., *Dynamics of Confined Laser Induced/Ablative Plasmas and Shock Waves*, in *Physics*. 2020, University of Hyderabad: Hyderabad. p. 211 (Ph. D Thesis)
- 63. Chen, Y.-L., J. Lewis, and C. Parigger, *Spatial and temporal profiles of pulsed laser-induced air plasma emissions*. Journal of Quantitative Spectroscopy & Radiative Transfer, 2000. **67**: p. 91-103.
- 64. Bindhu, C.V., et al., Energy Absorption and Propagation in Laser-Created Sparks. Applied Spectroscopy, 2004. **58**(6): p. 719-726.

### Chapter-4

### Interaction of Two Counter Propagating Laser Induced Air Plasmas

In this chapter, the interaction of two counter propagating laser induced air plasma is studied to understand the axial confinement effects on the evolution dynamics of laser induced air plasma. The two counter propagating plasma sources were generated along the laser axis (Z) with one energy source (S<sub>1</sub>) fixed to 50 mJ while the other source (S<sub>2</sub>) energy is varied as 50 and 100 mJ respectively. The interaction studies were performed for separation distances of d = 0 - 4 mm between the two plasmas. The study is performed over a duration of 30 µs from the generation of plasma. When the two expanding plasmas encounter each other, the interaction zone dynamics and the effect of the plasma/ shock wave of confining source ( $S_2 = 50/100$  mJ) on the other source ( $S_1 = 50$  mJ) show interesting results. During the interaction of the two plasmas, the plasma parameters such as, the number density, temperature, and the shock parameters such as, the mass density pressure were observed to be increasing at the interaction zone. The variation of these parameters at the interaction zone and at the plasma core (PC) of S<sub>1</sub> were studied in detail with respect to the energy of the confining source S<sub>2</sub> and the separation distance (d) between the seed plasmas. It is observed that for the separation distance d < 4 mm and when the energy of source  $S_2$  is double that of  $S_1$  ( $S_1$ :  $S_2 = 1:2$ ), the plasma of  $S_2$  is penetrating through the PC of  $S_1$  and compressing the PC of  $S_1$ . However, for d = 4 mm, the interaction between the two sources is limited to the outer regions only. The interaction between the sources is leading to formation of a plasma jet-let due to the compression of the PC by the shock front generated from S2. While, when two sources were generated with equal laser energy hard stagnation region is formed at the interaction zone for the separation distance d > 0 mm and d < 4 mm that last up to the time scales of 20 µs after which an interpenetration of the two seed plasmas is observed. The interpenetration or stagnation of the two sources at the interaction zone is confirmed by determining the collisionality parameter for all the separation distances. In the case of  $S_1$ :  $S_2 = 1:2$ , the maximum pressure of 25 MPa and a maximum temperature of  $3.6 \times 10^4$  K is observed at the interaction zone for a separation distance of 1 mm. While a maximum pressure of 19 MPa and maximum

temperature of  $3.11 \times 10^4$  K is observed at the interaction zone in the case of  $S_1$ :  $S_2 = 1:1$ . The electron temperature and number densities at the PC of low energy source  $S_1$  in the case of  $S_1$ :  $S_2 = 1:2$  were found to be increasing with decrease in the separation distance due to the compression the PC.

#### 4.1 Introduction

The complex behaviour of expansion dynamics and underlying physics of a freely expanding laser induced air plasma studied were presented in chapter-3. The pressures existing at the shock front were of the order of few tens of MPa (during initial times of < 100 ns), and mass densities were 3-4 times higher than the ambient air density  $(1.3 \times 10^{-3} \,\mathrm{g/cm^3})$  [1-7]. Spatial confinement of such laser generated air plasmas find a wide range of applications depending on the method chosen for confinement. Confinement effect on the plasma and shock parameters depend on the acoustic impedance, (Z =  $\varrho u$ , (where  $\varrho$  is the density and u is the velocity of the medium) of the medium with which the plasma is being confined. In the present chapter, the laser generated air plasma is confined using another laser generated air plasma (with nearly equal or slightly higher impedance) i.e., interaction of two counter streaming laser induced air plasmas and the effect of confinement on plasma and shock parameters is studied in detail. The expanding plasma source when approaches the second source (confining medium), a thick layer of high density and pressure is formed at the interaction zone called as the stagnation layer because of the compression of the medium between the two expanding plasma sources [8]. The stability of the stagnation layer depends on the acoustic impedance of the confining plasma. The interaction o-f two plasmas can lead to two different phenomena: collision dominated and collision-less interaction. Collision dominated plasma interaction leads to either formation of a stagnation layer or to an interpenetration of the two plasma sources, whereas in the case of collision-less interaction the two plasma sources tend to decelerate at the interaction zone. The interpenetration or stagnation of plasma or shock front (SF) at the interaction zone is determined by the collisionality parameter [8-13]. The collisionality parameter ( $\zeta$ ) is defined as the ratio of the separation (d) between the seed plasmas to the ion– ion mean free path ( $\lambda_{i-i}$ ) at the colliding region.

i.e., 
$$\zeta = d/\lambda_{i-i}$$
 (4.1)

If  $\zeta$  <1, then an interpenetration of the two plasmas will take place, where the interaction is a collision dominated. However, if  $\zeta$  >1, then the two plasmas will decelerate and stagnate at the interaction zone. The ion-ion mean free path is given by the relation [12]

$$\lambda_{i-i} = \frac{m_i^2 v_{1,2}^4}{4\pi e^4 z_i^4 N_i ln \Lambda_{1,2}}, \text{ (in cgs units)}$$
 (4.2)

where,  $v_{1,2}$  is the relative velocity between the seed plasmas,  $m_i$  is the ion mass,  $z_i$  is the average ionization state of the plasma,  $N_i$  is the average ion density at the collision plane,  $ln\Lambda$  is the Coulomb logarithm which is given by the expression [14, 15],

$$ln\Lambda = ln \left[ \frac{3}{2z_i e^3} \left( \frac{k_B T_e^3}{\pi n_e} \right)^{1/2} \right]$$
 (4.3)

where,  $k_B$  is the Boltzmann constant,  $T_e$  is the electron temperature at the interaction zone. The ion-ion mean free path (mfp) depends on the relative velocity between the seed plasmas, the ion density, ionization number and Coulomb logarithm. The interaction between the approaching plasmas depends on the ion-ion mfp of the colliding fronts. Hence, it can be understood that if the seed plasmas have a large relative velocity and density gradient at the collision plane, the plasma plumes will tend to interpenetrate. On the other hand, when the relative velocities between the plasmas are small, plasma constituents will tend to rapidly decelerate at the collision plane, forming a hard stagnation layer.

The stagnation layer dynamics under different interaction/confinement geometries of interacting plasmas such as angular [11] lateral [9, 16-18] orthogonal [19, 20] counter propagating [8, 11, 21-23] interactions have been studied under vacuum conditions and a few studies in the presence of ambient air [16, 24, 25] have been performed. However, in almost all the studies, the interaction and stagnation layer dynamics were performed by generating the ablated (front surface of the target) or blow-off (rear surface of the target) plasmas from solid targets. Despite of low intensities and low shock pressures generated during the laser induced breakdown in air, interacting laser induced air plasmas have a variety of applications in ignition of fuel mixtures [26] such as increasing the plasma temperature, longevity, and the resulting spectral emissions [10, 27-30]. In addition, the interacting plasmas are being used to understand the design of inertial confinement fusion (Hohlraums), x-ray laser research [31], high ionic temperature and charged particle acceleration using Thomson scattering in conjunction with proton radiography [32] understanding Supernovae (SNe), and Supernovae remnants (SNR) [33, 34] to model and understand various astrophysical processes via noble gases [35]. An experimental study on the evolution of plasma and shock wave (SW) dynamics, in the counter propagating geometry with varying separation between the seed plasmas, was studied by Guthikonda et al.[24]. However, a deep insight into plasma dynamics during the interaction of counter propagating laser created air plasmas in terms of the plasma parameters such as temperature and density is required. The present work focuses on interaction of two counter propagating ns laser generated air plasmas and the associated shockwaves up to tens of microseconds to get a complete insight into (a) the physical mechanism taking place at the interaction zone via 2D hydrodynamic simulations using two temperatures (Te, Ti) and to explicitly understand the role of electron and ions in the interaction process up to tens of microseconds, (b) role of ion-ion collisions at the interaction zone, (c) shock-shock and shock-plasma interaction leading to jet-let initiation and its evolution, and (d) validation of the numerical simulations with the experimental results observed via shadowgraphic imaging. The interaction dynamics and the evolution of the counter propagating collinear 10 ns laser pulse induced air plasmas (of equal and unequal energies) under similar experimental conditions as reported by Guthikonda et al. [24] are simulated. The simulations were performed using 2D FLASH radiation hydrodynamic (FLASH 2D RHD) code [14] for the interaction of the two plasma sources separated by an optimal distance of 4 mm over a duration of 30 µs. The FLASH code was modified to match the experimental conditions, by considering appropriate equation of state and ionization models as described in chapter-2. An insight into the physical mechanism taking place during the interaction of the SFs and the factors affecting the interpenetration or the stagnation were discussed. The evolution of plasma parameters such as the number density, temperature at the interaction zone and at the seed plasmas, compression of the low energy seed plasma leading to the jet-let formation were mainly highlighted for the two sources S<sub>1</sub> and S<sub>2</sub>. The numerical simulations were validated by comparing with that of the experimental observations. To explain the plasma-shock and shock-shock interaction, two sources S<sub>1</sub> and S<sub>2</sub> with the laser pulse energy in the ratio of 1:1 and 1:2 were considered. These are referred to as equal energy and unequal energy cases, respectively throughout the chapter. Factors supporting the formation of the stagnation layer, the interpenetration of the two SWs of unequal strength, the SW interaction with PC, and the formation of the plasma jet-let by considering two unequal sources. The formation of the stagnation layer, evolution of plasma parameters in the case of interaction of equal energy sources is discussed for different separation distances of the seed plasmas.

#### 4.1.1 Simulation details

The two sources  $S_1$  and  $S_2$  are created by focusing the 10 ns laser pulses at wavelength of 532 nm in ambient atmospheric air separated by a distances of 0, 1, 2 and 4 mm. The two sources

were generated in air medium with background pressure 0.1 MPa, at room temperature of 300 K, and density of ambient air  $1.3 \times 10^{-3}$  g/cm<sup>3</sup>.

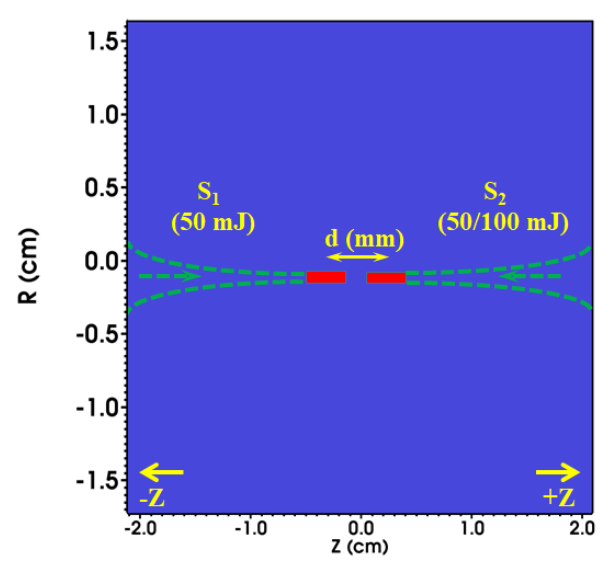


Fig. 4. 1 Simulation domain showing the focal regions at which the laser beams were focused and the separation distance between the two sources

The spot size of the focused laser beam is taken as  $500 \pm 100 \,\mu\text{m}$  in line with the experimental parameters. The simulation was performed in a domain of size  $6 \times 6$  cm along the longitudinal (laser axis) and radial directions ( $Z \times R$ ). The laser energy to generate source  $S_1$  is kept fixed at  $50 \, \text{mJ}$ . While the laser energy for second source  $S_2$  is taken as  $50 \, \text{and} \, 100 \, \text{mJ}$  giving  $S_1:S_2 = 1:1$  and 1:2 respectively.

### 4.2 Interaction of unequal energy sources

The interaction of the two unequal sources  $S_1$ :  $S_2$  =1:2 in the counter propagation direction were discussed in the present section. The two sources considered were  $S_1$  = 50 mJ and  $S_2$  = 100 mJ, focused in the opposite directions separated by a distance d = 4 mm. The coupling between the input laser beam and the generated plasma is governed by the inverse bremsstrahlung absorption followed by avalanche breakdown [14, 36, 37]. In the simulations the laser absorption percentage is considered to be between 25-35% of the input laser energy [5, 24, 38]. In Fig. 4.2 (a-f) the simulated mass density showing the interaction dynamics of the two sources over a duration of 30  $\mu$ s. The corresponding experimental shadowgrams are shown in fig.4.2 (g-l).

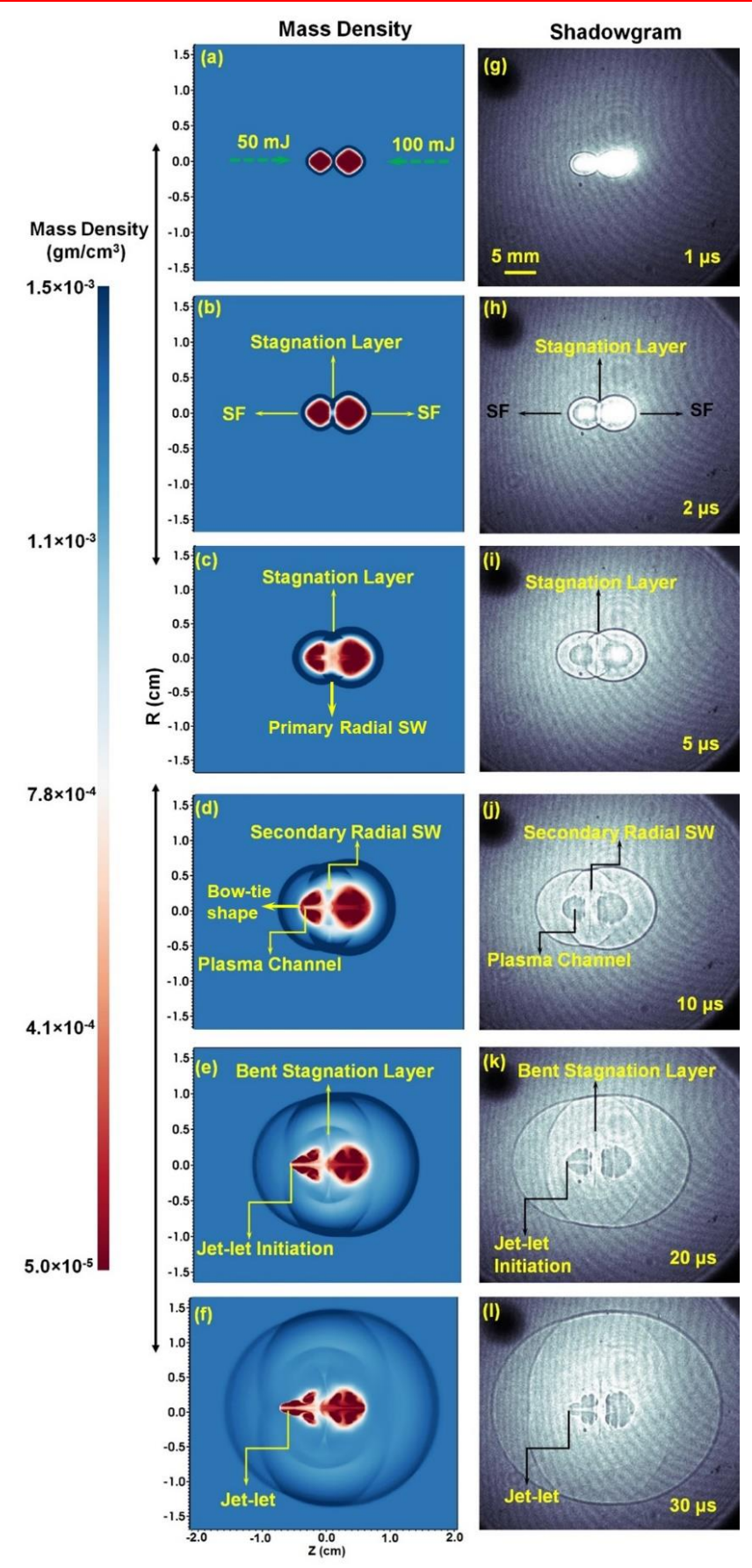


Fig. 4. 2 A comparison of evolution of (a) – (f) simulated mass density and (g) – (l) shadowgram images [24] at 1, 2, 5, 10, 20 and 30  $\mu$ s, for the case S1:S2 =1:2.

The two plasma sources S<sub>1</sub> and S<sub>2</sub> were generated as shown in Fig.4.1 and were allowed to evolve. The two freely expanding sources encounter each other at 1 µs as shown in Fig. 4.2 (a) & (g). The interaction is taking place between the outer regions of the two sources i.e., the shock fronts from the two sources were interacting with each other. The two shock waves during interaction with each other lead to formation of stagnation layer [8, 12, 24] at around 2 us as shown in Fig. 4.2 (b) & (h). After few hundreds of nanoseconds, the two shock fronts (SFs) at the interaction zone were interpenetrating with each other and traversing towards the plasma core of the other source. The interpenetration of the two SFs and interaction with the plasma core of the other source can be observed in Fig. 4.2 (c) & (i) at 5 µs. During the interaction of the two SFs at the interaction zone, the pressure builds up at the stagnation layer as a result, a radial split of mass density is observed which leads to the development of a radial shock wave at the stagnation layer. The radially expanding SW at the stagnation layer can be seen in Fig. 4.2 (d) & (j) at 10 µs. The radial SW generated along the -Y and +Y directions is building upto 8 µs, after which the SF is expanding freely into the surrounding atmosphere. The SF along the laser propagation axis while advancing through the PC is creating a plasma channel due to the mass drag created by the SF [25]. The initiation of the plasma channel can be observed in Fig. 4.2 (c) & (i). The plasma channel created in the source S<sub>1</sub> due to SF<sub>2</sub> can be visualized at 10 µs. However, the SF from lower energy source (SF<sub>1</sub>) is not able to efficiently create a plasma channel because of its lower energy. Due to the high energy SF i.e., SF<sub>2</sub> traversing through the source S<sub>1</sub>, the stagnation layer is bent and is slightly shifted towards the lower energy source S<sub>1</sub>. The shifting of the stagnation layer is observed because of the density gradient existing between the stagnation layer and the source S<sub>1</sub>. The expanding SF<sub>2</sub> is forming a bow-tie shape at the end of the source S<sub>1</sub>. The SF<sub>2</sub> while exiting from the PC of source S<sub>1</sub> initiates a plasma jet-let as can be seen in Fig. 4.2 (e) & (k). A bubble-like structure is observed to be emanating from -Z direction with time. This is observed to be formed because of the drag created by the SF<sub>2</sub> expanding through the plasma. A completely evolved plasma jet-let can be clearly visualized in Fig. 4.2 (f) & (l).

## 4.2.1 Stagnation layer dynamics in the unequal source interaction

It is a well-known fact that the SW advancing into the background gas compresses the medium ahead of it leading to an increase in the density and pressure of the background gas [5, 36]. Similarly, the compression of the medium between the approaching SFs of the two sources

leads to a raise in the mass density and pressure at the interaction zone. This is observed because of the increase in the kinetic energy of plasma at the interaction zone because of the increased electron – ion collisions that is converted into thermal energy. Fig. 4.3 (a)-(d) shows the spatio-temporal evolution of the mass density, pressure, number density and electron temperature respectively along the laser propagation axis. The line profiles were plotted at 0.9, 1.1, 2 and 5 µs respectively.

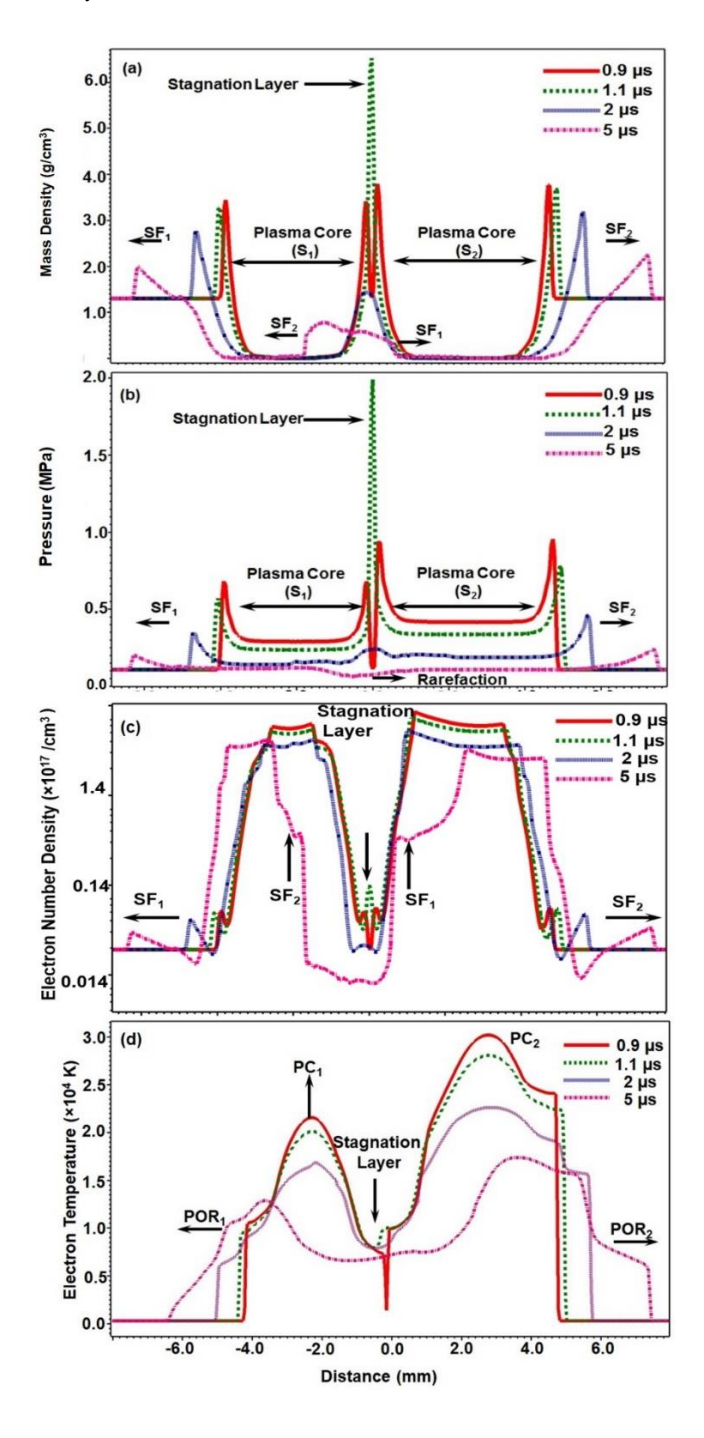


Fig. 4. 3 Spatio-temporal evolution Spatio-temporal evolution of (a) mass density, (b) pressure and (c) number density and (c) electron temperature along the laser propagation axis of the two sources for the separation distance between the plasmas d = 4 mm

The mass density (fig. 4.3 (a)) plot shows that at 0.9  $\mu$ s the two SFs generated from S<sub>1</sub> and S<sub>2</sub> are about to interact. The interaction of two SFs takes place after these times. At 1.1  $\mu$ s the maximum mass density of 6.4  $\times$ 10<sup>-3</sup> g/cm<sup>3</sup> is attained at the interaction zone i.e., at Z = 0 (considered as zone of interaction). The maximum mass density attained at Z =0 is higher than that of the density at the individual SFs before interaction at 0.9  $\mu$ s which is 4.9 times higher than the ambient air density. After 1.1  $\mu$ s, the two SFs were interpenetrating with each other leading to a decrease in the density at Z=0 as can be observed at 2  $\mu$ s from Fig. 4.3 (a). Since, the density existing at the individual SFs is very less (of the order 10<sup>-3</sup> g/cm<sup>3</sup>) as a result, the two SFs were interpenetrating with each other rather than reflection at Z=0 [24, 25]. The interpenetration of the SFs can be confirmed from the line profile of mass density at 5  $\mu$ s. The line profile clearly shows that the SF of higher energy is travelling towards the lower energy source S<sub>1</sub>, while that of lower energy source is travelling towards the higher energy source resulting in decrease in mass density at Z=0.

Fig. 4.3 (b) shows the line profile of pressure along the laser propagation axis. The pressure existing at  $SF_1$  and  $SF_2$  before interaction i.e., at 0.9  $\mu$ s is observed to be 0.7 and 0.9 MPa respectively. The pressure attained at the stagnation layer i.e., at Z=0 during the time of maximum interaction 1.1  $\mu$ s is 1.9 MPa which is higher than the sum of the pressures at the individual SFs before interaction [39]. The maximum pressure attained at Z=0 is 19 times higher than the ambient air pressure. However, at latter times > 1.1 $\mu$ s the pressure at Z=0 is decreasing as can be seen at 2  $\mu$ s. A rarefaction wave that is followed by  $SF_2$  along Z=0 direction can be observed in the line profile of pressure at 5  $\mu$ s.

Fig. 4.3 (c) shows the number density line profile. The number density is also observed to follow a similar trend as that of mass density and pressure. A spike in number density at Z=0 at 1.1  $\mu$ s is observed which has decreased after 1.1  $\mu$ s. During the interaction of two shocks, the maximum number density is estimated to be  $1.28 \times 10^{16}/\text{cm}^3$  which is equal to the sum of number densities before interaction. A reflection of the two SFs at the interaction zone was proposed in the literature [16] for the plasma number density of the order  $10^{18}/\text{cm}^3$  and that at the SFs of the order  $10^{19}/\text{cm}^3$ . However, an interpenetration of the SFs is observed in the present case because of the lower number density existing at the SF (of the order  $10^{16}/\text{cm}^3$ ). This is also confirmed from the experimental results [24].

Fig. 4.3(d) shows the line profile of the electron temperature taken along the laser propagation axis. It can be observed that the temperature existing at the plasma outer regions (POR<sub>1</sub> and

POR<sub>2</sub>) of the two sources is  $\sim 0.89 \times 10^4 \, \mathrm{K}$  and  $\sim 1.0 \times 10^4 \, \mathrm{K}$  respectively during the initiation of the interaction at 0.9  $\mu s$ . However, it is to be noted that the maximum temperature attained at the stagnation layer is  $\sim 1.0 \times 10^4 \, \mathrm{K}$  at 1.1  $\mu s$ , which has further decreased to  $\sim 0.89 \times 10^4 \, \mathrm{K}$  by 5  $\mu s$ . The temporal variation of the electron temperature at the stagnation layer is discussed in detail in the following section.

# 4.2.2 Temporal evolution of electron temperature at stagnation layer

As discussed in the previous section, the temperature at the interaction zone (Z=0) is increasing during the formation of the stagnation layer. Since, the interaction of the two sources is taking place > 1  $\mu$ s, the ion-ion collisions are dominant and play a crucial role in determining the nature of the interaction process. The compression of the medium between the two sources increases the KE of the medium as a result, the system temperature increases. However, the mfp between the ions decreases due to the compression that resulted in the energy exchange between the ions and finally leading to fall in the temperatures at later times [12]. Before interaction the temperature of Z=0 zone is at room temperature (300 K). However, at 1.1  $\mu$ s, the temperature has increased to 1.05 × 10<sup>4</sup> K, which is 1.9 times higher than the temperature attained at the SF<sub>1</sub> (5540 K, in the absence of the second source). Fig. 4.4 shows the temporal evolution of electron temperature at positions Z=-0.5, 0 and 0.5 mm respectively.

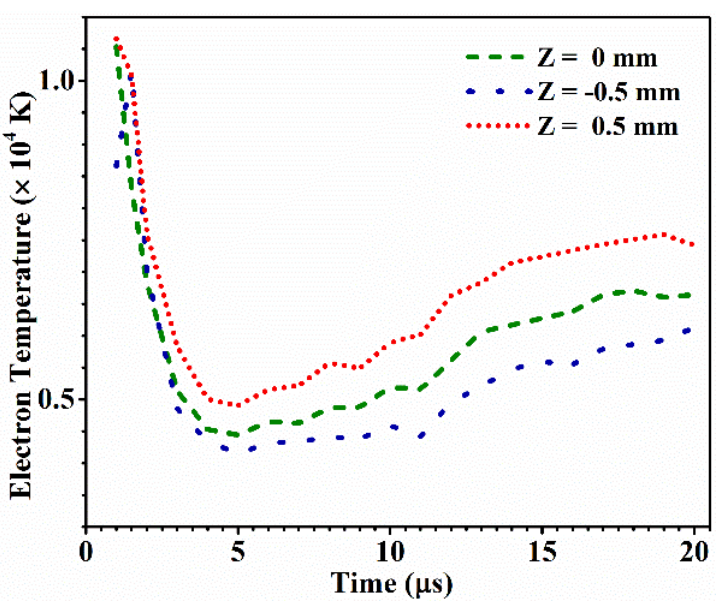


Fig. 4. 4 Temporal evolution of electron temperature at stagnation layer Z=0, -0.5 mm (towards S1) and 0.5 mm (towards S2) formed due to interaction of 1:2 sources separated by d=4 mm

From Fig.4.4 it can observed that the electron temperature at Z=0 ( $T_{e,Z=0}$ ) is decreasing rapidly after 1.1  $\mu$ s. This is observed because of the interpenetration of the interacting SFs and expansion in the opposite direction. The temperature at Z=0.5 ( $T_{e,Z=0.5}$ ) is always more than that observed at Z=-0.5 and 0 ( $T_{e,Z=0.5}>T_{e,Z=0}>T_{e,Z=0.5}$ ). This is observed because of the high energy source  $S_2$  along the +Z direction. After 5  $\mu$ s an increase in the electron temperature is observed at all the three positions, Z=-0.5, 0 and 0.5 due to transfer of energy between the sources via ion - ion collisions. This is observed because of the shifting of the stagnation layer towards the lower energy source.

The stagnation layer is observed to shift by 1.8 mm towards the lower source. The relative momentum of the stagnation layer towards the lower energy source is due to the pressure gradient pointing towards the lower source between the SF<sub>2</sub> and PC of S<sub>1</sub>. It is also observed from Fig. 4.2 (e & k) at 20 µs and Fig. 4.2 (f & l) the PC of S<sub>2</sub> is slightly crossing the interaction zone and interacting with the PC of S<sub>1</sub>. The extent of the interaction/ interpenetration of the two plasma sources is controlled by a parameter known as the collisionality parameter [8, 12, 13, 19, 24, 25, 40].

For the separation distance d=4 mm between the two seed plasmas, the estimated relative velocity between the two sources  $v_{l,2}$  is  $2\times10^5$  cm/s, and average ionization  $z_0$  of the seed plasmas at 50 and 100 mJ is estimated to be 1.6 and 2.06, respectively. The simulated average ion density  $N_i$  during the interaction of two sources (~1 µs) at the interaction region is found to be in the range  $10^{17}$  /cm<sup>3</sup>. In our case, the interaction between the seed plasmas is dominated by the ion–ion collisions as the density is in the range  $10^{16}$ – $10^{19}$  cm. The interaction between the particles is decided by collisionality parameter  $\zeta$  which is estimated to be 9. It was proposed by Dardis et al.[12] that  $\zeta$  <1 indicate that the two seed plasmas interpenetrate with each other. This interaction is dominated by collisions between ionic species from each of the opposing seed plasmas. From the simulations, we observed that for the considered seed plasma separation, the plasma–plasma core interpenetration is not taking place but, instead the two plasma outer regions were interacting. During the ion–ion interaction process, the ions with high kinetic energies (velocity) collide with the residing ions of lower energy and exchange their energy. During the exchange of the energy, the ions decelerate to lower velocities (momentum).

# 4.2.3 Shock wave dynamics for unequal source interaction $(S_1:S_2=1:2)$

In Fig. 4.5 (a - d) the temporal evolution of SFs from the two sources along –Z and +Z directions in the presence of the second source were compared to their corresponding evolution in the absence of second source were presented. Fig. 4.5 (a) shows the SF<sub>1</sub> (from S<sub>1</sub>) evolution along – Z direction. It can be observed from Fig. 4.5(a) that the interaction of the SF<sub>1</sub> at Z=0 with SF<sub>2</sub> is not affecting the SF<sub>1</sub> evolution along –Z direction. i.e., the presence of the second source is not affecting the temporal evolution of SF<sub>1</sub> along –Z direction. It can be observed that though the SF<sub>2</sub> (from S<sub>2</sub>) along –Z is traversing through the PC of S<sub>1</sub> and reaching the other end of the plasma at around 15 μs. However, the SF<sub>2</sub> is not effecting the SF<sub>1</sub> expansion along –Z direction because, by the time the SF<sub>2</sub> reaching the outer edge of PC<sub>1</sub> (15 μs) the SF<sub>1</sub> along –Z direction has completely detached from the PC<sub>1</sub> and is freely expanding into the surrounding medium. However, the SF<sub>1</sub> evolution along +Z direction is slightly effected due to its interaction with the PC of S<sub>2</sub>.

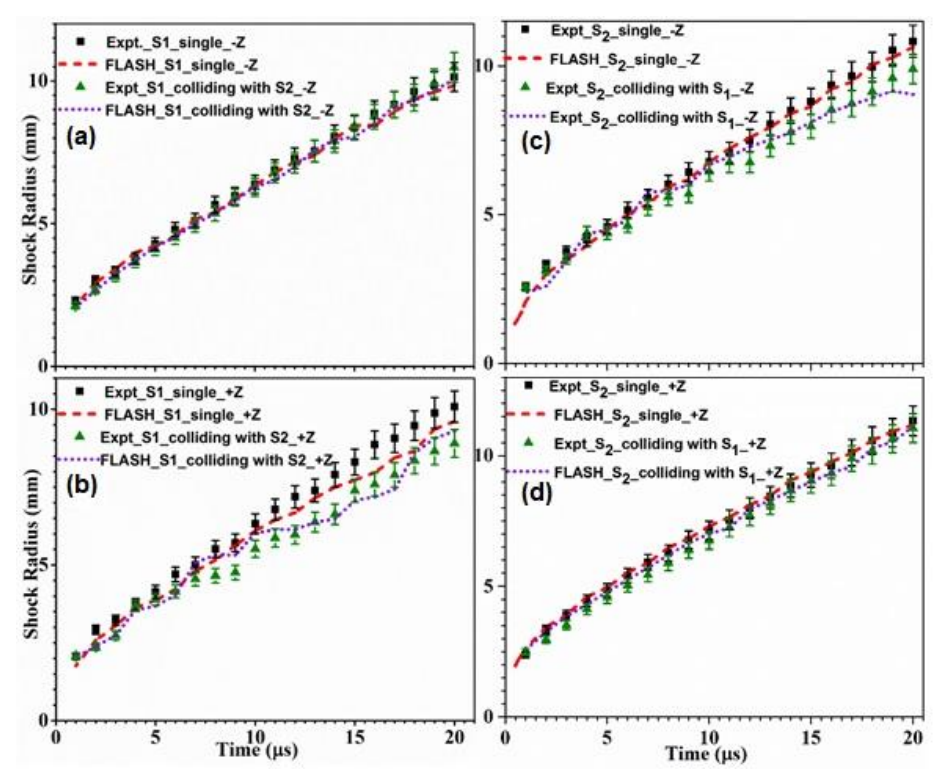


Fig. 4. 5 Comparison of axial variation of shock radius source S1 along (a) -Z, (b) +Z and from source S2 along (c) -Z and (d) +Z directions respectively.

Fig. 4.5 (b) shows the temporal evolution of the  $SF_1$  along +Z direction. The  $SF_1$  evolution is similar both in presence and in the absence of the second source until 7  $\mu$ s. After 7  $\mu$ s the  $SF_1$  is slightly slowed down when compared to the freely expanding  $SF_1$ . This is the time where

the SF<sub>1</sub> is interacting with the PC of source S<sub>2</sub>. This can be correlated with the mass density evolution in Fig. 4.2. It is to be noted from Fig. 4.2 (e) that SF<sub>1</sub> along +Z direction is crossing the PC of S<sub>2</sub> around 18  $\mu$ s. Hence, a slight rise in shock radius is observed. The slowing down of the SF<sub>1</sub> inside the PC of S<sub>2</sub> and increase in the shock radius after exiting the PC can be attributed to the low pressure inside the PC when compared to the ambient pressure ( $V = \sqrt{\gamma P/\rho}$ , V being the velocity of the SW,  $\gamma$  is the adiabatic constant, P is the pressure and  $\varrho$  is the density of the SW).

Similar to  $SF_1$  along +Z direction the  $SF_2$  along -Z direction is observed to be slowing down slightly after 10  $\mu$ s as can be seen in Fig. 4.5 (c). This is due to the  $SF_2$  while traversing through the PC of source  $S_1$  sweeps the plasma thus, initiating the plasma jet-let. A completely evolved jet-let is observed by 30  $\mu$ s as can be seen in Fig.4.2 (f & l).

Hence a slightly decreased shock radius is observed between 10-20  $\mu$ s as can be seen in Fig. 4.5(c). The SF<sub>2</sub> along + Z direction is expanding freely as there is no confining source ahead of it as can be observed in Fig. 4.5(c). A comparison of the simulated mass density evolution of 50 mJ source expanding freely in the absence of second source and confined in presence of the second source S<sub>2</sub> is shown in Fig. 4.6 (a & b) at 8  $\mu$ s.

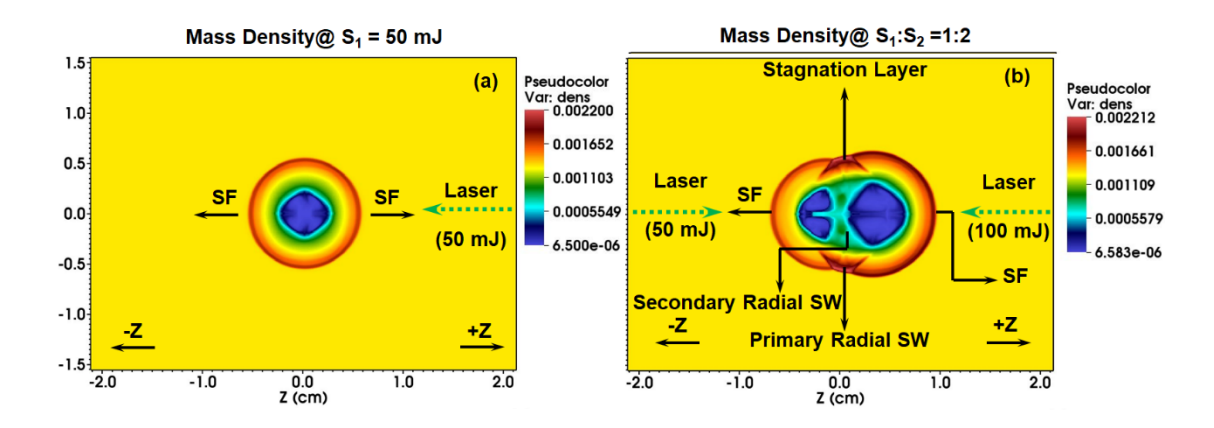


Fig. 4. 6 A comparison of mass density evolution at 8  $\mu$ s generated from (a) single source and (b) when two unequal sources were interacting

It can be observed from Fig. 4.6 (a) that the SF in all the directions is expanding freely without any obstruction. The expanding SW has attained a spherical nature hence the expansion is almost the same in all the directions. Fig. 4.6 (b) shows a pseudo plot of the 50 mJ source at 8 µs which is interacting with a 100 mJ source. A clear view of the stagnation of the mass density at the interaction zone can be visualized in Fig. 4.6 (b). The formation of the secondary radial SW due to the compression of the mass at the interaction zone along the laser propagation

axis can be observed. The formation of the plasma channel in the source  $S_1$  can be observed because of the  $SF_2$  traversing through  $PC_1$ . Freely expanding  $SF_1$  along -Z direction can be visualized which is not effected by the interaction taking place at Z=0. Similarly  $SF_2$  along +Z direction is unaffected due to the interaction at Z=0. However, an initiation of the plasma channel formation in source  $S_2$  due to the interaction of  $SF_1$  with the  $PC_2$ .

## 4.3 Interaction dynamics of two equal sources separated by 4 mm

Since, the SFs traversing through the PCs of the two sources were of equal strength, the stagnation layer at the interaction zone is straight and stable not being shifted towards  $S_1$  or  $S_2$ . This can be observed at the longer timescales i.e., from Fig. 4.7 (d) - (f).

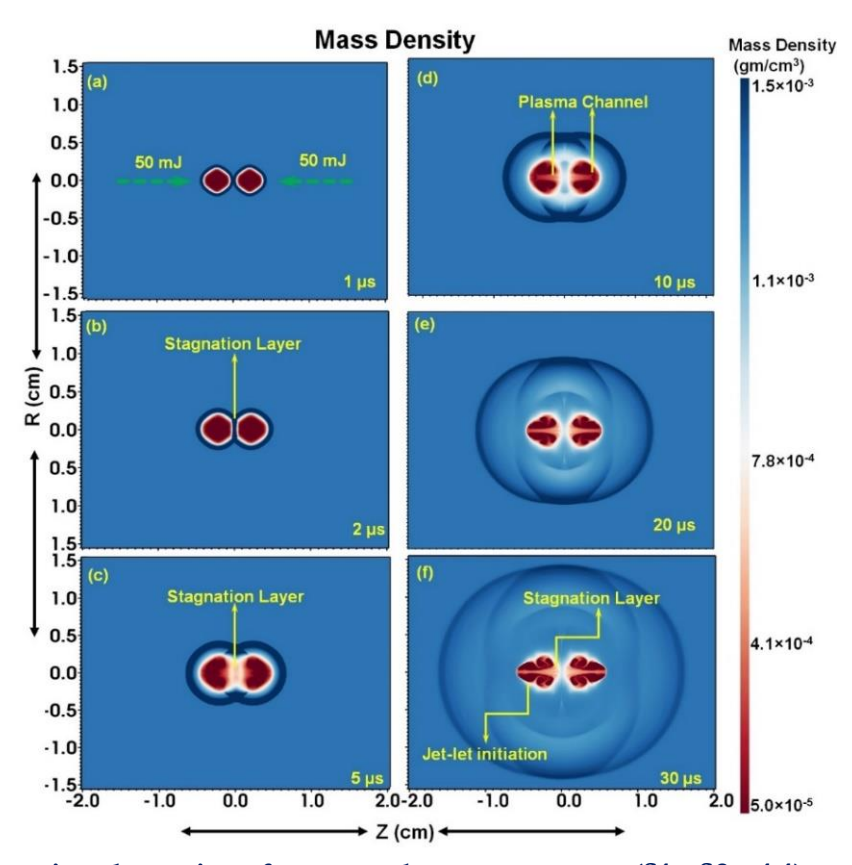


Fig. 4. 7 Interaction dynamics of two equal energy sources (S1 : S2 =1:1) at (a) 1  $\mu$ s, (b) 2  $\mu$ s, (c) 5  $\mu$ s, (d) 10  $\mu$ s, (e) 20  $\mu$ s and (f) 30  $\mu$ s, respectively.

In contrast to this, in the case of unequal source interaction (Fig. 4.2 (d)), the stagnation layer shifts toward lower energy source S1 and formed as bow-shaped during their interaction. In this case (1:1), the SFs were observed to reach the edge of the PC by 20 µs after which an initiation of plasma jet-let can be observed at 20 µs on both sides of the stagnation layer. The initiation of the jet-let is more clearly observed at 30 µs. The SF of one source while

propagating through the PC of other source, loses a part of its energy to the PC which is manifested as the drag, resulting in a jet-let formation

# 4.3.1 Stagnation layer dynamics in case of equal source interaction ( $S_1:S_2=1:1$ )

The spatio-temporal variation of mass density, pressure and electron number density along the laser propagation axis is presented in Fig. 4.8 (a-c) respectively. It is observed from the line profile of mass density and pressure that the interaction between the two sources is initiated at  $1.05 \, \mu s$ .

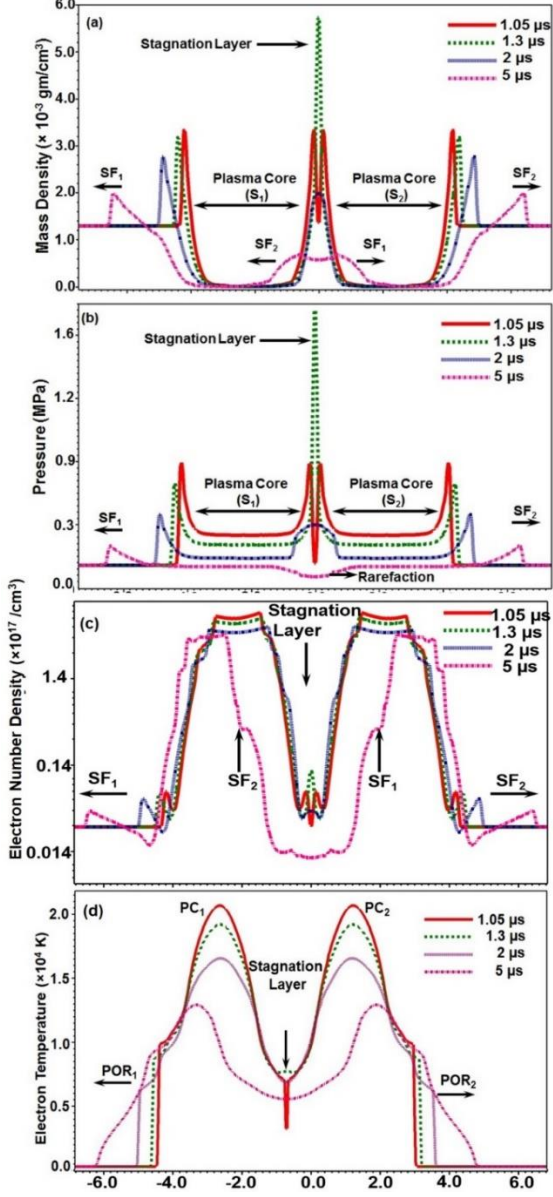


Fig. 4. 8 Axial variation of (a) mass density, (b) pressure, (c) electron number and (d) electron temperature around the interaction zone at 1.05, 1.3, 2 and 5  $\mu$ s respectively in the case of equal energy source interaction S1 = S2

A maximum interaction is taking place between the two SFs at 1.3  $\mu$ s (Fig. 4.8(a)), at Z= 0. The maximum density of  $5.8 \times 10^{-3} \text{g/cm}^3$  is attained at Z=0 which is greater than the density existing at the individual SFs before interaction. Also the maximum density is 4.5 times higher than the ambient air density. After 1.3  $\mu$ s, the density at the interaction zone is observed to decrease because of the interpenetration of the SFs to their opposite sources. The line profile of mass density at 5  $\mu$ s clearly shows the two interpenetrated SFs traversing towards the PC of the other source.

Fig. 4.8 (b) shows the line profile of pressure along the laser propagation axis at different time scales. By the time of interaction at 1.05 μs, the pressure at the two SFs is observed to be 0.58 MPa. The maximum pressure reached at the stagnation layer is 1.3 MPa at 1.3 μs, which is greater than the sum of the individual shock pressures (1.16 MPa) before interaction. The enhancement of the SF pressure is observed to be increased by a factor of 2.2, compared to that of a single source shock pressure. Similarly, the pressure is increased by a factor of 13, compared to that of ambient pressure.

After 1.3  $\mu$ s, the interpenetration of the two SFs takes place resulting in a fall of pressure at the stagnation layer. A rarefaction wave at Z= 0 followed by the SF at the stagnation layer can be visualized from Fig. 4.8 (b) at 5  $\mu$ s. The spatial variation of the electron number density is presented in Fig. 4.8(c). The number density at the two SFs before interaction is  $6.06\times10^{15}/\text{cm}^3$ , and the resultant number density at the maximum interaction time, i.e., at 1.3  $\mu$ s is  $1.18\times10^{16}/\text{cm}^3$ .

The spatial variation of the electron temperature along the laser propagation axis is shown in Fig. 4.8 (d). The peak temperature attained at the plasma core of the two sources is  $2.0 \times 10^4$  K while the temperature existing at the plasma outer regions of the two sources is  $\sim 0.89 \times 10^4$  K at  $1.05~\mu s$ . The maximum temperature attained at the stagnation layer is  $0.89 \times 10^4$  K. The temperature at the stagnation layer has decreased to  $0.5 \times 10^4$  K at  $5~\mu s$ . The temporal evolution of the electron temperature at the stagnation layer is presented in the following section.

## 4.3.2 Temporal evolution of electron temperature at interaction zone

Fig. 4.9 shows the temporal evolution of the electron temperature at the stagnation layer. The temperature at Z=0 is at 300 K before interaction, which started to increase during the interaction and rises to a maximum of 8900 K. It is 29 times higher than the ambient

temperature. After the maximum interaction, an interpenetration of the SFs is observed as confirmed from Fig. 4.8.

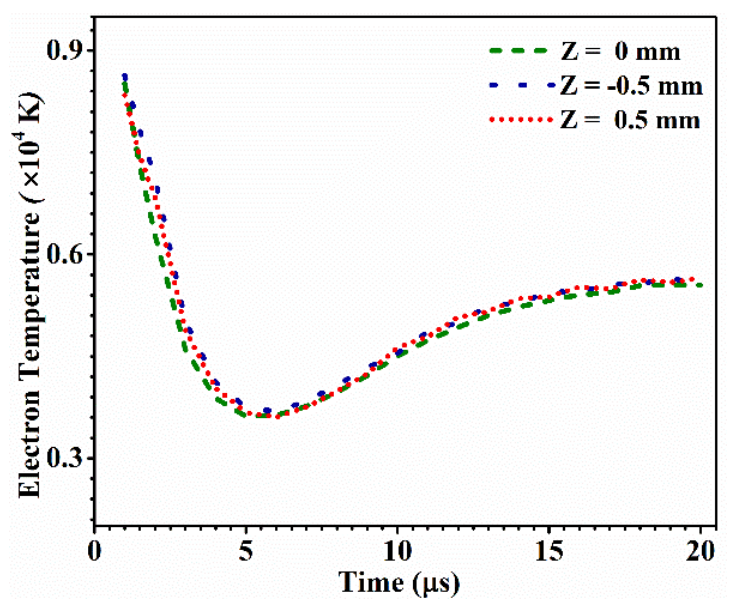


Fig. 4. 9 Temporal evolution of electron temperature at the stagnation layer formed due to interaction of two equal energy sources (S1:S2 = 1:1).

Later, they traverse towards the PC of the other source resulting in the relaxation of the compressed medium during the time of interaction. As a result the temperature at the three regions Z=-0.5, 0 and 0.5 mm started to decrease rapidly. However, during the interaction of the SF of one source (say  $S_1$ ) with the PC of the second source ( $S_2$ ) the PC of  $S_1$  is shifted towards the stagnation layer resulting in the increase of the electron temperature at Z=-0.5, 0 and 0.5 mm. The temperature at these three regions, is observed to be almost equal ( $T_{e,Z=-0.5}$  = $T_{e,Z=0}$  = $T_{e,Z=0.5}$ ). A stagnation layer of 1 mm thick has formed at the interaction zone of the two plasma sources  $S_1$  and  $S_2$ . At the interaction zone, the interpenetration of the plasmas is not observed which is in contrast to that of 1:2 source interaction where the interpenetration is observed. The two plasmas were decelerating at the stagnation layer forming a hard stagnation layer. This is confirmed from the collisionality parameter ( $\zeta$ ).

For the separation distance of d = 4 mm between the two seed plasmas, the estimated relative velocity between the two sources  $v_{1,2}$  is  $2\times10^5$  cm/s, and average ionization  $z_i$  of the seed plasmas at 50 ns is estimated to be 1.6. The simulated average ion density  $N_i$  during the interaction of two sources ( $\sim1.3~\mu$ s) at the interaction region is found to be in the range  $10^{17}$  /cm<sup>3</sup> and  $\ln\Lambda = 3.4$  with the ion—ion mfp of 0.6  $\mu$ m. The collisionality parameter  $\zeta = d/\lambda_{i-i}$  >1, hence confirming the formation of collision dominated stagnation layer. This indicates that the two plumes will decelerate rapidly at the interaction zone leading to little or no

interpenetration of the seed plasmas. This interaction is dominated by collisions between ionic species from each of the opposing seed plasmas.

# 4.4 Temporal evolution of plasma parameters in counter propagating equal ( $S_1$ : $S_2 = 1:1$ ) and unequal sources ( $S_1$ : $S_2 = 1:2$ )

Fig. 4.10 (a) and (b) compares the temporal evolution of electron temperature ( $T_e$ ) and number density ( $n_e$ ) at the plasma core of  $S_1$  alone and that of  $S_1$  under the influence of the source  $S_2$ , along the axial direction (laser propagation axis) for the case of equal sources and unequal sources. The evolution of  $T_e$  and  $n_e$  are similar with and without the presence of plasma source ( $S_1$ ) before the interaction times of up to 2  $\mu$ s.

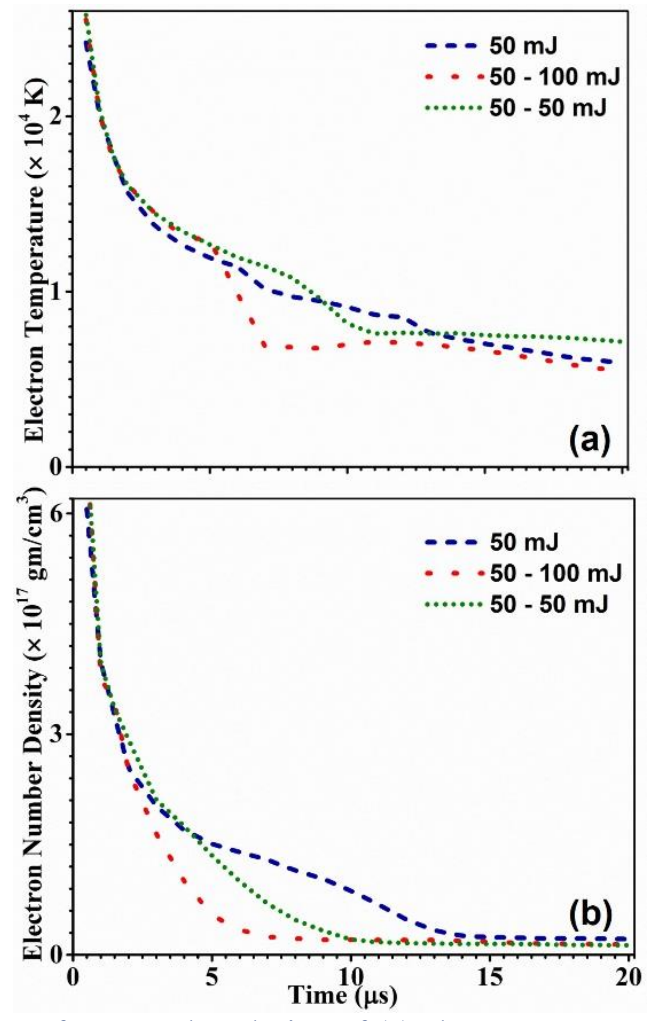


Fig. 4. 10 Comparison of temporal evolution of (a) electron temperature and (b) number density at the PC of single plasma source (50 mJ) alone, in the presence of equal (1:1) and unequal (1:2) sources.

In the case of unequal sources, the interaction of  $SF_2$  with the PC of  $S_1$  takes place at 2  $\mu$ s. As a result, a slight increment in the plasma temperature is observed, which lasts up to 4  $\mu$ s. The pressure at  $SF_2$  (1:2 case) during the interaction with plasma is 0.11 MPa, while the pressure at the PC of  $S_1$  is 0.12 MPa. Since the gradient in the pressure is very small, an effective rise in the plasma is not observed. After traversal of  $SF_2$  through PC of  $S_1$  (at  $> 5 \mu$ s), a fall in the PC temperature is observed. During the expansion, the shocked region tries to return to its original state via the rarefaction wave, leading to a fall in the temperature. A rarefaction wave is an expansion wave (unloading wave) that helps the shocked medium to reach its initial state. Due to the interaction of the SF with the plasma core, a rarefaction wave (fan) propagates toward the stagnation layer, which tends to reduce the pressure at the stagnation layer. In the present context, the rarefaction wave associated with the  $SF_2$  interacts with the PC of  $S_1$  (see Fig. 4.3) resulting in the reduction of pressures at the stagnation layer. Hence, a fall in temperature in the PC of  $S_1$  is observed after 5  $\mu$ s, which is less than the plasma temperature in the case of free expansion of  $S_1$ . Though a slight rise in plasma temperature is observed, the rise and fall of  $T_c$  are delayed for the case of 1:1 compared to the 1:2 case.

The maximum rise in temperature of between  $\sim 1 \times 10^3$  K is observed between 3 - 5 µs. However, from 5 - 11  $\mu$ s, a decrease in the temperature of  $\sim 0.25 \times 10^4$  K is observed. The rise and fall in temperatures are within the statistical error ( $0.26 \times 10^4$  K). Hence, the SW does not effectively raise the plasma temperature. However, an effective variation in the number density  $(1.0 \times 10^{17}/\text{cm}^3)$ , during the compression of the SW is observed, which falls above the statistical error (0.82 ×10<sup>17</sup>/cm<sup>3</sup>). The simulated statistical error is estimated by comparing the plasma parameters (electron temperature and number density) from simulations performed in the first and third order of Harten-Lax-van Leer-Contact (HLLC) scheme [41]. Details of the statistical error determination were presented in Chapter 2. The decrease in the number density along the laser propagation axis is observed because of the compression and squeezing of the PC by the SW, that is leading to the movement of density along the radial direction. However, an efficient energy transfer between the plasma and SF does not occur which is confirmed as there is no increment in the electron temperature. Physically, this can also be understood by calculating the energies associated with the electrons (E<sub>ele</sub>), ions (E<sub>ion</sub>), and the total energies ( $E_{tot}$ ). Though the total pressure  $P = P_{ele} + P_{ion}$ , the total energy E is not equal to  $E_{ele} + E_{ion}$ . The additional energy is due to the kinetic energy term  $\frac{1}{2} \vec{v} \cdot \vec{v}$ . The difference in the energy is being utilized in the compression of the plasma. The statistical error is estimated to be 65 J/g.

When the simulations are performed for order 1, the sum of the ion energy and the electron energy is  $3.29 \times 10^3$  J/g, which is not equal to the total energy. The sum of the electron and ion energies is 3.92×10<sup>3</sup> J/g. Hence, a loss in the total energy is observed, which does not appear in the electron and ion energies. The difference of the total energy observed, and the sum of the electron and ion energies is  $5.8 \times 10^2$  J/g. The loss in the energy is above the estimated statistical error. Hence, from energy conservation (refer to chapter 2) it can be understood that the corresponding energy is converted into kinetic energy used in the expansion of the plasma during the process of SW compression along the laser propagation direction. As we know, that  $E_{tot} = E_e + E_i + KE$ , the difference in the  $E_{tot}$  and  $(E_e + E_i)$ , goes as KE which is used to compress the plasma. From the above understanding of the energy conversion, it can be confirmed that the dominant energy in the plasma and at the interaction zone is in the form of kinetic energy. The energy at the SF is not sufficient enough to effectively convert it to the thermal energy, however, induces compression of the mass along the propagation axis. This leads to the compression of mass at the SF and evolution of the plasma jet-let and formation of the plasma channel behind the SF. A similar trend in the number density inside the plasma is observed over the timescales of 2 - 14 µs, as can be seen in Fig. 4.8(b). It can be observed from Figs. 4.2(d &j) that the compression of the plasma by SF along the laser direction (axial direction) created an axial channel. This has resulted in dispersal of mass along the radial direction. Hence, a decrease in the axial number density is observed. No significant change in the plasma parameters of the source S2 is observed either in the simulations. A rise in temperature is observed because of the shifting of the plasma outer region of the two sources into the stagnation layer. It is noteworthy that the temperature is more at the stagnation layer (8520 K) than that appeared at the plasma front and the SF during the evolution in a single source (5540 K) by a factor of 1.54. However, the temperature at the stagnation layer during the interaction of two equal sources is small (8520 K) in comparison with that of two unequal sources were interacting (9330 K). Hence, it can be concluded that the variation of  $T_e$  and  $N_e$  is higher for the  $S_1:S_2=1:2$  case compared to that of the 1:1 case.

From the above sections, the physical mechanism such as interaction of two SWs at the interaction zone, compression of the plasma by the SF from the other source, the mass drag created by the expanding SW through the plasma, evolution of plasma jet-let taking place during the interaction of the two sources were clearly understood. The effect of the separation distance between the seed plasmas on the plasma parameters of 50mJ source and stagnation layer dynamics were discussed in the following sections.

### 4.5 Effect of separation distance on plasma parameters

It is observed that the separation distance between the seed plasmas is playing a crucial role in the plasma evolution and on its plasma parameters. It is a well-known fact that decrease in the separation distance between the seed plasmas leads to an early interaction of the plasma sources. It is noteworthy that the pressure at the SF will be more at the initial times (< 100 ns), while the density at the SF increases during its build up time and decreases as soon as it detaches from the plasma [2, 5, 7, 42]. The pressure existing at the interaction zone during the early time scales is more compared to that at latter time scales, as the SF from both 50 and 100 mJ sources were detaching after 1  $\mu$ s. Hence, the maximum density at the interaction zone is increasing with separation distance. Table 4.1 summarizes the maximum pressure and density existing at the interaction zone in both the equal and unequal source interaction for different separation distances of seed plasmas (d = 1, 2 and 4 mm).

Table 4. 1 The maximum pressure existing at the interaction zone for the equal and unequal source interaction for different separation distances were presented.

Configuration	d (mm)	Time of Maximum Interaction (µs)	@ Stagnation Layer		
			Max. Pressure (MPa)	Max. Density (g/cm³)	
1:2	1	0.075	25	3.5×10 <sup>-3</sup>	
1:2	2	0.25	8.6	5.9×10 <sup>-3</sup>	
1:2	4	1.1	1.9	6.4×10 <sup>-3</sup>	
1:1	1	0.1	19	3.8×10 <sup>-3</sup>	
1:1	2	0.3	6.9	6.4×10 <sup>-3</sup>	
1:1	4	1.1	1.66	5.8×10 <sup>3</sup>	

It can be observed that the maximum pressure (25 MPa) obtained at the interaction zone in the case of unequal source interaction ( $S_1$ :  $S_2 = 1:2$ ) is for the separation distance of 1 mm, while a maximum mass density ( $6.4 \times 10^{-3}$  g/cm3) is observed at the separation distance of 4 mm. While in the case of equal source interaction ( $S_1$ :  $S_2 = 1:1$ ), a maximum pressure of 19 MPa is observed at separation distance of 1 mm and a maximum density of  $6.4 \times 10^{-3}$  g/cm<sup>3</sup> for the separation distance of 2 mm. It is noteworthy that in the case of unequal source interaction, for separation distance d < 4 mm the two seed plasmas were interacting with each other and forming as a single plasma. However, for equal source interaction for separation distance d < 4 mm, the two sources were stagnating and decelerating at the interaction zone over 20 µs, however forming as a single source plasma after 20 µs. As we know that the

interpenetration or stagnation of the two seed plasmas is determined by the collisionality parameter. Table 4.2 summarizes the collisionality parameter obtained at the interaction of the two seed plasmas for the separation distances d = 1, 2 and 4 mm.

Table 4. 2 Summarizing the collisionality parameter for the two energy ratios and for different separation distances between the seed plasmas.

Energy Ratio	Distance (d) (mm)	$n_i (1/cm^3)$	<i>v</i> <sub>12</sub> (cm/sec)	T (eV)	ζ
1:2	4	$1.9 \times 10^{18}$	$2.0 \times 10^{5}$	1.1	$9.0 \times 10^{-10}$
1:2	2	$3.3\times10^{18}$	11×10 <sup>5</sup>	1.9	7.0×10 <sup>-7</sup>
1:2	1	$3.4\times10^{18}$	13.6×10 <sup>5</sup>	3.3	5.2×10 <sup>-4</sup>
1:1	4	9.0×10 <sup>17</sup>	2.0×10 <sup>5</sup>	0.9	71.0
1:1	2	$2.7 \times 10^{18}$	4.8×10 <sup>5</sup>	1.7	$2.0 \times 10^{3}$
1:1	1	$3.9 \times 10^{18}$	7.6×10 <sup>5</sup>	3.1	$6.0 \times 10^{4}$

The ion number density ( $n_i$ ) and the electron temperature ( $T_e$ ) given in the Table 4.2 were the parameters existing at the stagnation layer by the time of interaction and  $v_{12}$  is the relative velocity with which the two plasmas were approaching each other. It is noted that the parameters  $n_i$ ,  $T_e$  and  $v_{12}$  were increasing with the decrease in the separation distance between the seed plasmas. This is observed because of the early time interaction of the sources where the temperatures existing at the plasmas and the ion number densities were high.

The ion-ion mean free path is calculated using the equations (4.1) - (4.3). Collisionality parameter is obtained by determining the ratio of the separation distance and the ion-ion mean free path. It can be seen from the table 4.2 that for all the separation distances the collisionality parameter is less than 1 for energy ratio 1:2 and is greater than 1 for 1:1. Hence it can be confirmed that the stagnation layer formed in the case of unequal energy sources is a soft stagnation layer, allowing the energy transfer between the two sources. While the stagnation layer formed in the case of equal energy source interaction is a hard stagnation layer where the two plasmas were deccelerating at the stagnation layer. However, it is noteworthy that the decclerated plasmas at the stagnation layer in the case of equal source interaction were interacting with each other at longer time scales i.e., after 25  $\mu$ s and forming as a single plasma source. Fig. 4.11 (a & b) shows a comparison of the variation of the electron tempearture at the stagnation layer for both the uneual and equal energy combinations (S1: S2 = 1:2 & 1:1) for the separation distances of d = 1, 2 and 4 mm respectively.

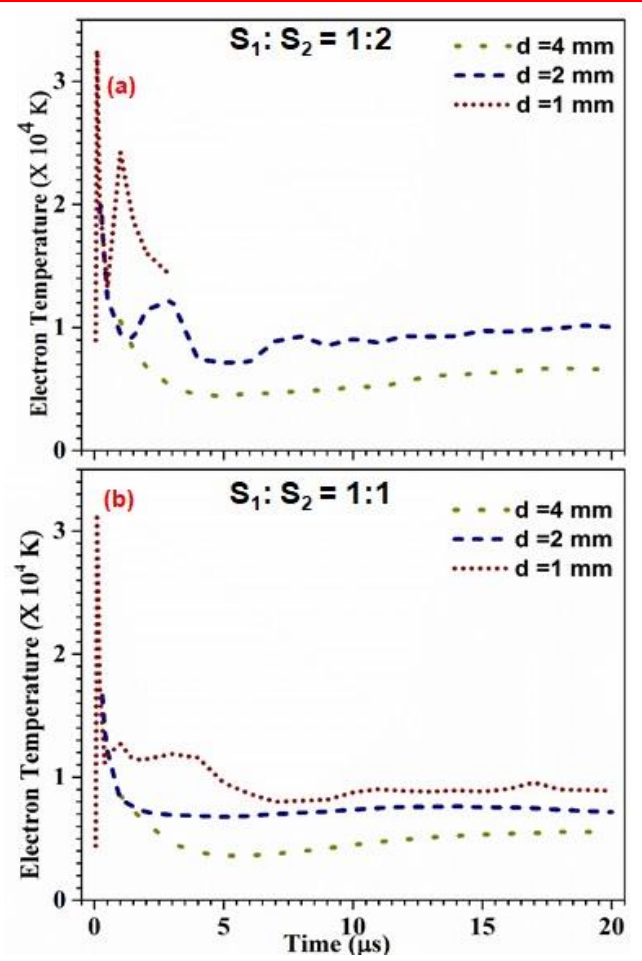


Fig. 4. 11 Temporal evolution of maximum temperature at the stagnation layer for d= 1, 2 and 4 mm in the case of (a) unequal source and (b) equal source interaction

The comparison of d=0 mm is not shown as both the sources were generated at the same point where no stagnation layer formation is observed. Fig. 4.11 (a) compares  $T_e$  for unequal sources interaction for all the three separtion distances d=1, 2 and 4 mm. The temperature has raised to a maximum during the time of maximum interaction of the two sources. It is observed that the interaction is dominated by the plasma- plasma interaction in all the cases as the SF from the source has not detached. However, the interaction in the case of d=4 mm is dominated by the outer regions of the two plasmas whereas, in the case of d<4 mm the interaction has extended to PC regions of the two plasmas sorces.

A maximum temperature of  $3.6 \times 10^4$  K is observed for d=1 mm, while it is  $2 \times 10^4$  K and  $1.05 \times 10^4$  K for d= 2 mm and d= 4 mm respectively. The raise in temperature is high in case of d = 1 mm and decreases as d is increased to 2 & 4 mm. A raise in temperature for d = 4 mm is observed after 6  $\mu$ s, and for d = 2 mm after 3  $\mu$ s. After the time of maximum interaction, the temperature has decreased because of the interpenetration of the SFs in the outer regions of plasma sources. However, after few microseconds an increase in the temperature is

observed at the stagnation layer because of the shifting of the plasma towards the interaction zone. The stagnation layer is not visible in case of d=1 mm after 3  $\mu$ s because of interpenetration of the two plasmas in case of unequal source interaction. Conversely, the stagnation layer is stable in all the three cases of d=1, 2 and 4 mm in case of equal source interaction.

Fig. 4.11 (b) shows the temperature evolution in the case of equal source interaction for all the three separation distances. Though the trend followed by the electron temeperature at the interaction zone is similar to that of the unequal source interaction, the stagnation layer is stable for the time span < 20  $\mu$ s. However, after 25  $\mu$ s, it has disappeared because of the interpenetration of the two plasma sources. The maximum temperatures obtained were 3.11  $\times$  10<sup>4</sup> K, 1.66  $\times$  10<sup>4</sup> K and 0.89  $\times$  10<sup>4</sup> K for d = 1, 2 and 4 mm respectively. These temperatures were observed to be lower than that obtained for unequal source (S<sub>1</sub>: S<sub>2</sub>=1:2) for all the separation distances. It is also observed that the stagnation layer, is disappearing in case of unequal source interaction because of the compression of the PC of S<sub>1</sub> by the dense PC of S<sub>2</sub>. However, in case of equal source interaction, the temperature at the stagnation layer is still in the range of 1×10<sup>4</sup> K because the two plasmas at the interaction zone are still trying to interact with each other.

# 4.5.1 Comparison of temporal evolution of plasma parameters for varied separation distance between seed plasmas

The effect of the interaction of SF from source  $S_2$  with PC of  $S_1$  is discussed in detail in case of unequal source and equal source interactions in section 4.4. It was understood that due to the delayed interaction of the SF<sub>2</sub> with the PC<sub>1</sub> ( > 2  $\mu$ s), an effective increment in plasma parameters is not observed for d = 4 mm. Fig. 4.12 (a-d) shows the temporal evolution of plasma parameters of source  $S_1$  (50 mJ) in the presence of  $S_2$  (50 & 100 mJ) compared to that of the freely expanding single source plasma generated using 50 mJ. Fig. 4.12 (a) shows the average electron temperature evolution at the PC of  $S_1$  along the laser propagation axis, with the varying separation distance for the unequal source interaction. For all the time scales  $T_e$  is maximum for the separation distance d = 0 mm because of the overlapping of the two sources. For d=1 mm, the temperature evolution is nearly same as that of freely expanding plasma source (50 mJ).

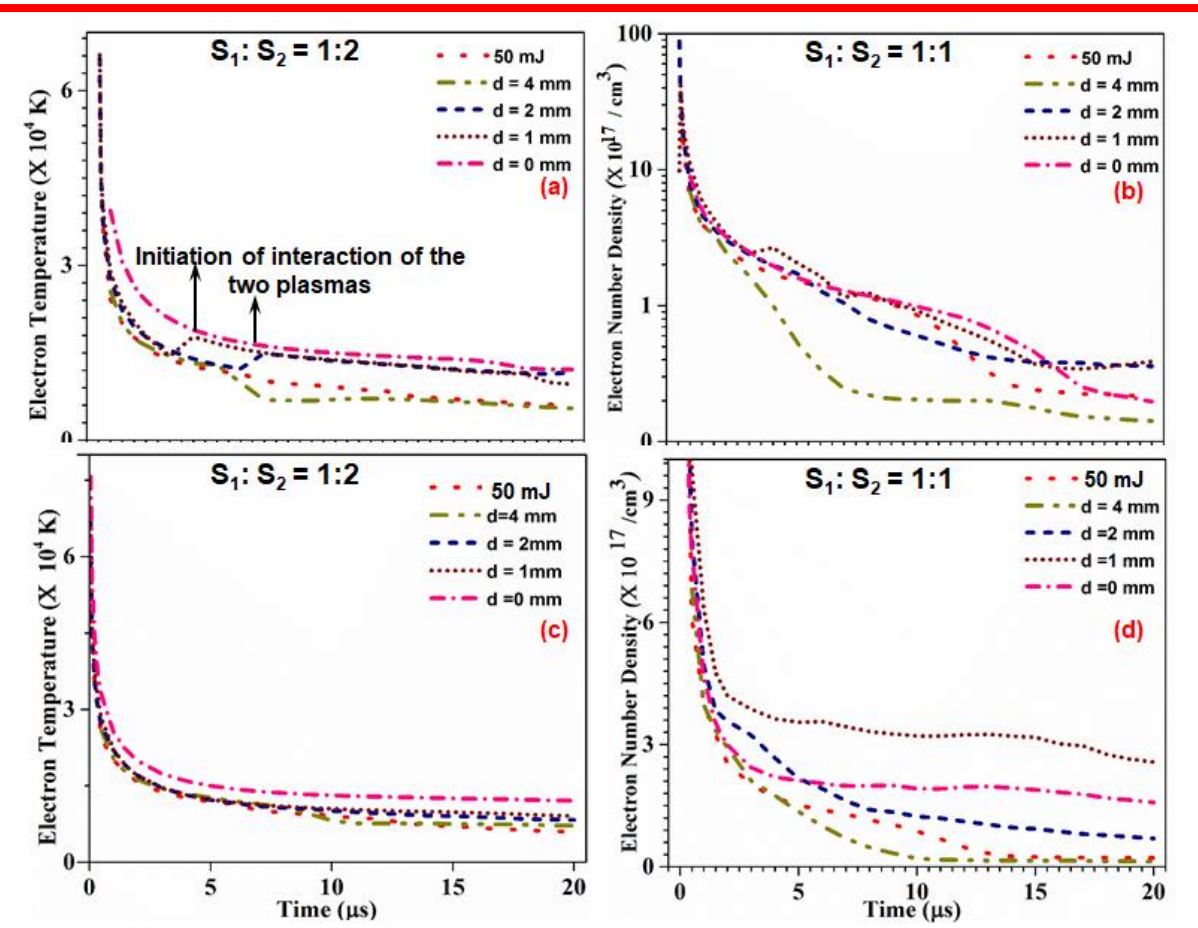


Fig. 4. 12 Temporal evolution of electron temperature and electron number density at PC along the laser propagation axis compared for unequal source interaction (a, b), and equal source (c, d) interaction in PC<sub>1</sub>.

However, after 3 µs, a raise in temperature is observed indicating the time of the initiation of the interaction of the two sources plasma cores (PC). Thus leading to formation of a single plasma source. The maximum temperature obtained after 3 µs is found to be equivalent to that of the temperature of 100 mJ. Likewise, for d=2 mm also, the interpenetration of the two plasmas is taking place after 6 µs and the raise in the temperature is observed after these times.

Fig. 4.12 (b) shows the average electron number density along the laser propagation axis. It is understood that the increase in the number density for d=1 and 2 mm is because of the penetration of the PC<sub>2</sub> through S<sub>1</sub>. Fig. 4.11 (c &d) show the electron temperature and number density for the equal source were interaction. It is observed that for d=1 and 2 mm not much variation is observed in the plasma parameters because, the two sources were still not interacting with each other.

### 4.5.2 Mass density with respect to separation distance

A comparison of mass density evolution for all the separation distances for both equal and unequal source interactions at different time scales were discussed in the present section. Fig. 4.13 (a) - (h) shows the mass density evolution at 5  $\mu$ s when two plasma sources were interacting for the separation distances d = 4, 2, 1 and 0 mm respectively.

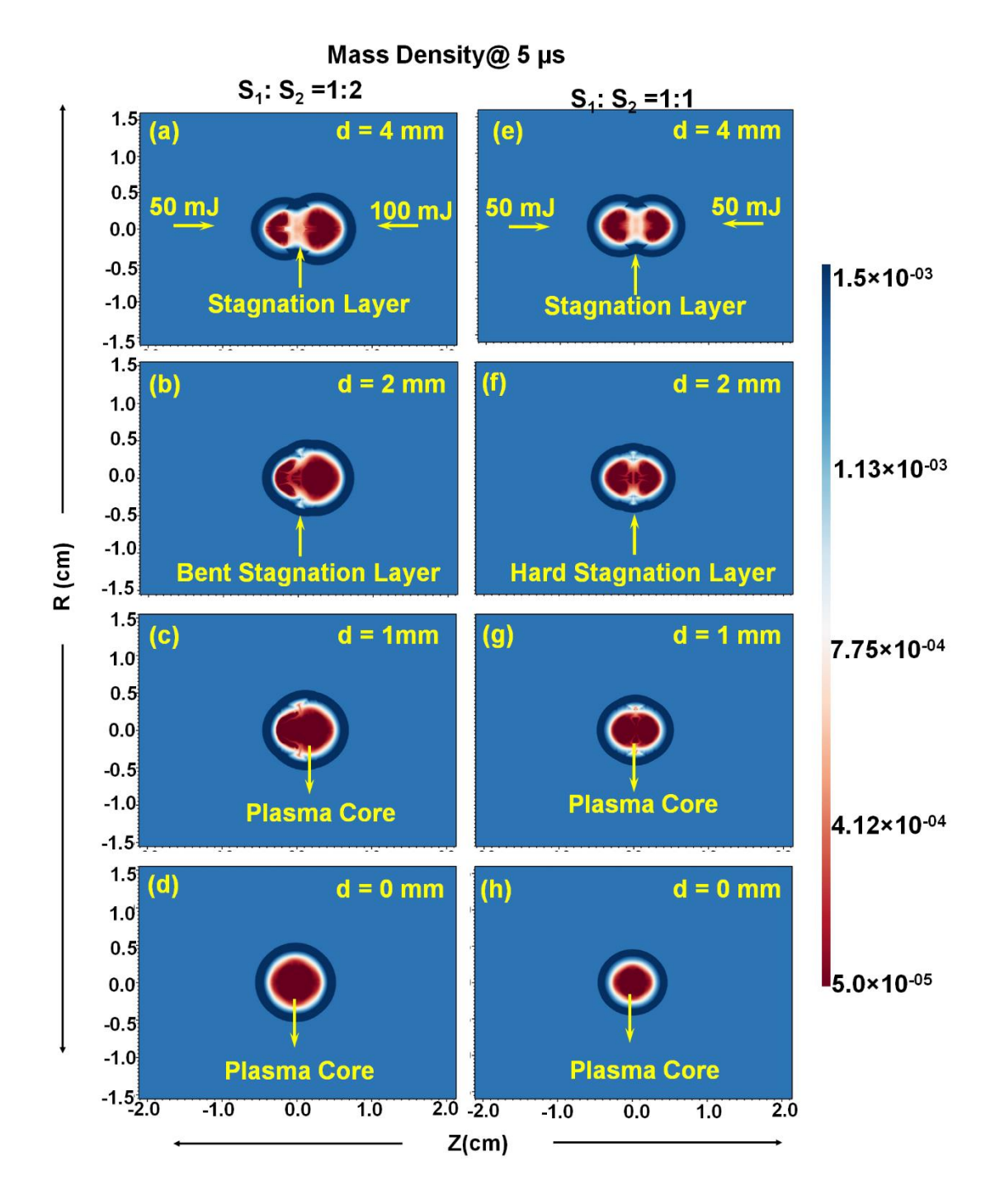


Fig. 4. 13 A comparison of mass density evolution at 5  $\mu$ s in the case of unequal source interaction for the separation distance of (a) d= 4 mm, (b) d= 2 mm, (c) d= 1 mm and (d) d= 0 mm and in case of equal source interaction for the separation distance of (e) d= 4

Fig. 4.13 (a) shows the mass density when two unequal sources were interacting with the separation distance d = 4 mm. The formation of the stagnation layer can be observed at Z=0. The PC of the two sources were on the either side of the stagnation layer and were not interacting with each other at this time of visualization. Initiation of the plasma channel in PC<sub>1</sub> due to the interaction of the SF<sub>2</sub> along -Z direction can be observed. While the plasma channel formation is not still visible in PC<sub>2</sub>. While the SF<sub>1</sub> along -Z direction and SF<sub>2</sub> along +Z direction were expanding freely.

Interpenetration of the higher energy plasma source  $S_2$  into the source  $S_1$  at 5  $\mu$ s can be visualized in Fig. 4.13 (b) for the separation distance of d=2 mm. The stagnation layer has bent towards the lower energy source  $S_1$  due to the high energy  $SF_2$  traversing through the  $PC_1$ . However, the stagnation layer is slightly visible in Fig. 4.13 (c) and not visible in Fig. 4.13 (d) due to the interpenetration of the PC from the two sources. While the two sources have formed like a single source for d=0 mm.

Fig. 4.13(e) - (h) shows the mass density evolution when two equal sources were interacting with each other with different separation distances d = 4, 2, 1 and 0 mm respectively. The stagnation of the two sources at the interaction zone for the separation distance of d = 4 mm is shown in Fig. 4.13 (e) at 5  $\mu$ s. The two sources were on the either side of the stagnation layer where the two sources were not interacting with each other.

A similar case is observed in Fig. 4.12(f) for the separation distance of d = 2 mm. The two sources were just at the stagnation layer, where the interaction of the PC is just initiated. However, no plasma channel formation is observed in the both the sources. For the separation distance d = 1mm also the two sources were observed to be stagnating at the interaction zone with the initiation of the interaction between the two sources. While the interpenetration of the two sources and formation as a single source can be observed for d = 0 mm.

Fig. 4.14 (a) - (f) shows the mass density evolution of the two interacting plasma sources at 10  $\mu$ s for all the separation distance d = 4, 2, 1 and 0 mm respectively. Bending of the stagnation layer is observed to be more prominent in for d = 4 mm (Fig 4.14 (a)). Formation of the plasma channel due to the compression of the PC by the SF of the other source can be observed in PC of both the sources for d = 4 mm. However, the plasma channel formation is more prominent in S<sub>1</sub> when compared to that observed in S<sub>2</sub>. Formation of a secondary radial SW at the stagnation layer due to the compression of the region at the stagnation layer along the

laser propagation axis is observed. Bending of the stagnation layer is also observed in Fig 4.14 (b).

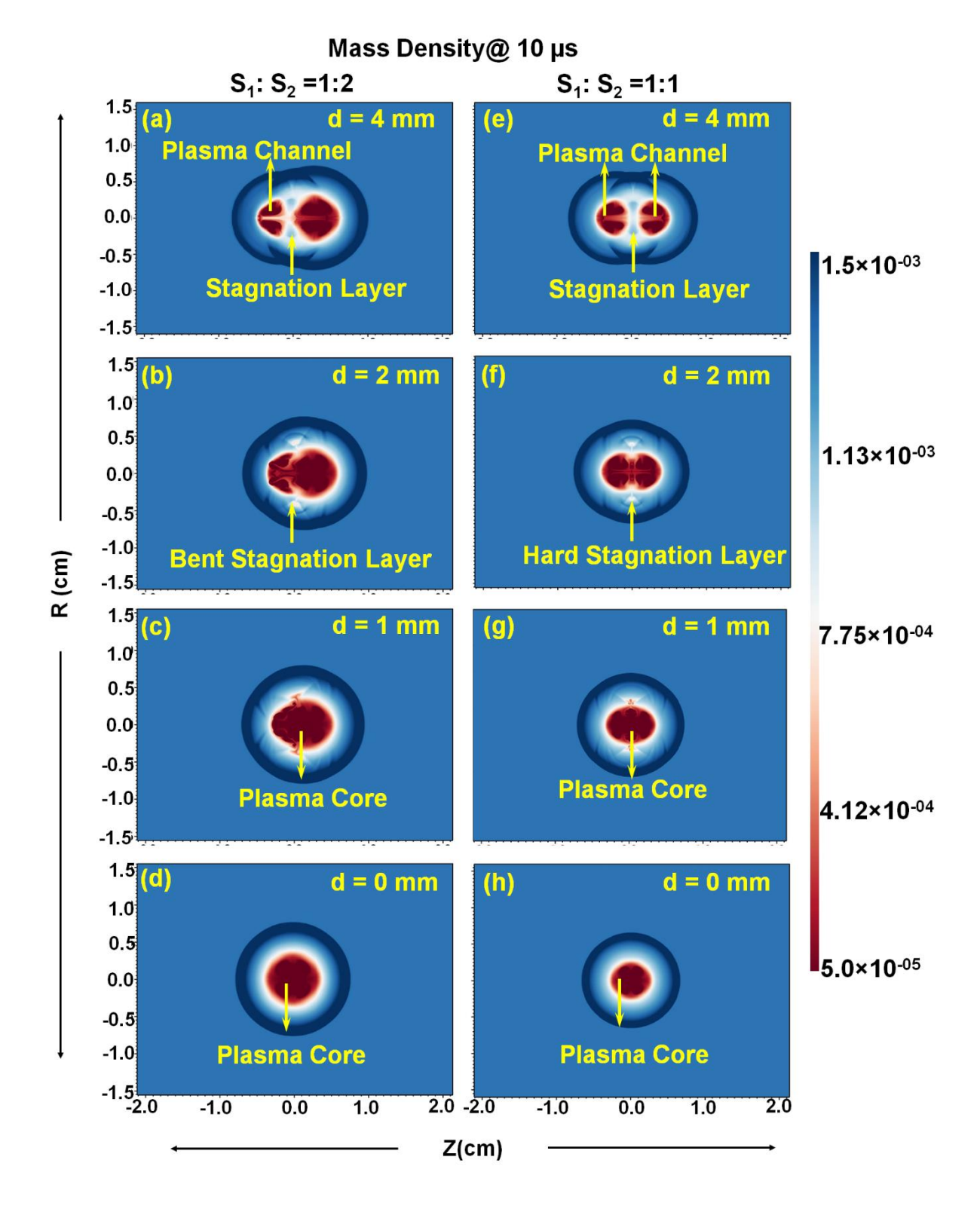


Fig. 4. 14 A comparison of mass density evolution at 10  $\mu$ s in the case of unequal source interaction for the separation distance of (a) d= 4 mm, (b) d= 2 mm, (c) d= 1 mm and (d) d= 0 mm and in case of equal source interaction for the separation distance of (e) d= 4 mm

#### Interaction of Two Counter Propagating Laser Induced Air Plasmas

The higher energy PC<sub>2</sub> has penetrated through the PC<sub>1</sub> of the source  $S_1$  and compressing the PC along the laser propagation axis. It is to be observed that the plasma channel formation is not observed for all d < 4 mm in both the equal and unequal source interaction. The interaction of the SF with the PC of the second source has led to the mass drag in the PC leading to formation of the plasma channel in case of d = 4 mm. However, in the case of d < 4 mm, the interaction between the two sources is initiated at early time scales at which the SF has not detached from the plasma. Hence, the interaction of the SF with PC is observed for d = 4 mm and interaction between two plasma sources is observed for d < 4 mm. Though the stagnation layer is still visible in case of d = 1 mm (Fig 4.14 (b)), the two plasma cores were interpenetrating with each other forming like a single source plasma core. However, for d = 0 mm a single plasma core is formed expanding freely in all the directions.

Fig. 4.14 (e) shows the interaction of two equal source interaction (50 mJ - 50 mJ) with the separation distance of d = 4 mm. The plasma channel formation is visible in both the sources  $S_1$  and  $S_2$ . However, it is to be noted that the stagnation layer formed for d = 4, 2 and 1 mm is stable and hard which is not movable towards any source. However, for d = 0 mm a single plasma source is formed expanding with shock radius less than that generated from two unequal source interaction.

The spatial evolution of mass density with respect to the interacting source and with respect to the separation distance at 20 µs is shown in Fig. 4.15 (a) - (h). Initiation of the plasma jet-let formation in the source S<sub>1</sub> is observed in Fig. 4.15 (a). This is observed because of the mass drag taking place in the PC<sub>1</sub> due to the SF<sub>2</sub> traversing along –Z direction. The plasma jet-let formation in equal source interaction is not visible at 20 µs (Fig. 4.15 (e)).

With the separation distance d < 4 mm, interpenetration of the two sources has initiated as can be seen in Fig. 4.15 (b-h). Fig. 4.16 (a-h) shows a clear visualization of the variation in the PC evolution with respect to varied separation distances at 30  $\mu$ s. From these images it can be clearly seen that the plasma length is decreasing from d = 4mm to d = 0 mm. A clear formation of plasma channel and plasma jet-let can be observed at d = 4mm (Fig. 4.15 (a)).

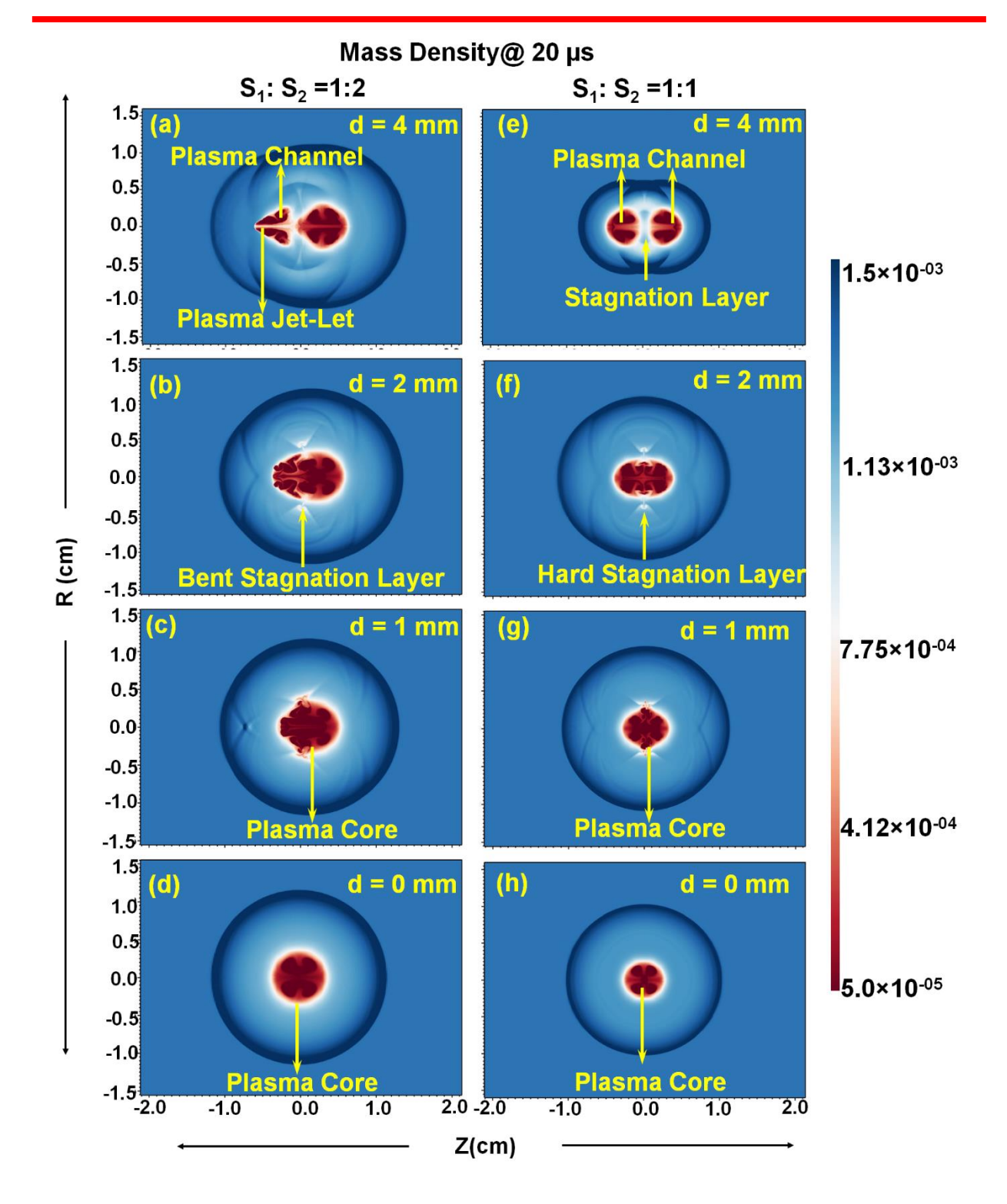


Fig. 4. 15 A comparison of mass density evolution at 20  $\mu$ s in the case of unequal source interaction for the separation distance of (a) d= 4 mm, (b) d= 2 mm, (c) d= 1 mm and (d) d= 0 mm and in case of equal source interaction for the separation distance of (e) d=4mm

Hence one can confirm that for the considered energy ratios, the two plasma sources generated at separation distance of 4mm is found to be more suitable for the generation of the plasma jet-lets. The concept of plasma jet-let formation and its underlying physics finds application in

a varying range of fields such as laser propulsion systems such as laser thrusters [43] for wave drag reduction in a vehicle, localized flow control of blunt bodies [44]. The concept of interpenetration of the plasma sources find application in the ignition of combustible mixture by determining the fuel to air mixing ratio [45].

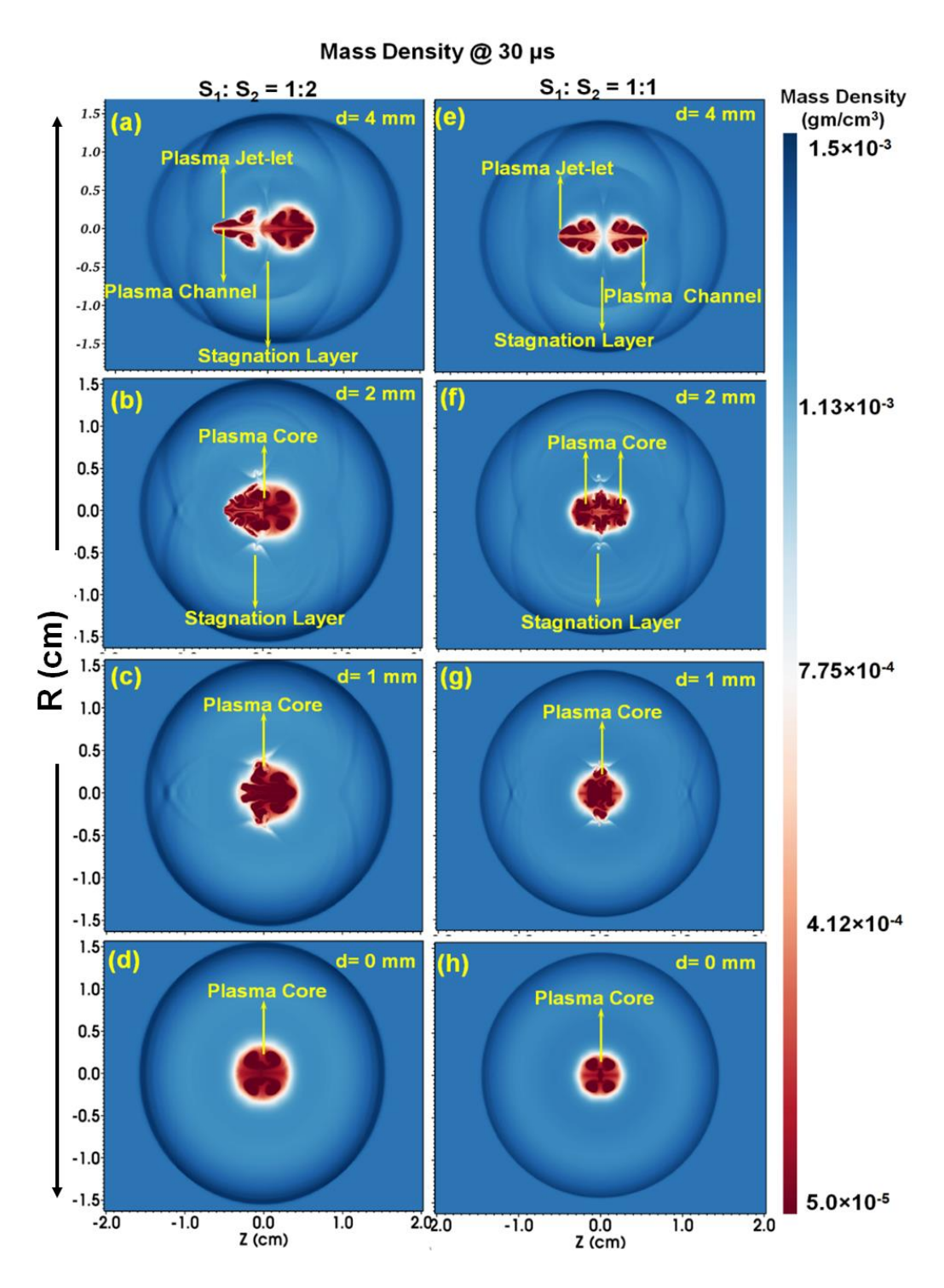


Fig. 4. 16 Mass density images at 30  $\mu$ s for unequal source interaction at (a) d= 4mm, (b) 2 mm, (c) 1mm, (d) 0 mm and for equal source interaction (e) d= 4 mm, (f) 2 mm, (g) 1 mm and (h) 0 mm

A clear formation of a secondary radial SW at the stagnation layer can be observed for d = 4 mm, whose strength has decreased for d = 2mm and is not visible in case d = 1 and 0 mm respectively. For d = 2 mm, the penetration of the high energy source into the lower energy source can be clearly seen in Fig. 4.16 (b). A slight initiation of the plasma jet-let can also observed at d = 2 mm. However, in case of d = 1 and 0 mm (Fig. 4.16 (c-d)), the two sources have completely overlapped with each other, forming a single plasma source and the plasma has shrunk along the laser propagation axis because of their shifting towards the interaction zone.

Fig. 4.16 (e-h) shows the mass density evolution for equal source interaction. Similar to unequal sources interaction a plasma jet-let formation is initiated for d=4 mm (Fig. 4.15(e)). A secondary radial SW is observed at the interaction zone. A clear initiation of the plasma jet-let from the two sources can be observed for d=4 mm. However, for d=2 mm, the interaction of the two sources is initiated (Fig. 4.16(f)) and the jet-let is about to form. Similarly, the interpenetration of the two sources has been observed for d=1 and 0 mm respectively. However, it is noteworthy that the interpenetration/interaction of the two sources has been initiated only after 25  $\mu$ s, which is not observed up to 20  $\mu$ s. This is also confirmed from the plasma parameters presented in the previous section.

### 4.6 Conclusions

The confinement effects of a laser induced air plasma of nearly equal or higher density source on the plasma and shock parameters of a 50 mJ source were studied in detail. The dynamics of the interaction process due to the two laser plasma sources of equal and unequal energies, generated at different separation distances is studied over a duration of 30  $\mu$ s. The dynamics of shock – plasma and shock – shock interaction have revealed the interpenetration of the shock fronts across the stagnation layer/interaction zone. The evolution of mass density and pressure at the stagnation layer due to the SF interaction with the plasma core resulted in the enhancement of the plasma parameters. The stagnation layer formed in the case of unequal sources has allowed propagation of energy across the interaction zone. The transport of the stagnation layer is governed by the collisionality parameter and the pressure gradient. In the case of unequal energy sources, the relative velocity of the SF along S<sub>1</sub> (S2 $\rightarrow$ S1) is more due to higher pressure gradient for d = 1 and 2 mm. Hence, a shift of the stagnation layer toward S<sub>1</sub> is observed, while in the case of equal energy sources, a stationary hard stagnation layer is formed. A slight enhancement in plasma parameters for the 50 mJ source is observed because

of the interaction of the  $SF_2$  with the  $PC_1$  in both equal and unequal energy source. At the interaction zone the resultant pressure, density and the temperature increase is observed to be maximum in the case of d=1 mm in both equal and unequal source interaction. The ion–ion dynamics and conversion of kinetic energy to the thermal energy are observed to be the major processes leading to the enhanced parameters at the interaction zone. The numerical simulations were validated by the experimental observations via shadowgraphic imaging in case of d=4 mm and were simulated for the remaining separation distances. The pressure and temperatures generated at the stagnation layer were increasing with the decrease in the separation distance. However, not much variation in the plasma parameters were observed for d<4 mm. A plasma jet-let formation is observed for d=4 mm and unequal source interaction and an initiation of plasma jet-let in case of d=4 mm and equal source interaction over the considered time duration. For d<4 mm the higher energy source is penetrating through the source  $S_1$  and forming as a single source. However, in case of equal source interaction for d=1 and 2 mm, the two sources were stagnating over a duration of 20  $\mu$ s after which the two sources were interpenetrating with each other.

### 4.7 References

- 1. Yan, H., et al., Laser Energy Deposition in Intersecting Shocks. 2002.
- 2. Ghosh, S. and K. Mahesh, Numerical simulation of the fluid dynamic effects of laser energy deposition in air. Journal of Fluid Mechanics, 2008. **605**: p. 329-354.
- 3. Yan, H., et al., Laser Energy Deposition in Quiescent Air. AIAA Journal, 2003. 41(10): p. 1988-1995.
- 4. Leela, C., et al., *Dynamics of laser induced micro-shock waves and hot core plasma in quiescent air.* Laser and Particle Beams, 2013. **31**(2): p. 263-272.
- 5. Sai Shiva, S., et al., Numerical investigation of nanosecond laser induced plasma and shock wave dynamics from air using 2D hydrodynamic code. Physics of Plasmas, 2017. **24**(8): p. 083110.
- 6. Harilal, S., B. Brumfield, and M. Phillips, *Lifecycle of laser-produced air sparks*. Physics of Plasmas, 2015. **22**: p. 063301.
- 7. Sai Shiva, S., et al., Role of laser absorption and equation-of-state models on ns laser induced ablative plasma and shockwave dynamics in ambient air: Numerical and experimental investigations. Physics of Plasmas, 2019. **26**(7): p. 072108.
- 8. Rambo, P.W. and R.J. Procassini, *A comparison of kinetic and multifluid simulations of laser-produced colliding plasmas.* Physics of Plasmas, 1995. **2**(8): p. 3130-3145.
- 9. Rumsby, P.T., J.W.M. Paul, and M.M. Masoud, *Interactions between two colliding laser produced plasmas*. Plasma Physics, 1974. **16**(10): p. 969-975.
- 10.Davitt, S.J., et al., *Colliding laser plasmas formed in air*. Journal of Physics: Conference Series, 2019. **1289**: p. 012032.
- 11.Luna, H., K.D. Kavanagh, and J.T. Costello, *Study of a colliding laser-produced plasma by analysis of time- and space-resolved image spectra*. Journal of Applied Physics, 2007. **101**(3): p. 033302.
- 12. Dardis, J. and J.T. Costello, Stagnation layers at the collision front between two laser-induced plasmas: A study using time-resolved imaging and spectroscopy. Spectrochimica Acta Part B: Atomic Spectroscopy, 2010. **65**(8): p. 627-635.

- 13. Chenais-Popovics, C., et al., *Kinetic to thermal energy transfer and interpenetration in the collision of laser-produced plasmas.* Physics of Plasmas, 1997. **4**(1): p. 190-208.
- 14.Fryxell, B., et al., FLASH: An Adaptive Mesh Hydrodynamics Code for Modeling Astrophysical Thermonuclear Flashes. The Astrophysical Journal Supplement Series, 2000. 131(1): p. 273-334.
- 15. Raizer, Y.B.Z.d.a.Y.P., *Physics of Shock Waves and HighTemperature Hydrodynamic Phenomena.* 2012: (Dover Publications.
- 16. Yang, Z., et al., Experimental study of the behavior of two laser produced plasmas in air. Physics of Plasmas, 2015. **22**(7): p. 073511.
- 17. Mondal, A., et al., Spectroscopic investigation of stagnation region in laterally colliding plasmas: Dependence of ablating target material and plasma plume separation. Physics of Plasmas, 2019. **26**(2): p. 022102.
- 18. Kumar, B., et al., *Propagation dynamics of laterally colliding plasma plumes in laser-blow-off of thin film.* Physics of Plasmas, 2014. **21**(8): p. 083510.
- 19. Al-Shboul, K.F., et al., *Interpenetration and stagnation in colliding laser plasmas*. Physics of Plasmas, 2014. **21**(1): p. 013502.
- 20. Gupta, S.L., P.K. Pandey, and R.K. Thareja, *Dynamics of laser ablated colliding plumes*. Physics of Plasmas, 2013. **20**(1): p. 013511.
- 21. Sánchez-Aké, C., et al., *Analysis of two colliding laser-produced plasmas by emission spectroscopy and fast photography.* Spectrochimica Acta Part B: Atomic Spectroscopy, 2010. **65**(5): p. 401-408.
- 22. Ross, J.S., et al., Characterizing counter-streaming interpenetrating plasmas relevant to astrophysical collisionless shocks. Physics of Plasmas, 2012. **19**(5): p. 056501.
- 23. Zastrau, U., et al., *Tracking the density evolution in counter-propagating shock waves using imaging X-ray scattering.* Applied Physics Letters, 2016. **109**(3): p. 031108.
- 24. Guthikonda, N., et al., *Interaction of two counterpropagating laser induced plasmas and shock waves in air.* Physics of Plasmas, 2020. **27**(2): p. 023107.
- 25. Kameswari, D.P.S.L., et al., Investigation of stagnation layer dynamics of counterpropagating laser induced air plasmas: Numerical simulations vis-à-vis experimental observations. Physics of Plasmas, 2021. **28**(4): p. 043104.
- 26. Phuoc, T.X., Laser-induced spark ignition fundamental and applications. Optics and Lasers in Engineering, 2006. 44(5): p. 351-397.
- 27. Yeates, P. and E.T. Kennedy, *Spectroscopic, imaging, and probe diagnostics of laser plasma plumes expanding between confining surfaces.* Journal of Applied Physics, 2010. **108**(9): p. 093306.
- 28. Varvarezos, L., et al., The Effect of Confinement Angle on Self-Colliding Aluminium Laser Plasmas Using Spectrally Resolved Fast Imaging. Materials, 2020. 13(23): p. 5489.
- 29. Radziemski, L.J., From LASER to LIBS, the path of technology development. Spectrochimica Acta Part B: Atomic Spectroscopy, 2002. 57(7): p. 1109-1113.
- 30. Zavoiskii, E.K., *Collective interactions and the production of a high-temperature plasma*. Soviet Atomic Energy, 1963. **14**(1): p. 51-58.
- 31. Dittrich, T.R., et al., Review of indirect-drive ignition design options for the National Ignition Facility. Physics of Plasmas, 1999. **6**(5): p. 2164-2170.
- 32. Malka, V., et al., Laser-driven accelerators by colliding pulses injection: A review of simulation and experimental results. Physics of Plasmas, 2009. **16**(5): p. 056703.
- 33. Spicer, D.S., R.W. Clark, and S.P. Maran, A Model of the Pre-Sedov Expansion Phase of Supernova Remnant--Ambient Plasma Coupling and X-Ray Emission from SN 1987A. The Astrophysical Journal, 1990. 356: p. 549.
- 34. Smith, R.A., et al., Colliding Blast Waves Driven by the Interaction of a Short-Pulse Laser with a Gas of Atomic Clusters. Astrophysics and Space Science, 2007. **307**(1): p. 131-137.
- 35. Raga, A.C., et al., *The connection between laboratory and astrophysical jets.* AIP Conference Proceedings, 2005. **784**(1): p. 195-204.
- 36. Zel'dovich, Y.B. and Y.P. Raizer, *Physics of Shock Waves and HighTemperature Hydrodynamic Phenomena*. 2012: (Dover Publications).

#### Interaction of Two Counter Propagating Laser Induced Air Plasmas

- 37. DeMichelis, C., Laser induced gas breakdown: A bibliographical review. IEEE Journal of Quantum Electronics, 1969. **5**(4): p. 188-202.
- 38. Chen, Y.-L., J. Lewis, and C. Parigger, *Spatial and temporal pro" les of pulsed laser-induced air plasma emissions*. Journal of Quantitative Spectroscopy & Radiative Transfer, 2000. **67**: p. 91-103.
- 39. Cooper, P.W., Explosives engineering. 1996: Wiley-VCH.
- 40. Harilal, S.S., et al., *Charge-exchange collisions in interpenetrating laser-produced magnesium plasmas.* Laser and Particle Beams, 2001. **19**(1): p. 99-103.
- 41. Toro, E.F., Riemann Solvers and Numerical Methods for Fluid Dynamics: A Practical Introduction. 2009: Springer Berlin Heidelberg.
- 42. Harilal, S.S., et al., *On- and off-axis spectral emission features from laser-produced gas breakdown plasmas.* Physics of Plasmas, 2017. **24**(6): p. 063304.
- 43. Phipps, C., et al., *Review: Laser-Ablation Propulsion*. Journal of Propulsion and Power, 2010. **26**: p. 609-637.
- 44. Soubacq, S., et al., *Investigation of a gas breakdown process in a laser-plasma experiment.* Journal of Physics D: Applied Physics, 2004. **37**(19): p. 2686-2702.
- 45.Phuoc, T., Laser-induced spark for simultaneous ignition and fuel-to-air ratio measurements. Optics and Lasers in Engineering, 2006. 44: p. 520-534.

# Chapter -5

# Dynamics of Radially Confined Plasma and Shock Waves

This chapter deals with the evolution of laser induced air plasma confined along the radial direction (perpendicular to axial or the laser propagation direction) using a rectangular cavity of different materials (glass, aluminum, copper) whose acoustic impedance is much different than the medium where plasma is generated. A detailed study of the effect of spatial confinement on laser generated air plasma and shock waves (SW) for different laser intensities, confining cavity dimensions and confined material properties were presented. The dynamics of the plasma/SW in the confined geometry were quite interesting. The SW generated from the plasma expands adiabatically in the free ambient atmosphere, and reflects back when a boundary is placed in the expansion zone. The SW reflected from rectangular cavity walls interacts with the plasma and compresses the plasma radially which is resulting in an interesting changes in the dynamics and the physical parameters of the air plasma. Due to the radial compression, the air plasma expansion favor along the axial direction. As a result the plasma remain in the cavity for longer time. The exiting times of SW from cavity depends on the energy of the incident laser beam and length of the confining geometry. The mass density while exiting from the ends of the cavity forms a vortex around the corners of the cavity. The underlying physics of the SW reflection, SW interaction with the plasma, compressing and squeezing the plasma, exit of SW from the cavity ends, formation of cell like structures and formation of vortices that are happening within the confining geometry is explained. It is also observed that the compression of the air plasma by the SW is leading to a remarkable enhancement in the plasma parameters such as plasma temperature  $(T_c)$  and number density  $(N_c)$ . Hence, to understand this, a detailed study of all the physical processes such as, spatio – temporal evolution of plasma, SW, plasma parameters were presented in this chapter. The separation distance between the cavity walls is varied as d = 2, 4 and 8 mm for the three cavity materials glass, aluminum and copper to study the combined effect of the cavity dimensions and material on the plasma parameters. It is observed that the electrical conductivity of the cavity material is playing a role in the enhancement of plasma parameters for separation distance d = 2mm.

The enhancement in the plasma parameters is decreasing with the increase in the separation distance.

### 5.1 Introduction

The plasma produced in the ambient air expands freely into surrounding atmosphere. If this freely expanding plasma is obstructed by placing the walls of the medium, with appropriate material properties, then the expansion gets confined locally and the corresponding shock wave interacts with the walls of boundaries, reflects back. Depending on the geometry of the boundaries, the reflected SW can be made to interact with the plasma. Further, the presence of this physical barrier is seen to have its effects on the expansion of the plume and its lifetime due to the interaction of the reflected shock wave with the plume. It is expected that the reflection of the shock wave, back into the plasma medium, would prolong its effect on the plasma/medium and hence the disturbance created by shock wave in medium will last longer than what it would have been in the case of freely expanding shock wave. A detailed understanding of the effects of forward moving and the reflected shock waves on the lifetime of plasma would let us have greater control over the plasma dynamics [1]. Hence, the understanding of the propagation of the SW and its interaction with boundary occurring over longer times of few tens of microseconds is of considerable interest. A detailed understanding of the SW dynamics and plasma evolution gives a holistic view of the SW propagation through confined channels.

A range of studies related to the confinement of the plasma plume and the shock generated due to the rapid expansion of the plume have been reported [2-5]. These studies were proven to have a wide range of application such as, understanding of the explosions in gas/oil pipes [6, 7], flow of the fluids in capillaries i.e., microfluidics [8], aerodynamics and aero acoustics [9, 10]. In fields like aerospace, military, and transportation to mitigate blast or shock impact foam materials are placed in the lateral direction [11-15]. Surface cleaning based on the laser-induced shock wave generation can remove small particles from solid surfaces finds a good application in semiconductor industry for cleaning of contamination from the surface of the material [16, 17] and also find application in laser induced breakdown spectroscopy (LIBS) [18-20]. A numerous work has been done on the spectroscopic diagnostics of confined plasma [1, 5, 21-23], where the role of shape of confining geometry such as cylindrical [24-26], hemispherical [27, 28], and parallel wall cavity [29-33] were understood. A few studies were performed on comparison of plasma evolution with the target composed of few cavities on a

plane target [34]. These studies have provided shock wave evolution, and an enhancement in the electron temperature (T<sub>e</sub>), and number density (N<sub>e</sub>). However, a detailed insight into the physical process undergoing inside the cavity such as, interaction of SW with the core plasma, multiple SW reflections from the glass walls, squeezing of the plasma core by the SW generated after coalescence of primary and secondary reflected SWs were sparsely studied. Also, the effect of input laser energy on the SW dynamics and its influence on the enhancement in the plasma parameters, effect of separation distance between the cavity walls and material properties of the confining geometry were sparsely discussed. Hence, this chapter emphasizes mainly on the dimensions of the confining geometry suitable for the chosen incident laser energy and determining the material suitable for the confining cavity to increase the longevity of the plasma. It is noteworthy that an enhancement in the plasma parameters is such that the lifetime of the plasma has increased to 10 µs when compared to that of a freely expanding plasma. The details of the simulation domain, initial conditions were discussed in the following section.

### 5.1.1 Simulation details

The simulations were performed in a axi-symmetric geometry over a computational domain of 6×6 cm with a minimum mesh size of 30×30 µm along laser (Z) and radial (R) directions. Fig. 5.1 show the computational domain where two glass plates are placed opposite to each other parallel to the laser propagation direction in surrounding ambient air. The ambient air conditions are considered at normal temperature and pressure (NTP) with initial mass density of 1.3×10-3 g/cm<sup>3</sup>, temperature of 300 K and pressure of 0.1 MPa. The length of the cavity is fixed at 12 mm and the separation distance is varied to be 2, 4 and 8 mm respectively.

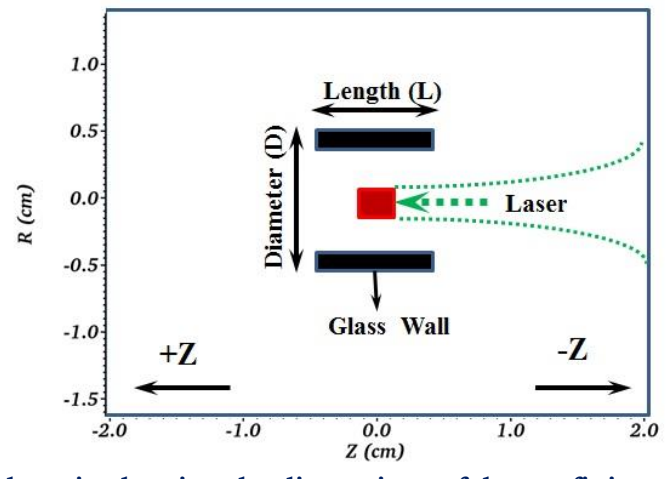


Fig. 5. 1 Simulation domain showing the dimensions of the confining geometry considered for simulations and focal point where laser energy deposition is taking place.

A laser beam is focused to a spot- diameter of 500  $\mu$ m at the centre of the cavity as shown in Fig. 5.1. The study has been performed for different input laser energies i.e., 50, 200 and 400 mJ. To focus the laser beam at the required position a small cylindrical domain whose size varied from 250×300  $\mu$ m (radius×length) to 250×900  $\mu$ m depending on the input laser energy is considered. [35, 36]. The temperature within this cylindrical domain is less than 0.5 eV and assumed to be pre – ionized such that the total energy within the volume exceeding the air breakdown threshold energy of 5 – 7 mJ.

# 5.2 Plasma and SW dynamics in confined geometry

The laser beam of energy 200 mJ is focused at the centre of the confining cavity interacts with the air medium at the focal region leading to generation of plasma which expands freely in all directions as shown in Fig. 3.7 of earlier chapter[37].

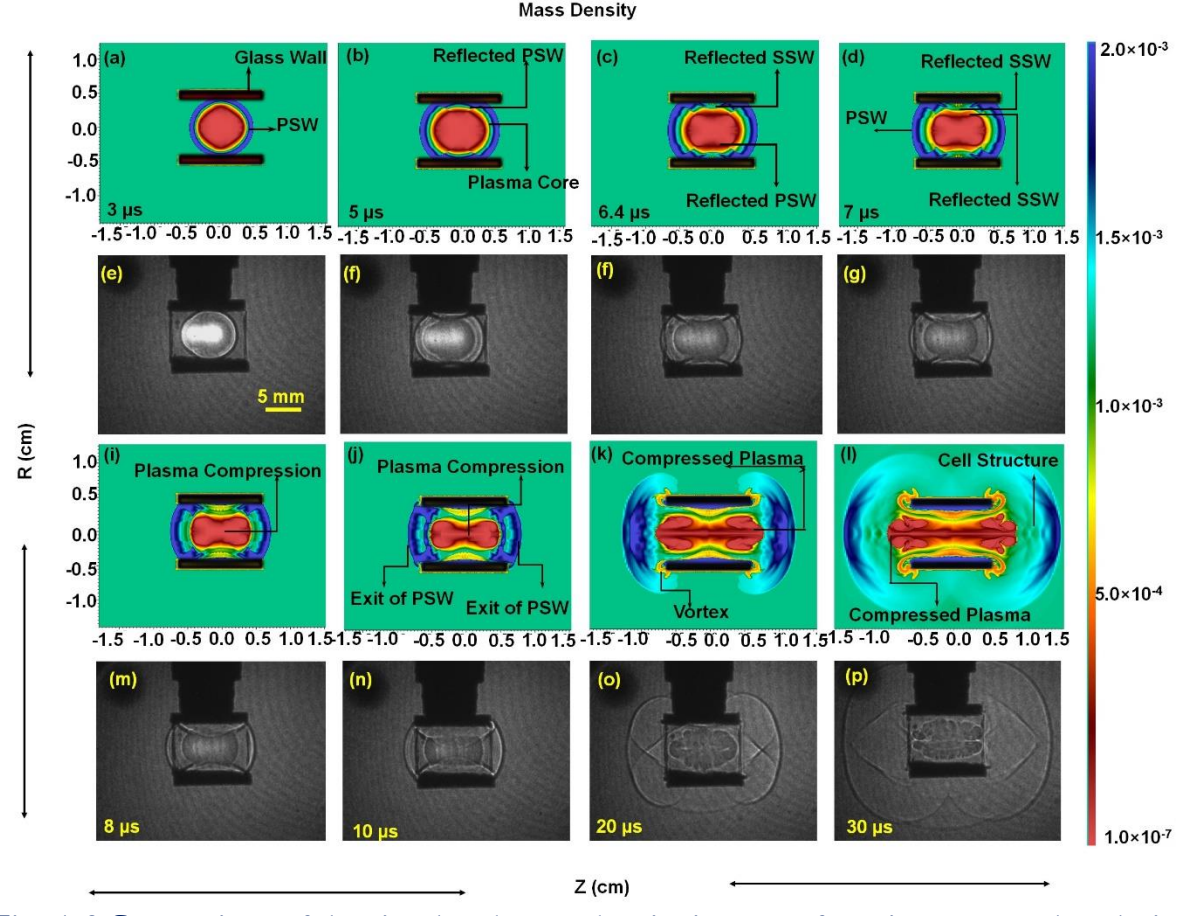


Fig. 5. 2 Comparison of the simulated mass density images of spatio - temporal evolution of SW ((a)-(d) & (i)-(j)) inside the glass cavity with experimental shadowgrams [38] ((e)-(h)) & ((m)-(p)) obtained at different time scales for the input laser energy of 200 mJ.

The shock wave initially travels with the air plasma and then detaches from the plasma when it is completely built and expands freely into the background gas leaving the plasma behind it. Fig.

5.2 (a-p) shows the dynamics of the SW generated using 200 mJ plasma source, confined inside the cavity of length 12 mm and diameter 8 mm. A comparison of the simulated mass density with the experimental shadowgram images is presented at different time scales. It is observed that the expanding SW reaches the glass wall at 2.8 µs and starts to reflect back after 3 µs and head towards the centre of the cavity (Fig. 5.2 (a, b) & (e, f)). In contrast to this, the primary shock wave (PSW) along the laser axis is observed to be expanding unaffectedly as there is no obstacle present ahead of it. The tails of the primary reflected SW on either ends were observed to be sliding along the length of the cavity as the SW advances. At 4 µs the interaction of the reflected SW with the plasma outer region (pre-ionized region) has been initiated. As the reflected primary SW (PSW) moves forward, towards the centre of the cavity, the PSW along the laser axis is expanding towards the ends of the glass cavity. The interaction of the reflected RSW with plasma outer region (POR) is initiated at 3.5 µs which results in the compression of the plasma and plasma reheating, this results in the generation of a secondary SW. At 6.4 µs the primary reflected SW is interacting with the plasma core (PC), resulting in the compression of the PC as shown in Fig. 5.2 (c) & (g). The secondary SW generated travel towards the glass wall and reflects back [38]. The secondary reflected SW is generated at 4.8 µs which also progresses towards the centre of PC.

At 7.2 µs the two radially reflected SWs start coalescing with each other leading to formation of a single SW. This is observed to occur almost up to 10 µs. As the two SWs interact with each other constructively, the strength of the resultant SW increases that leads to compression of the PC. A maximum compression of the plasma is observed during 8 – 9 µs because of the compression of the two reflected SW generated from either sides of the glass cavity (-Y & +Y directions) as can be observed in Fig. 5.2 (i) & (m). The resultant SW is reaching the centre of the SW at 9 µs. After 9 µs, the two SW from either sides (-Y & +Y directions) passes through the plasma, and transmit through each other in short duration such that they travel in the opposite directions [38] (+Y & -Y directions) with respect to each other. During this interpenetration a cell like structure is formed along the –Z & +Z directions expanding towards the ends of the cavity [39] as can be seen in the fig. 5.2 (k) & (o) at 20 µs. The cell structure also expands towards the –Z and +Z directions which further follows the PSW expanding in the free air as can be seen in Fig. 5.2 (l) & (p). A line plot of pressure and temporal evolution of SW is presented in Fig. 5.3 which explains reflection of the PSW, SSW, interaction of the two SWs and their combined effect on the PC.

At 10 µs, the exit of the PSW is observed from either ends of the cavity. The SW while exiting from the cavity curls forming a vortex [39, 40] due to abrupt change in the mass density and pressure between plasma/SW and ambient air. This vortex formation has taken place due to the existence of the pressure gradient between cavity inside and outside regions [40] as can be observed at 20 µs. Hence, four vortices were observed at the corners of the cavity. The two reflected SWs along –Y & +Y directions interacting at the PC interpenetrate with each other and traverse towards the cavity wall of opposite direction.

# 5.2.1 Internal dynamics during SW reflection

A lineplot of pressure is presented in Fig. 5.3 which explains the temporal evolution of SW, reflection of the PSW, SSW, interaction of the two SWs and their combined effect on the PC.

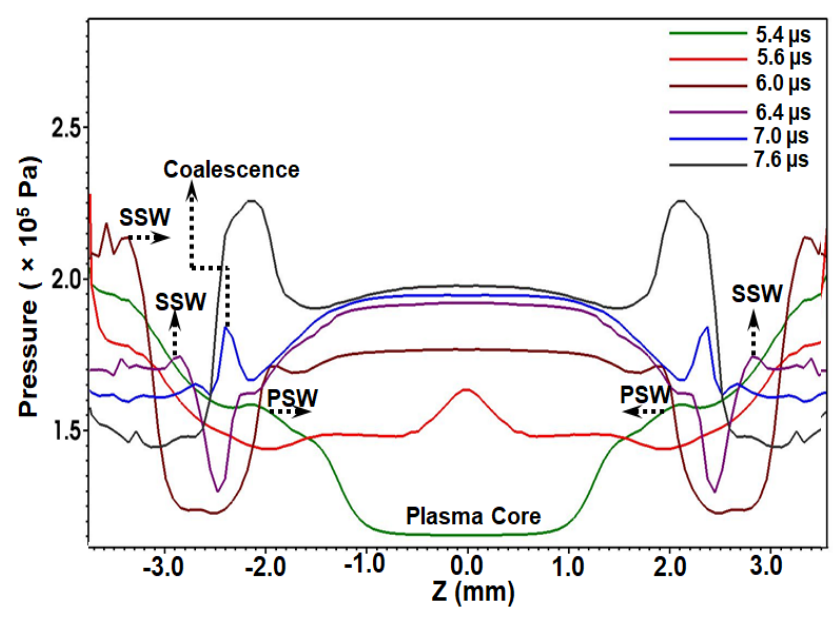


Fig. 5. 3 Line plot of plasma pressure along the radial axis showing pressure variation at the shock front and plasma core for input energy of 200 mJ

The pressure of both the primary reflected shock wave (RSW) and the plasma core (PC) before interacting with each other (4 µs) were found to be 3.50 × 10<sup>5</sup> Pa and 1.13 × 10<sup>5</sup> Pa respectively. After the reflection from the walls, the SW heads towards the PC, at 6 µs the SF pressure has decreased to 1.60 × 10<sup>5</sup> Pa whereas the pressure at the PC increases to 1.64× 10<sup>5</sup> Pa because of the compression induced by the advancement of the SW. At 4.8 µs a secondary RSW is observed to be launched. The pressure of this secondary RSW at 6 µs is observed to be 2.42 × 10<sup>5</sup> Pa which is lower than the primary RSW. An energy transfer between SW and PC has taken place during the interaction. The SW with high pressure interacts with the PC and squeezes resulting in a raise in the pressure at the PC, and a simultaneous fall in pressure at the shock front (SF). At 6.4 µs the pressure at the primary reflected SF and PC has slightly increased to

 $1.66 \times 10^5$  Pa and  $1.72 \times 10^5$  Pa respectively, because of the compression induced by the secondary RSW. At 7 µs the secondary RSW approaches closer to the primary RSW with a pressure nearly equal to that of the primary RSW i.e.,  $1.70 \times 10^5$  Pa whereas, the pressure at the PC has increased to  $1.80 \times 10^5$  Pa. The primary SW continues to reflect back slightly at 7.2 µs the two SWs i.e., primary RSW and the secondary RSW coalesce with each other forming single strong SW. This leads to increase in the pressure at the SF to  $1.82 \times 10^5$  Pa as well as at the PC to  $1.96 \times 10^5$  Pa due to the compression by the coalesced SW. It is also observed that the strength at the coalesced SF increasing with time because of the continuous interaction between the two counter propagating RSWs. As expected the resultant SW pressure is observed to be greater than the sum of the pressures at the two RSWs before interaction i.e., greater than 3.40  $\times$  10<sup>5</sup> Pa [41, 42]. However, the pressure at the SF has increased to 3.45 $\times$  10<sup>5</sup> Pa at 9.7 µs. The two reflected SW from either side reach the centre of the PC hence, at this time PC is compressed to the maximum after which the PC has started expand. During the interaction time of RSW with the plasma outer region to the maximum compression time of PC, a raise in the electron temperature and number density of the plasma were observed as the plasma is compressed during these times. The effect of primary RSW, coalesced strong SW on electron temperature and number density of the plasma were presented in detail in sub-section 5.2.2

# 5.2.2 Electron Temperature and Electron Number Density

The temporal evolution of electron temperature ( $T_e$ ) and number density ( $n_e$ ) of the plasma starting from the initial laser-matter interaction times up to 20  $\mu$ s is compared between freely expanding and confined plasmas (Fig. 5.4 (a & b)) for input laser energy of 200 mJ .

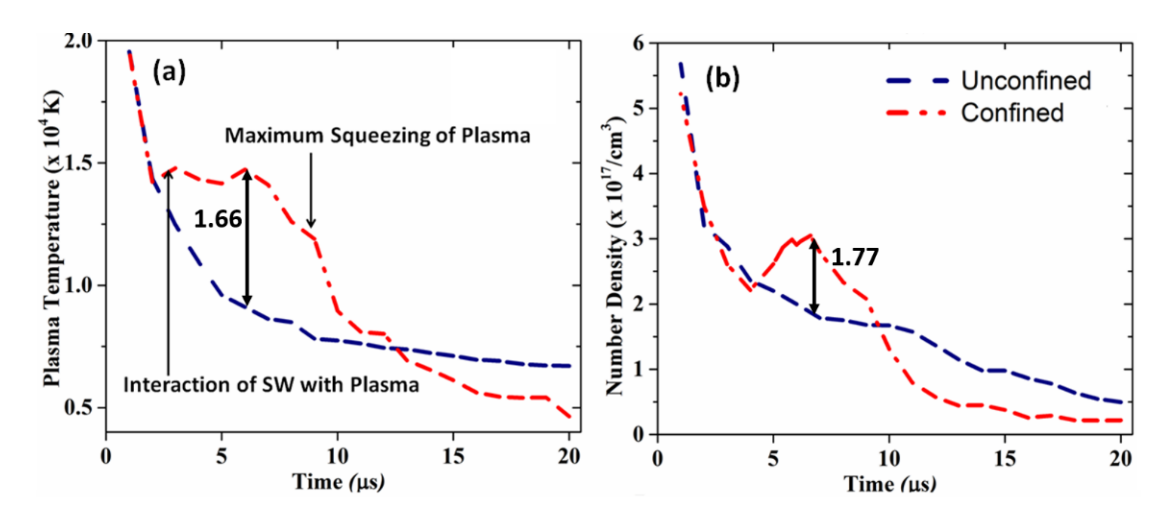


Fig. 5. 4 Comparison of temporal evolution of (a) electron temperature and (b) number density of plasma along radial direction with and without glass confinement for 200 mJ

The electron temperature and number density follow a similar trend as that of free expanding plasma until the RSW started interacting with the outer region of plasma at 4 µs. Due to this a sudden raise in temperature is observed as can be clearly seen from Fig. 5.4 (a). The electron temperature in the cavity has increased [2, 43-45] to  $1.47 \times 10^4$  K which is 1.33 times greater than that of free expansion in air  $(0.75 \times 10^4 \, \text{K})$ . However, no effect is observed in the electron number density. When the RSW is interacting with the PC i.e., at 6.4 µs the electron temperature ( $T_e$ ) has further increased to 1.49  $\times$  10<sup>4</sup> K which is 1.63 times higher than the free expansion in air. A raise in number density (Ne) [44] is observed at 6.6 µs. The raise in Ne is  $(3.05 \times 10^{17} \text{ /cm}^3) 1.79 \text{ times higher than the freely expanding plasma } (1.60 \times 10^{17} \text{ /cm}^3). \text{ The}$ RSW upon interaction is compressing the plasma, resulting in an increase in the kinetic energy of the electrons because of the increased collisions between the electrons and the surrounding electrons and ions existing at the plasma. The raised kinetic energy is efficiently converted into thermal energy (greater than the statistical error in calculating the temperature i.e., > 2600 K) as a result raise in temperature is observed. The pressure at the shock front (SF) is more when compared to that existing at the PC as discussed in the above section. The SF is able to advance through the plasma because of the pressure gradient existing between the SF and PC. The compression of the PC by the coalesced SW (primary RSW and secondary RSW) has resulted in the increase of number density because of the increased pressure along radial direction. However, after few microseconds as the coalesced SW from -R and +R directions is approaching towards R = 0, the compression of the plasma has resulted in the expelling of the density along the laser propagation axis resulting in the decrease of the number density along Z=0 plane. A schematic of the process taking place during the interaction of the radial SW with the PC is shown in Fig. 5.5 for a better understanding of the physical process. This has resulted in the formation of the cell structure along the laser propagation axis, which can be observed in Fig. 5.2 (1 &p). This formation of the cell structure (a secondary wave) is similar to the secondary radial SW that is observed in chapter – 4 (Fig. 4.2 (d) & (j)) when two plasma sources were interacting along the laser propagation axis. However, as the SW is freely expanding along the radial direction in that case a spherical SF is observed. However, in the present case, the presence of the cavity walls has resulted in the confinement of the expanding SW resulting in the formation of a cell like structure.

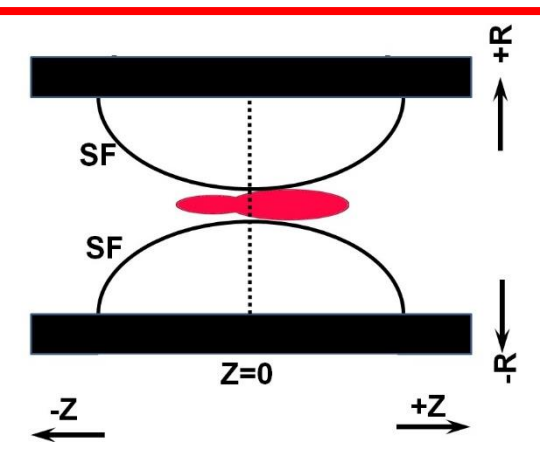


Fig. 5. 5 A schematic showing the interaction of the reflected radial SW with the PC along the Z=0 plane

After 6.6  $\mu$ s, the plasma parameters both  $T_e$  and  $N_e$  were decreasing as the plasma is being squeezed along the radial direction. As a result more elongation is observed along the laser axis (axial direction) which leads to a fall in plasma parameters.

At 9  $\mu$ s the two SWs reflected from both ends of the cavity have reached the centre of the PC and in due course of time they transmit through each other and travel in the opposite directions with respect to each other. During the expansion of these two RSWs the plasma left behind the SWs starts to expand leading to a decrease in  $T_e$  and  $N_e$  of the plasma. The plasma at latter times undergoes a sequential expansions and contractions due to the expanding and reflecting SWs. If the energy of the input laser increases then the strength of the SW increases which leads to the generation of a strong RSW and more compression of the plasma and it is expected that the enhancement in the plasma parameters will be more pronounced. Hence it would be interesting to determine the effect/role of input laser energy on the enhancement in the plasma parameters. These details were discussed in the following section.

# 5.3 Effect of laser energy on SW and plasma dynamics

An increase in the input laser energy leads to an increment in the shock velocity [46, 47] however, the increment in radius is not as prominent as it is observed along the laser propagation direction. This is because of increase in asymmetric expansion of plasma and SW along the laser direction with respect to increase in the input laser energy [47, 48]. The strength of the SW i.e., velocity, pressure accumulated at the SF, and temperature at the PC also increases along the radial direction. Hence, to study the effect of input laser energy on plasma and SW dynamics generated inside the confined rectilinear cavity of length (L) 12 mm and diameter (D) 8 mm were carried out for three laser energies 50, 200 and 400 mJ, respectively

with the spot size of 500  $\mu$ m and excitation wavelength of 532 nm. Since, the dimensions of the cavity is same for all the three energies considered, the SW generated with the higher energy reaches the glass boundary early when compared to lower energy case. Fig. 5.6 (a) –(i) shows a comparison of evolution of mass density for the sources generated using 50, 200 and 400 mJ, spatially confined by a cavity of length 12 mm and separation distance d = 8 mm.

Fig. 5.6 (a) - (i) shows a clear variation of the mass density with respect to the incident laser energy at different time scales. Fig. 5.6 (a-c) shows the mass density evolution at 5  $\mu$ s for the three input laser energies 50, 200 and 400 mJ respectively. It can be observed that the 50 mJ has just started to interact with the cavity walls (Fig. 5.6 (a)). Fig. 5.6 (b) shows the mass density evolution of a 200 mJ source. It is discussed in the previous sections that the radial SW of the 200 mJ source is interacting with the cavity wall at 3  $\mu$ s and reflecting back, interacting with the plasma outer region between 3.5 - 6.4  $\mu$ s. It can be confirmed from Fig. 5.6 (b) that the radial SW is interacting with the POR. While the 400 mJ is being compressed by the primary RSW as can be seen in Fig. 5.6 (c) and an initiation of a secondary RSW can also be observed.

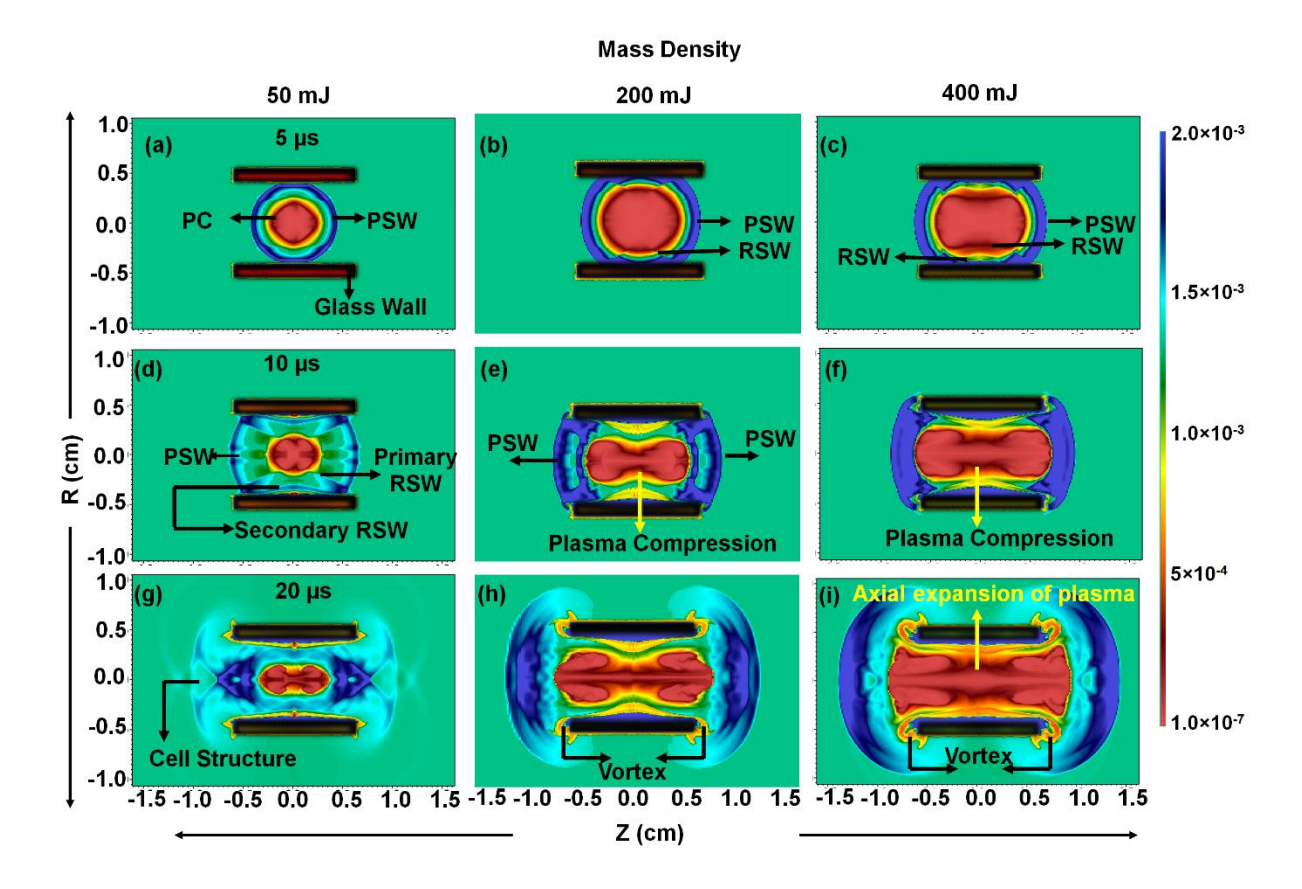


Fig. 5. 6 Spatial evolution of mass density of the source that is generated using 50, 200 and 400 mJ at (a) 5, (b) 10 and 20 us respectively when confined in a cavity of L = 12 mm and d = 8 mm

Fig. 5.6 (d) - (f) shows the mass density evolution of the three sources in the confined geometry at 10 μs. An initiation of the interaction of the primary RSW and a clear initiation of the secondary RSW can be observed in the 50 mJ source (Fig. 5.6 (d)). While, the primary SW along the laser propagation axis is expanding unaffectedly. In Fig. 5.6 (e), a maximum compression of the 200 mJ plasma source along the radial direction due to the RSW from –R and +R directions. While the 400 mJ (Fig. 5.6 (f)) has started to expand along the axial direction and relaxation along the radial direction.

A clear expansion of the plasma along the laser propagation axis due to the compression along the radial direction at 20 μs from the three sources can be observed in Fig. 5.6 (g) - (i). It is to be observed in the 50 mJ source that the effective expansion of the PC along the laser propagation axis is less when compared to that of the higher energy sources 200 and 400 mJ. This is observed because of the lower shock strength while interacting with the PC. It can be observed in Fig. 5.6 (a) & (d) that the initiation of the reflection of SW from the cavity walls (4.5 μs), interaction with the PC at longer time scales by which the pressure, density at the SF decreased. Formation of a cell like structure in the 50 mJ source is clearly visible at 20 μs. This is observed because of the interpenetration of the radial SWs at the PC and expanding towards the opposite direction and also along the laser propagation axis. The mass density while expanding and exiting from the cavity forms vortices at the corners of the cavity due to the pressure and mass density gradients existing in and outside of the cavity. The formation of the vortices can be clearly observed at 20 μs in all the three expanding sources (Fig. 5.6 (g)-(i)). A clear explanation of the expansion of the radial SW in all the three energy sources is discussed in Fig. 5.7 (a)-(c).

For convenience, the centre of the PC (or the laser focusing point) is considered as the origin, hence the distance from the origin to cavity wall is 4 mm. The generated primary SW travel up to the glass wall (4 mm), and reflect back from there and again travel towards the origin. Fig. 5.7(a) shows the comparison of numerically simulated SW evolution before hitting the wall and after reflection from the wall for the input energy of 50 mJ with the experiments. It is observed that the freely expanding SW reaches the glass wall at 4.6 µs for 50 mJ, whereas for 200 mJ at 2.8 µs (Fig. 5.7(b)) and for 400 mJ at 1.8 µs (Fig. 5.7 (c)) respectively, then reflecting back after few hundreds of nano-seconds. It is obvious that as the laser energy (intensity) decreases, the energy/strength with which the SW hitting the wall and its reflection from the wall becomes very less. Hence, the effect of the reflected SW on the plasma is less prominent

when compared to that of higher energy sources. Thus, a prominent change in the shock radius is not observed with 50 mJ (5.6(a)) after coalescence of primary RSW and secondary RSW compared to that of 200 and 400 mJ cases.

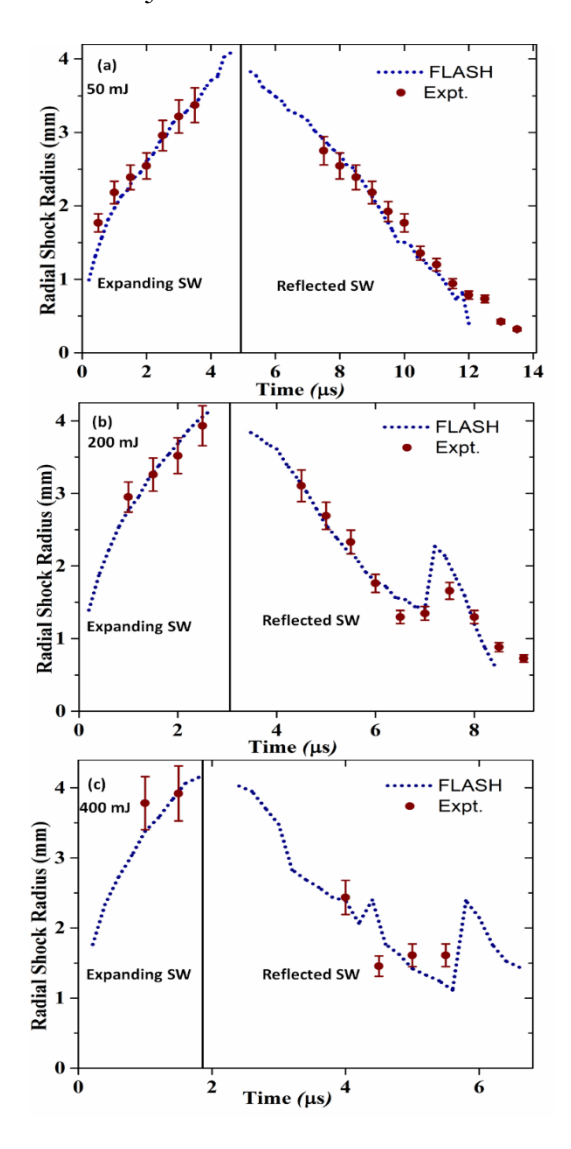


Fig. 5. 7 Temporal variation of shock radius in the radial direction for (a) 50, (b) 200 and (c) 400 mJ respectively within a confining cavity of length 12 mm and diameter 8 mm (Vertical line indicates the time of SW interacting with the glass boundary)

Fig. 5.7(b) compares the SW evolution for 200 mJ. It is clearly visible that the SW reaching the glass wall at 2.8 μs, interacts with glass wall for some time, reflecting back after 3 μs and expanding towards the centre of the PC where a smooth fall in radius is observed up to 7.2 μs. At times between 7.2 - 7.8 μs, a raise in the shock radius is observed which means that the SW has reflected back by 0.5 mm after which a fall in shock radius observed. This is observed because of high pressure, energy that were created at the PC due to compression. At later time scale, a secondary RSW is interacting with the primary RSW. The two reflected SWs were

coalescing with each other resulting in the increase in the strength of the RSW (explained in Fig. 5.3). Thus the reflected and coalesced SW (RSW) is compressing the plasma and reaching the centre of the PC at  $9~\mu s$ .

A similar phenomenon is also observed in the case of 400 mJ as shown in Fig. 5.6 (c). The freely expanding primary SW is reaching the wall by 1.8 μs, interacting with the wall and a strong RSW is observed after 2.4 μs. The primary RSW which is expanding towards the centre of the PC is slightly reflected back by 1 mm between 5.6 – 7 μs and reached the centre of the PC by 7 μs due to combined effect of primary and secondary RSWs. Hence, it is clearly understood that the SW is reaching the centre of the PC by 14, 9, 7 μs for 50, 200 and 400 mJ respectively. A temporal evolution study of plasma parameters clearly explains the effect of input laser energy on the enhancement which is explained in the following sub-section 5.3.1

# 5.3.1 Electron temperature and number density

The temporal evolution of plasma temperature and number density with respect to input laser energy is presented in Fig. 5.8 (a-c) and Fig. 5.8 (d-f), respectively. The evolution of the plasma parameters in the confined geometry is similar to that in the unconfined geometry till the RSW interacts with the plasma/PC.

In Fig. 5.8 (a) for 50 mJ the primary RSW is interacting with plasma at 6 μs so, maximum raise in temperature from 5426 K to 7000 K is observed which is 1.29 times higher than the unconfined geometry. Due to cooling of the rapidly expanding plasma, its temperature dropped down below 1 eV (11605 K). Hence, the plasma can now be treated as a hot air (as there are very small fraction of ionized species available) which is consisting of dissociated molecular species existing in the excited states [35, 48-50]. A maximum raise in temperature is also observed at 14 μs due to the SFs from either side of the plasma were reaching the center of the PC (maximum squeezing of the hot air) is observed. The enhancement in the plasma temperature is 1.25 times when compared to unconfined geometry. In line with the temperature, a similar trend is also observed in number density however, a maximum enhancement of 3.35 is observed at 12 μs as can be seen in Fig. 5.8 (d). It is to be noted that the increase in the temperature is initiated at 3.5 μs, whereas the increase in the number density is observed after 5 μs. It is a known fact that the increase in temperature leads to an increase in the generation of number of free electrons. Hence, a time lag is observed between the increase in the temperature and number density. It is observed that the secondary RSW coalesce with

the primary RSW at 12.8  $\mu$ s and combined SW compressing the hot air. Later on after 14  $\mu$ s, the two SWs from either side of plasma are transmitted through each other due to which the plasma is splitting along the radial direction and expanding along the axial direction. This is leading to a sudden decrease in the number density along radial direction. A decrement in electron temperature is observed after 16  $\mu$ s for 50 mJ, 12  $\mu$ s for 200 mJ and 15  $\mu$ s for 400 mJ because of the free expansion of the hot air with the expanding RSWs.

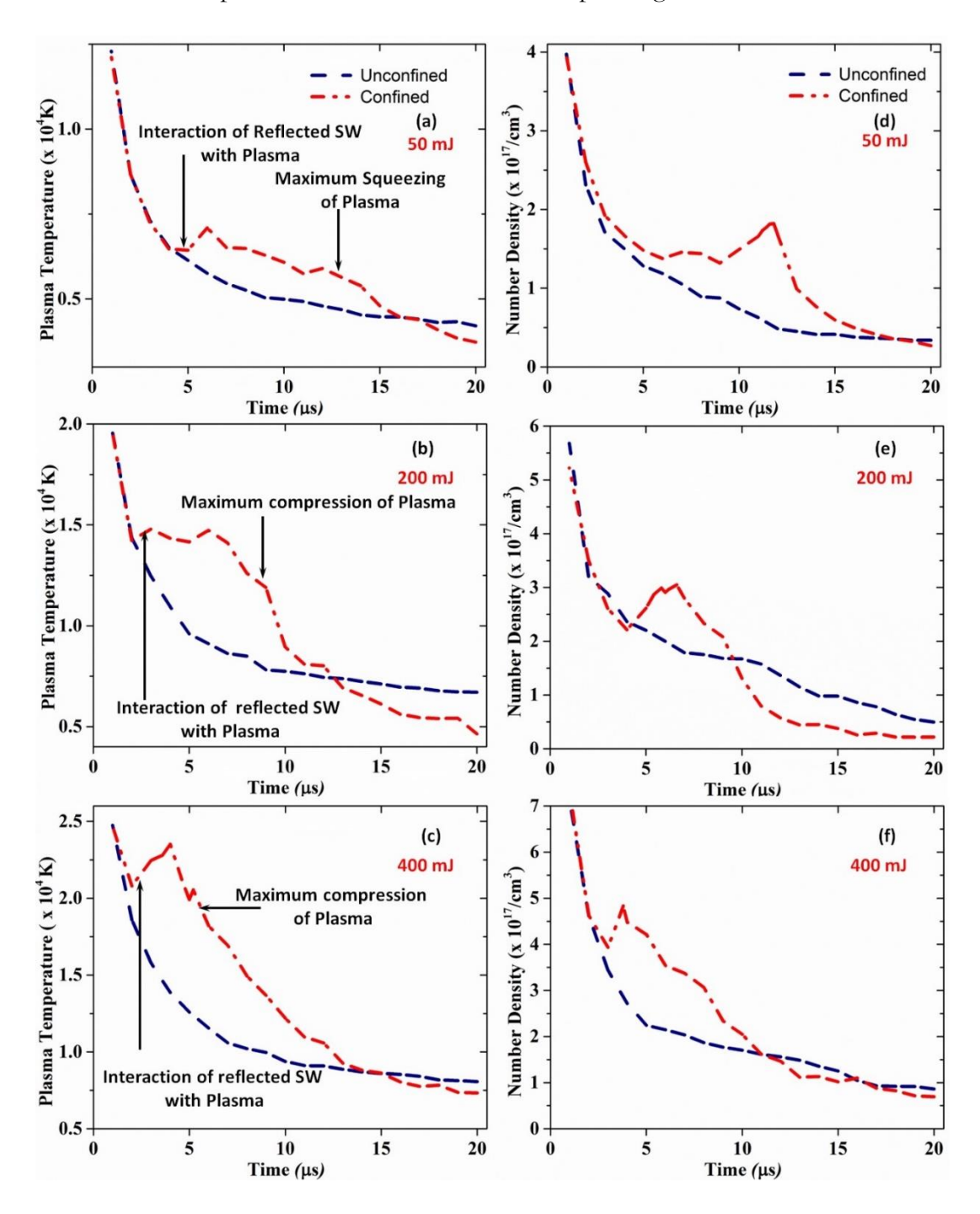


Fig. 5. 8 Temporal evolution of electron temperature (a-c) and number density (d-f) for input laser energies of 50, 200 and 400 mJ

In Fig. 5.8 (c & f) for 400 mJ, because of increase in the laser energy absorption, the SW strength increases, hence quickly reaches the glass wall by 1.8 μs. A strong SW is observed after reflection at 2.4 μs. The RSW is interacting with plasma at 3 μs after which maximum raise in temperature of 2.3×10<sup>4</sup> is observed at 5 μs (Fig. 5.8(c)) which is 1.91 times higher than freely expanding plasma. This is observed when the primary RSW is interacting with the PC. At 7 μs a maximum squeezing occurs as the two SWs from either side of the plasma reaching the centre of the PC. Similarly, a maximum enhancement of 1.92 is observed in the number density as can be seen in Fig. 5.8 (f).

The maximum enhancement factor of Te is observed to be 1.16, 1.66 and 1.91 for the laser energies of 50, 200 and 400 mJ, respectively at 14, 10 and 5 µs from t=0. The time of maximum squeezing point is delayed for lower energy compared to higher energy SW evolution because of low initial velocity. However, the enhancement in number density is observed to decrease with the increasing laser energy. A slight increase in the enhancement in the number density from 200 mJ to 400 mJ is observed. However, the variation in the enhancement is under the calculated statistical error. A similar trend is proposed by Hayat et. al [44] where lateral confinement of laser ablative plasma from a Magnesium target is presented for different fluences and by Atiqa et. al. [51] where magnetic confinement of the laser ablative plasma from a graphite target is discussed.

As discussed earlier, the increase in the input laser energy leads to an increment in the pressure of the SW. However, the increment in shock pressure along radial direction is not much significant when compared to that obtained along the axial direction. This is due to most of the laser energy deposition taking place along the laser propagation axis (mostly in the direction opposite to the laser propagation direction), which leads to an asymmetric expansion of plasma and SW. By the time of the SW interaction with the PC is initiated, the pressure at the PC almost reaches the ambient atmospheric pressure. Hence, a slight compression by SW is leading to a maximum enhancement in number density. The pressure gradient between the reflected SW and PC in case of 200 mJ is not much prominent and hence enhancement in the number density due to SW compression is small when compared to 50 mJ. The density gradient between the PC and SW is high during the time of interaction. This happens because of the interaction during the early time scales, which has led to an effective enhancement in the number density.

Table. 5.1 Variation of enhancement factor in electron temperature (Te) and number density (Ne) showing the time at which the maximum enhancement in the parameter is taking place

Input Laser Energy	Time	Enhancement	Time	Enhancement
(mJ)	(µs)	Factor in Te	(µs)	Factor in Ne
50	13	1.16	14	3.60
200	10	1.66	10	1.77
400	10	1.91	9	1.92

This concludes that a maximum enhancement in the temperature is observed with increasing energy. Table 5.1 gives an over view of the variation of enhancement factor in plasma temperature (T<sub>e</sub>) and number density (N<sub>e</sub>), for energies 50, 200 and 400 mJ, respectively with respect to the evolution in unconfined medium.

It is a known fact that the pressure and density across the SF are high during the initial time scales (up to 1 µs) [52, 53]. If the diameter is reduced keeping the energy fixed, then the SW reaches the glass wall earlier and a more strong reflection is expected leading to a more enhancement in the electron temperature. Hence, the effect of separation distance between the walls of the confining geometry is discussed in the following section.

# 5.4 Effect of separation distance and material of confining geometry on SW and plasma dynamics

To study the effect of the cavity dimensions on the plasma parameters, the separation distance between the cavity walls is varied over d= 2, 4 and 8 mm respectively and the cavity material is also changed for all the separation distances. The cavity materials chosen were glass, aluminum and copper. The equation of state (EoS) of the three materials (glass. Aluminum and copper) were generated by Sai Shiva et. al. [54] by making the necessary changes to the IONMIX code by Mac Farlane et.al [55]. Hence a combined effect of the separation distance, "d" and the cavity material is studied in the present section. Fig. 5.9 (a) - (i) shows a comparison of the spatial variation of electron temperature with respect to confining cavity dimensions and cavity material at 0.2 µs for the input laser energy of 200 mJ.

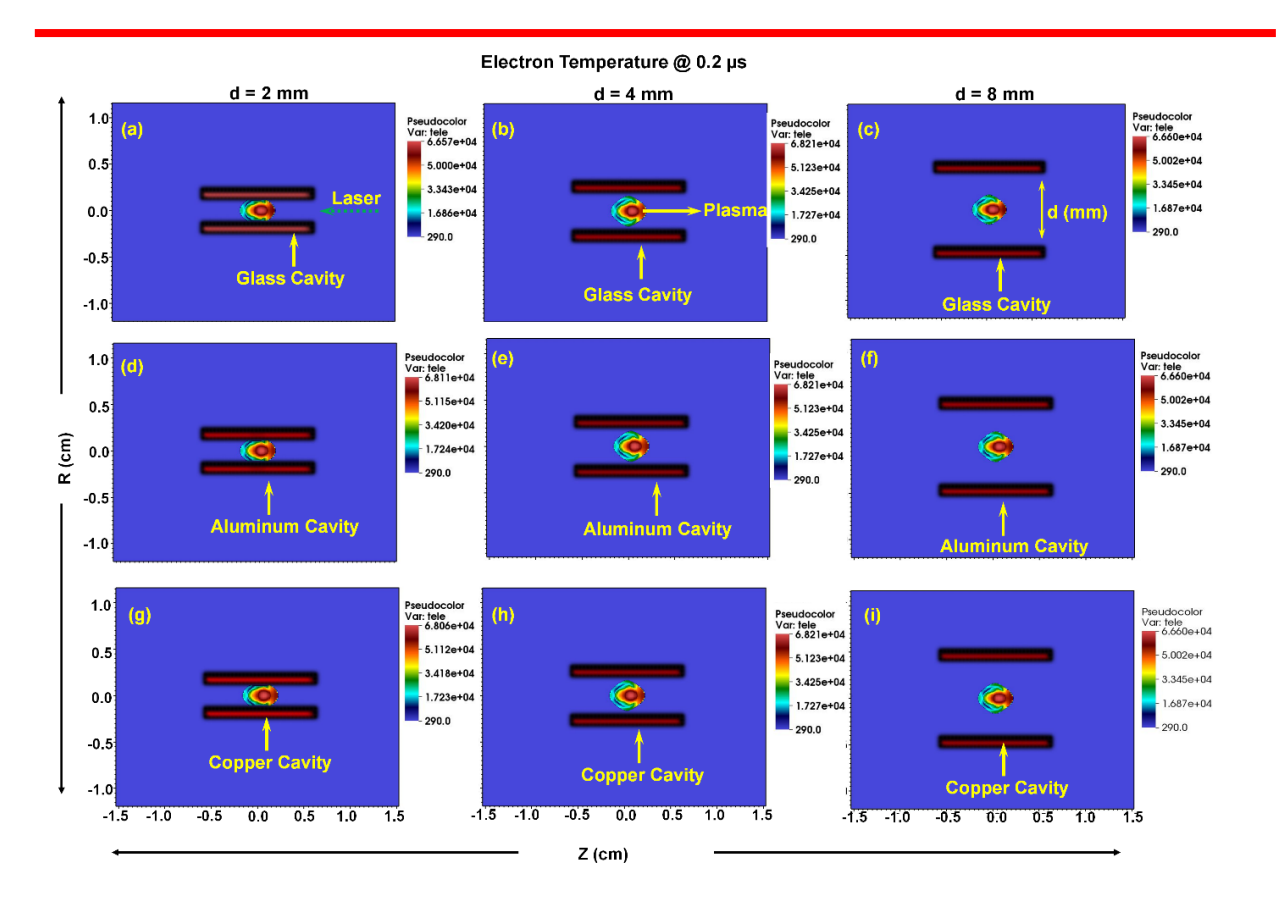


Fig. 5. 9 Comparison of the spatial variation of the electron temperature confined using (a -c) glass cavity, (d -f) aluminum cavity and (g -i) copper cavity with separation distances d = 2, 4 and 8 mm respectively at 0.2  $\mu$ s for the input laser energy of 200 mJ.

For separation distance d = 2 mm, it can be observed from Fig. 5.9 (a), (d) and (g) the interaction of the plasma with the cavity walls is initiated in all the three cavities (glass, aluminum and copper). It is to be noted that the plasma is interacting with the cavity, but not the SW. Hence, it is to be noted that the plasma with number of free electrons is interacting with the cavity wall. Hence, the electrical conductivity of the cavity material plays a role in the enhancement in the plasma parameters. However, since the interaction of the plasma with the cavity walls is just initiated, the plasma temperature is almost the same i.e.,  $6.8 \times 10^4$  K, for all the three cavities (glass, aluminum and copper).

For the separation distance d = 4 mm (Fig. 5.9 (b), (e) and (h)) the plasma is still approaching the cavity walls. While for d = 8 mm (Fig. 5.9 (c), (f) and (i)), the plasma is still far away from the cavity walls. Hence, the evolution of the plasma is still unaffected by the presence of the cavity. Hence, the temperature existing at the plasma and its expansion is similar to a 200 mJ plasma source freely expanding in ambient gas. The spatial variation of the electron temperature for the three separation distances d = 2, 4 and 8 mm inside the three cavities at 1  $\mu$ s is shown in Fig. 5.10 (a) - (i).

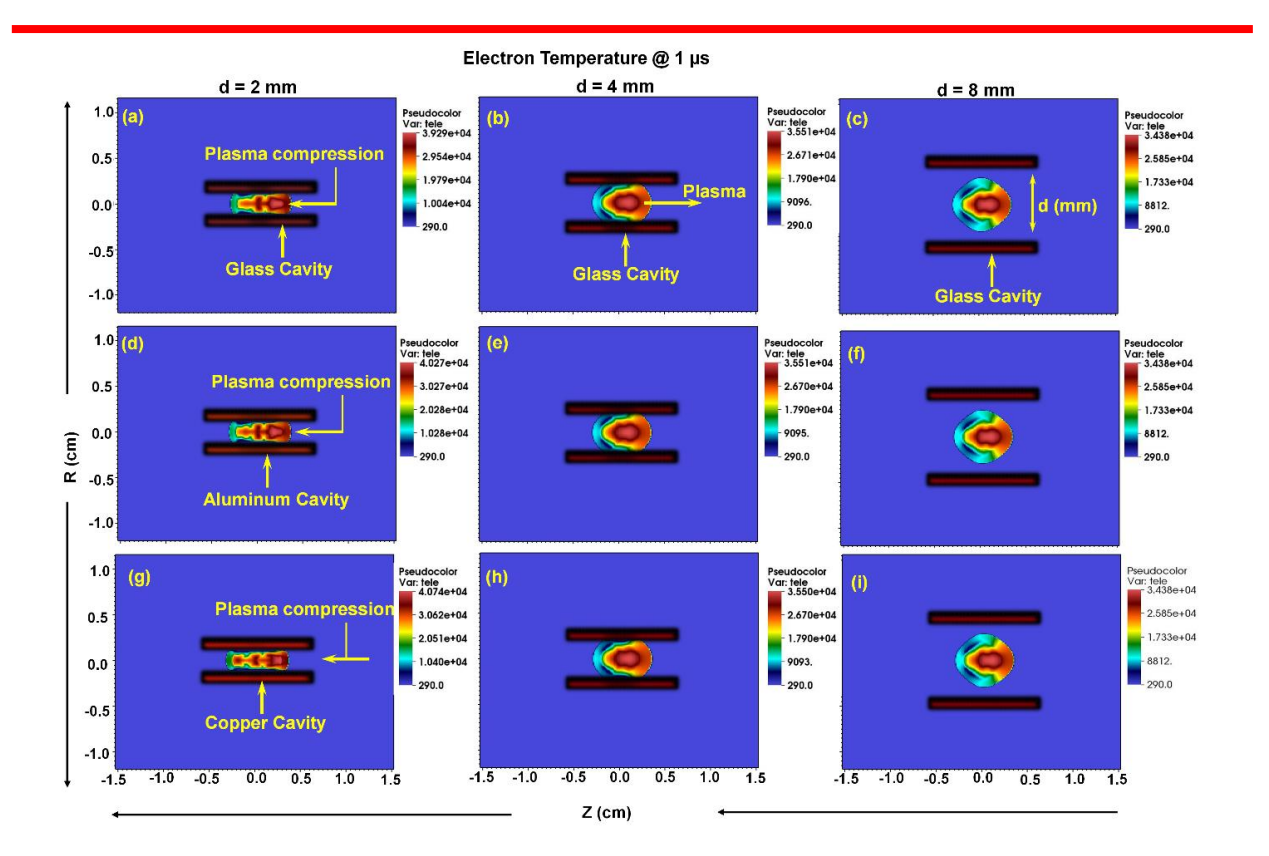


Fig. 5. 10 Comparison of the spatial variation of the electron temperature confined using (a -c) glass cavity, (d -f) aluminum cavity and (g -i) copper cavity with separation distances d = 2, 4 and 8 mm respectively at 1  $\mu$ s for the input laser energy of 200 mJ.

For the separation distance d = 2 mm, the interaction of the plasma with the cavity is initiated at 0.2  $\mu$ s. The plasma outer region (POR) is reflecting from the cavity walls towards the PC. The reflected POR is interacting with the PC and compressing the PC. The compression of the PC along the radial direction has resulted in the expansion of the PC along the laser propagation axis. The expanding plasma is sliding along the cavity walls as can be seen in Fig. 5.10 (a), (d) and (g).

However, for the separation distance d = 4 mm, the POR has just started to reflect from the cavity walls Hence, no much variation in the plasma temperature is observed. However, the peak temperature existing at the PC is slightly less when compared to that existing at the PC for d = 2 mm ( $\sim 3.95 \times 10^4 - 4.0 \times 10^4$  K for d = 2 mm and  $3.55 \times 10^4$  K for d = 4 mm). The variation is greater than the statistical error in determining the temperature ( $0.27 \times 10^4$  K, discussed (Fig. 5.10 (b), (e) and (h)) in Chapter-2).

Fig. 5.10 (c), (f) and (i) shows that the plasma is still approaching the cavity walls, hence not effected by the presence of the cavity of any material. The plasma is still expanding freely. The peak temperature existing at the PC is  $3.45 \times 10^4$  K which is less than that existing at the PC

for d = 2 mm. Fig. 5.11 (a) - (i) shows the spatial variation of the electron temperature at 5  $\mu$ s, with respect to the separation distance d = 2, 4 and 8 respectively and confining material glass, aluminium and copper respectively, for the input laser energy of 200 mJ.

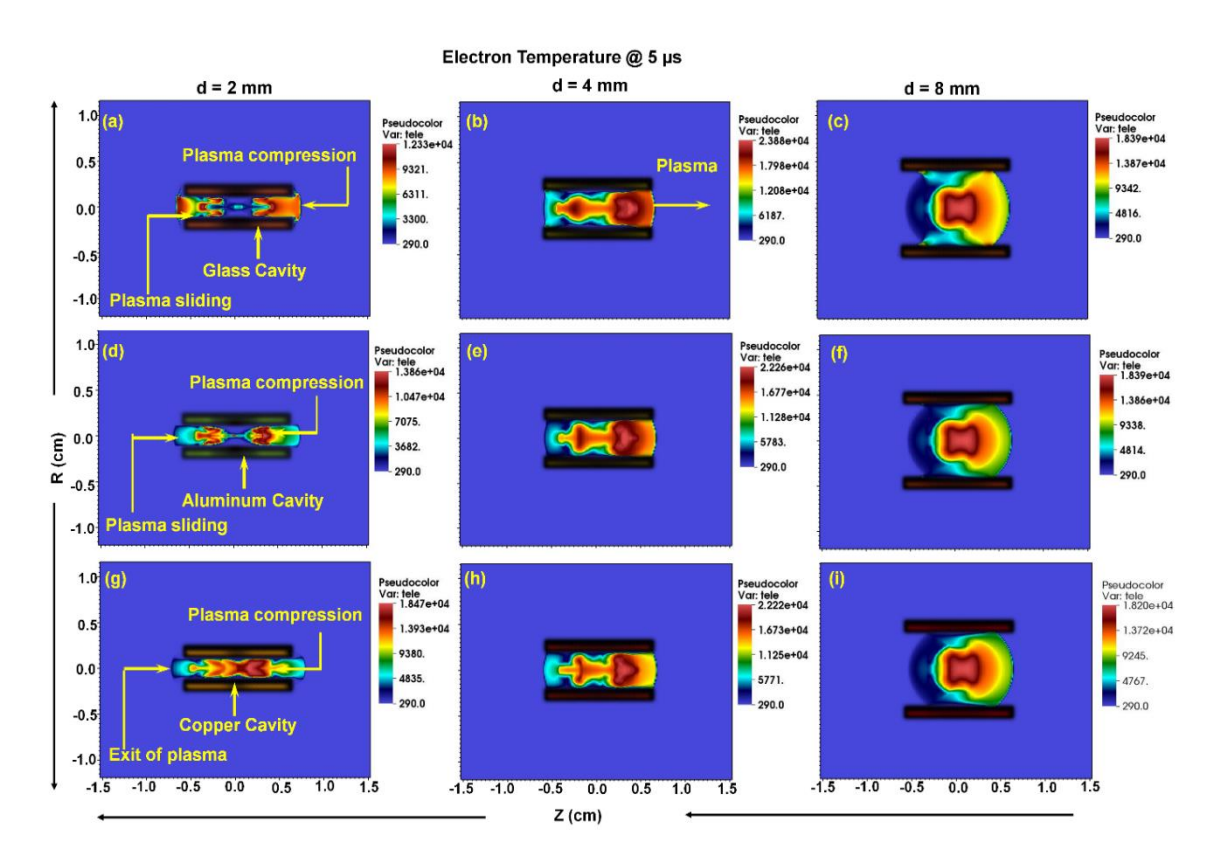


Fig. 5. 11 Comparison of the spatial variation of the electron temperature confined using (a -c) glass cavity, (d -f) aluminum cavity and (g -i) copper cavity with separation distances d = 2, 4 and 8 mm respectively at 5  $\mu$ s for the input laser energy of 200 mJ.

From Fig. 5.11 (a) it can be observed that the plasma in the glass cavity is expanding more along the laser propagation axis with a minimum temperature existing at Z=0 plane (refer to Fig. 5.5) i.e., a maximum compression of the PC is taking place at Z=0 plane. The plasma is sliding along the tube boundary and the plasma with high temperature is about to exit from the cavity. However, in the aluminium cavity (Fig. 5.11 (d)) though a maximum compression of the PC is taking place, the sliding of the plasma along the laser propagation axis is less when compared to that of a glass cavity. And the plasma outer region (POR) is about to exit from the cavity, while the high temperature PC is still at the centre of the cavity. While, the plasma inside the copper cavity (Fig. 5.11 (g)), the compression of the plasma is still taking place. The peak temperature PC is existing at the centre of the cavity i.e., at Z=0 plane. A similar trend is observed for the separation distance d=4 mm for the three cavity materials (glass, aluminium and copper). As can be seen in Fig. 5.11 (b) & (e), the plasma with high temperature

region is about to exit from the cavity along +Z direction, while the PC is at the centre of the cavity at Z=0 plane for the copper cavity (Fig. 5.10 (h)). The POR is sliding over the cavity walls and is about to exit from the copper cavity. A detailed study of the temporal variation of the plasma temperature along Z=0 plane is presented in Fig. 5.12 (a) - (i) for all the three cavity materials glass, aluminium and copper with separation distances d=2, 4 and 8 mm respectively for the input laser energy of 200 mJ.

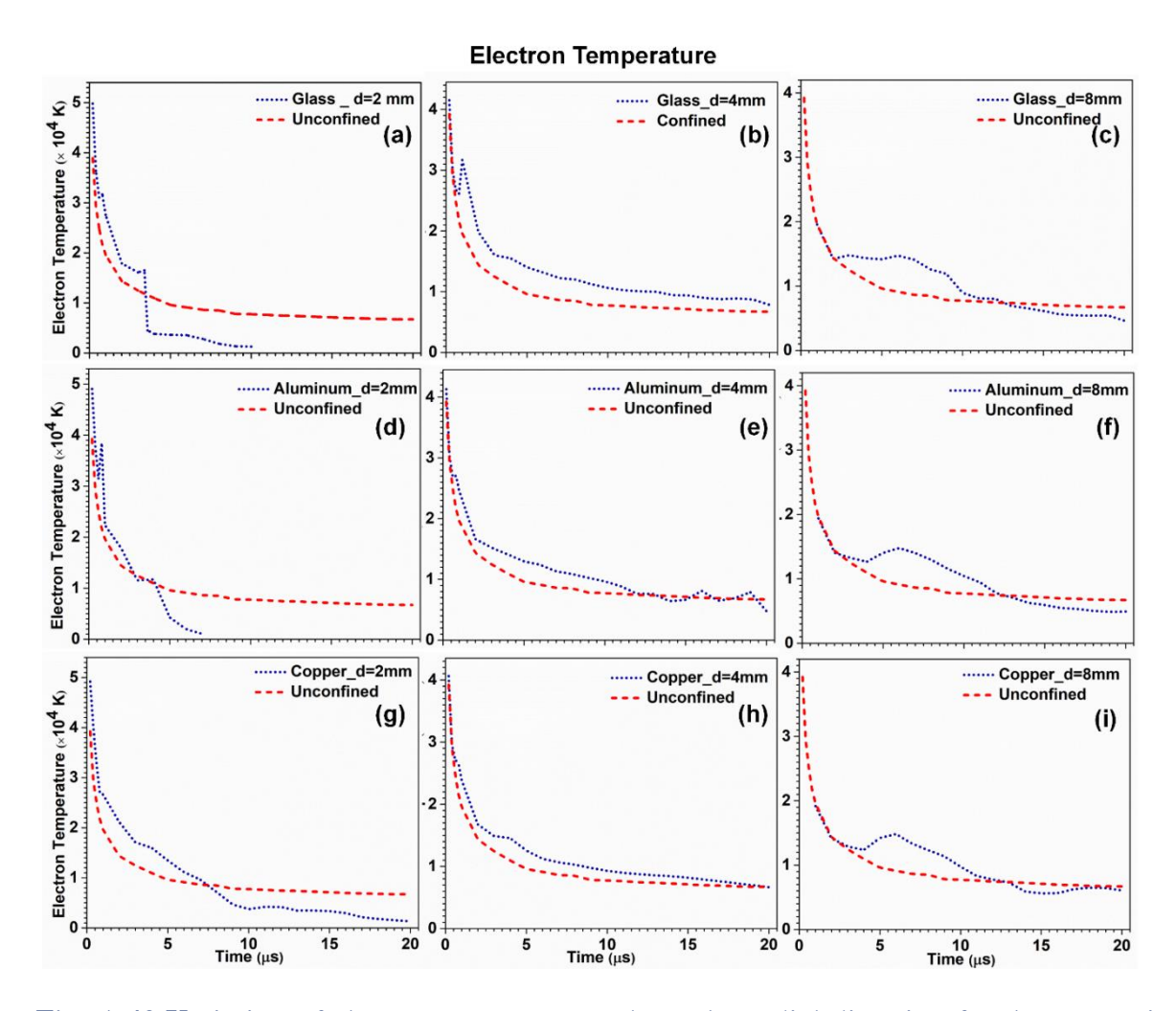


Fig. 5. 12 Variation of electron temperature along the radial direction for the separation distances (a) d= 2mm (b) 4 mm, (c) 8 mm and the electron number densities for (d) d=2mm, (e) 4 mm and (f) 8 mm with materials of cavity glass, aluminium and copper for the input laser energy of 200 mJ.

It is observed that for d=2 mm (Fig. 5.12 (a), (d) and (g)) that the reflection of the SW from the cavity walls along the radial direction is taking place at 0.2  $\mu$ s. By this time (0.2  $\mu$ s), the SW has not detached from the plasma, hence, it can be understood both the SW and the plasma outer region were interacting with the cavity and reflecting back towards the PC. A raise in electron temperature is observed because of the reflection of the plasma outer region. A maximum raise of temperature of (3.847  $\times$  10<sup>4</sup> K) is observed in the aluminium cavity at 0.8  $\mu$ s (Fig. 5.12 (d))

when compared to that in a glass (Fig. 5.12 (a)) and copper cavities (Fig. 5.12 (g)). However, the plasma is observed to be sliding through the glass and aluminium cavities and exiting from the cavity before 10 µs. Hence, a decrease in radial temperature at the point from which the reflection of the plasma outer region (POR) has taken place is observed after 3 µs. However, the plasma has sustained in the copper cavity over a longer time, but the temperature at the contact point has decreased.

Fig. 5.12 (b), (e) and (h) represents the electron temperature evolution in the cavities for separation distance of 4 mm, which is nearly equal to the plasma size along the radial direction [38]. The reflection from the cavity walls is taking place at 0.6 µs. The reflection from glass cavity (Fig. 5.12 (b)) is showing a pronounced enhancement at 1 µs after which the electron temperature evolution in all the three cavities were similar. It can be understood that for the separation distance equal to plasma length, the enhancement in the plasma parameters were independent of the material chosen (The obtained enhancement in temperature were below the statistical error determined in Chapter -2). A similar trend is also observed for the separation distance of 8 mm (Fig. 5.12 (c), (f) and (i)) where the plasma is allowed to completely expand and the SW is about to detach from the plasma. Hence, it is the reflection of the SW that is taking place for d = 8 mm, which is interacting with the plasma and leading to a pronounced enhancement in the plasma parameters. A maximum enhancement of 1.66, 1.62 and 1.62 is observed in the glass, aluminium and copper cavities respectively at 7, 7 and 6 µs respectively. The enhancement observed in electron temperature in all the three cavities is almost the same (in the range of statistical error). Fig. 5.13 (a) - (i) shows the temporal variation of the electron number density with respect to the dimensions of the cavity and cavity material.

In the case of the separation distance d = 2 mm, it is to be noted that the plasma with higher number density in the outer region (of the order  $10^{18}/\text{cm}^3$ ) is interacting with the cavity walls at 0.2 µs. It is a known fact that the absorption or reflection of a radiant energy by a material depends on the electrical conductivity of the interacting material [56]. Hence, the electrical conductivity of the cavity material plays a major role in the enhancement in the number density of the plasma.

Since, the electrical conductivity of glass and aluminum were less hence, the plasma is just interacting with the cavity and reflecting back towards the PC. The net effect on the cavity material is negligible. However, the reflected plasma is compressing the PC resulting in a pronounced enhancement in the number density at the PC. Since, the number density at the

POR is high i.e., of the order of  $10^{18}$  /cm<sup>3</sup>. A maximum enhancement of 13.8 is observed in the number density in the glass cavity at 4  $\mu$ s, while that in case of aluminium cavity is observed to be 7.3 at 4  $\mu$ s.

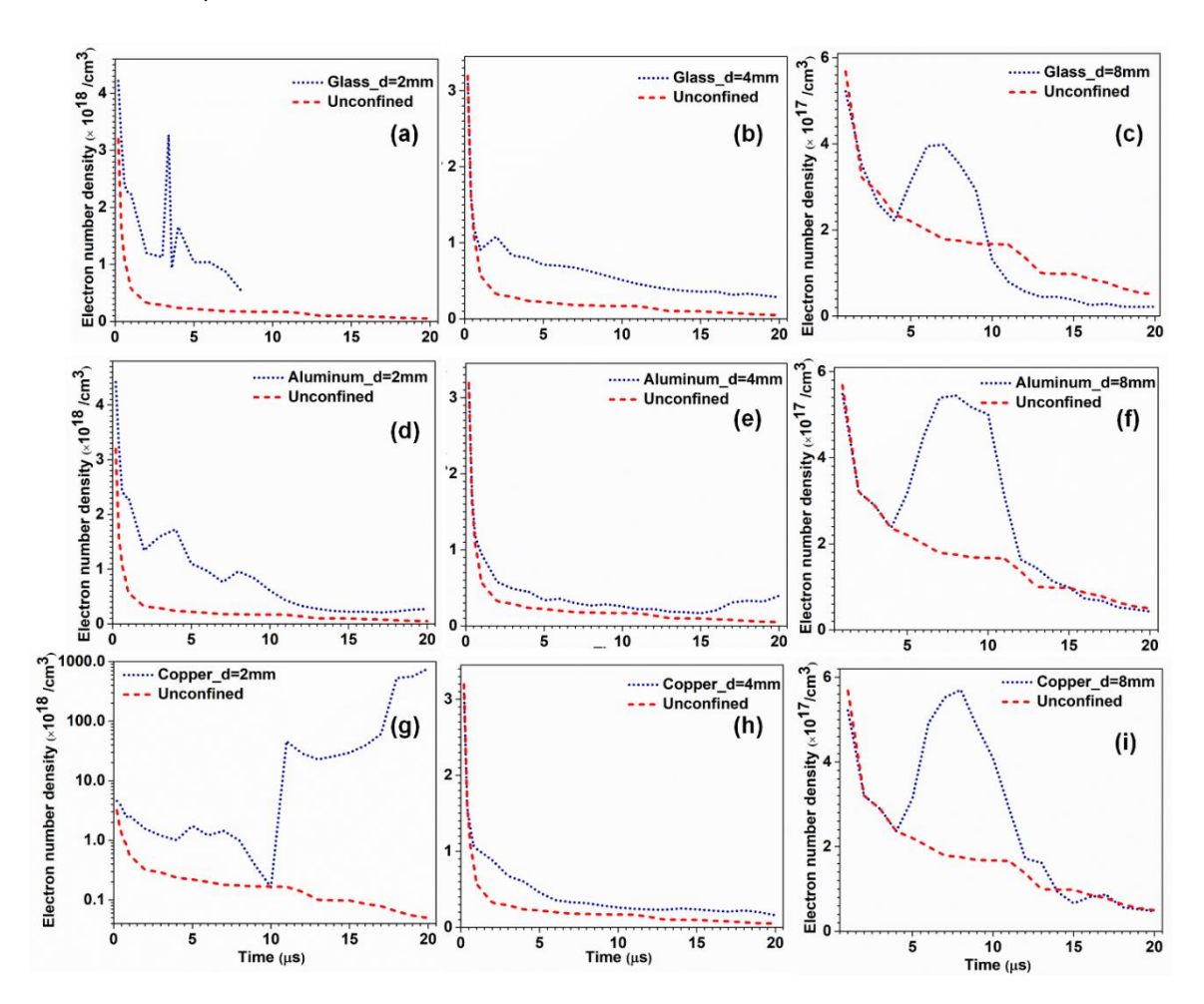


Fig. 5. 13 Variation of electron number density along the radial direction for the separation distances (a) d= 2mm (b) 4 mm, (c) 8 mm and the electron number densities for (d) d=2mm, (e) 4 mm and (f) 8 mm with materials of cavity glass, aluminum and copper for the input laser energy of 200 mJ.

However, when the plasma is interacting with the copper wall, a fractional ionization at the contact point of the plasma is taking place. The raise in the electron number density is observed from the time of reflection and while interacting with the PC. The order of the increased number density at the PC along Z=0 has reached nearly of the order of  $10^{20}$  /cm³ which is very high for a plasma generated from air. The pressure existing at the plasma front after reflection from glass, aluminium and copper cavities and before interaction with the PC were found to be 4.8, 5.4 and 6 MPa, respectively. While, the pressure existing at the PC is 3.19 MPa. Because of the pressure gradient existing between the plasma front and the PC, an effective compression of the PC is taking place resulting in an effective increment in the number density. Similarly,

the enhancement in number density for d=4 mm is slightly less than that observed for d=2 mm, because of the delay in the reflection. This has led to the decrease in the pressure at the plasma front. The enhancement in the number densities were observed to be decreasing with the increase in the separation distance.

Fig. 5.13 (c), (f) and (i) shows the temporal evolution of the electron number density, for the separation distance of d = 8 mm. It is to be observed that the temporal evolution of the number density till 4  $\mu$ s is similar to the number density evolution in the unconfined plasma. However, after 4  $\mu$ s, the number density has increased and reached the maximum enhancement at 7, 8 and 8  $\mu$ s in the glass, aluminum and copper cavities respectively. In all the three cavities, the enhancement in the number density has decreased with the increase in separation distance. For d = 8 mm, the SW has detached from the plasma by the time of interaction with the cavity. Hence, the interaction is taking place between the SF and the cavity wall. However, for d = 2 and 4 mm the interaction is taking place between the plasma and the cavity wall. Since, the interaction is taking place at the early time scales for d = 2 and 4 mm, the number density at the POR is high, the enhancement in the plasma parameters is pronounced for lower separation distances. However, for d = 8 mm, the SF with number density of the order  $10^{17}$  /cm<sup>3</sup> is interacting with PC resulting in a less enhancement in plasma parameters.

The enhancement in the temperature and number densities with respect to separation distance and the material of cavity were summarized in table 5.2.

Table 5. 2 A summary of the enhancement factor in the plasma parameters with respect to the separation distance between the walls and material of the cavity

Material	Diameter d (mm)	Time of maximum enhancement (µs)	Enhancement in electron temperature	Time of maximum enhancement (µs)	Enhancement in electron number density
Glass	2	0.8	1.46	4	13.8
	4	1.0	1.61	20	5.65
	8	7	1.66	7	2.22
Aluminum	2	0.5	1.77	4	7.31
	4	5	1.36	20	7.93
	8	7	1.62	8	3.11
Copper	2	2	1.47	7	8. 0
	4	4	1.32	19	3.64
	8	6	1.62	8	3.26

From table 5.2 it is to be observed that for the separation distance of 2 mm, the maximum enhancement in the plasma number density is observed for glass, while that in case of d = 4

mm, aluminium is showing a maximum enhancement, and that in case of d = 8 mm, Cu is showing a maximum enhancement. Studying the thermodynamic variables (pressure, temperature, energy and shock velocity) just before and after reflection of the PSW at the cavity wall, it is understood that the electrical conductivity of the material is playing a role on the amount of enhancement in the plasma parameters with respect to the separation distance.

Hence, the three cases, where separation distance (d) is less than the radial plasma length (d = 2 mm), nearly equal to plasma length (d = 4 mm) and greater the plasma length (d = 8 mm) were studied. Among the three dimensions, d = 2 and 4 mm were showing a pronounced enhancement in plasma parameters. However, in case of d = 2 mm, since the plasma reflection is taking place at early timescales, a fractional ionization of the cavity material is taking place and the plasma is exiting from the cavity. Hence, d = 2 mm is not suitable for effective confinement of the laser plasma. Where, d = 8 mm can be chosen as the suitable separation distance for effectively increasing the lifetime of plasma. A brief discussion on the effect of electrical conductivity of the confining material in case of d = 2 mm is given in the following section.

## 5.5 Plasma interaction with cavity material (d = 2 mm)

It is presented in the section 5.4 that the electrical conductivity of the cavity material is playing a role in the enhancement of the electron number density for the separation distance d = 2 mm. It is observed that a fractional ionization of the cavity is taking place due to the interaction of the plasma with the cavity. Fig. 5.14 shows a confirmation that, fractional ionization of the copper cavity is taking place during the plasma interaction.

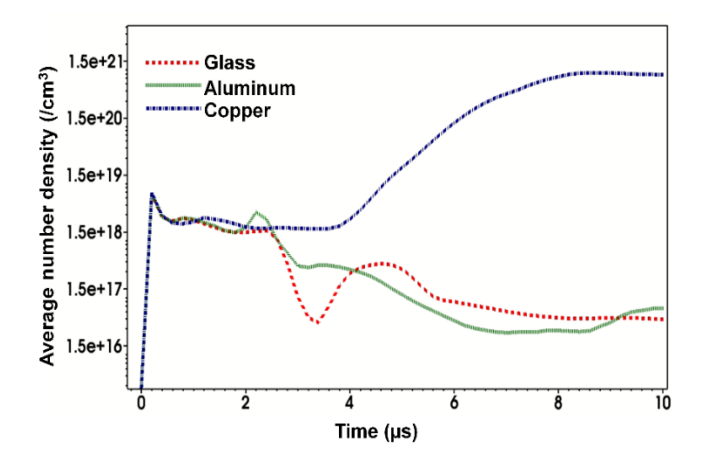


Fig. 5. 14 Average electron number density at region just before the contact point of the plasma with the cavity wall (glass, aluminium and copper) along the radial direction for the input laser energy of 200 mJ

Temporal evolution of the electron number density at the region just before the contact of plasma with the cavity wall for the input laser energy 200 mJ for the three cavity material (glass, aluminium and copper) can be seen in Fig 5.14. It can be observed that the number density during the time of interaction and reflection (0.2  $\mu$ s) is almost the same for the three cavity materials. However after 2  $\mu$ s, the number density at the glass and aluminium walls has decreased. This is observed because of the reflected POR traversing towards the POR. A slight raise in the number density of glass and aluminium plasma is observed after 3  $\mu$ s. This is observed because of the POR retracing back after interaction with the PC. This confirms that multiple reflections of POR is taking place between the cavity wall and PC. However, as observed in Fig. 5.13 at 10  $\mu$ s the plasma is exiting from the glass and aluminium cavity. Hence, a decrease in the number density is observed. However, in the case of copper cavity, the plasma is sustaining inside the cavity, due to the multiple reflections taking place inside the cavity a fractional ionization of the cavity is taking place leading to a pronounced increment in the number density. Hence, a copper cavity of d = 2 mm is not suitable for effective confinement of laser plasma.

### 5.6 Conclusion

The effect of radial confinement of laser generated air plasma using a cavity is studied in detail. The internal dynamics taking place during the interaction of reflected plasma/SW with the plasma core is studied in detail. It is observed that the RSW while interacting with the PC along the radial direction is leading to an increase in the plasma temperature and number density because of the compression of the RSW. This is observed because of the increase in the collisions between the electrons and the surrounding electrons and ions, leading to increase in the kinetic energy. The increased kinetic energy is converted into thermal energy. An optimization study on the dimensions of the cavity, input laser energy and cavity material suitable in designing a millimetre size shock tube is performed. It is observed that 8 mm separation distance between the cavity walls is suitable for any material chosen for cavity. However, for d=4mm, aluminium and copper were showing a maximum increment in the plasma parameters and d=2mm is not suitable for any material chosen as the plasma is directly interacting with the cavities, a fractional ionization of the cavity material is taking place which is multiplying because of the confinement effects. Moreover, the plasma is exiting from the cavity at timescales less than 10 us which is not suitable for increasing the longevity of the plasma.

### 5.7 References

- 1. Choudhury, K., et al., *Time resolved interferometric study of the plasma plume induced shock wave in confined geometry: Two-dimensional mapping of the ambient and plasma density.* Physics of Plasmas, 2016. **23**(4): p. 042108.
- 2. Guo, L.B., et al., Enhancement of optical emission from laser-induced plasmas by combined spatial and magnetic confinement. Optics Express, 2011. **19**(15): p. 14067-14075.
- 3. Fabbro, R., et al., *Physical study of laser-produced plasma in confined geometry*. Journal of Applied Physics, 1990. **68**(2): p. 775-784.
- 4. Saxena, A.K., et al., *Spectroscopic investigation of molecular formation in laterally colliding laser-produced carbon plasmas.* Applied Optics, 2019. **58**(3): p. 561-570.
- 5. Yeates, P. and E.T. Kennedy, Spectroscopic diagnostics of plume rebound and shockwave dynamics of confined aluminum laser plasma plumes. Physics of Plasmas, 2011. **18**(6): p. 063106.
- 6. Schildberg, H.-P., Gas-Phase Detonations in Pipes: the 8 Possible Different Pressure Scenarios and their Static Equivalent Pressures Determined by the Pipe Wall Deformation Method (part 1) CHEMICAL ENGINEERING TRANSACTIONS, 2016. 48: p. 241-246.
- 7. Heilig, W. and O. Igra, *CHAPTER 10 Shock Waves in Channels*, in *Handbook of Shock Waves*, G. Ben-Dor, O. Igra, and T.O.V. Elperin, Editors. 2001, Academic Press: Burlington. p. 319-VI.
- 8. Li, S., et al., A Numerical Investigation of the Cold Spray Process Using Underexpanded and Overexpanded Jets. Journal of Thermal Spray Technology, 2012. **21**(1): p. 108-120.
- 9. Hollingsworth, W.A., A Schlieren Study of the Interaction between a Vortex and a Shock Wave in a Shock Tube. British Aeronaut. Research Council Rept. 17,985, 1955.
- 10. Zhang, S., Y.-T. Zhang, and C.-W. Shu, *Multistage interaction of a shock wave and a strong vortex*. Physics of Fluids, 2005. **17**(11): p. 116101.
- 11. Skews, B.W., M.D. Atkins, and M.W. Seitz, *The impact of a shock wave on porous compressible foams.* Journal of Fluid Mechanics, 1993. **253**: p. 245.
- 12. Onodera, H. and K. Takayama, *Shock Wave Structure in Polyurethane Foam.* JSME International Journal Series B, 1994. **37**(2): p. 268-274.
- 13. Dorodnitsyn, V. and B.V. Damme, *Analytical analysis of slow and fast pressure waves in a two-dimensional cellular solid with fluid-filled cells.* The Journal of the Acoustical Society of America, 2016. **139**(6): p. 3332-3340.
- 14.Song, B., B. Sanborn, and W.-Y. Lu, Experimental Measurement and Analysis of Stress/Shock Wave Propagation Speed through Pre-strained Silicone Foam Pads under Lateral Confinement. Journal of Dynamic Behavior of Materials, 2019. 5(2): p. 170-179.
- 15.Delale, C.F., S. Nas, and G. Tryggvason, *Direct numerical simulations of shock propagation in bubbly liquids.* Physics of Fluids, 2005. **17**(12): p. 121705.
- 16. Jang, D., et al., Enhanced efficiency of laser shock cleaning process by geometrical confinement of laser-induced plasma. Journal of Applied Physics, 2009. **106**(1): p. 014913.
- 17.Lee, J.M. and K.G. Watkins, Removal of small particles on silicon wafer by laser-induced airborne plasma shock waves. Journal of Applied Physics, 2001. **89**(11): p. 6496-6500.
- 18. Radziemski, L.J., From LASER to LIBS, the path of technology development. Spectrochimica Acta Part B: Atomic Spectroscopy, 2002. **57**(7): p. 1109-1113.
- 19. Khalil, A.A.I., W.O. Younis, and M.A. Gandol, A comparative study of highly-ionized Al plasma based on dual pulse laser-induced breakdown spectroscopy. Indian Journal of Physics, 2017. 91(3): p. 327-336.
- 20.Hahn, D.W. and N. Omenetto, Laser-Induced Breakdown Spectroscopy (LIBS), Part I: Review of Basic Diagnostics and Plasma—Particle Interactions: Still-Challenging Issues within the Analytical Plasma Community. Applied Spectroscopy, 2010. **64**(12): p. 335A-336A.
- 21. Yeates, P. and E.T. Kennedy, *Diagnostics of laser plasma plume dynamics within an electrically biased confining cavity.* Journal of Applied Physics, 2011. **110**(6): p. 063303.
- 22. Huang, F., et al., Confinement effects of shock waves on laser-induced plasma from a graphite target. Physics of Plasmas, 2015. **22**(6): p. 063509.

- 23. Qiu, Y., et al., Spatial confinement of laser-induced plasma by laser-induced and obstacle-reflected shock wave and its effect on optical emission of laser-induced plasma. AIP Advances, 2019. 9: p. 095021.
- 24. Popov, A., F. Colao, and R. Fantoni, *Enhancement of LIBS signal by spatially confining the laser-induced plasma*. Journal of Analytical Atomic Spectrometry J ANAL ATOM SPECTROM, 2009. **24**.
- 25. Popov, A.M., F. Colao, and R. Fantoni, *Spatial confinement of laser-induced plasma to enhance LIBS sensitivity for trace elements determination in soils.* Journal of Analytical Atomic Spectrometry, 2010. **25**(6): p. 837-848.
- 26. Hou, Z., et al., Signal quality improvement using cylindrical confinement for laser induced breakdown spectroscopy. Optics Express, 2013. 21.
- 27. Guo, L., et al., Accuracy improvement of quantitative analysis by spatial confinement in laser-induced breakdown spectroscopy. Optics Express, 2013. 21.
- 28. Yin, H., et al., *Application of spatial confinement for gas analysis using laser-induced breakdown spectroscopy to improve signal stability.* Journal of Analytical Atomic Spectrometry, 2015. **30**(4): p. 922-928.
- 29. Shen, X.K., et al., *Spatial confinement effects in laser-induced breakdown spectroscopy.* Applied Physics Letters, 2007. **91**(8): p. 081501.
- 30. Yeates, P. and E.T. Kennedy, *Spectroscopic, imaging, and probe diagnostics of laser plasma plumes expanding between confining surfaces.* Journal of Applied Physics, 2010. **108**(9): p. 093306.
- 31. Wang, Q., et al., *The role of cavity shape on spatially confined laser-induced breakdown spectroscopy.* Physics of Plasmas, 2018. **25**(7): p. 073301.
- 32. Yeates, P. and E.T. Kennedy, *Plasma dynamics of a confined extreme ultraviolet light source*. Physics of Plasmas, 2010. **17**(9): p. 093104.
- 33. Shen, X.K., et al., *Spectroscopic study of laser-induced Al plasmas with cylindrical confinement.* Journal of Applied Physics, 2007. **102**(9): p. 093301.
- 34. Fu, Y., Z. Hou, and Z. Wang, *Physical insights of cavity confinement enhancing effect in laser-induced breakdown spectroscopy.* Optics Express, 2016. **24**(3): p. 3055-3066.
- 35. Sai Shiva, S., et al., Numerical investigation of nanosecond laser induced plasma and shock wave dynamics from air using 2D hydrodynamic code. Physics of Plasmas, 2017. **24**(8): p. 083110.
- 36. Sai Shiva, S., et al., Role of laser absorption and equation-of-state models on ns laser induced ablative plasma and shockwave dynamics in ambient air: Numerical and experimental investigations. Physics of Plasmas, 2019. **26**(7): p. 072108.
- 37. Y. P. Raizer, V.I.K., and J. E. Allen, *Gas Discharge Physics*. 1 ed. 2011: (Springer, Berlin, Heidelberg.
- 38. Guthikonda, N., *Dynamics of Confined Laser Induced/Ablative Plasmas and Shock Waves*, in *Physics*. 2020, University of Hyderabad: Hyderabad. p. 211.
- 39. Harald Kleine, C.V.L., Kohsei Takehara, T. Goji Etoh, *Time-resolved visualization of shock–vortex systems emitted from an open shock tube.* Journal of Visualization, 2010. **13**: p. 33-40.
- 40. Hejazialhosseini, B., D. Rossinelli, and P. Koumoutsakos, *Vortex dynamics in 3D shock-bubble interaction*. Physics of Fluids, 2013. **25**(11): p. 110816.
- 41. Cooper, P.W., Explosives engineering. 1996: Wiley-VCH.
- 42. Kameswari, D.P.S.L., et al., *Investigation of stagnation layer dynamics of counterpropagating laser induced air plasmas: Numerical simulations vis-à-vis experimental observations.* Physics of Plasmas, 2021. **28**(4): p. 043104.
- 43. Li, X., et al., *Spatial confinement in laser-induced breakdown spectroscopy*. Journal of Physics D: Applied Physics, 2017. **50**: p. 015203.
- 44. Hayat, A., et al., The role of spatial confinement for improvement of laser-induced Mg plasma parameters and growth of surface features. Applied Physics A, 2017. **123**(8): p. 505.
- 45. Sakai, T., et al., *Interaction between laser-induced plasma and shock wave over a blunt body in a supersonic flow.* Proceedings of The Institution of Mechanical Engineers Part G-journal of Aerospace Engineering PROC INST MECH ENG G-J A E, 2008. **222**: p. 605-617.

#### Dynamics of Radially Confined Plasma and Shock Waves

- 46. Sai Shiva, S., Numerical Investigations of ns Laser InducedShock Waves from Aluminum and Air. 2016, University of Hyderabad: Hyderabad. p. 188.
- 47. DeMichelis, C., Laser induced gas breakdown: A bibliographical review. IEEE Journal of Quantum Electronics, 1969. **5**(4): p. 188-202.
- 48. Harilal, S.S., B.E. Brumfield, and M.C. Phillips, *Lifecycle of laser-produced air sparks*. Physics of Plasmas, 2015. **22**(6): p. 063301.
- 49. Villagran-Muniz, M., H. Sobral, and E. Camps, *Shadowgraphy and interferometry using a CW laser and a CCD of a laser-induced plasma in atmospheric air.* IEEE Transactions on Plasma Science, 2001. **29**(4): p. 613-616.
- 50. Raizer, Y.B.Z.d.a.Y.P., *Physics of Shock Waves and High-Temperature Hydrodynamic Phenomena*. Dover Publications, 2012.
- 51. Arshad, A., et al., Effect of magnetic field on laser-induced breakdown spectroscopy of graphite plasma. Applied Physics B, 2016. **122**(3): p. 63.
- 52. Ghosh, S. and K. Mahesh, *Numerical simulation of the fluid dynamic effects of laser energy deposition in air.* Journal of Fluid Mechanics, 2008. **605**: p. 329-354.
- 53. Harilal, S.S., et al., On- and off-axis spectral emission features from laser-produced gas breakdown plasmas. Physics of Plasmas, 2017. **24**(6): p. 063304.
- 54. Sai Shiva Sakaraboina, P.K.P., Venkata Ramana Ikkurthi, *Three-dimensional radiation hydrodynamic simulations of laser-produced air plasma aluminum slab interaction\**, in *APS March Meeting 2021*. 2021.
- 55. Macfarlane, J.J., IONMIX a code for computing the equation of state and radiative properties of LTE and non-LTE plasmas. Computer Physics Communications, 1989. **56**(2): p. 259-278.
- 56. Hecht, E., Optics. 2016: Pearson Education.

# Chapter-6

# Laser Irradiated Aluminum foil: ablation and blowoff shock waves

A preliminary study of generation of the laser ablative plasma and SW from a 20 µm thick aluminum foil is studied under different ambient pressures. The ambient pressure is varied between 0.1-1 atm in presence of ambient air and helium (He) gas. The strength of the ablative SW is observed to be increasing with the increase in the ambient pressure. The expansion of the SW is more in the low ambient pressure, while it is spatially confined under high ambient pressures. This has led to the increase in the electron temperature (T<sub>e</sub>) and number density (N<sub>e</sub>) of the plasma, and the pressure at the shock front (SF) in both the ablation (from front surface) and blow-off regimes (rear side of the target). On comparing the expansion dynamics in presence of air and He, the plasma and SW parameters are low in presence of He, at all the considered ambient pressures. Though the strength of the SF in the blow-off regime is increasing with increasing pressure and changing the ambient gas (from He to air), flyer ejection is not observed in the blow-off regime. To enhance the strength of the blow-off SW, the ablative plasma generated in presence of air medium at 1 atm background pressure is spatially confined using a glass substrate (SiO<sub>2</sub>) of thickness 1.8 mm the front end of Al foil of 20 µm thickness is stuck to the glass substrate. A laser beam of energy 50 mJ is focused at the Al - glass interface and the ablative plasma and SW were confined along the laser propagation axis. It is observed that a blow-off SW of maximum density 1.0 gm/cm<sup>3</sup> is launched into air at 0.1 µs. The density of the blow-off SW generated in the confined geometry (confined axially along laser propagation axis) is much higher than that generated without confinement (bare Al foil). Plasma ejection is not observed in the case of unconfined geometry, however, plasma ejection and expansion is observed in the case of confined geometry. The blow-off shock velocities were compared with the experimental results. To verify the strength of the blowoff plasma and SW, a cavity (in a two dimensional view two walls with separation distance 'd') is introduced at the rear side of the Al foil. The cavity confines the plasma and SW along radial direction. The confining cavity dimensions considered were d = 2 mm, and length L= 7 mm. However, no effective change in the blow-off shock pressures is observed because of the dimensions of the cavity considered.

### **6.1 Introduction**

The process of removal of material from a target surface is known as the laser ablation (LA). The ejection of material/particles from a target surface and their interaction with the background gas is receiving much interest due to its application in high temperature superconductor film growth and deposition [1]. The process of generation and expansion of plasma can be classified into three stages: 1) interaction of the laser beam with the target material and formation of plasma, 2) interaction of the laser beam with the material evaporated from the target material, isothermal expansion of the plasma and 3) adiabatic expansion of the plasma and shock wave into the background gas. In the first stage when the laser beam is incident on the target surface, a part of the incident radiation is reflected while the remaining part is absorbed by the target surface. The fraction of radiation reflected or absorbed depends on the target material properties and energy of the incident laser beam.

The incident optical energy interacts with the medium such that atoms in the target material are excited to the higher energy states, further the electrons in the corresponding atoms become free leading to the ionization of the atom. During the initial times of laser-matter interaction the electron density will be very small compared to the neutral atom densities. The free electrons present in the metals are more likely to absorb the incoming laser photons during the free – free transitions in collisions with neutral atoms. Hence, the electron – ion collisions play a dominant role in the absorption mechanism [2, 3]. The dominant absorption mechanisms taking place are the inverse bremsstrahlung mechanism (IB) and photoionization (PI) [4, 5] which depends on the pulse duration. The number of atoms ionizing increases with the increase in the absorption of the laser energy leading to a rapid growth in the free electron number density and electron temperatures [6, 7] leading to formation of plasma. The material removed from the hot target is further heated by the absorption of the laser radiation. During this process, the specific internal energy and pressure of the medium increases rapidly.

The optical breakdown threshold laser intensity of most of the solids is  $\sim 10^7$  W/cm². At very low intensities ( $\sim 10^4$  W/cm²) the material undergoes heating without ablation or formation of plasma. However, at intensities ranging between  $10^4 - 10^7$  W/cm², the material vaporizes and leads to surface melting. Further increase in the intensity of the input laser beam to greater than  $10^8$  W/cm² results in heating, melting and evaporation and finally to breakdown of the matter and formation of plasma [4, 8].

The material ablated from the focal volume is accumulated at the plasma front expanding in the ambient atmosphere, forming a thin dense layer called as the shock front. The accumulation of mass continues until the SW is completely built. The SW at later times detaches from the plasma and expands adiabatically into the background gas. The ablative SW expanding into ambient atmosphere launches a compression wave on to the material due to momentum conservation. The launched SW travels through the material medium. Depending on the thickness of the target material, target properties and intensity of the incident beam, the SW reaches the rear end of the target and in few cases may lead to a blow-off of material from the rear end of the target. The interaction of sufficiently intense ns laser pulse with thin foil target induces the material blow-off (plasma) or ejection of flyer from the rear side of target [9-11].

Most prominent applications of laser produced plasma (LPP) and laser ablation (LA) are pulsed laser deposition [12], nanoparticle synthesis and cluster formation [13-15], laser surgery[16], LA inductively coupled plasma mass spectrometry (LA-ICP-MS) [17], laser induced breakdown spectrometry (LIBS) to mention a few. A numerous work has been done on the study of LA and generation of SW from bulk targets. However, the study of ablation and blow-off from thin metal foil were limited.

Spatial confinement of the ablative plasma/SW leads to an increase in the strength of the blow-off SW. A wide range of studies have been performed in spatially confining the plasma by changing the background pressure [18-22], back ground gas species (He, N, O<sub>2</sub>, Ar, air) [13, 23-28], overlaying transparent material on the target [11, 29-31]. Spatial confinement of ablative plasma /SW is useful in the study of material behavior under shock compression [32-35], generation of EOS [36, 37], thrust generation for propulsion [38].

In the present chapter an initial simulative study of the effect of the spatial confinement of ablative and blow-off plasma and shock wave is studied under four different methods.

- 1. Effect of background gas pressure (varied between 0.1 1 atm) on the expansion dynamics of SW
- Effect of background gas (air and He) species with respect to the varying background pressure, to explicitly understand the role of the ambient gas on plasma and SW dynamics
- 3. Spatial confinement of ablative plasma and SW using a glass substrate and

4. Spatial confinement of blow-off SW using a glass cavity.

### 6.2 Laser ablation from a thin foil

The expansion dynamics of plasma and SW from Al foil in presence of ambient air under normal temperature and pressure (NTP) conditions were presented in this section. A laser beam of energy 50 mJ, spot size of 500  $\mu$ m, pulse duration of 10 ns is focused onto the thin metal aluminum (Al) foil of thickness 20  $\mu$ m. The density of Al is considered to be 2.7 g/cm<sup>3</sup>, while that of air is  $1.3 \times 10^{-3}$  g/cm<sup>3</sup>. Fig. 6.1 shows the schematic of the computational domain in Z×R geometry.

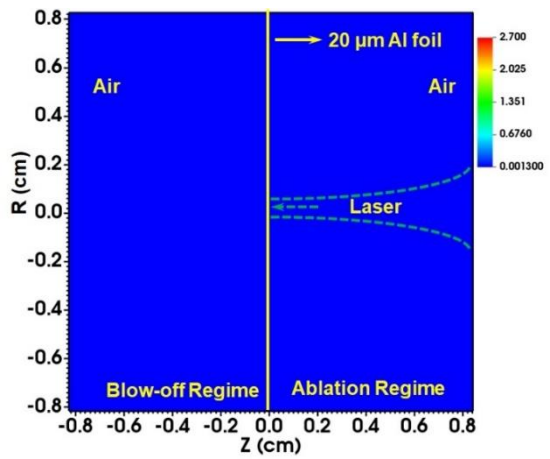


Fig. 6. 1 Schematic showing the simulation domain where the laser beam is focussed onto the front surface of aluminium foil

Laser energy deposition, generation of plasma and SW were studied by solving the three hydrodynamic equations (1.1-1.3). The model considers the ideal gas equation of state (EoS) for air medium and tabulated IONMIX EOS is used for the Al foil to close the system of equations (1.1-1.3). The main absorption mechanism considered were inverse bremsstrahlung [39][40, 41].

# 6.2.1 Spatio - temporal evolution of plasma and shock wave parameters

Laser beam of sufficient intensity is focused onto the target surface results in melting and rapid evaporation of the target material leading to formation of plasma. The plasma plume is generated after breakdown of the target [20]. The plasma plume thus formed absorbs the incoming laser energy resulting in a raise in temperature and internal energy of the plasma. At the end of the laser pulse, the plume consisting of the high internal energy, and ablated material, expands freely in hemispherical shape in the laser propagation axis with high velocity

compressing the background gas ahead of it. When the intensity of the incident radiation is much higher (>  $2.7 \, \mathrm{GW/cm^2}$ ) [20, 42], a large amount of energy is delivered both to the target surface and to the plume resulting in an increase in the material evaporation rate and quantity of ablated material. However, in case of lower intensity of incident radiation, the ablated plume has less energy hence the plasma expansion limit is reached much closer to the target surface. In such case the radial expansion appears to be more prominent when compared to that along the laser propagation axis. The spatial evolution of electron temperature and pressure generated from the 20  $\mu$ m thick aluminium foil using a laser beam of intensity 2.5 GW/cm² with back ground pressure of 1 atmospheric pressure (0.1 MPa) were presented in Fig. 6.2 (a) – (f).

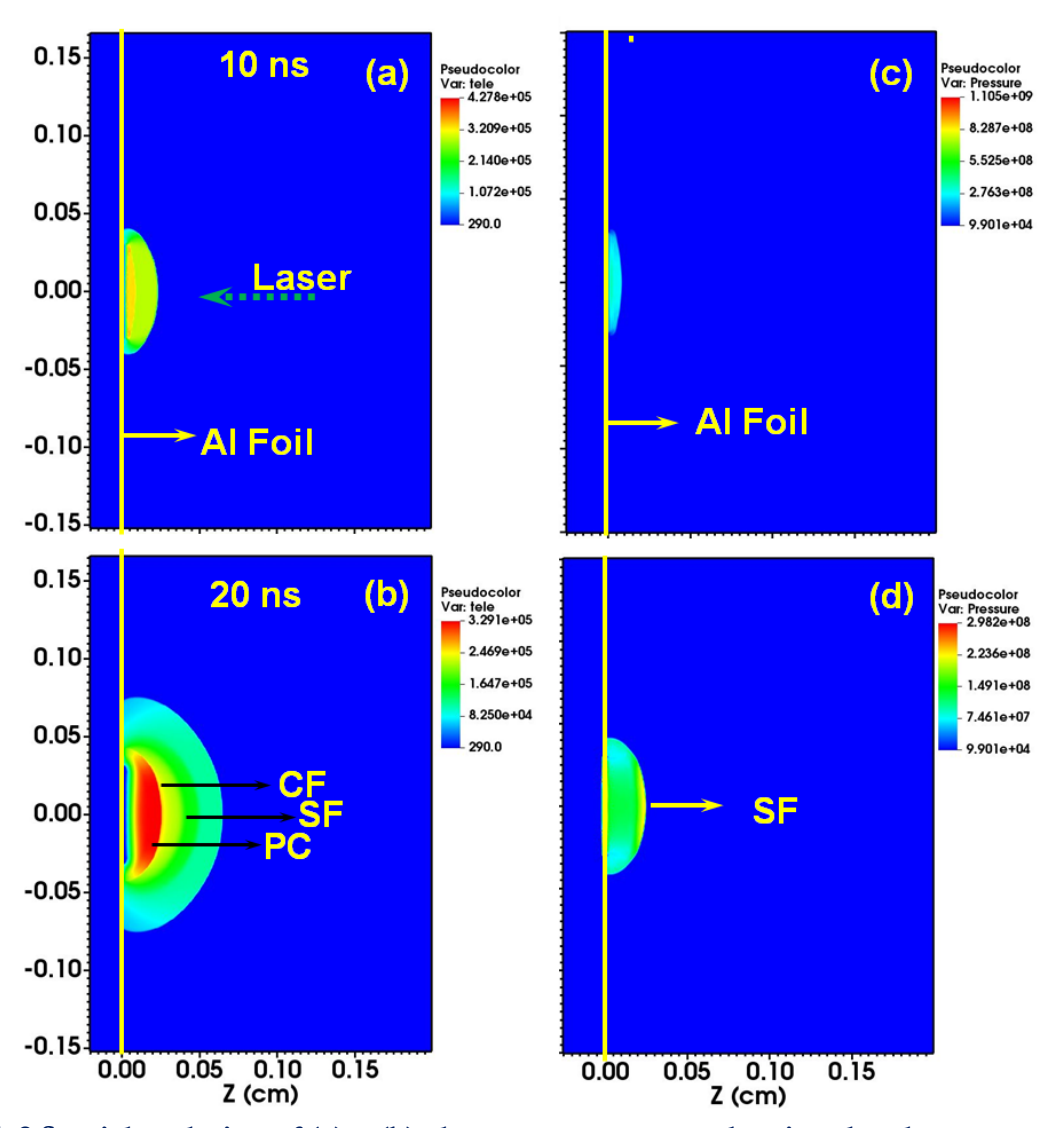


Fig. 6. 2 Spatial evolution of (a) – (b) electron temperature showing the plasma core (PC), shock front (SF) and contact front (CF) and (c) – (d) pressure at 10 and 20 ns respectively for the input laser energy of 50 mJ

Fig. 6.2 (a) - (b) shows the evolution of the electron temperature while fig. 6. 2 (c) - (d) shows the evolution of pressure at the early time scales of 10 and 20 ns respectively. The plasma formed during the leading edge of the input laser can be observed in fig. 6.2 (a). The maximum temperature of the plasma is observed to be 4.27 × 10<sup>5</sup> K at 10 ns, which decreases later on because of the expansion of the plasma into the ambient atmosphere. The plasma formed by 10 ns (FWHM) interacts with the trailing edge of the laser beam, absorbs the energy and expands in the direction opposite to laser beam. The plasma thus generated consists of three main regions: (i) plasma core region where very high temperatures (of the order of 10<sup>5</sup> K) exists where number of collisions take place between the electrons and ions, (ii) absorption front and (iii) shock front with higher density, pressure due to the accumulation of the material ablated from the focal volume The expansion of the plasma is clearly observed as shown by electron temperature at 20 (fig 6.2 (b)).

Plasma core (PC) is the region predominantly containing heated and ionized ablated matter. The temperature at the PC is very high due to the continuous collisions between the electrons and ions. The edges of the PC corresponds to the ablated matter and air interface forming a thin layer called as the shock front (SF). Across the shock front, the ambient gas gets heated and ionized forming new thin plasma layer capable of absorbing laser radiation called as the absorption front.

The pressure at the SF is less than the pressure existing at the target – air interface at 10 ns as can be seen in Fig. 6.2 (c). The maximum pressure at the SF is found to be 0.28 GPa at 10 ns, which later decreases due to rapid adiabatic expansion of the SW. As the time advances the internal pressure of the plasma is decreases and becomes high across the SF. This can be visualized in fig. 6.2 (d). The spatio - temporal evolution of the SW in the ablative and blow-off regimes generated using 50 mJ is shown in Fig. 6.3

Fig. 6.3 shows the spatio – temporal evolution of SW at the time scales of 10, 30, 50, 100, 200 and 500 ns respectively showing the Mach number with which the SW is travelling. Mach number can be defined as the ratio of the speed of the SW with the local sound speed in the medium in which the SW is travelling. If the Mach number is greater than one then propagation is called as a supersonic propagation. A shock wave is a hypersonic wave traversing through the medium compressing the medium ahead of it.

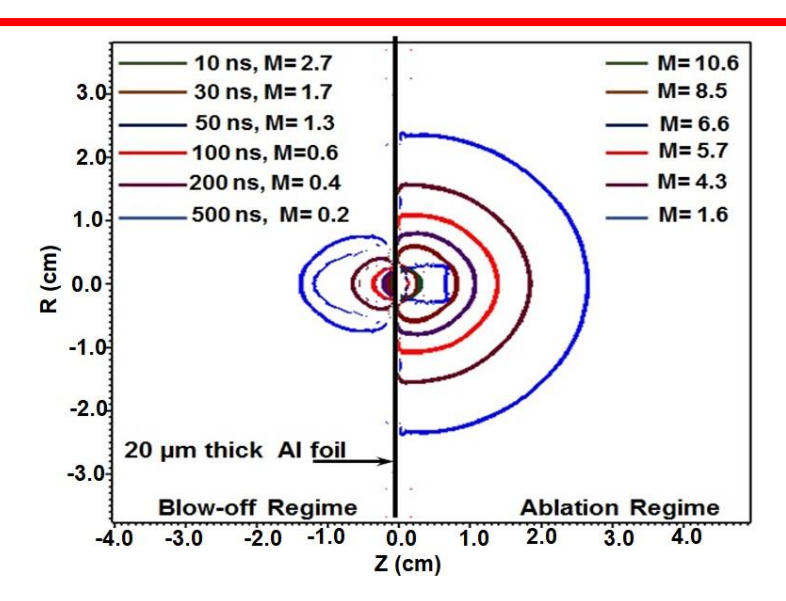


Fig. 6. 3 Spatio-temporal evolution of the shock front in the ablative and blow-off regimes generated using 50 mJ laser source in presence of ambient pressure of 1 atm.

It can be observed that the SW is launched into the ablation regime at 10 ns. At 10 ns the ablative SW is travelling with a Mach number of 10.6. The ablative SW expanding into the ambient air launches a compression wave into the metal foil. The compression wave launched into the target travels through the target and is launched into the rear side of the target called as the blow-off SW. Though the blow-off SW is launched at 10 ns, the visibility and expansion of the SW were observed prominently after 100 ns. The Mach number is decreasing with time indicating a decrease in shock velocity because of the exchange of energy between the SF and the surrounding medium while adiabatically expanding into the background gas. Fig. 6.4 shows the spatial evolution of electron temperature and pressure at 100, 200 and 500 ns for the input energy of 50 mJ.

Fig. 6.4 (a) & (e) shows the spatial variation of electron temperature and pressure at 100 ns. The maximum temperature at the PC is observed to be  $7.26 \times 10^4$  K. The blue colored region ahead of the PC is the pre-ionized gas because of the high temperatures existing at the PC. Thin region behind SF is the absorption front (AF) or the contact front (CF). The peak pressure existing at the SF is  $1.88 \times 10^7$  Pa (18.8 MPa) while that existing at the PC is  $4.82 \times 10^7$  Pa. A blow-off SW can be observed in the rear side of the Al foil. The peak pressure observed at the blow-off SF is  $9.44 \times 10^6$  Pa.

Fig. 6.4 (b) & (f) shows the electron temperature and pressure at 200 ns. The peak temperature at the PC has decreased to  $4.14 \times 10^4$  K.

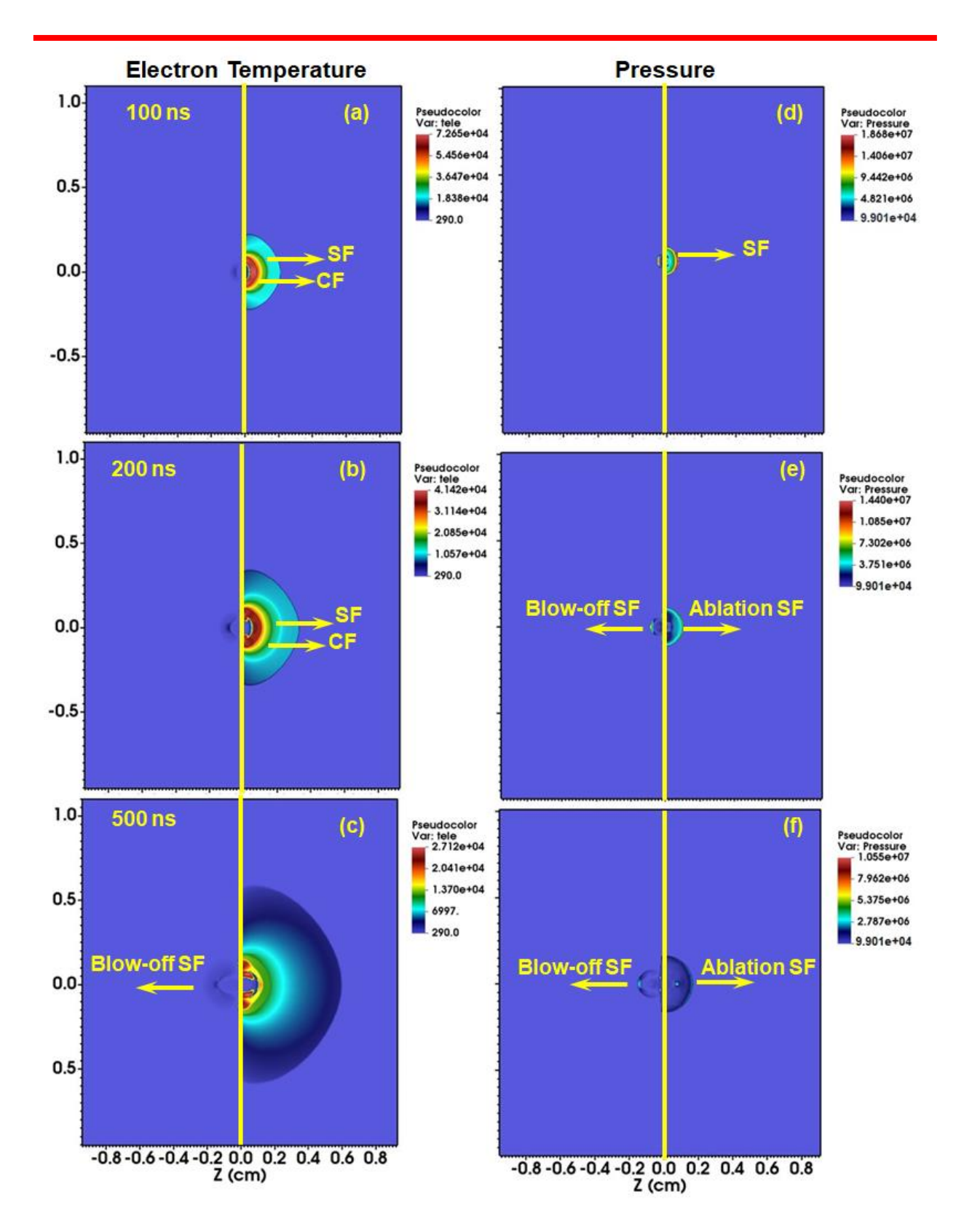


Fig. 6. 4 Two dimensional spatial evolution of (a)-(c) electron temperature and (d)-(e) pressure at 100, 200 and 500 ns respectively for the input laser energy of 50 mJ under the ambient pressure of 1 atm.

The decrease in the plasma temperature is observed because of the utilization of fraction of internal energy for expansion along axial and radial directions [41]. Similar to electron

temperature, the peak pressure at the SF has decreased to  $3.7 \times 10^6$  Pa. The pressure at SF decreases as the SF expands freely into the ambient gas, because of the exchange of the energy between SF and the surrounding medium. The blow-off SW with velocity of nearly 1 km/sec is expanding freely into the ambient atmosphere.

The plasma core temperature has further decreased to 2.7 × 10<sup>4</sup> K by 500 ns (Fig. 6.4 (d)). The temperature at the pre-ionized gas expanding has decreased and is much nearer to the background temperature. It is to be understood that the dominant collisions taking place at the plasma core (higher temperatures) are electron-ion collisions, while at the outer region (pre-ionized gas) the ion-ion collisions are dominant. It is also observed that the temperature of the blow-off material generated at the rear surface is very low (< 1000 K). Hence, it cannot be called as plasma but just a hot gas. The temporal evolution of SW and plasma parameters generated from 50 mJ source were presented in Fig. 6.5 (a)-(c).

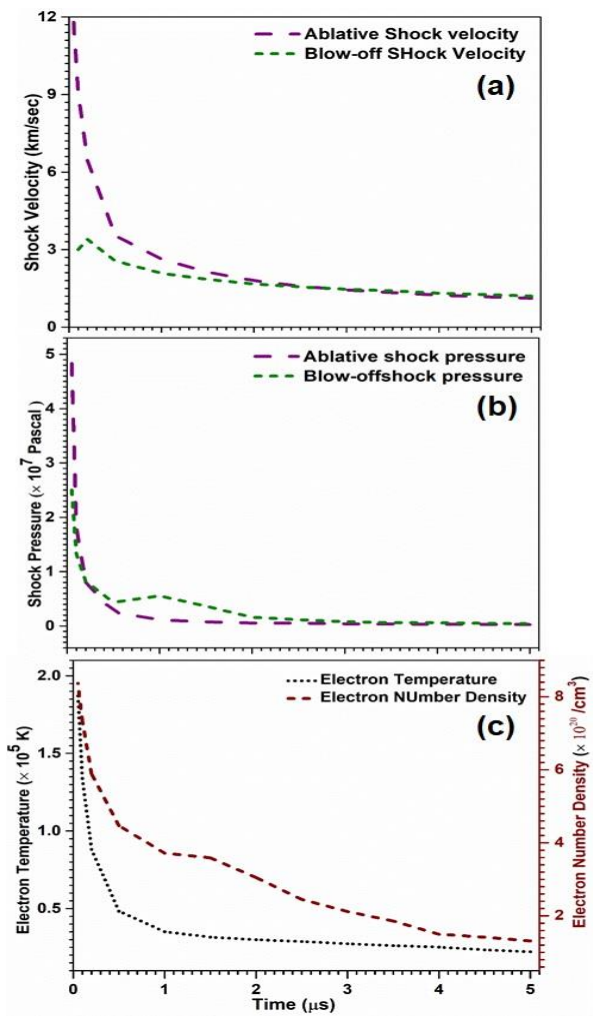


Fig. 6. 5 Comparison of (a) Shock velocity (b) shock pressure (c) peak electron temperature and number density along laser propagation axis in the ablation and blow-off regimes for the input energy of 50 mJ

Fig. 6.5(a) compares the temporal evolution of the ablation and blow-off shock velocities over a time duration of 0.05 - 5 µs. It is clearly observed that the ablation SW is travelling with much higher velocity (12 km/sec) when compared to that of the blow-off SW (3.5 km/sec). However, the ablative SW is freely expanding into the ambient atmosphere and hence the shock velocity is decreasing over the considered time duration. While, the blow-off SW is building up, upto 300 ns after which is freely expanding into the ambient atmosphere. However, the blow-off shock velocity has not increased more than the ablative shock velocity. After 2 µs, the shock velocities in both the regimes have reached nearly equal. During the initial time scales the KE of the SW is very high leading to a fast expansion of the SW. However, during the expansion of the SW, the collision between the particles at the shock front and ambient gas interface results in the transfer of energy to the ambient gas. It was confirmed by Sai Shiva et.al. [43, 44] that the SW expansion is planar in nature during the initial timescales, while it transforms into spherical nature in the later time scales. The decrease in the KE and momentum of the SW is manifested in the form of the volume of the SW expansion. When the SW expansion attains the spherical nature, the shock velocities were same in all the directions. However, the shock velocities were still above 1.5 km/sec over the considered time duration of 3 µs.

Fig. 6.5(b) compares the temporal evolution of shock pressures in the ablative and blow-off regimes. The maximum shock pressure in the ablative regime at 0.05 µs is 48 MPa, while that in the blow-off regime is 25 MPa. It is observed that the strength of the SW launched at the rear side of the metal foil is very less. If the considered target is a bulk target (few mm) then the strength decreases and in few cases cannot reach the rear side. The shock pressures were decaying quickly during the first 500 ns as the SW is expanding freely into the ambient atmosphere.

Fig. 6.5(c) shows the temporal evolution of peak electron temperature and electron number density of the plasma over a duration of 5  $\mu$ s along the laser propagation axis. The peak temperature has decreased from  $2\times10^5-0.2\times10^5$  K. While the number density is in the range of  $8.4-1\times10^{20}$  /cm³ over the considered duration of time. During the initial time scales the decrease in the temperature is fast. However, at later time scales the decrease in the electron temperature is less because of the energy regain due to the recombination of ions [13]. During the adiabatic expansion the thermal energy of the plasma is converted into kinetic energy

resulting in a fast decay in the plasma temperature. The expanding plume equilibrates with the background pressure resulting in a decay of the number density [45]..

# 6.2.2 Effect of background gas pressure on SW and plasma parameters

The expansion and dynamics of the plasma plume is greatly affected by the background gas pressure. The behavior of plasma plume generated at low background pressure significantly differs from that generated at atmospheric pressure. The plasma plume expands freely in a low background pressures when compared to that at high background pressures [19, 21, 22]. An increase in background pressure leads to strong shock front formation, and slowing of the plasma plume compared to propagation in under low ambient pressure resulting in spatial confinement of the plasma plume. To get an insight into the effect of background gas pressure on plasma and SW evolution, the background pressure is varied between 0.1 – 1 atmospheric pressure (atm), to study the effect of the background pressure on the plasma and SW dynamics.

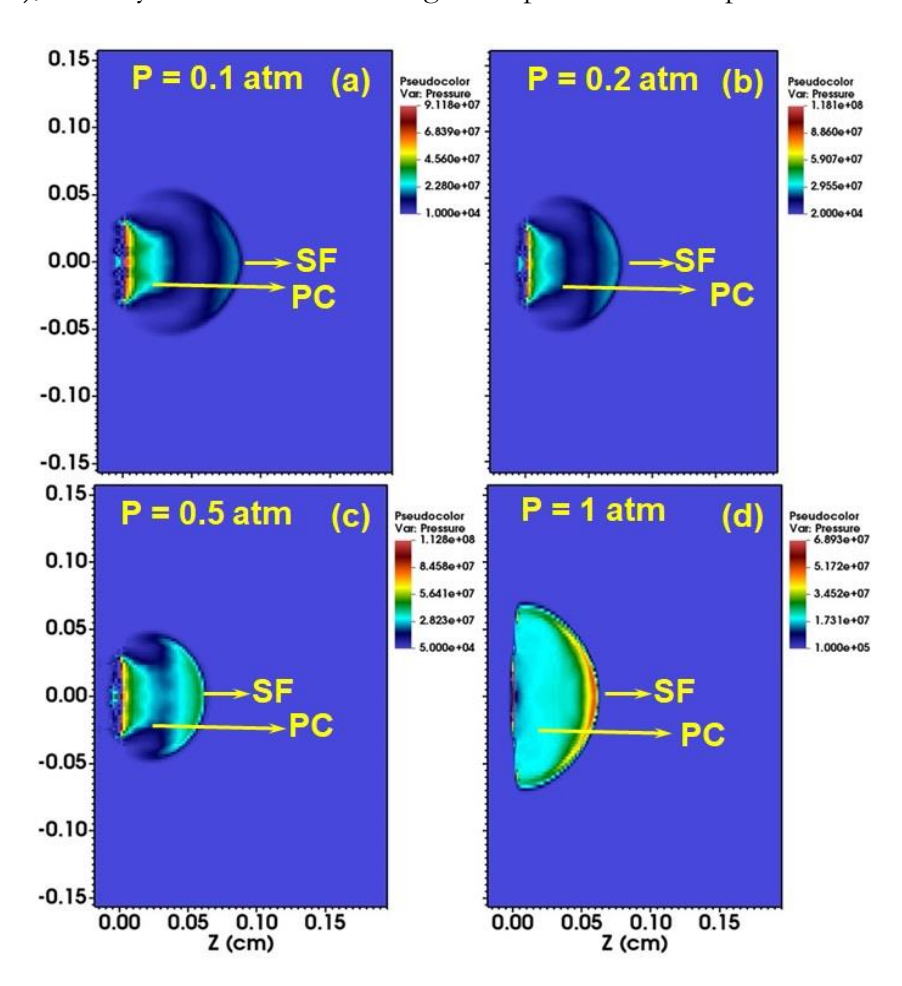


Fig. 6. 6 A comparison showing the pseudo plot of pressure at 50 ns when the background pressure is (a) 0.1 (b) 0.2 (c) 0.5 and (d) 1 atm for the input laser energy of 50 mJ

Fig. 6.6 (a) - (d) shows the pseudo plot of the pressure generated from 20 μm thick Al foil, for the input laser energy of 50 mJ when the background pressure is varied between 0.1 – 1 atm. It can be observed that the expansion of the SW is fast in case of lower background pressure (0.1 atm) and has decreased as the pressure is increasing. It is also observed that the strength of the SF increasing with the increase in pressure. The pressure existing at the SFs are -18.7, 25.3, 42.6, 67.5 MPa in case of 0.1, 0.2, 0.5 and 1 atm respectively. For lower background pressures, the plasma and SW expansion is more along the laser propagation axis when compared to that along the radial direction. However, in the case of 1 atm pressure, the expansion is hemispherical with expansion both along the laser propagation axis and along the radial directions. It is a known fact that the SW launched at the front surface of the target travels through the target and towards the rear side of the target. A clear initiation of the blow-off SW at the interface of the rear side of Al foil is observed in Fig. 6.6 (d) (1 atm background pressure). However, in the case of lower background pressures, the SF is not still launched at the rear side of the target. Fig. 6.7 (a) - (d) shows the temporal evolution of the shock front (SF) and contact front (CF) evolution over a duration of 50 - 500 ns in the ablation regime.

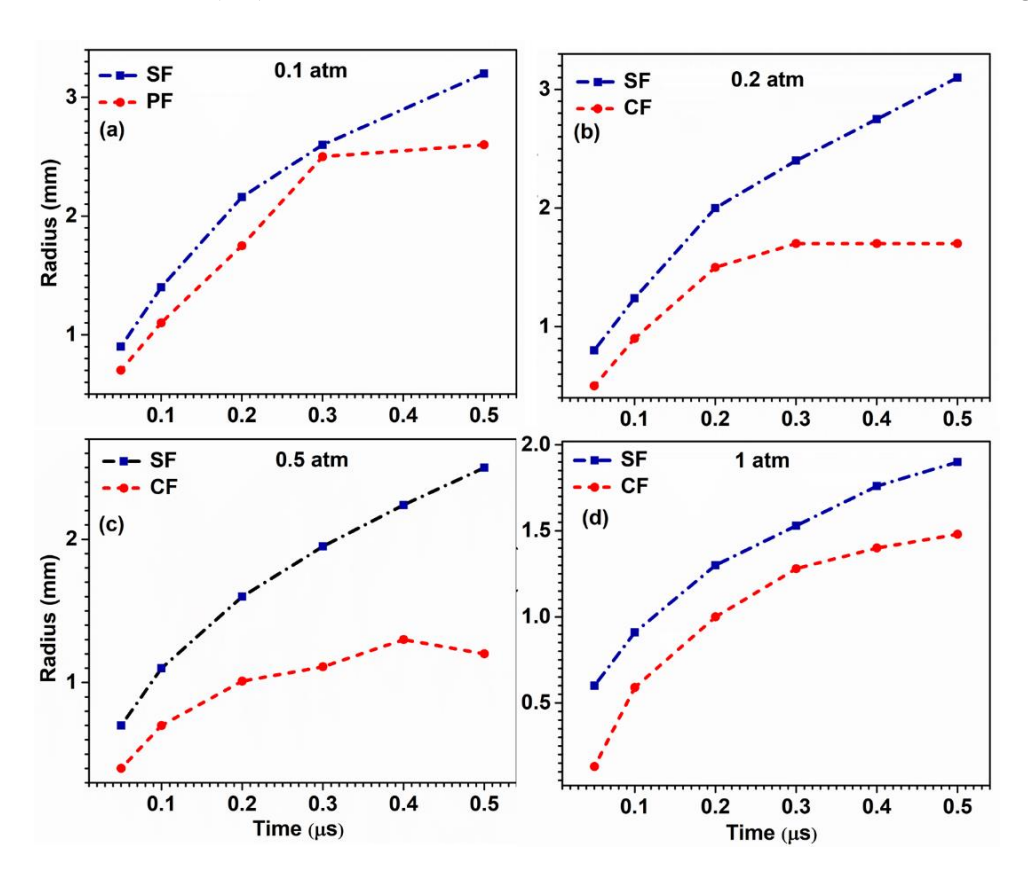


Fig. 6. 7 Temporal evolution of the shock front (SF) and contact front (CF) of SW and plasma generated at the background pressure of (a) 0.1 atm, (b) 0.2 atm, (c) 0.5 atm and (d) 1 atm respectively for the input laser energy of 50 mJ

From fig. 6.7 (a) – (d) it can be observed that the radius of the SF and plasma front were high for 0.1 atm and is decreasing with the increase in the background pressure. If a difference of the radii of SF and CF were determined, it can be observed that at the initial time (50 ns) the difference of the radii were observed to be 0.25, 0.25, 0.3 and 0.4 mm for 0.1, 0.2, 0.5 and 1 atm respectively. However, at 500 ns a reverse in the condition is observed i.e., the variation is radii were 1.5, 1.3, 1.5, 0.5 mm respectively with the increasing background pressure. This confirms that as the time is progressing the spatial confinement of the plasma and SW is taking place as the background pressure is increasing. The reason for the spatial confinement of the plasma and SW generated at high background pressure is explained based on the peak pressure and shock parameters with respect to the ambient pressure over a duration of 3  $\mu$ s in Fig. 6.8 (a)-(b).

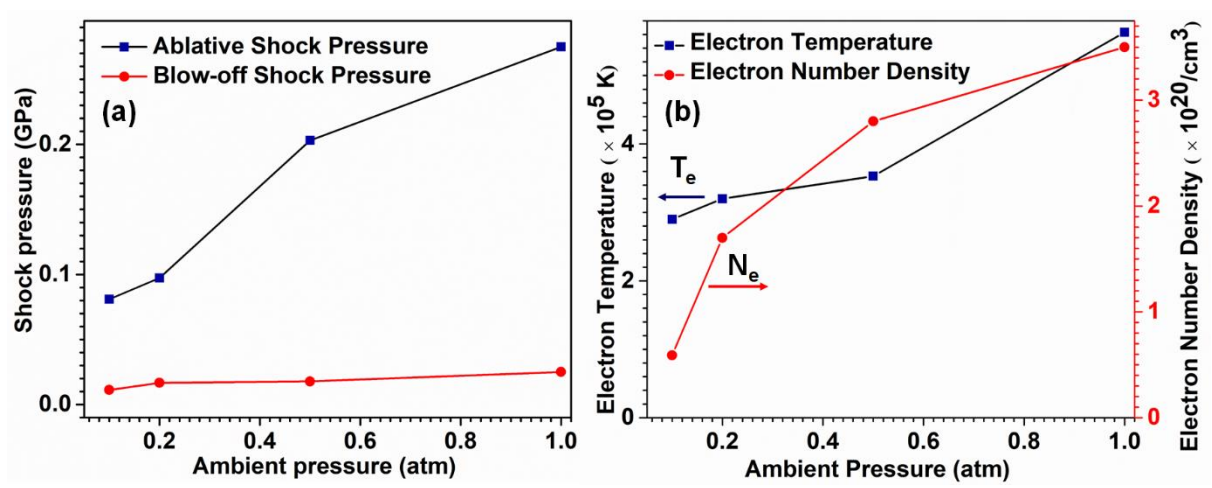


Fig. 6. 8 A comparison of (a) peak shock pressure in the ablation and blow-off regimes and (b) peak electron temperature and electron number density existing at the plasma with respect to the ambient pressure in the range 0.1 - 1 atm

Fig. 6.8 (a) shows that the ablative shock pressure is increasing with the increase in the ambient pressure. The ablative shock pressure has increased from 0.08 GPa to 0.28 GPa by almost 3 times when the ambient pressure is varied from 0.1 - 1 atm. However, it is observed that the background pressure is not showing much effect on the blow-off shock pressure under the considered experimental conditions (lower pulse energy). The blow-off shock pressure has lesser strength than that of the ablative shock pressures under all the ambient pressures considered.

Fig. 6.8 (b) shows that the electron temperature and number density were increasing with the increase in the pressure. It is known that in inverse bremsstrahlung (IB) absorption, the free electrons absorb the photons from the input laser pulse leading to the increase in the electron

temperature. This mechanism further enhance the ionization and excitation of the hot air generated and background gas ionization and plasma generation. The IB coefficient ( $\alpha_{IB}$ ) via free electrons depends on the electron number density given as [39]:

$$\alpha_{IB} \propto Z N_e^2 T_e^{-3/2} \tag{6.1}$$

where Z is the average ionization,  $N_e$  is the electron number density and  $T_e$  is the electron temperature of the plasma. The density of plasma generated under low pressure is less when compared to that generated under high pressure. This is observed because of the increased mean free path and free expansion of the plasma into the ambient gas resulting in decrease in the collisions between the electrons and ions. However, at high ambient pressures the collisional effects between the plume species and ambient gas species increases which is responsible for excitation/de-excitation of species that leads to the confinement of the plasma plume [22, 46]. Thus increase in the background pressure results in a spatial confinement of the plasma leading to the increase in the plasma temperature and number density. The plasma lifetime decreases with decrease in the ambient pressure due to the decrease in collisional excitation and ambient confinement which depends on the intensity of the incident laser energy.

## 6.2.3 Effect of background gas: Air Vs Helium

A combined effect of the background gas and pressure on the plasma and shock parameters is discussed in the present section. The background pressure is varied between 0.1 – 1 atm in presence of air and helium (He) background gases. It is to be noted that the plasma expands rapidly with a constant velocity in presence of vacuum. However, the plasma while expanding in presence of a background gas experiences an opposing force due to the interaction of the plasma with the atoms and molecules of the background gas [47]. This results in the spatial confinement of the plasma depending on the nature of the background gas. Fig. 6.9 (a)-(f) shows the spatial variation of shock pressure at 100, 200 and 500 ns respectively with respect to ambient gas (air and He) at 1 atm of background pressure.

Fig. 6.9 (a) & (d) shows the two dimensional spatial variation of pressure in presence of air and He backgrounds respectively. It can be observed that a maximum pressure of  $1.86 \times 10^7$  Pa (18 Mpa) is existing at the SF in air background (Fig. 6.9 (a)) while the the pressure existing at SF in He background is  $\sim 1.1 \times 10^7$  Pa (Fig. 6.9 (d)). The maximum pressure is existing at the Al foil – air interface in the case of He background. The plasma and SW expansion were

hemispherical in case of air background i.e., expanding almost equally in the axial and radial directions. However, the plasma and SW expansion were more prominent along the laser propagation axis in case of He background. A launching of the blow-off SW at the rear side of the foil can be visualized in the air background. However, the blow-off SW is not much visible for He background.

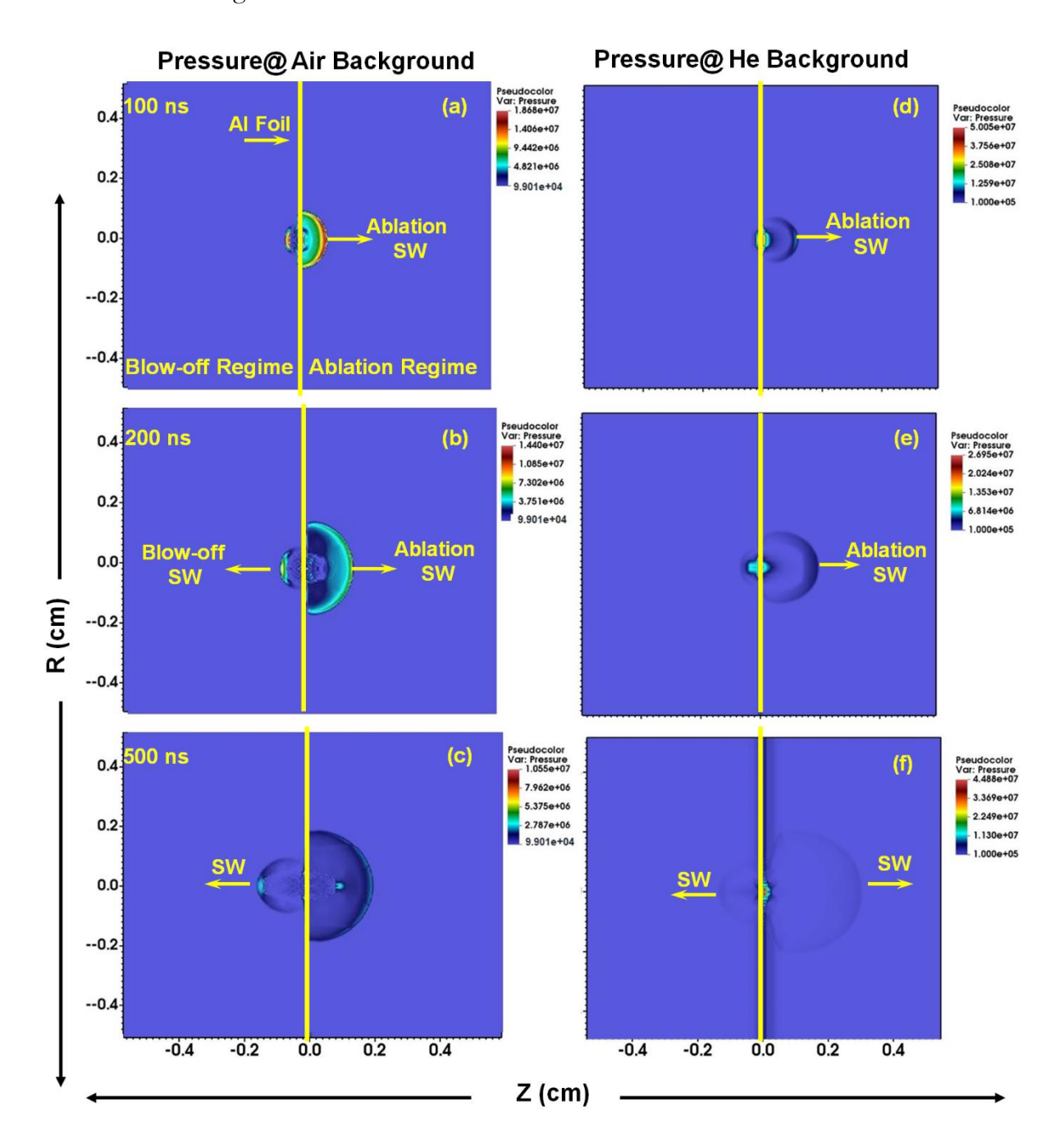


Fig. 6. 9 Spatial evolution of the pressure in presence of (a)-(c) air and (d)-(f) He background at 1 atm background pressure at 100, 200 and 500 ns respectively.

The pressure variation in air and He background gases at 200 ns can be seen in Fig. 6.9 (b)& (e). The hemispherical expansion of the plasma and SW can be prominently observed in Fig.

6.9 (b) (in presence of air) and dominant expansion of the SF along axial direction can be observed in Fig. 6.9 (e) (in presence of He). The pressure at the SF is still high (1.44 × 10<sup>7</sup> Pa) in the ambient air when compared to that existing in the He background (~6.0 × 10<sup>6</sup> Pa). The free expansion of the blow-off SW in the air background can be visualized in Fig. 6.9(b), where, the blow-off SW is just launched in the He background (Fig. 6.9 (e)). The expansion of the ablative SW is more in the He background than that in case of air background as can be observed at 500 ns in Fig. 6.9 (c) & (f). However, as can be visualized the strength of the SF (in terms of pressure) is still high in the ablative and blow-off regimes in the air background when compared to that in case of He background (Fig. 6.9 (c) & (f)). Fig. 6.10 (a) - (c) shows the variation of the peak pressure at the SF and plasma parameters with respect to the background gas (air, He) and background pressure (0.1, 0.2, 0.5 and 1 atm).

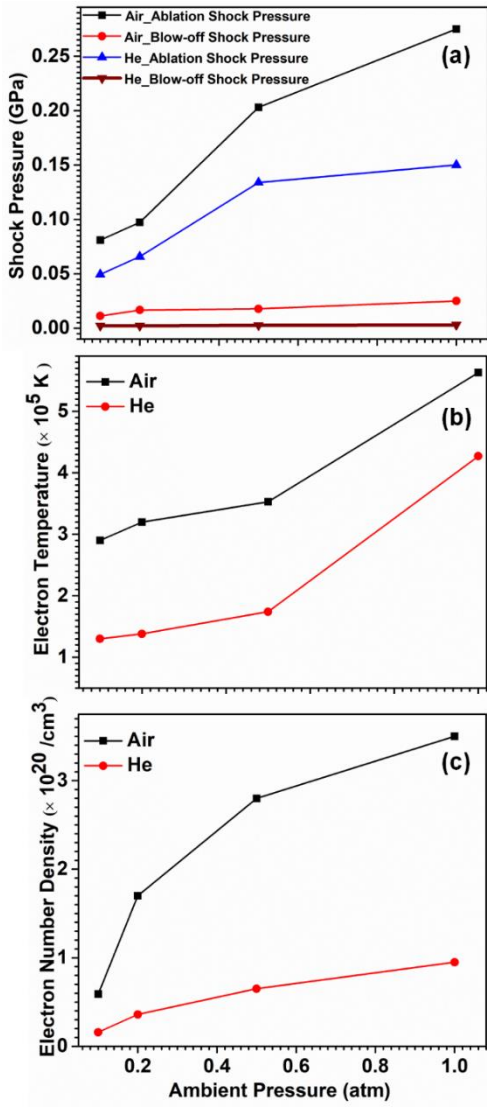


Fig. 6. 10 Variation of the (a) peak pressure at the shock front in the ablation and blow-off regimes (b) peak electron temperature and (c) electron number density of plasma in presence of air and helium with the background pressure varied between 0.1 - 1 atm.

It is observed that the shock pressure is high in case of air background when compared to that of the He background (Fig. 6.6 (a)). Moreover, the shock pressure in presence of both He and air background is observed to be increasing with the increase in ambient pressure. The maximum ablative pressure obtained in presence of air background is 0.28 GPa while that in presence of He is 0.13 GPa (at 1 atm of background pressure). While the strength of the blow-off SW is very less in both the background gases. Fig. 6.6 (b) & (c) shows that the electron temperature (T<sub>e</sub>) and number density (N<sub>e</sub>) were high in presence of air compared to that of He. As discussed above, the confinement of the plasma is due to the interaction of the plasma with the background gas atoms and molecules. The increase in the T<sub>e</sub> and N<sub>e</sub> in He is less because of the high ionization potential of He (24 eV) when compared to that of air (14.5 eV first ionization potential of oxygen, assuming the contribution of nitrogen is negligible) [3, 43, 48]. It is to be noted that the strength of the blow-off SW can be increased with the increased pressure and varied background gas, but the enhanced strength is not much pronounced since flyer ejection is not observed under given conditions.

### 6.3 Axial confinement using glass substrate

To confine the ablative plasma and SW generated from  $20 \, \mu m$  thick Al foil, a glass substrate of thickness 1.8 mm is attached to the front surface of the foil. The laser beam is focused at Al – glass interface. The study is performed for an input laser energy of 50 with spot size of  $500 \, \mu m$  and pulse duration of  $10 \, ns$ .

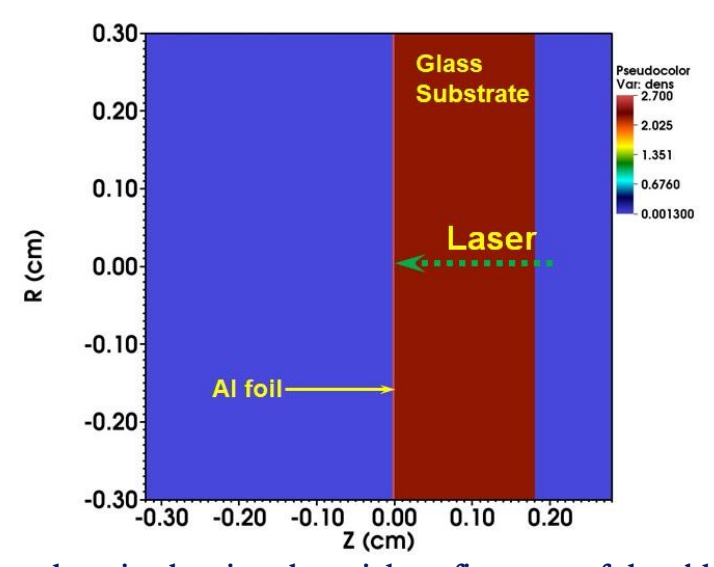


Fig. 6. 11 Simulation domain showing the axial confinement of the ablative regime using a glass substrate.

Fig. 6.11 shows the simulation domain showing the geometry in which the ablative regime is confined using a glass substrate. When the laser beam is focused onto the Al foil, the material in the focal region absorbs the energy, starts to melt, vaporization followed by ionization during the time of energy deposition leading to formation of plasma and shock wave in the ablative regime. The maximum plasma temperature and shock pressure observed during the first 20 ns are  $3.35 \times 10^5$  K and 1.49 GPa respectively. Fig. 6.12 (a) - (c) shows the spatial evolution of the electron temperature at 10 and 20 and 50 ns respectively.

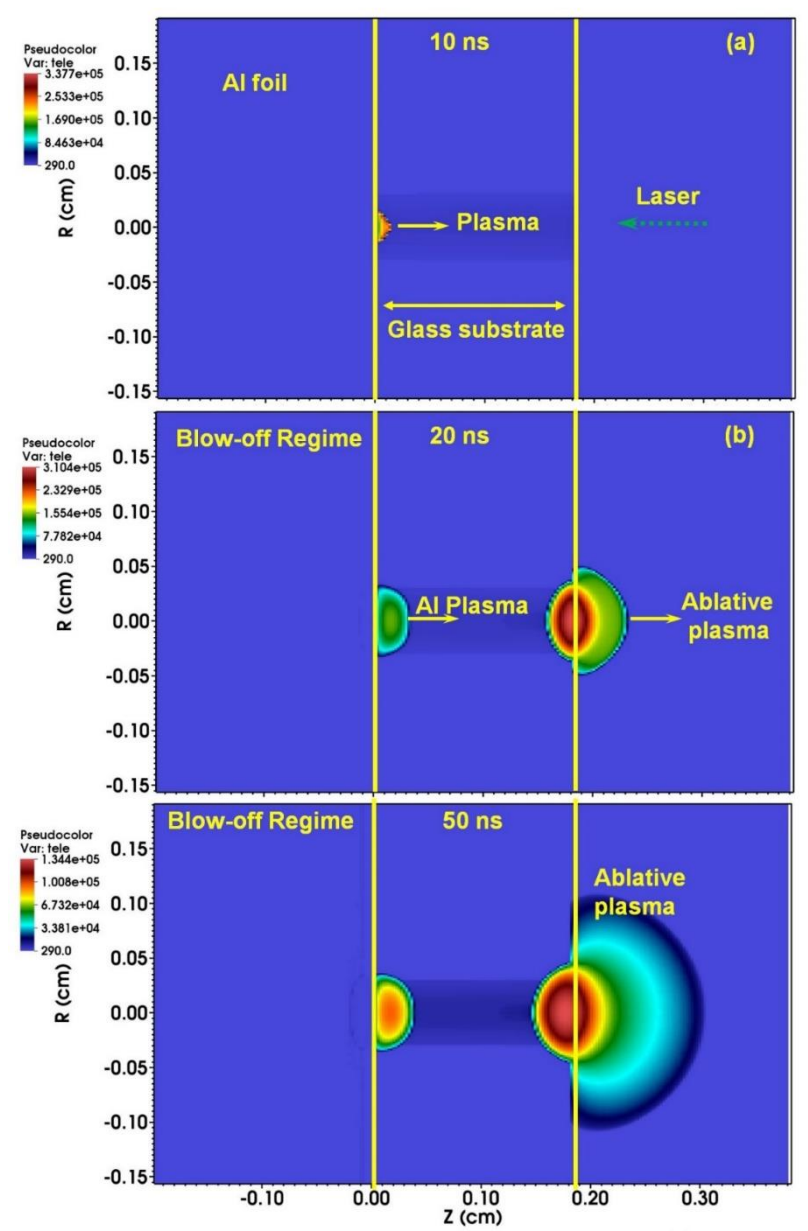


Fig. 6. 12 Spatial variation of electron temperature at (a) 10, (b) 20 and (c) 50 ns respectively for the input laser energy of 50 mJ

Fig. 6.12 (a) shows the spatial variation of electron temperature at 10 ns. During the time of interaction of the leading edge of laser pulse a maximum absorption of the energy is taking

place at the Al-glass interface resulting in the generation of aluminium plasma at the Al-glass interface. The maximum temperature generated at 10 ns at the Al-glass interface is  $3.37 \times 10^5$  K. To account for the deposition of energy in accordance with the spatial variation of the laser energy, a part of energy deposition is considered at the glass – air interface (10% of the total incident energy as considered from experimental data) [49]. This has resulted in the generation of the plasma at the front end of the glass substrate (glass-air interface). The peak temperature of the plasma generated at the ablation regime of the glass substrate is  $3.1 \times 10^5$  K, while the peak temperature at the Al-glass interface has decreased to  $1.5 \times 10^5$  K, because of the shielding of the ablative plasma.

Fig. 6.12(c) shows the temperature variation at 50 ns showing the expansion of the ablative plasma into the background gas and Al plasma (generated at the Al-glass interface). The peak temperature at the Al-glass interface has decreased to  $1.0\times10^5$  K while that at the ablative regime has decreased to  $1.3\times10^5$  K. A slight variation in the temperature in the glass substrate along the laser propagation axis is observed due to the absorption of the energy taken place during the laser energy deposition.

As observed in the fig. 6.12 (a)-(c), the plasma temperature is increasing from the initial time of irradiation of laser pulse to 10 ns, after which the temperature is decreasing and expanding more along the laser propagation axis. When the pressure at the SF exceeds the shear strength of the material the un-vaporized part ahead of the affected region ruptures, leading to the ejection of blow-off plasma and/or flyers in the rear side of the Al foil. Fig 6.13 (a) & (b) shows the temporal variation evolution of mass density over a duration of 0.2 µs and blow-off SW radius over a duration of 3 µs.

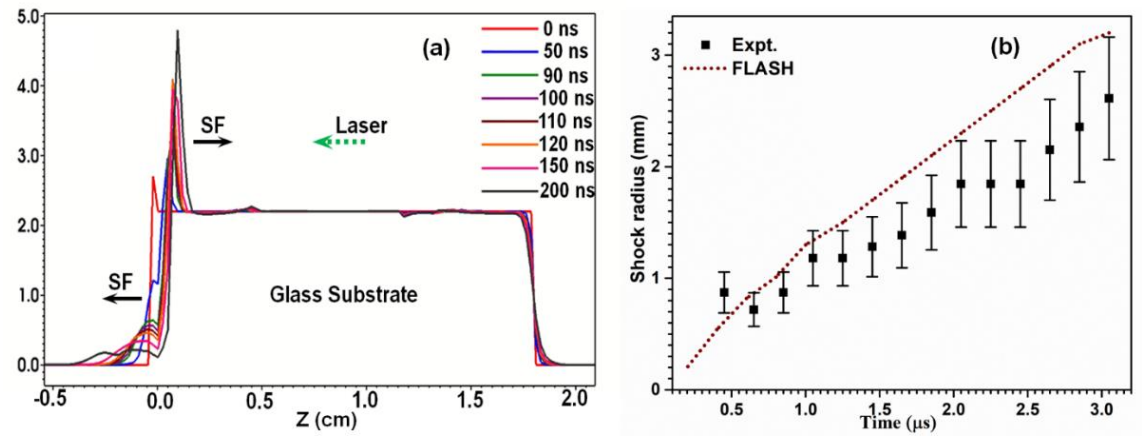


Fig. 6. 13 A line plot of mass density showing the launching of the blow-off SW at the rear side of Al foil and its evolution and temporal evolution of the blow-off shock radius

It can be observed that the density at the ablative region of the aluminium foil has increased over the considered duration of time (Fig. 6.13 (a)). The maximum density attained in the ablation regime over the 200 ns is observed to be 4.8 g/cm<sup>3</sup>.

The maximum density attained at the blow-off SF is 1.0 g/cm³ at 0.05 µs. Fig. 6.13 (b) shows the temporal evolution of the blow-off SF over a duration of 3 µs. The obtained shock radius is compared with the experimentally obtained shock radius[49, 50] and was found to be in line with the experiments. A slight variation in the shock radius is observed in simulated shock radius with experimental as the energy losses due to Fresnel reflections at glass - air and Alglass interfaces were not considered.

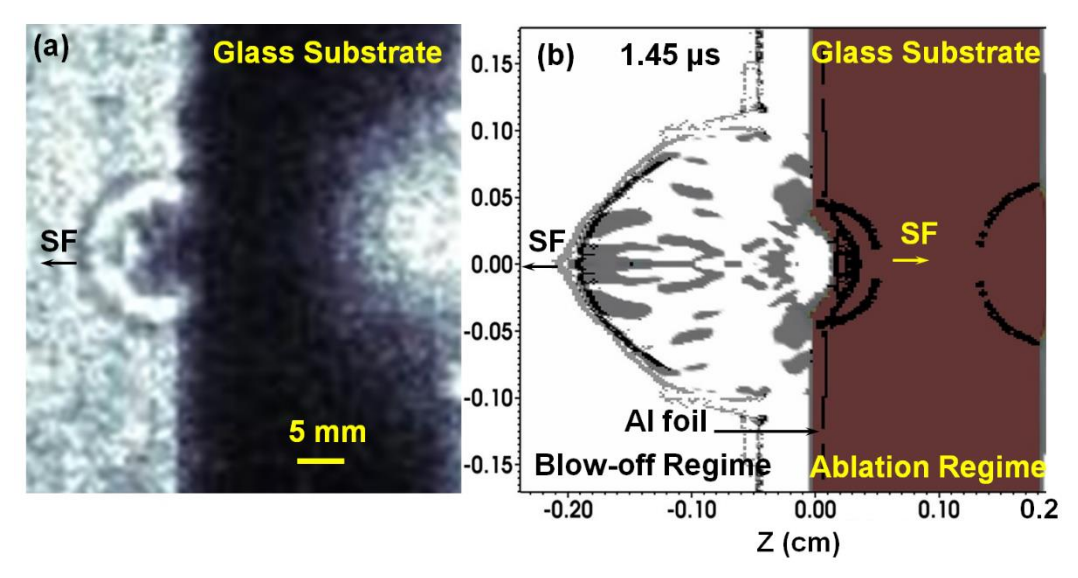


Fig. 6. 14 (a) Shadowgram image of the blow-off SW and (b) mass density obtained from simulations at 1.45 µs generated using 50 mJ energy laser source

Fig. 6.14 (a) & (b) shows a comparison of the spatial evolution of the blow-off shock expansion at 1.45 µs. It can be observed from both the shadowgram and from mass density that the SF in the ablative and blow-off regimes is hemispherical in nature. However, particle ejection is still taking place in addition to the expanding SW. The particle ejection can be seen in Fig. 6.14 (b), at the centre of the SW, along the laser propagation axis.

#### 6.4 Radial confinement of blow-off shock wave

This section discusses the spatial confinement of blow-off SW generated from the Al foil that is confined by a glass substrate as discussed in the above section. To enhance the strength of the blow-off and to study the shock propagation in a macro channel (a shock tube), the blow-off SW is confined radially using a cavity. The radial confinement of the blow-off SW is

discussed in the present section. The blow-off SW so generated is further spatially confined using a glass cavity of length 12 mm and separation distance D between the glass walls 4 mm.

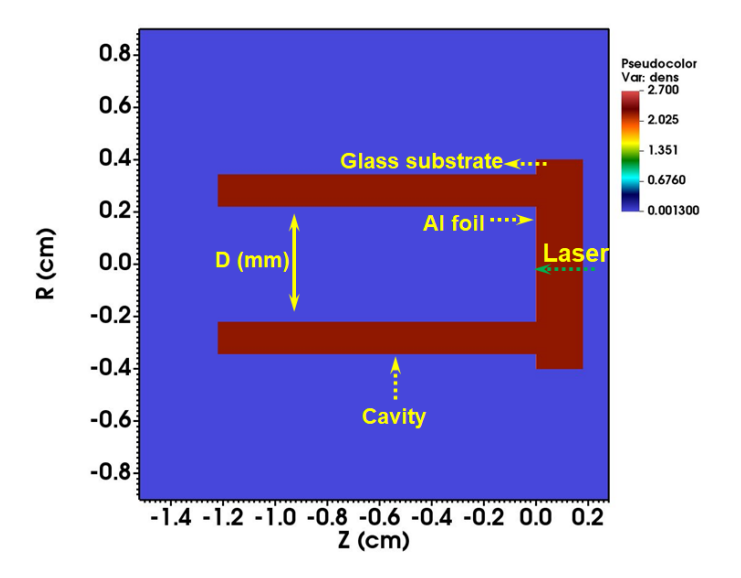


Fig. 6. 15 Simulation domain showing the spatial confinement of the blow-off SW using a glass cavity

Fig. 6.15 shows the simulation domain in which the blow-off SW is confined using a glass cavity with separation distance D. The physical process involved and the generation of the blow-off SW, expansion is discussed in the above section. In the present section, the material blow-off SW generated using a 50 mJ laser source generated at 1 atm background pressure is confined radially using a cavity (assuming two rigid walls) with separation distance 2 mm is discussed. Fig. 6.16 (a)-(d) shows the evolution of mass density in the blow-off regime generated by axial confinement of ablative plasma using a glass substrate (discussed in above section) using 50 mJ laser source at 1 atm background gas pressure.

Fig. 6.16 (a) shows the mass density evolution at 0.5 μs. It can be observed that the plasma and the SW generated were expanding freely in the blow-off regime (For visualization of the details of the plasma and the SW expansion the maximum density is considered to be 0.1 gm/cm<sup>3</sup> as the density at the SW is less when compared to glass and aluminum densities 2.2 and 2.7 gm/cm<sup>3</sup>). It can be observed from Fig. 6.16 (b) & (c) that the SW is still freely expanding irrespective of the presence of the cavity along the radial direction. At 1.5 μs (Fig. 6.16 (c)) the SW starts to interact with the cavity wall.

Fig. 6.16 (d) shows the mass density evolution at 2  $\mu$ s, where the SW is still interacting with the cavity walls. The reflection of the SW from the cavity walls is taking place after 2  $\mu$ s. Fig. 6.17 (a)-(d) shows the mass density evolution between 2.5- 4  $\mu$ s.

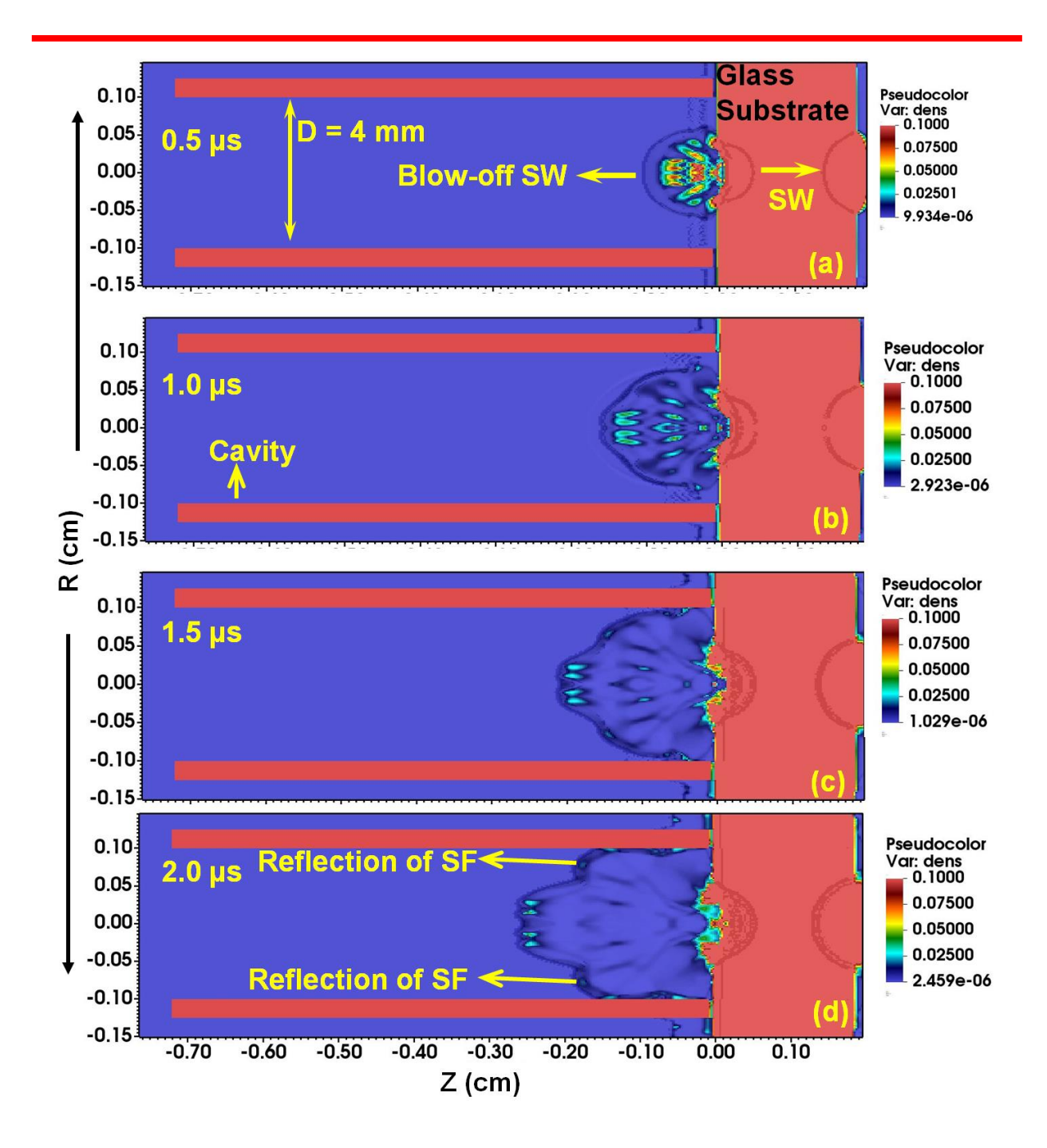


Fig. 6. 16 Spatial evolution of mass density in the blow-off regime confined radially by a cavity at (a) 0.5, (b) 1.0, (c) 1.5 and (d) 2.0 µs respectively generated using a 50 mJ laser source.

Fig.6.17 (a) shows the mass density evolution at 2.5 µs. The reflection of the blow-off SW at the cavity can be observed in Fig. 6.17(a). However, the density at the SF while interacting is very less, while the SW along laser propagation axis is expanding unaffectedly.

The reflection of the SW along radial direction towards the center of the cavity can be observed in Fig. 6.17 (b) - (d) i.e, over a duration of 4  $\mu$ s.

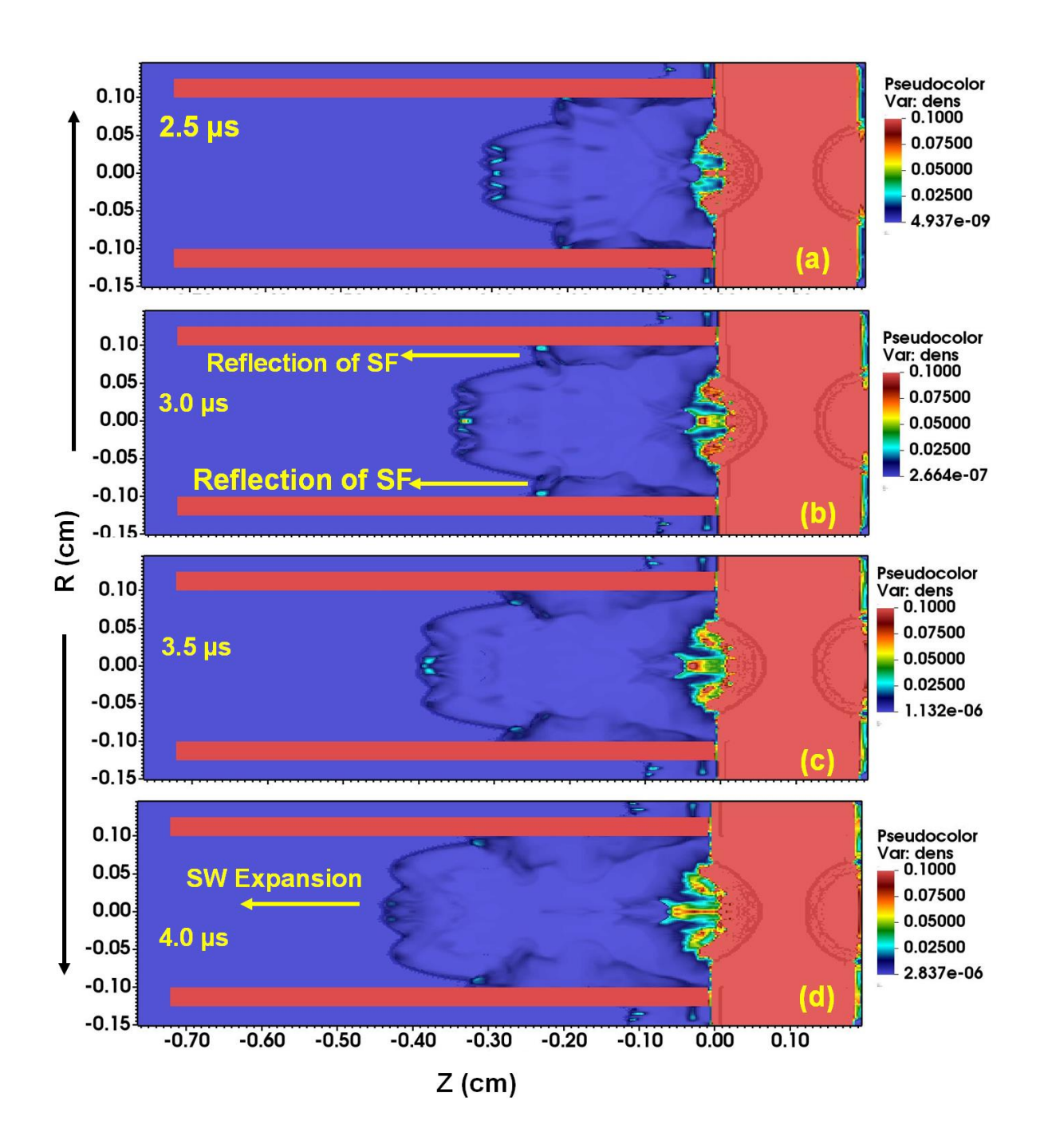


Fig. 6. 17 Spatial variation of mass density in the blow-off regime confined radially by a cavity at (a) 2.5, (b) 3.0, (c) 3.5 and (d) 4.0 µs respectively generated using a 50 mJ laser source.

However, it is to be noted in Fig. 6.17 (d) that no effective variation in the mass density is observed due to its reflection at the cavity or at the center of the cavity. To understand the effect of the radial confinement using the cavity the temporal evolution of the shock pressure in the blow-off regime is compared in radial confinement and without radial confinement. Fig. 6.18 shows the evolution of the blow-off shock pressure with and without radial confinement.

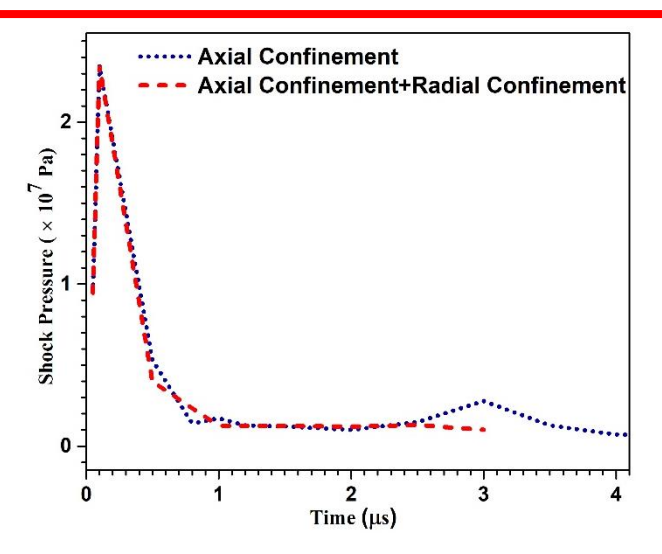


Fig. 6. 18 Temporal evolution of the blow-off shock pressure over a duration of 4  $\mu$ s compared in presence and in absence of the cavity in the blow-off regime.

It can be observed in Fig. 6.18 that the blow-off shock pressure has increased till 0.1  $\mu$ s and is decreasing after 0.1  $\mu$ s. The peak pressure is observed to be 2  $\times$  10<sup>7</sup> Pa. However, it is to be observed that the shock pressure is the same with and without cavity in the radial direction. A slight raise in the shock pressure after 2.5  $\mu$ s is observed which has decreased again after 3  $\mu$ s. Hence, it is understood that the considered dimensions of the cavity are too large to observe an effective reflection of the SW from the glass walls and to interact with the plasma. It is also to be noted that increasing the efficient coupling of the input energy with the plasma generated at the Al-glass interface increases the strength of the blow-off SW.

This results in the effective reflection of the SW, which further interacts with the plasma leading to an enhanced and multiple reflections leading to a micro blast.

#### 6.5 Conclusions

A detailed study on the spatial confinement of ablative and blow-off SW generated from Al foil of thickness 20 µm is studied under different conditions is performed. Initially the ablative and blow-off plasma/shock parameters from the thin foil were studied by varying the background pressure (0.1 – 1 atm) and ambient gas (air, He). It is observed that the pressure and temperature were high at the high background pressure. Similarly, the parameters were high in presence of air when compared to that in presence of He. This can be attributed to the high ionization potential of helium gas when compared to that of air. It is understood that though background conditions were spatially confining the ablative plasma and SW, an effective increase in the blow-off SW is not observed. Hence, to increase the blow-off SW

strength and to generate the material SW in the rear side of the foil, the metal foil is attached to a glass substrate in the front end of the foil to confine the ablative plasma. This is observed to be an efficient method for confining the ablative plasma. A SW of density 1.0 g/cm³ is generated during the initial time scales which is further expanding in the blow-off regime. The SW pressure in the ablation regime has increased by one order due to the confinement. An initial study to further confine the blow-off SW using a glass cavity is performed. However, the dimensions used to confine the SW were found to be not suitable to observe a pronounced enhancement in the shock parameters.

#### **6.6 References**

- 1. Park, H., S. Nam, and S. Park, *Laser Ablation of a Zn Target in Electric Field.* Journal of Physics: Conference Series, 2007. **59**: p. 384-387.
- 2. Singh, R.K. and J. Narayan, *Pulsed-laser evaporation technique for deposition of thin films: Physics and theoretical model.* Physical Review B, 1990. **41**(13): p. 8843-8859.
- 3. Raizer, Y.B.Z.d.a.Y.P., *Physics of Shock Waves and HighTemperature Hydrodynamic Phenomena.* 2012: (Dover Publications.
- 4. Amoruso, S., *Modeling of UV pulsed-laser ablation of metallic targets*. Applied Physics A, 1999. **69**(3): p. 323-332.
- 5. Aghaei, M., S. Mehrabian, and S.H. Tavassoli, *Simulation of nanosecond pulsed laser ablation of copper samples: A focus on laser induced plasma radiation.* Journal of Applied Physics, 2008. **104**(5): p. 053303.
- 6. DeMichelis, C., Laser induced gas breakdown: A bibliographical review. IEEE Journal of Quantum Electronics, 1969. 5(4): p. 188-202.
- 7. Ireland, C.L.M. and C.G. Morgan, *Gas breakdown by a short laser pulse*. Journal of Physics D: Applied Physics, 1973. **6**(6): p. 720-729.
- 8. Raizer, I.P. Laser-induced discharge phenomena. 1977.
- 9. Bakos, J.S., et al., *Laser blow-off plasma propagating in low-pressure gas.* Applied Physics Letters, 1987. **51**(10): p. 734-736.
- 10.Skeen, C.H. and C.M. York, *LASER-INDUCED* "BLOW-OFF" PHENOMENA. Applied Physics Letters, 1968. **12**(11): p. 369-371.
- 11. Fabbro, R., et al., *Physical study of laser-produced plasma in confined geometry*. Journal of Applied Physics, 1990. **68**(2): p. 775-784.
- 12. Ashfold, M., et al., *Pulser Laser Ablation and Deposition of Thin Films*. Chemical Society Reviews, 2004. **33**: p. 23-31.
- 13. Harilal, S.S., et al., *Internal structure and expansion dynamics of laser ablation plumes into ambient gases.* Journal of Applied Physics, 2003. **93**(5): p. 2380-2388.
- 14.Donnelly, T., et al., Angular distributions of plume components in ultrafast laser ablation of metal targets. Applied Physics A, 2010. **100**(2): p. 569-574.
- 15. Hahn, D.W. and N. Omenetto, Laser-Induced Breakdown Spectroscopy (LIBS), Part I: Review of Basic Diagnostics and Plasma—Particle Interactions: Still-Challenging Issues within the Analytical Plasma Community. Applied Spectroscopy, 2010. **64**(12): p. 335A-336A.
- 16.R. M. Kurtz, J.A.S., V. M. Elner, D. Du, X. B. Liu, A. Sugar, and G.A. Mourou, Invest. Ophthalmol. Visual Sci, 1994. **35**(4).
- 17. Hassane and P. Kulkarni, *The effect of ultrafast laser wavelength on ablation properties and implications on sample introduction in inductively coupled plasma mass spectrometry*. Journal of Applied Physics, 2013. **114**(2): p. 023103.

- 18.Mahmood, S., et al., On the plume splitting of pulsed laser ablated Fe and Al plasmas. Physics of Plasmas, 2010. 17(10): p. 103105.
- 19. Tao, Y., et al., Effect of shockwave-induced density jump on laser plasma interactions in low-pressure ambient air. Journal of Physics D: Applied Physics, 2006. **39**: p. 4027.
- 20. Cirisan, M., et al., Laser plasma plume structure and dynamics in the ambient air: The early stage of expansion. Journal of Applied Physics, 2011. **109**(10): p. 103301.
- 21. Gomes, A., et al., Experimental and theoretical study of the expansion of a metallic vapour plasma produced by laser. Journal of Physics D: Applied Physics, 2004. **37**(5): p. 689-696.
- 22. Farid, N., et al., *Emission features and expansion dynamics of nanosecond laser ablation plumes at different ambient pressures.* Journal of Applied Physics, 2014. **115**(3): p. 033107.
- 23. Wynne, A.E. and B.C. Stuart, Rate dependence of short-pulse laser ablation of metals in air and vacuum. Applied Physics A, 2003. **76**(3): p. 373-378.
- 24. Capitelli, M., et al., *Laser-induced plasma expansion: theoretical and experimental aspects.* Spectrochimica Acta Part B: Atomic Spectroscopy, 2004. **59**(3): p. 271-289.
- 25.Bogaerts, A. and Z. Chen, Effect of laser parameters on laser ablation and laser-induced plasma formation: A numerical modeling investigation. Spectrochimica Acta Part B: Atomic Spectroscopy, 2005. **60**(9): p. 1280-1307.
- 26.Chen, Z. and A. Bogaerts, *Laser ablation of Cu and plume expansion into 1 atm ambient gas.* Journal of Applied Physics, 2005. **97**(6): p. 063305.
- 27. Harilal, S.S., et al., *Influence of ambient gas on the temperature and density of laser produced carbon plasma*. Applied Physics Letters, 1998. **72**(2): p. 167-169.
- 28. Clair, G. and D. L'Hermite, 1D modelling of nanosecond laser ablation of copper samples in argon at P = 1 atm with a wavelength of 532 nm. Journal of Applied Physics, 2011. **110**(8): p. 083307.
- 29. Devaux, D., et al., Generation of shock waves by laser-induced plasma in confined geometry. Journal of Applied Physics, 1993. **74**(4): p. 2268-2273.
- 30.Kumar, B., R.K. Singh, and A. Kumar, *Dynamics of laser-blow-off induced Li plume in confined geometry*. Physics of Plasmas, 2013. **20**(8): p. 083511.
- 31.Zhang, P., et al., Numerical simulation of the temperature field in laser-driven flyer plates by high power nanosecond laser-material interactions. Journal of Physics D: Applied Physics, 2009. **42**(22): p. 225302.
- 32.Benuzzi-Mounaix, A., et al., Laser-driven shock waves for the study of extreme matter states. Plasma Physics and Controlled Fusion, 2006. **48**(12B): p. B347-B358.
- 33.Batani, D., *Matter in extreme conditions produced by lasers.* EPL (Europhysics Letters), 2016. **114**(6): p. 65001.
- 34. Chaurasia, S., et al., *Development of in situ time-resolved Raman spectroscopy facility for dynamic shock loading in materials.* Journal of Instrumentation, 2017. **12**(11): p. P11008-P11008.
- 35. Rastogi, V., et al., Raman spectroscopy of laser shocked polystyrene. Journal of Raman Spectroscopy, 2017. **48**(3): p. 458-464.
- 36.Batani, D., et al., Equation of State Data for Iron at Pressures beyond 10 Mbar. Physical Review Letters, 2002. **88**(23): p. 235502.
- 37. Dezulian, R., et al. Equation of state data of plastic foams at Mbar pr essur es. in 33rd EPS Conference on Plasma Phys. 2006. Rome,.
- 38. Phipps, C., et al., *Review: Laser-Ablation Propulsion*. Journal of Propulsion and Power, 2010. **26**: p. 609-637.
- 39. Fryxell, B., et al., FLASH: An Adaptive Mesh Hydrodynamics Code for Modeling Astrophysical Thermonuclear Flashes. The Astrophysical Journal Supplement Series, 2000. 131(1): p. 273-334.
- 40.Raizer, Y.B.Z.d.a.Y.P., *Physics of Shock Waves and High-Temperature Hydrodynamic Phenomena*. Dover Publications, 2012.
- 41. Sai Shiva, S., et al., Numerical investigation of nanosecond laser induced plasma and shock wave dynamics from air using 2D hydrodynamic code. Physics of Plasmas, 2017. **24**(8): p. 083110.

- 42. Conesa, S., S. Palanco, and J.J. Laserna, *Acoustic and optical emission during laser-induced plasma formation*. Spectrochimica Acta Part B: Atomic Spectroscopy, 2004. **59**(9): p. 1395-1401.
- 43.Sai Shiva, S., Numerical Investigations of ns Laser Induced Shock Waves from Aluminum and Air. 2016, University of Hyderabad: Hyderabad. p. 188.
- 44. Shiva, S.S., et al., The effects of electron thermal radiation on laser ablative shock waves from aluminum plasma into ambient air. Physics of Plasmas, 2016. **23**(5): p. 053107.
- 45. Hussein, A.E., et al., *The role of laser wavelength on plasma generation and expansion of ablation plumes in air.* Journal of Applied Physics, 2013. **113**(14): p. 143305.
- 46. Harilal, S.S., et al., *Background gas collisional effects on expanding fs and ns laser ablation plumes.* Applied Physics A, 2014. **117**(1): p. 319-326.
- 47. Mahmood, S., et al., *Investigation of plume expansion dynamics and estimation of ablation parameters of laser ablated Fe plasma*. Journal of Physics D: Applied Physics, 2009. **42**: p. 135504.
- 48.Dawood, M.S. and J. Margot, Effect of ambient gas pressure and nature on the temporal evolution of aluminum laser-induced plasmas. AIP Advances, 2014. 4(3): p. 037111.
- 49. Guthikonda, N., et al., Effect of Focusing Plane on Laser Blow-off Shock Waves from Confined Aluminum and Copper Foils. Journal of Physics D: Applied Physics, 2021.
- 50.Guthikonda, N., *Dynamics of Confined Laser Induced/Ablative Plasmas and Shock Waves*, in *Physics*. 2020, University of Hyderabad: Hyderabad. p. 211.

## Chapter -7

## Laser Interaction of nanoparticle doped HEMs

Nanoparticles have unique thermochemical, physical and optical properties. Doping of metal nanoparticles to a condensed matrix significantly changes the properties of the obtained composite materials. The aim of the present chapter is to study the optical absorptivity of the composite materials containing various sizes (20-400 nm) of spherical aluminum (Al), silver (Ag), and gold (Au) nanoparticles included in high energy materials (HEMs) such as Penta Erythrtol Tetra Nitrate (PETN), Octahydro-1,3,5,7- tetranitro-1,3,5,7- tetrazocine (HMX), Azides. The presence of photosensitive metal nanoparticles in the High Energy Material (HEM) highly effects the optical absorption of the composite material leading to increase in the sensitivity of the HEM. A detailed study on the effect of the wavelength of the incident laser beam (400-1200 nm), metal nanoparticle that is being doped (Al, Ag and Au), size of the nanoparticle doped (20-400 nm) on the optical absorption (Qabs) of the composite material were presented. The temperature evolution of the Ag – PETN composite is studied with respect to the size of the doped Ag nanoparticle doped. A steep raise in the temperature at the nanoparticle-HEM interface is observed during the incident laser pulse duration (14 ns). Owing to the increased optical absorption by the metal nanoparticles. It is observed that Ag nanoparticles with radius 35 nm is more suitable for doping in PETN leading to pronounced increase in the temperature at the nanoparticle-HEM interface.

#### 7.1 Introduction

Metal nanoparticles are well-known to enhance the optical absorption due to surface plasmon resonance at the interfaces. The optical properties of nanoparticles depends on the particle size, shape, chemical composition, and the local environment. The metal nanoparticles has many further applications in solar cell [1], imaging [2], sensing [3], nano electronics, and storage systems, they are the promising candidates for single-electron switches, transistors [4] and constructing nano structures [5] etc. The composites, based on metal nanoparticles are of the great interest for the optical physics and optoelectronics, nonlinear optical phenomenon [6], application to the thermal cancer therapy [7, 8] due to the enhanced absorption and scattering of light by nanoparticles.

Doping of metal nanoparticles of suitable radius in high energy materials (HEM) has been one of the strategies to increase the coupling of optical radiation into the composites that in turn increases the hotspots and reduce the critical energy density. The composite material with increased optical absorption in turn will result in an effective raise in the temperature, speed of reaction and the release of pressure upon irradiation with a laser beam. The main consequence of the light absorption by the inclusions is their rapid heating that takes them directly to gaseous phase from a solid phase resulting in rise of the temperature of surrounding HEM leading to a self-sustained exothermal reaction site. According to Aduev et. al. [9] the average distance between HEM and metal inclusions in a matrix at which the minimum initiation energy density is reached is  $\approx 2 \,\mu m$ . This distance is an order of magnitude larger than the inclusion size ( $\approx 300 \, \text{nm}$ ), and, hence, their mutual influence can be neglected.

According to the effective medium theory, the linear response of a bulk material consisting of metal nano clusters embedded in it, to the external field (the dielectric functions or polarizabilities of the metal nanoparticle clusters and matrix material) can be replaced by a single effective dielectric function. It is simple averaging powers of dielectric functions of two individual components [4]. The quasi-static approximation act as the basis for the effective medium concept. According to Uwe Kreibig [4], a nano cluster behaves similar to homogeneous material, and its electro dynamic response can be explained by a uniform dielectric function using effective field theory if the size factor of the cluster  $(d/\lambda) \le 10^{-2}$  [10], where d is the size (diameter) of the nanoparticle and  $\lambda$  being the wavelength incident on the composite material. However, the optical response of the cluster matter changes drastically if  $(d/\lambda) > 10^{-2}$ . Hence, the optical effect of light scattering becomes more effective for  $(d/\lambda)$  not

covered by effective medium theory. In this case the quasi-static approximation does not hold any longer. The nanoparticle size we are considering are in the range of 20-400 nm and the wavelength incident is 400-1200 nm, the size factors in the extreme cases are (300/400) 0.75 and (20/1200) 0.016, hence the scattering is supposed to be more dominant. In the present case, the nanoparticle size is comparable to the wavelength of the incident radiation, the light propagation senses the heterogeneity of the composite material, where by the scattering dominates [11, 12].

The collective excitations in metal-dielectric interface is surface plasmons. When the frequency of the incident light is equal to the surface plasmon frequency of the metal particles, the surface plasmon resonance occurs which depends on size and shape of metal nanoparticles. Surface plasmon resonance is one of the unique optical properties of metal nanoparticles [13]. Coinage metals such as copper (Cu), silver (Ag) and gold (Au), support strongly localized surface plasmon resonances in the visible and NIR region while aluminium exhibit the plasmonic resonance in the deep ultraviolet (UV) region [14]. The aim of the present work is to investigate the relationship between the sizes of nanoparticle with surface plasmon frequency in simple spherical shaped nanoparticles. The interaction of light with spherical shape metallic nanoparticles can be examined with the Mie theory [15, 16].

## 7.2 Hot Spot Model

When the laser radiation is incident on the composite material of nanoparticle doped HEM, the metal nanoparticles which are more photosensitive, absorb the radiation. Fig. 7.1 shows the flow chart of process taking place from the time of initiation of the composite material with a laser beam to the energy release from the composite material due to the raise in temperature at the interface between the nanoparticle and HEM.

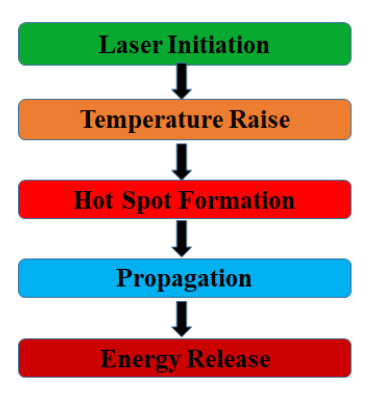


Fig. 7. 1 Flow chart showing the process taking place during the irradiation of laser beam on the nanomaterial-HEM composite

According to the mechanism proposed, the additive metal nanoparticle selectively absorbs laser radiation, heats up, and eventually evaporates, thereby creating a hotspot, which, in turn, initiates the ignition of the surrounding HEM material resulting in an exothermic reaction [8, 9]. Due to the inclusion of the metal nanoparticles in the HEM, there will be an effective decrement in the critical energy density of the HEM [8, 17]. The minimum energy required to initiate a HEM is defined as the critical energy density. The maximum temperature gained by the material during the laser pulse depends on two factors: the optical absorption ( $Q_{abs}$ ) and the energy density of the incident radiation [18] ( $\delta T \propto Q_{abs}$  H). Hence, we present the optical absorption ( $Q_{abs}$ ) by nano composites of 20-400 nm sizes over wavelength range of 400-1200 nm.

## 7.3 Optical Absorption and Scattering

## 7.3.1 Effect of metal nanoparticles on optical absorption

The optical absorption of the composite material depends on the size of the nanoparticle doped in the HEM and the wavelength of the incident radiation. The radiation incident on the nanoparticle undergo multiple reflections at the surface boundaries of the nanoparticle assuming a spherical symmetry [7, 18]. The absorptivity of the inclusions were determined according to Mie theory of scattering. The Mie theory of scattering describes the scattering of a plane monochromatic wave by a homogeneous sphere surrounded by a homogeneous medium [19]. According to Mie theory when radiation is incident on the spherical particle of radius comparable to the wavelength of the incident radiation, a part of radiation is absorbed by the particle and the other part is scattered. Hence, scattering and absorption is leading to a reduction in the incident radiation after traversing a particle. The net amount of radiation loss from the incident radiation is called as extinction [20]. The absorption coefficient  $Q_{abs}$  can be calculated as a difference between coefficient of extinction (Q) and the scattering coefficient  $(Q_{sca})$   $Q_{abs} = Q - Q_{sca}$  [7, 21].

The scattering and extinction coefficients are calculated as the sum of an infinite series of the coefficients of expansion of the electric and magnetic fields of a scattered light wave in the special Riccati–Bessel functions[17]:

$$Q_{sca} = \frac{2}{\rho} \sum_{l=1}^{\infty} (2l+1)(|c_l|^2 + |b_l|^2),$$

$$Q = \frac{2}{\rho^2} Im \sum_{l=1}^{\infty} (2l+1)(c_l - b_l)$$
 (7.1)

Where  $\rho = 2\pi R m_0/\lambda$ ,  $m_0$  is the refractive index of HEM (1.594 for HMX, 1.54 for PETN), R being the radius of the inclusion,  $\lambda$  is the wavelength of light incident,  $c_l$  and  $b_l$  are the coefficients which can be determined using the boundary conditions for nano inclusion's surface.

$$c_l = i \frac{\psi_l(\rho) \, \psi_l'(n\rho) - n\psi_l(\rho)\psi_l(n\rho)}{\varsigma_l(\rho)\psi_l'(n\rho) - n\varsigma_l'(\rho)\psi_l(n\rho)} \tag{7.2}$$

$$b_l = -i \frac{\psi_l'(\rho)\psi_l(n\rho) - n\psi_l(\rho)\psi_l'(n\rho)}{\varsigma_l'(\rho)\psi_l(n\rho) - n\varsigma_l(\rho)\psi_l'(n\rho)}$$
(7.3)

Where  $\psi_b$   $\zeta_l$  are the Bessel's functions,  $n=m_i/m_0$  is the complex refractive index of the nanoparticle relative to the matrix [22].  $\psi_b$   $\zeta_l$  and their derivatives can be determined using the following recurrence relations:

$$\psi_{l+1}(z) = \frac{2l+1}{z}\psi_l(z) - \psi_{l-1}(z), \psi'_l(z) = \psi_{l-1}(z) - \frac{l}{z}\psi_l(z)$$
 (7.4)

If l=1;2 the special functions are:

$$\psi_0(z) = \sin z, \psi_1(z) = \frac{\sin z}{z} - \cos z,$$

$$\psi_0 = ie^{-iz}, \varsigma_l(z) = -e^{-iz}(1 - i/z)$$
(7.5)

Solving the equations (7.1) - (7.5) the optical absorption and scattering coefficients can be determined for the considered composite material. A matlab code is written to solve the above equations and to obtain the extinction co-efficient. The refractive index of the metal nanoparticles varies with the wavelength of the incident laser beam. The refractive index for metals is complex in nature represented by n-ik. Where n being the real part is the refractive index and k being the extinction co-efficient [22]. The values of the complex refractive indices for the three metal nanoparticles i.e., Al, Ag and Au nanoparticles with respect to wavelength were given in table 7.1

## 7. 1 Variation of refractive index of metal nanoparticles (Al, Ag and Au) with respect to wavelength

λ (nm)	Al (m <sub>i</sub> )[17]	$Ag(m_i)[22]$	Au (m <sub>i</sub> )[22]
400	0.32-3.72i	0.173-1.95i	1.658-1.956i
532	0.5-4.59i	0.129-3.25i	0.402-2.54i
600	0.77-5.46i	0.121-3.66i	0.306-2.88i
800	1.78-6.87i	0.145-5.50i	0.188-5.39i
1064	0.98-8.03i	0.226-6.99i	0.272-7.07i
1200	0.78-9.16i	0.329-8.49i	0.312-7.93i

The variation of optical absorption and scattering with respect to the size of the nanoparticle varied from 20 - 300 nm and wavelength of the incident laser beam varied from 400 - 1200 nm were presented in Fig. 7.2 (a-f).

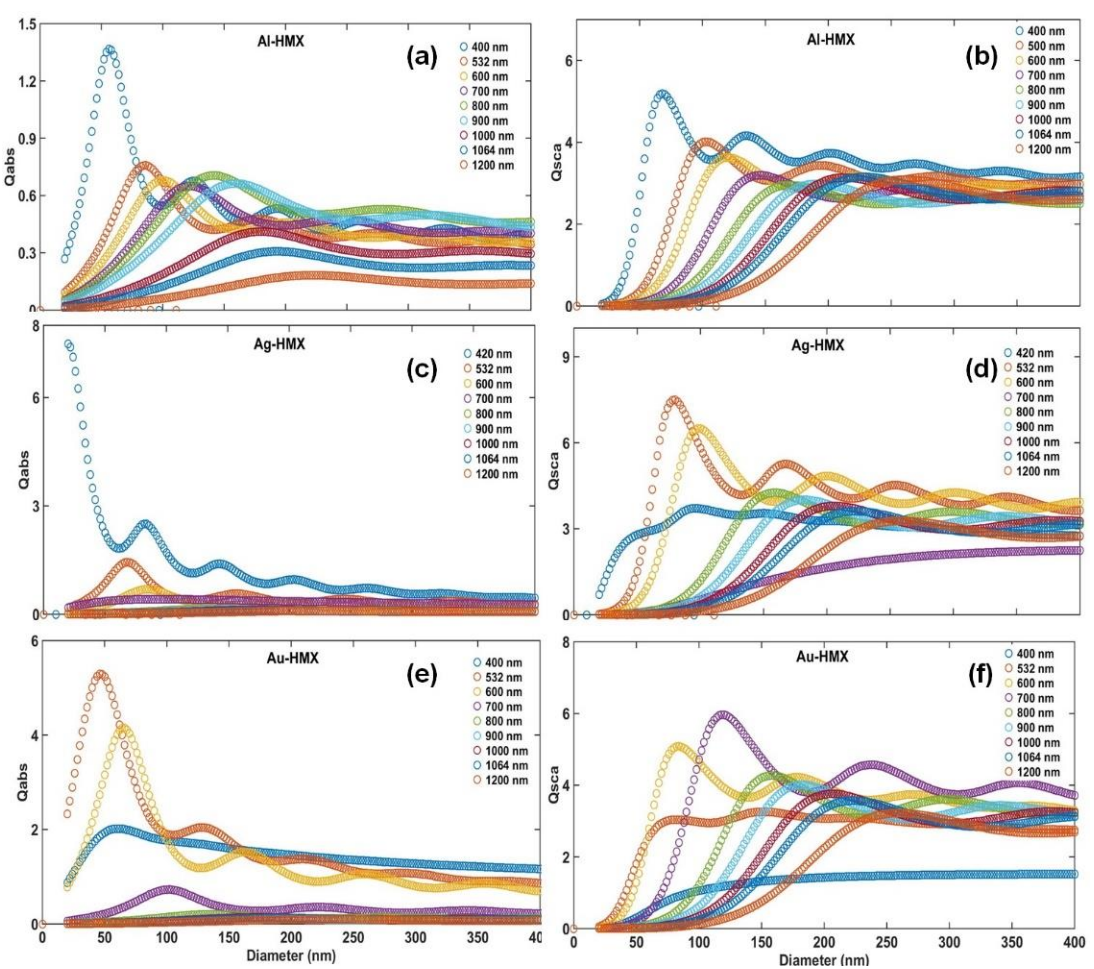


Fig. 7. 2 Variation of optical absorption and scattering when (a-b) Al, (c-d) Ag and (e-f) Au nanoparticles were doped to HMX respectively.

Fig. 7.2 (a&b) shows the variation of optical absorption and scattering when aluminum nanoparticles of different sizes were doped to HMX. The maximum optical absorption is observed for  $\lambda = 400$  nm, d = 55 nm (d/  $\lambda \sim 0.13$ ) and maximum scattering is observed for  $\lambda = 400$  nm, d = 60 nm (d/  $\lambda = 0.15$ ). It is to be observed that different wavelengths have different suitable sizes of the nanoparticle to show a pronounced absorption or scattering. The peaks and dips observed in the Fig. 7.2 (a-f) are because of the changes in the complex refractive indices of the metal nanoparticles.

The absorption tends to zero as the radius tends to zero which is in accordance with the Rayleigh-Jeans law. According to Mie theory, the wavelength influences the  $Q_{abs}$  because of the arguments of special functions  $\varrho = 2\pi R m_0/\lambda$  and  $m_i \varrho/m_0$ . If  $m_i$  i.e., the refractive index of metal nanoparticles do not depend on the wavelength, the  $Q_{abs}(\varrho)$  for all the wavelengths

would coincide. With the increasing wavelength the absorption coefficient is observed to be decreasing. However for  $\lambda$ =800 nm, a slight increment in the absorption co-efficient is observed because of the local maxima occurring in real and imaginary parts of the refractive index of aluminum nanoparticles. However, it is to be noted that the scattering co-efficient is more than the absorption co-efficient at considered wavelengths and sizes of the metal nanoparticles. This indicates that the scattering is more dominant than the absorption.

Fig. 7.2 (c & d) shows the variation of optical absorption and scattering of Ag nanoparticle doped HMX with the varying particle size and incident wavelength. The maximum absorption is observed for d = 25 nm and  $\lambda$  = 400 nm with  $Q_{abs}$  = 1.8 and maximum scattering is observed for d = 75 nm and  $\lambda$  = 532 nm with  $Q_{sca}$  = 7.6. While Fig. 7.2 (e & f) shows the optical absorption and scattering when gold nanoparticles were doped to HMX. It is observed that the optical absorption in gold nanoparticle – HMX composite is more than Al and Ag nanoparticles added to HMX. The maximum is observed at d = 45 nm and  $\lambda$  = 532 nm with  $Q_{abs}$  = 5.2. This is observed because of the surface plasmon resonance (SPR) of gold nanoparticles is takes place at 532 nm. While the SPR of Ag nanoparticles takes place at 420 nm. From all the above observations and from Fig. 7.2 (a-f) it is to be understood that the absorption and scattering were dominant for particle size of nanoparticles (d) less than 200 nm (d < 200 nm). Hence it is understood that when a laser beam of a particular wavelength is incident on a metal nanoparticle doped HEM composite, there exists a suitable size of the nanoparticle which shows maximum optical absorption.

Fig. 7.3 (a) & (b) shows the variation of the optical absorption of aluminum nanoparticle doped PETN with respect to the nanoparticle size (d). It is to be noted that the refractive index of PETN is 1.54 while that of HMX is 1.594. Comparing Fig. 7.2 with Fig. 7.3 one can understand the effect of the refractive index of the HEM on the optical absorption by the composite material. From Fig. 7.3 (a) it can be seen that the maximum optical absorption of the al-PETN composite is 1.2 for the excitation wavelength of 400 nm. While for Al-HMX composite Q<sub>abs</sub> is 1.4 i.e., a slight increase in the optical absorption is observed with the increase in the refractive index of the HEM to which nanoparticle is doped. However, no much variation in the scattering co-efficient is observed. The maximum optical absorption for the al-PETN composite is observed at the excitation wavelength of 400 nm for the nanoparticle size d = 55 nm. The study was performed over 400-1200 nm excitation wavelengths. With the increase in the excitation wavelength, the optical absorption is observed to be decreasing.

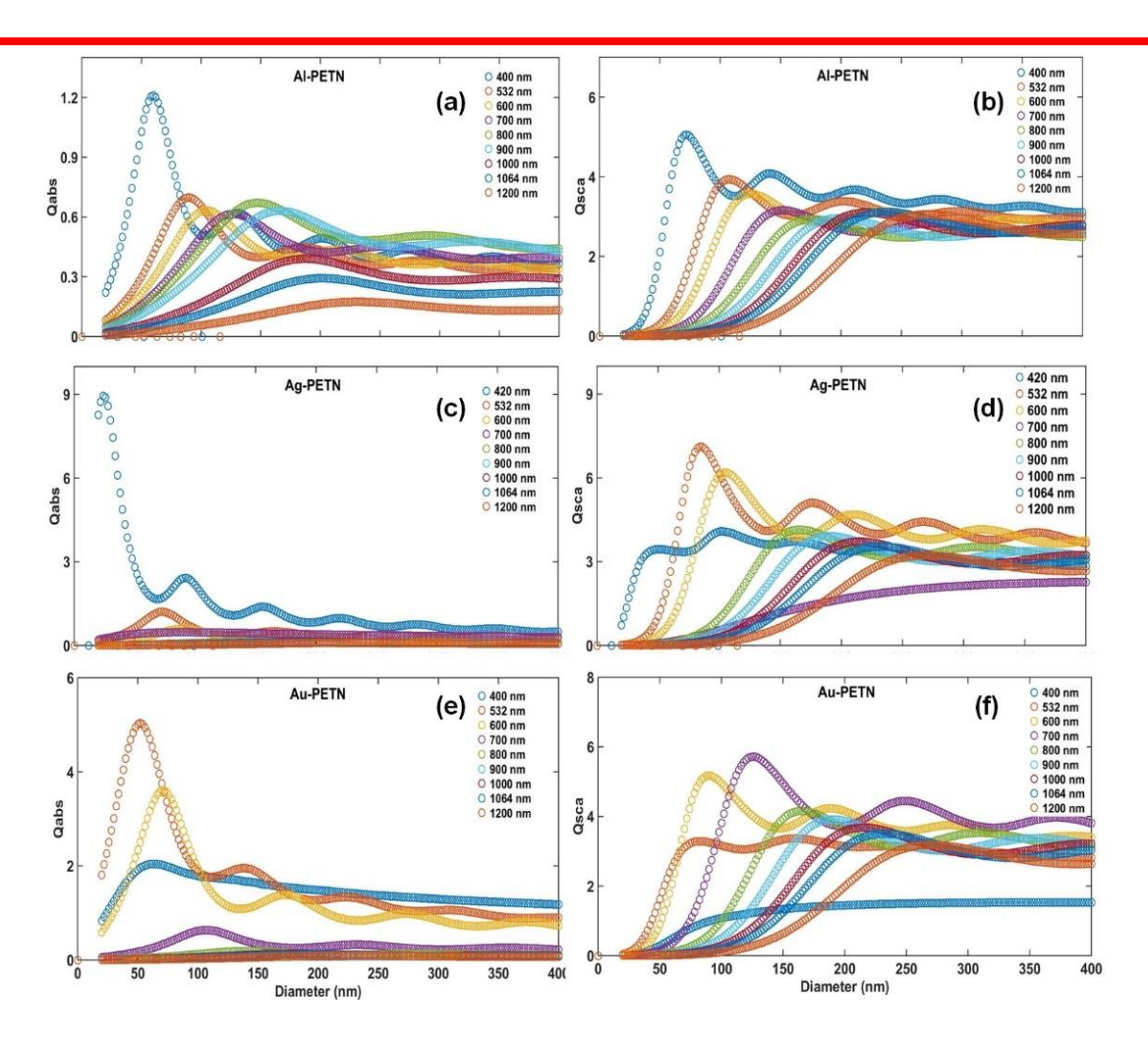


Fig. 7. 3 Variation of optical absorption and scattering when (a-b) Al, (c-d) Ag and (e-f) Au nanoparticles were doped to PETN respectively.

Fig. 7.3(c) & (d) shows the variation of the optical absorption in Ag-PETN composite with respect to the size of the doped nanoparticle. The maximum optical absorption is observed to be 9 for the excitation wavelength of 420 nm. It is to be noted that for the excitation wavelength of 420 nm, the absorption is more dominant than scattering (Fig. 7.3(d)). However, for all the other excitation wavelengths (532-1200 nm), scattering is more prominent than absorption. It is to be observed that a maximum absorption is taking place for the excitation wavelength less than 532 nm after which the absorption is much less than 0.5.

Fig. 7.3 (e) & (f) were showing the optical absorption and scattering co-efficient for Au-PETN composite. The absorption co-efficient is observed to be increasing from 400 to 532 nm of excitation wavelength and decreasing after 532 nm. This can be attributed to the SPR of Au nanoparticles taking place at 532 nm. A similar phenomenon is also observed in the scattering co-efficient. The scattering co-efficient is increasing from 400 – 700 nm of incident wavelength, reached a maximum of 8 at 700 nm and is decreasing after 700 nm. Fig. 7.4 (a) –

(d) shows the suitable combination of size of the metal nanoparticles (Al. Ag and Au) that can be added to PETN, HMX, Lead azide and silver azide when excited by laser beam of wavelength in the range of 400 -1200 nm.

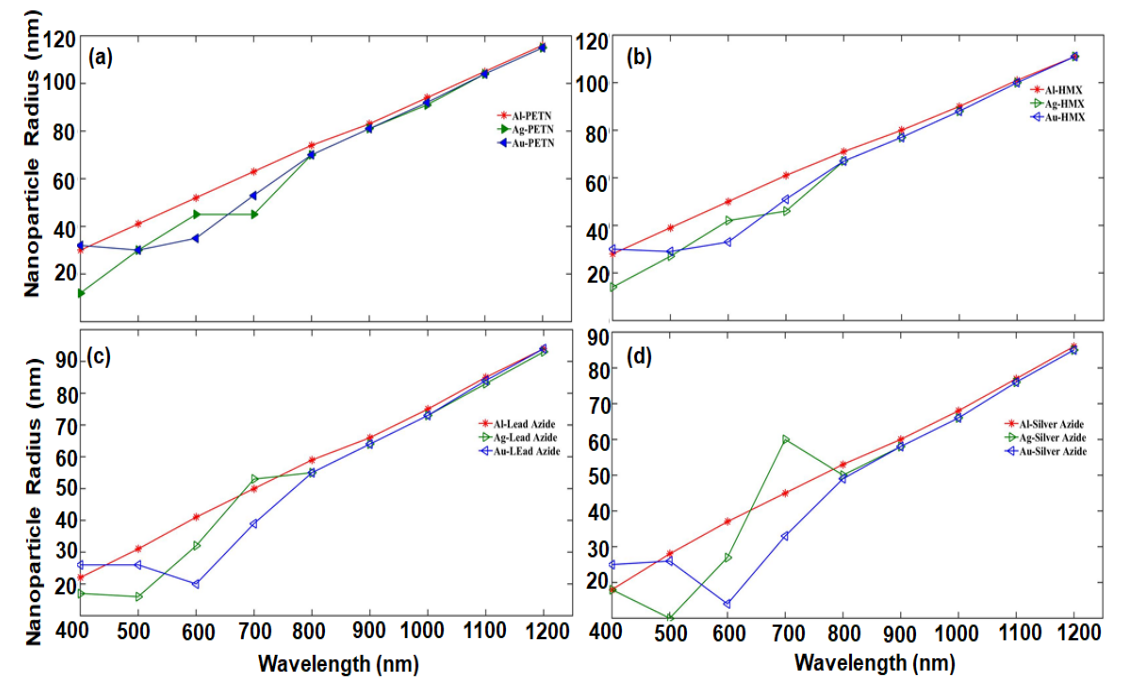


Fig. 7. 4 Identifying the suitable metal nanoparticle Al, Ag and Au size to be added to PETN when initiated with laser beam of different wavelengths

The suitable nanoparticle size is determined by determining the maximum optical absorption taking place in a given combination of the metal nanoparticle-HEM composite and the incident wavelength. Fig. 7.4 (a) determines the suitable nanoparticle size that can be doped to PETN. When Al nanoparticles were doped to PETN, the suitable particle size is increasing almost linearly with the increasing incident wavelength. The ratio  $d/\lambda$  is determined to be in the range of 0.075 - 0.09 to observe a maximum observation when Al nanoparticles were doped to PETN. When Ag nanoparticles were doped to PETN, the suitable nanoparticle size is also increasing with the incident wavelength. However, the suitable size for the wavelengths for 600 and 700 nm is the almost the same. After 700 nm, the suitable particle radius is increasing linearly with incident wavelength. The ratio  $d/\lambda$  for Ag-PETN suitable combination is observed to be in the range of 0.035 - 0.09. While that in case of Au-PETN is observed to be in the same range of 0.05-0.09. A slight decrease in the suitable nanoparticle radius is observed between 500 – 800 nm. The three composites were showing a similar trend and were finding almost the same suitable particle size. However, it is to be noted that only particle size less than 120 nm is showing a prominent absorption in the metal nanoparticle - PETN composite.

Fig. 7.4(b) shows the size of the metal nano particles suitable for doping to HMX. It can be observed that the addition of the three metal nanoparticles (Al, Ag and Au) to HMX is showing almost the similar trend as observed in Fig. 7.4(a). This may be observed because of the refractive indices of PETN and HMX were nearly equal (1.54 and 1.594 respectively). The ratio  $d/\lambda$  for Al, Ag and Au were in the range of 0.075 - 0.09, 0.035 - 0.09 and 0.05 - 0.09 respectively.

Fig. 7.4(c) determines the suitable metal nanoparticle size that can be doped to lead azide, the refractive index of lead azide is 1.85. The maximum nanoparticle size that can be doped to lead azide is less than 100 nm. It is to be noted that the increase in the refractive index of the HEM has resulted in the decrease in the maximum nanoparticle size that can be added. The ratio  $d/\lambda$  for Al, Ag and Au nanoparticles were in the range of 0.05 - 0.08, 0.03 - 0.08 and 0.04 - 0.08 respectively.

The maximum nanoparticle size that can be doped has decreased to less than 90 nm when doping to silver azide (refractive index = 2.0, Fig. 7.4(d)). The ratio  $d/\lambda$  were in the range of 0.04-0.07, 0.05-0.07 and 0.02-0.07 respectively for Al, Ag and Au nanoparticles respectively. As a conclusion from Fig. 7.4 one can confirm that the nanoparticles with radius less than 120 nm is showing a prominent optical absorption. The increase in the refractive index of HEM is leading to a decrease in the nanoparticle radius that can be used. Suitable radius of Al nanoparticles is linearly increasing with the excitation wavelength irrespective of the HEM used. After 800 nm of the incident wavelength all the three metal nanoparticles were having almost the same suitable size that can be added to HEM. The effect of addition of the gold nanoparticles to different HEMs at the excitation wavelength of 532 nm is discussed in the following section.

## 7.3.2 Effect of Hem on optical absorption

The effect of the background material i.e., HEM to which the metal nanoparticles were added on the optical absorption is studied below. Table 7.2 shows the values of refractive indices for different HEMs i.e., PETN, HMX, lead azide and silver azide in the input laser wavelength range of 400 - 1200 nm.

Table 7. 2 Refractive indices of different high energy materials in the wavelength range of 400 - 1200 nm

HEM	Refractive Index in Wavelength Range 400 – 1200 nm [15]		
PETN	1.54		
HMX	1.594		
Lead Azide	1.85		
Silver Azide	2.0		

The effect of doping Ag nanoparticles of different sizes to different HEMs on optical absorption of composite materials for input wavelength of 420 nm is shown in Fig. 7.5. It is observed from Fig.7.5 that with the increase in the refractive index of the HEM, the optical absorption is decreasing for all the sizes of the nanoparticles doped to HEMs. However, with the increase in the refractive index of the HEM a shift in the absorption towards the lower end of the particle sizes is observed. The maximum absorption is observed to be at 35, 35 25 and 25 nm for PETN, HMX, lead azide and silver azide respectively.

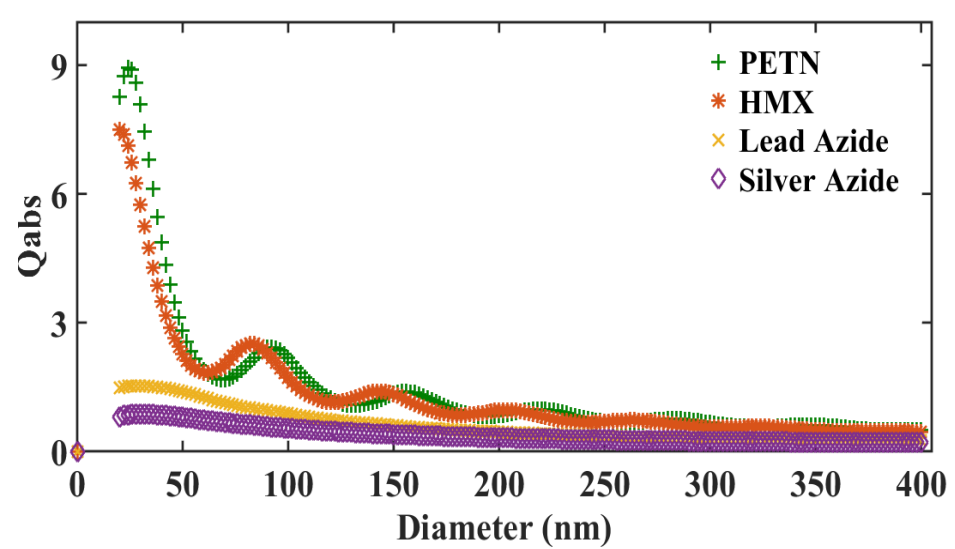


Fig. 7. 5 Variation of optical absorption when Ag nanoparticles of different sizes were doped to different HEMs (PETN, HMX, Lead azide and Silver azide) excited at 420 nm

Among the HEMs considered in the above discussion PETN is showing more optical absorption when doped with Ag nanoparticles. In the present case PETN is ignited by adding the Ag nanoparticle of suitable size. The increase in the optical absorption leads to a maximum raise in temperature at the nanoparticle - HEM interface. Ag nanoparticles show high plasmonic absorption than gold nanoparticles [23]. Doping of Au nanoparticles to PETN and when excited with its SPR frequency ( $\lambda = 532$  nm), the maximum absorption observed is 5 (Please see Fig. 7.3 (e)). However, when silver nanoparticles of suitable size were doped to PETN and excited with its SPR frequency ( $\lambda = 420$  nm), the maximum absorption observed

is 9. Fig. 7.6 (a-c) shows the maximum optical absorption of the three metal nanoparticles were doped to PETN, HMX, lead azide and silver azide.

Fig. 7.6 (a) shows the variation of the maximum absorption when Al nanoparticles were doped to different HEMs. It is observed that the maximum optical absorption ( $Q_{abs-max}$ ) is taking place at the excitation wavelength of 400 nm.  $Q_{abs-max}$  is decreasing with the increase in the incident wavelength. However, in converse to the observation from Fig. 7.5 it is observed that  $Q_{abs-max}$  is increasing with the increase in the refractive index of the HEM at all the excitation wavelengths. i.e., PETN is showing less absorption when compared to silver azide.

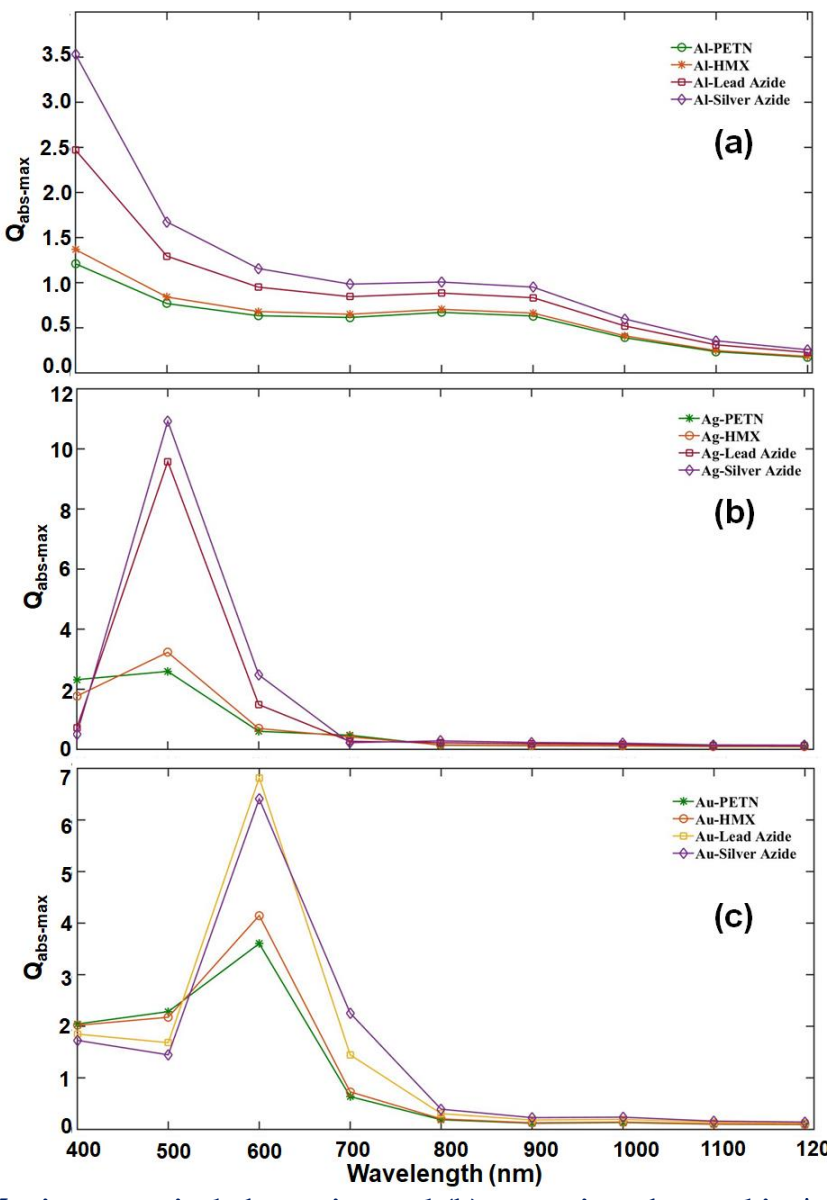


Fig. 7. 6 (a) Maximum optical absorption and (b) scattering observed in Ag nanoparticle doped PETN at different excitation wavelengths

Fig. 7.6 (b) shows the variation of  $Q_{abs-max}$  with respect to the incident wavelength when Ag nanoparticles doped to different HEMs.  $Q_{abs-max}$  of all HEMs is observed at 500 nm. It is observed that at  $\lambda$ =400 nm, the  $Q_{abs-max}$  is high for PETN and less for silver azide ( $Q_{abs-max}$ (PETN) >  $Q_{abs-max}$ (HMX) >  $Q_{abs-max}$ (Lead azide) >  $Q_{abs-max}$ (Silver azide)). However, at and after 500 nm, the condition has reversed i.e.,  $Q_{abs-max}$  is more for silver azide and less for PETN (increasing with the increase in refractive index of HEM).  $Q_{abs-max}$  has almost decreased to less than 0.5 after  $\lambda$ =700 nm.

A similar trend as observed in Fig. 7.6(b) is observed in Au nanoparticle doped HEMs (Fig. 7.6 (c)).  $Q_{abs-max}$  is high for PETN and less for silver azide till 500 nm. After 500 nm i.e., at  $\lambda$ =600 nm,  $Q_{abs-max}$ (silver azide) is more when compared to that of  $Q_{abs-max}$ (PETN).  $Q_{abs-max}$  of all HEMs is observed at 600 nm. While, after  $\lambda$ =700 nm  $Q_{abs-max}$  has decreased to less than 0.5. As a conclusion from the Fig. 7.6 (a) – (c) one can use Al nanoparticle as dopant for excitation wavelength for  $\lambda$ =400 nm and in the range of 700 -900 nm, Ag nanoparticle in the range of  $\lambda$ =420 – 532 nm and Au nanoparticle in the range of 532- 700 nm.

It is to be noted that SPR of Al is less than 400 nm, that of Ag is at 420 nm and that of Au is at 532 nm. Hence, SPR resonating wavelength is acting as a threshold between the optical absorptions to be maximum or minimum with respect to doped HEM. It is discussed in the previous section 7.1 that increase in the optical absorption leads to an efficient raise in the temperature at the metal –HEM interface.

As observed from Fig. 7.6 (b) & (c), Q<sub>abs-max</sub> for Ag-PETN and Au-PETN were almost the same at incident wavelength of 532 nm. Hence, a study of the effect of doping Ag nanoparticles to PETN on temperature generated at the Ag – PETN interface is performed at the excitation wavelength of 532 nm

#### 7.4 Thermal Conduction

The heating of metal nanoparticles leads to a hotspot which is the center of a self-accelerating exothermic reaction. The system of equations, describing conductive heat-transfer processes in the nanoparticles and the exothermal decomposition of the composite media with spherical symmetry are given below [7, 8, 15, 18]:

$$\frac{\partial T}{\partial t} = \alpha \left( \frac{\partial^2 T}{\partial x^2} + \frac{2}{x} \frac{\partial T}{\partial x} \right) + \frac{Q}{c} k_0 n \exp \left( -\frac{E}{k_B T} \right) \text{ if } x > R$$

$$\frac{\partial n}{\partial t} = -k_0 n \exp\left(-\frac{E}{k_B T}\right) \text{ if } x > R$$
 (7.6)

$$\frac{\partial T}{\partial t} = \alpha_m \left( \frac{\partial^2 T}{\partial x^2} + \frac{2}{x} \frac{\partial T}{\partial x} \right) \text{ if } x < R$$
 (7.7)

The boundary conditions at the interface x=R are:

$$J + \alpha c \frac{\partial T}{\partial x}\Big|_{x \to R = 0} - \alpha_m c_m \frac{\partial T}{\partial x}\Big|_{x \to R \neq 0} = 0 \tag{7.8}$$

n is the relative concentration of the HEM (PETN in the present case), which decreases during the reaction from 1 to 0, a and  $a_m$  are the coefficients of thermal conductivity of the matrix and inclusion materials, R is the inclusion radius,  $k_B$  is the Boltzmann constant, E being the activation energy, Q is the heat efficiency of the decomposition,  $k_0$  is the pre-exponential factor, c is the volumetric heat capacity of the matrix. where  $c_m$  is the volumetric heat capacity of the nanoparticle, J(t) is the absorbed density of the laser pulse radiation power. c = 2.22 J/(cm<sup>3</sup> K),  $c_m = 2.7$  J/(cm<sup>3</sup> K),  $c_m = 1.65$  kJ/(mole-K),  $c_m = 1.2 \times 10^{16}$  s<sup>-1</sup>,  $c_m = 1.1 \times 10^{-3}$  cm<sup>2</sup> s<sup>-1</sup>,  $c_m = 0.97$  cm<sup>3</sup> [8].

The temporal dependence of the laser's radiating power is assumed to have normal distribution with the maximum impulse at t=0 as initial condition is given by the following equation

$$J(t) = \sqrt{\pi} Q_{abs} R^2 k_i H_0 \exp\left(\exp\left(-\left(k_i t\right)^2\right)\right)$$
 7.9

where  $k_i = 9.9 \times 10^7$  s<sup>-1</sup> determines the impulse duration (corresponds to the laser pulse duration of 14 ns);  $H_0$  is the impulse energy density;  $Q_{abs}$  is the optical absorption calculated at a particle radius of R using equations (7.1) - (7.5). The heat conduction equations (7.6)-(7.9) were solved using a finite central difference formula of fourth order accuracy. Fig. 7.7 shows the variation of the temperature at the Ag – PETN interface, showing that the maximum temperature is following the trend of the optical absorption with respect to the radius of the doped nanoparticle.

The maximum temperature i.e., the temperature near to the boiling point of Ag is obtained at a particle radius of 35 nm at the excitation wavelength of 532 nm. Hence, Ag nanoparticle of radius 35 nm is found to be more suitable for doping to PETN for an excitation wavelength of 532 nm. Fig. 7.8 (a) shows the spatio-temporal evolution of the temperature over the Ag-PETN composite with Ag nanoparticle radius 35 nm.

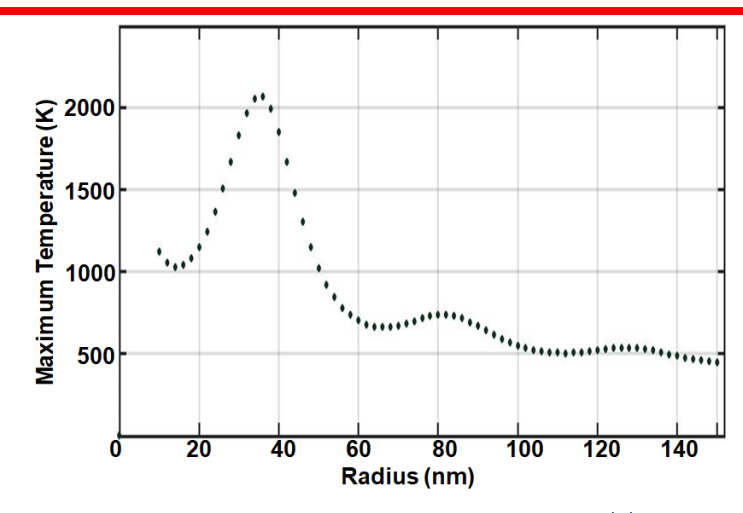


Fig. 7. 7 Temperature variation at the Ag nanoparticle and PETN interface with respect to size of the nanoparticle

The temperature profile of the Ag nanoparticles of radius 35 nm doped to PETN is shown in the Fig. 7. 8. Initial temperature on either side of the interface (surface of the nanoparticle) is assumed to be the room temperature, i.e., 300 K. The laser beam of energy density  $H_0$  is incident at the interface.

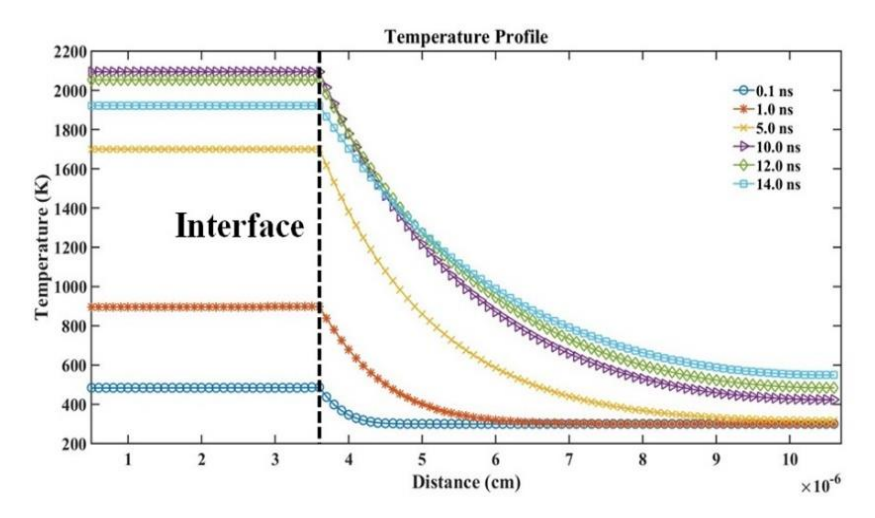


Fig. 7. 8 Temperature profile 35 nm radius Ag nanoparticle doped PETN at an excitation wavelength of 532 nm

Since, the thermal conductivity of the metal nanoparticles is more when compared to that of the HEM, the nanoparticle reaches a thermal equilibrium more quickly when compared to the HEM. The maximum temperature attained for 35 nm particles is 2200 K [24, 25]. For the composite with 35 nm particles the propagation of temperature is much higher than that with the composite of other higher radii nano particles as can be confirmed from Fig. 7.7. The temporal evolution of the surface temperature of the nanoparticle over a duration of 20 ns is presented in Fig. 7.9.

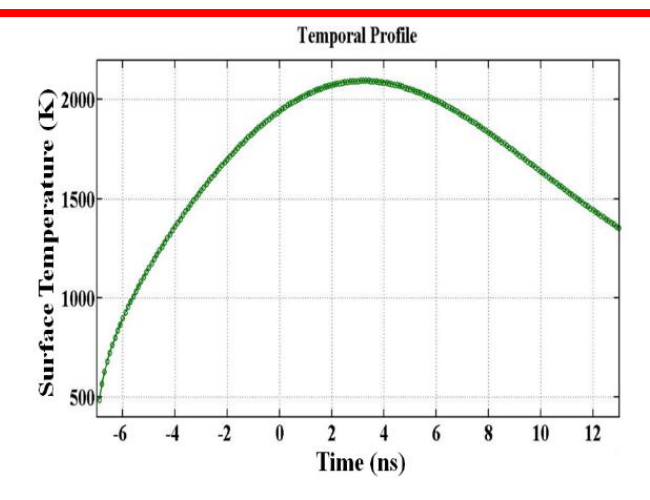


Fig. 7. 9 The temporal profile of the surface temperature of the nanoparticle of radius 35 nm over a duration of 20 ns. T=0 represents the centre of the laser pulse

The first 14 ns represents the duration of the laser pulse interaction with the composite material. The surface temperature has increased till a duration of first 9 ns (i.e., up to 3 ns after the peak of the pulse) after which started equilibrating with the surrounding HEM.

It is to be noted that at the maximum temperature attained at the Ag-PETN interface is 2200 K, the metal nanoparticles at this temperature rapidly blows off and give sufficient energy for the HEM to initiate. Because of the effective raise of the temperature of the surrounding material, the critical energy density of the HEM can be lowered.

#### 7.5 Conclusions

The optical absorption of high energy materials such as PETN, HMX were increased by adding the photosensitive metal nanoparticles such as Al, Ag and Au nanoparticles. The optical absorptivity and scattering of the composite material were determined using Mie theory of scattering assuming the doped nanoparticles to be spherical in nature. For a given combination of metal nanoparticle HEM composite, a suitable size of the nanoparticle to be doped, wavelength of laser suitable for excitation of the composite were determined. However, in all the combinations of metal nanoparticle HEM composites, a maximum absorption is observed for particle radius less than 120 nm. The absorption is observed to be more for metals (Ag and Au) with the more refractive index at certain excitation wavelengths. Ag and gold nanoparticles were showing a pronounced absorption for the excitation wavelengths of 420 and 532 nm respectively irrespective of the HEM to which they are doped. This is because of the excitation frequency matching with their corresponding surface plasmom resonance frequency. It is also determined that Al nanoparticle as dopant is more suitable for the excitation wavelength for

 $\lambda$ =400 nm and in the range of 700 -900 nm, Ag nanoparticle in the range of  $\lambda$ =420 – 532 nm and Au nanoparticle in the range of 532- 700 nm. The heat conduction mechanism taking place through the composite material due to the increased optical absorption is studied. The temporal evolution of temperature at the interface of the nanoparticle HEM is determined when Ag nanoparticles of radius 35 nm were doped to PETN. The maximum temperature attained at the interface is 2200 K which is near to the boiling point of the Ag. Hence, when the laser beam is incident on the composite material, the metal nanoparticles absorb the incident energy, leading to a rise in the temperature and formation of a hotspot at the interface of nanoparticle - HEM. The generated thermal energy is utilised in the ignition of HEM. The maximum temperature obtained at the interface is determined for varying size of Ag nanoparticles when doped to PETN. The maximum temperature is obtained for nanoparticle radius R= 35 nm.

#### 7.6 References

- 1. Markvart, T. and L. Castañer, *Chapter IA-2 Semiconductor Materials and Modelling*, in *Practical Handbook of Photovoltaics (Second Edition)*, A. McEvoy, T. Markvart, and L. Castañer, Editors. 2012, Academic Press: Boston. p. 33-62.
- 2. Novotny, L. and B. Hecht, *Principles of Nano-Optics*. 2006, Cambridge: Cambridge University Press.
- 3. Atwater, H., The Promise of Plasmonics. Scientific American, 2007. 296: p. 56-63.
- 4. Uwe Kreibig, M.V., *Optical Properties of Metal Clusters*. 1 ed. Springer Series in Materials Science. Vol. 25. 1995: Springer-Verlag Berlin Heidelberg. XX, 535.
- 5. Haes, A.J. and R.P. Van Duyne, A Nanoscale Optical Biosensor: Sensitivity and Selectivity of an Approach Based on the Localized Surface Plasmon Resonance Spectroscopy of Triangular Silver Nanoparticles. Journal of the American Chemical Society, 2002. 124(35): p. 10596-10604.
- 6. Sarkhosh, L., et al., Large thermally induced nonlinear refraction of gold nanoparticles stabilized by cyclohexanone. physica status solidi (a), 2010. **207**(10): p. 2303-2310.
- 7. Kalenskii, A.V., et al., *Influence of laser wavelength on the critical energy density for initiation of energetic materials.* Combustion, Explosion, and Shock Waves, 2014. **50**(3): p. 333-338.
- 8. A. V. Kalenskii, M.V.A., Spectral regularities of the critical energy density of the pentaerythriol tetranitratealuminum nanosystems initiated by the laser pulse. Nanosystems: Physics, Chemistry, Mathematics, 2014. 5(6): p. 803–810.
- 9. Aduev, B.P., D.R. Nurmukhametov, and A.V. Puzynin, *Effect of additives of nickel monocarbide nanoparticles on the sensitivity of pentaerythritol tetranitrate to laser irradiation*. Russian Journal of Physical Chemistry B, 2009. **3**(6): p. 923-925.
- 10.Hulst, H.C.v.d., *Light scattering by small particles*. Quarterly Journal of the Royal Meteorological Society. Vol. 84. 1958, New York: John Wiley and Sons, 198-199.
- 11. Prasad, P., Nanophotonics Wiley. New York, 2004.
- 12. Huffman, C.F.B.R., Particles Small Compared with the Wavelength, in Absorption and Scattering of Light by Small Particles. 1998. p. 130-157.
- 13. Becker, J., et al., *The Optimal Aspect Ratio of Gold Nanorods for Plasmonic Bio-sensing.* Plasmonics, 2010. **5**(2): p. 161-167.
- 14.Bharati, M.S.S., Rigid, Flexible SERS Substrates Fabricated using Femtosecond Laser Pulses for Explosives Detection, in ACRHEM. 2020, University of HYderabad: Hyderabad. p. 295.

- 15. Kriger, V.G., et al., Effect of laser radiation absorption efficiency on the heating temperature of inclusions in transparent media. Combustion, Explosion, and Shock Waves, 2012. **48**(6): p. 705-708.
- 16. Yang, Y., et al., Fast Spectroscopy of Laser-Initiated Nanoenergetic Materials. The Journal of Physical Chemistry B, 2003. **107**(19): p. 4485-4493.
- 17. Kriger, V.G., et al., Critical initiation-energy density as a function of single-crystal size in explosive decomposition of silver azide. Combustion, Explosion, and Shock Waves, 2008. 44(2): p. 190-192.
- 18. Kriger, V.G., et al., *Heat-transfer processes upon laser heating of inert-matrix-hosted inclusions*. Thermophysics and Aeromechanics, 2013. **20**(3): p. 367-374.
- 19. Huffman, C.F.B.R., Absorption and Scattering by a Sphere, in Absorption and Scattering of Light by Small Particles. 1998. p. 82-129.
- 20. Bohren, C.F. and D.R. Huffman, Absorption and scattering of light by small particles. 1983.
- 21. Huffman, C.F.B.R., Extinction, in Absorption and Scattering of Light by Small Particles. 1998. p. 286-324.
- 22. Lynch, D.W. and W.R. Hunter, *An Introduction to the Data for Several Metals*, in *Handbook of Optical Constants of Solids*, E.D. Palik, Editor. 1998, Academic Press: Boston. p. 341.
- 23. Blaber, M., M. Arnold, and M. Ford, *A review of the optical properties of alloys and intermetallics for plasmonics*. Journal of physics. Condensed matter: an Institute of Physics journal, 2010. **22**: p. 143201.
- 24. D. P. S. L.Kameswari, R.D., Manpreet Singh, P.Prem Kiran, Optical Absorption in Metal Nanoparticle Doped High Energy Material Composites, in 11th International High Energy Materials Conference & Exhibits, HEMCE-2017. 2017: Pune, INDIA. p. 500.
- 25. Kameswari, D.P.S.L. and P.P. Kiran, *Temperature evolution in silver nanoparticle doped PETN composite*. AIP Conference Proceedings, 2018. **1942**(1): p. 140051.

### Chapter-8

## Conclusions and Future Scope

The effect of spatial confinement of laser generated plasma and shock wave using different methods were simulated in the thesis. It is observed that the acoustic impedance of the confining medium is highly effecting the enhancement in the plasma and shock parameters. The simulations were performed using FLASH 2D radiation hydrodynamic code. The FLASH code is an open source available from university of Chicago. The code is modified according to the experimental conditions that were used in the laboratory. The major modifications include the change in the ionization model and absorption with the Atzeni model of ionization and Zel'dovich model of absorption.

The modified code is standardised by validating the plasma and shock wave dynamics with the experimental results. The laser induced breakdown of air, generation and evolution dynamics of plasma and shock wave were validated with experiments. The effect of the energy, pulse duration in short the effect of intensity on the plasma and shock parameters were studied. The asymmetry in the plasma evolution with the increase in the intensity is observed which is more prominent during the initial time scales. The rolling of plasma is observed due to the hydrodynamic instabilities existing between the plasma and the ambient atmosphere. The evolution dynamics of the plasma parameters such as electron number density and temperature were verified with the values existing in the literature. The laser generated plasma is then confined using different media with nearly equal, and high acoustic impedance.

Initially the laser induced air plasma is confined using another laser induced air plasma along the laser propagation axis. The air plasma generated using a laser beam of energy 50 mJ (S<sub>1</sub>), pulse duration 10 ns with the excitation wavelength of 532 nm is confined using another source (S<sub>2</sub>) generated using input energy of 50 mJ/100 mJ. The effect of the separation distance (d) between the two sources and the acoustic impedance ( $\varrho$ u) of the confining source (S<sub>2</sub>) on the evolution dynamics of the freely expanding source S<sub>1</sub> is studied in detail. The separation distance between the two sources is varied as d=0, 1, 2 and 4 mm. During the interaction of the two sources, the pressure and mass density were observed to be raised because of the interaction of the SFs. The interpenetration of the two SFs at the interaction zone is clearly

visualized and confirmed from the line profiles of mass density and pressure along the laser propagation axis. However, the extent of interaction or interpenetration of the PC of the two sources is explained using the collisionality parameter ( $\zeta$ ). The collisionality parameter is calculated for both the energy ratios and for all the considered separation distances. It is observed that when the higher energy plasma (more impedance) is interacting with the source S<sub>1</sub>, separation distance d< 4 mm, the interpenetration of the two PCs is observed, however, for d=4 mm, the interaction of the plasma outer regions (POR) is observed. However, when the two equal sources were interacting, for all d > 0 mm, the stagnation of the plasmas at the interaction zone is observed. Initiation of the interpenetration of the two sources is observed after 25 µs. While for d=0 mm for both equal and unequal source interaction, the two plasmas were interpenetrating with each other and forming as a single source. The SF from the two sources after interpenetration interact with the PC of the other source resulting in the modification of the plasma dynamics and plasma parameters. Hence, the effect of the interaction of the SW with the PC is studied over a duration of 30 µs. Having understood the effect of confinement of laser generated air plasma with a source of nearly equal acoustic impedance, the study is extended to the radial confinement of the air plasma using a solid target (very high impedance mismatch between the plasma/SW and the cavity material).

The lateral confinement of the laser induced air plasma using a rectangular cavity of different materials and different dimensions is presented in chapter-5. For a fixed length of cavity L=8 mm, varied separation distance between the cavity walls D = 2, 4 and 8 mm and varied cavity materials glass, aluminium and copper the plasma and SW dynamics were studied. A complete picture of the evolution of the freely expanding SW, its interaction and reflection from the cavity walls, interaction of the reflected SW with the plasma is clearly visualized and the corresponding effect on plasma parameters is studied over a duration of 30 µs. It is observed that the reflected SW while interacting with the plasma core, a plasma reheating is taking place resulting in the generation of a secondary radially expanding SW. Due to the compression of the PC along the radial direction, the plasma is squeezed along the laser propagation axis and a rise in plasma temperature and number density were observed. The formation of vortices at the tube ends due to the pressure gradient existing between the pressure inside the tube and that existing outside the tube (ambient atmosphere) is observed. It is observed that decrease in the separation distance between the cavity walls is leading to a quick reflection of the radial SW from the cavity walls leading to an increase in the enhancement in the plasma temperature with the decrease in the separation distance. However, it is understood that d=2mm is not suitable for any of the material chosen (glass, aluminium and copper) for the cavity, since the plasma is exiting from the cavity at early times i.e., time less than 10 µs. L=12 mm and D=8 mm were found to be more suitable for a pronounced enhancement in the plasma parameters and glass is found to be more suitable for the cavity material, such that no fractional ionization of the cavity takes place, during the interaction with the plasma/ SW.

From the above study it is observed that the confinement of the plasma and SW using a medium with much higher impedance when compared to the impedance of the medium in which plasma is generated is showing a pronounced enhancement.

For a more detailed understanding ablation of Al foil under different conditions were takenup in the chapter-6. This chapter is divided into three stages:

Stage – 1: The effect of varied background conditions such as background pressure (varied between 0.1 – 1 atm) and background gas (air, helium) on the expansion dynamics of the ablative plasma and shock wave for the input laser energy of 5 mJ were studied in detail. It is observed that the increase in the background pressure from 0.1 to 1 atm is resulting in the increase in the strength of the SW. The expansion of the plasma and SW in the low ambient pressure is more when compared to that of high ambient pressure. This is because of the inefficient coupling of the laser with the plasma under high ambient pressures. Thus leading to the spatial confinement of the plasma and SW. This has resulted in launching of a strong SW in the blow-off regime. Similarly, the strength of the SW is high in presence of air background when compared to that in presence of He. However, in both the cases of change in ambient pressure and ambient gas, no flyer ejection (material blow-off) is observed.

Stage - 2 The laser ablative plasma from the thin foil generated under background pressure of 1 atm in presence of air medium is confined using a glass slab of 1.8 mm thickness i.e., the aluminium metal foil is attached to a glass slab. The laser beam is focused directly at the aluminium-glass slab interface. The study is performed for the input laser energy of 50 mJ. When the laser beam is focussed at the metal-glass interface, the plasma and SW were generated from the metal foil were confined by the glass substrate. Hence, due to momentum conservation at the front end of the metal foil due to the SW, a SW is launched into the metal foil. However, since the metal foil is very thin, it is blown-off leading to the generation of a blow-off shock wave in the rear side of the metal foil. The density at the SF in the blow-off

regime has the density nearly equal to 1.0 g/cm<sup>3</sup> which is decreasing after few tens of nanoseconds.

Stage-3 The blow-off SW/plasma generated by confining using a glass slab that is generated in stage-2 is confined using a glass cavity of length L=8 mm and separation distance between the cavity walls D = 2 mm. It is observed that the considered dimensions of the cavity are too large to observe an effective reflection of the SW from the glass walls and to interact with the plasma. While in the case of foil confined with a glass slab enhanced coupling of the stronger blow-off SW is observed as the confining tube geometry resulted in a strong reflected SW. The reflected SW further interacts with the plasma leading to an enhanced and multiple reflections leading to a micro blast. It is understood that the effective coupling of the laser energy with the plasma generated increases the strength of the blow-off SW and ejection of the flyer.

An initial study to enhance the laser energy coupling with plasma is performed by adding the metal nanoparticles to the target and study thermal properties of the obtained compound. The variation of the optical absorption and the subsequent increment in the thermal properties is studied in a metal nanoparticle doped high energy material (HEM). The variation of the optical absorption when metal nanoparticles (aluminium, silver, gold) of different sizes (20-400 nm) were doped to HEMs (Penta Erythrtol Tetra Nitrate known as PETN, Octahydro-1,3,5,7-tetranitro-1,3,5,7-tetrazocine known as HMX) were studied in detail over the excitation wavelength of 400 – 1200 nm. Optical absorption of the composite material is determined using the concept of Mie theory. The presence of the metal nanoparticle is leading to the formation of a localized hotspot. The thermal energy generated from the hotspot is utilized in the ignition of the composite material. The increase in the temperature at the nanoparticle-HEM interface increases with the increase in the optical absorption.

The increase in the refractive index is leading to a pronounced enhancement in the optical absorption. Among the considered metal nanoparticles (NPs), Au NPs are having more refractive index for the excitation wavelength of 532 nm. Au doped PETN is showing more absorption at the excitation wavelength of 532 nm, while Ag NPs are showing prominent absorption when doped with HMX for the excitation wavelength of 420 nm. Where 532 nm and 420 nm are the wavelengths at which Au and Ag NPs show exhibit surface plasmon resonance (SPR) respectively. With the obtained optical absorption the spatio-temporal evolution of the temperature at the metal NP-HEM interface is determined by solving the one-dimensional heat conduction equation. The heat conduction equation is solved using finite

#### Conclusions and Future Scope

central difference method of fourth order accuracy. For a composite material of silver NP doped PETN, the NP radius of 35 nm is found to be more suitable and to obtain a maximum temperature of 2200 K at the NP-HEM interface. The critical energy density of the composite material i.e., energy required to initiate the ignition of the composite material is to be determined.

With all the above study the thesis summarizes the effect of spatial confinement on laser generated plasma. A step wise assembly of the confinement followed in the chapters can be used in designing a macro shock tube. A shock tube is device consisting two sections: a driver section, and a driven section separated by a diaphragm. The driver section is the high pressure region while the driven section is a low pressure region. Due to the pressure gradient existing at the diaphragm, the diaphragm burst generating a micro explosion. A study of micro blast generation in the shock tube when a composite of metal nanoparticles doped high energy material used in driver section of the shock tube is our interest. In this regard, a detailed study on the confined blow-off using the glass substrate is to be extended with varied experimental conditions and the dimensions of the confining cavity in the blow-off regime to observe a pronounced enhancement in the blow-off SW strength. Designing such device finds application in bio-medical research like inserting of medicine, blockage removal in arteries, surgical applications, characterization of novel composite materials for ignition/combustion to name a few.

#### **Research Publications**

- 1. Investigation of Stagnation Layer Dynamics of Counter Propagating Laser Induced Air Plasmas: Numerical simulations vis-à-vis experimental observations
  - **D. P. S. L. Kameswari**, Nagaraju Guthikonda, S. Sai Shiva, E. Manikanta, S. Sree Harsha, V. R.Ikkurthi and P. Prem Kiran, Phys. Plasmas 28, 043104 (2021)
- 2. Effect of Focusing Plane on Laser Blow-off Shock Waves from Confined Aluminum and Copper Foils

Nagaraju Guthikonda, S. Sai Shiva, E. Manikanta, **D. P. S. L. Kameswari**, Ikkurthi, V. R, C. D. Sijoy, Prem Kiran Paturi, J. Phys. D: Appl. Phys. **55** 115202 (2021)

### **Conference Proceedings**

- 1. D. P. S. L. Kameswari, P. Prem Kiran, "Temperature evolution in silver nanoparticle doped PETN composite", AIP Conference Proceedings 1942(1):140051(2018)
- 2. S. SaiShiva, Nagaraju Guthikonda, **D. P. S. L. Kameswari**, V. R.Ikkurthi and P. Prem Kiran, "A Three Dimensional Three Temperature Radiation Hydrodynamic Simulations Of Laser Produced Air Plasma Dynamics In Ambient Atmospheric Air", IEEE Transactions on Plasma Science (In Press) Paper ID: 357836
- 3. **D. P. S. L. Kameswari**, Nagaraju Guthikonda, S. Sai Shiva, E. Manikanta, S. Sree Harsha, V. R.Ikkurthi and P. Prem Kiran, 'Dynamics Of Collinear Counterpropagating Laser Plasmas Under Ambient Atmospheric Conditions', IEEE Transactions on Plasma Science (In Press) Paper ID: 357784
- 4. **D. P. S. L. Kameswari**, Nagaraju Guthikonda, E. Manikanta, S. Sai Shiva, S. Sree Harsha, V. R.Ikkurthi and P. Prem Kiran, "Material Dependence Of Lateral Confinement Of Laser Induced Air Plasma," IEEE Transactions on Plasma Science (In Press) Paper ID: 357837

## **Conferences Papers Presented**

#### 2020-2021

- 1. **D. P. S. L. Kameswari**, Nagaraju guthikonda, S. Sai Shiva, E. Manikanta, S. Sree Harsha, V. R. Ikkurthi, P. Prem Kiran, "Dynamics Of Collinear Counterpropagating Laser Plasmas Under Ambient Atmospheric Conditions", IEEE International Conference on Plasma Science (ICOPS-2020), 6th 10th December 2020, Online Conference (Oral)
- D. P. S. L. Kameswari, Nagaraju guthikonda, S. Sai Shiva, E. Manikanta, S. Sree Harsha, V. R. Ikkurthi, P. Prem Kiran, "Material Dependence Of Lateral Confinement Of Laser Induced Air Plasma" IEEE International Conference on Plasma Science (ICOPS-2020), 6th 10th December 2020, Online Conference (Poster)
- 3. S. Sai Shiva, Nagaraju guthikonda, **D. P. S. L. Kameswari**, V. R. Ikkurthi, P. Prem Kiran, "A Three Dimensional Three Temperature Radiation Hydrodynamic Simulations Of Laser Produced Air Plasma Dynamics In Ambient Atmospheric Air, IEEE International

- Conference on Plasma Science (ICOPS-2020), 6th 10th December 2020, Online Conference (Poster)
- 4. **D. P. S. L. Kameswari**, G. Nagaraju, S. Sai Shiva, P. Prem Kiran, "Early Expansion Dynamics Of Plasma And Shock Waves From 20 μm Aluminium Foil" NLS 28, 8th -11th January, 2020, VIT Chennai, Chennai (Poster)

#### **2019-2020**

- 5. **D. P. S. L. Kameswari**, G. Nagaraju, S. Sai Shiva, P. Prem Kiran, "Numerical Study Of Interaction Of Laser Induced Counter Propagating Shock Waves", PLASMA 2019, 3rd 6th December 2019, VIT Chennai, Chennai (Oral)
- 6. **D. P. S. L. Kameswari**, G. Nagaraju, S. Sai Shiva, P. Prem Kiran, "A Comparative Study of Laser Induced Ablative and Blow-off Pressures for Varied Foil Thickness", HEMCE 2019, 16th 18th December, 2019, IITM, Chennai (Poster) (AWARDED BEST POSTER)

#### 2018-2019

- 7. **D. P. S. L. Kameswari**, G. Nagaraju, S. Sai Shiva, P. Prem Kiran, "2D Numerical Simulation of spatio-temporal evolution of Laser Induced Shock Waves In Air", NLS-27, 3rd 6th December 2018, RRCAT, Indore (Poster)
- 8. **D. P. S. L. Kameswari**, G. Nagaraju, S. Sai Shiva, P. Prem Kiran, "Effect of Intensity on Spatio Temporal Evolution of Laser Induced Plasma in Air", PLASMA 2018, 4th 7th December 2018, Delhi University, Delhi (Poster)
- 9. G. Nagaraju, **D. P. S. L. Kameswari**, S. Sai Shiva, P. Prem Kiran, "Dynamics Of Confined Laser Induced Plasma: Effect On Shock Waves", PLASMA 2018, 4th 7th December 2018, Delhi University, Delhi (Poster)
- 10. S. Sai Shiva, G. Nagaraju, **D. P. S. L. Kameswari**, P. Prem Kiran, "Numerical Study Of Laser Induced Blow-off Shock Wave From 10 μm Al Foil In Glass Confinement And Its Comparison With Experiments", PLASMA 2018, 4th 7th December 2018, Delhi University, Delhi (Poster)

#### 2017-2018

- 11. **D. P. S. L. Kameswari**, S. Sai Shiva, P. Prem Kiran, "Numerical Simulation of Laser Induced Shock Waves from Aluminum film in Presence of Helium Gas At Different Ambient Pressures", HEMCE-2017, 23rd 25th November 2017, Pune, Maharashtra (Oral)
- 12. **D. P. S. L. Kameswari**, Ritu Daipuriya, Manpreet Singh, P. Prem Kiran, "Optical Absorption In Metal Nanoparticle Doped High Energy Material Composites" HEMCE-2017, 23rd 25th November 2017, Pune, Maharashtra (Oral)

13. **D. P. S. L. Kameswari**, P. Prem Kiran, "Temperature Evolution In Silver Nanoparticle Doped PETN Composite" DAE Solid State Physics Symposium 26th – 30th December 2017, BARC, Mumbai (Poster)

#### **2016-2017**

- 14. **D. P. S. L. Kameswari**, S. Sai Shiva, P. Prem Kiran, "Light Absorption in Metal Nanoparticle Doped High Energy Materials", NLS-25, 20th -23rd December 2016, KIIT University, Bhubaneswar. (Poster)
- 15. **D. P. S. L. Kameswari**, S. Sai Shiva, P. Prem Kiran, "Effect of Aluminum Nanoparticle Size on Absorptivity of Light In High Energy Materials", Recent Advances in Optical Sciences-II (RAOS) Conference, 06th 07th May 2016, University of Hyderabad, Hyderabad (Poster)

#### **Award Received:**

❖ Received **Out Standing Paper award** for the poster "A Comparative Study of Laser Induced Ablative and Blow-off Pressures for Varied Foil Thickness", presented at HEMCE 2019, 16th − 18th December, 2019, IITM, Chennai

## Spatio-Temporal Evolution of Spatially Confined Laser Ablative Plasma and Shockwaves: A 2D Numerical Simulative Approach

by PSL Kameswari Durvasula

Submission date: 29-Dec-2021 10:30AM (UTC+0530)

Submission ID: 1736207587

File name: Phanisri\_Final\_Thesis\_Similarity\_Check\_29-12-2021.pdf (9.22M)

Word count: 54503

Character count: 260915

Associate Professor School of Physics University of Hyderabad Hyderabad-500 046. (TS) INDIA Librarian

Indira Gandhi Memorial Library UNIVERSITY OF HYDERABAD Central University P.O.

HYDERABAD-500 046.

# Spatio-Temporal Evolution of Spatially Confined Laser Ablative Plasma and Shockwaves: A 2D Numerical Simulative Approach

ORIGINALITY REPORT 21% 5% SIMILARITY INDEX INTERNET SOURCES **PUBLICATIONS** STUDENT PAPERS **PRIMARY SOURCES** D. P. S. L. Kameswari, Nagaraju Guthikonda, 8% S. Sai Shiva, E. Manikanta, S. Sree Harsha, V. R. Ikkurthi, P. Prem Kiran. "Investigation of stagnation layer dynamics of counterpropagating laser induced air plasmas: Numerical simulations vis-à-vis experimental observations", Physics of Plasmas, 2021 Publication D. P. S. L. Kameswari, P. Prem Kiran. 2% "Temperature evolution in silver nanoparticle doped PETN composite", AIP Publishing, 2018 Publication Submitted to University of Hyderabad, Hyderabad Student Paper S. Sai Shiva, Ch. Leela, P. Prem Kiran, C. D. Sijoy, V. R. Ikkurthi, S. Chaturvedi. "Numerical investigation of nanosecond laser induced

plasma and shock wave dynamics from air

Out of 221, 121 Similarity is from Student's publication @ 1, 2,3,601 Primary sources. P. Frem Cirons 20,112/2

Dr. P. Prem Kiran Associate Professor School of Physics University of Hyderabad Hyderabad-500 046. (TS) INDIA

## using 2D hydrodynamic code", Physics of Plasmas, 2017

Publication

Nagaraju Guthikonda, Sai Shiva S, E.
Manikanta, Kameswari P S L D, V. R. Ikkurthi,
C. D. Sijoy, Paturi Prem Kiran. "Effect of
Focusing Plane on Laser Blow-off Shock
Waves from Confined Aluminum and Copper
Foils", Journal of Physics D: Applied Physics,
2021

Publication

S. Sai Shiva, Ch. Leela, P. Prem Kiran, C. D. Sijoy, V. R. Ikkurthi, S. Chaturvedi. "Role of laser absorption and equation-of-state models on ns laser induced ablative plasma and shockwave dynamics in ambient air: Numerical and experimental investigations", Physics of Plasmas, 2019

Publication

S. Sai Shiva, Ch. Leela, P. Prem Kiran, C. D. Sijoy, S. Chaturvedi. "The effects of electron thermal radiation on laser ablative shock waves from aluminum plasma into ambient air", Physics of Plasmas, 2016

flash.uchicago.edu



1%

<1%

